5-2018

Analysis and Design of Lubricating Interfaces in External Gear Machines for High and Low Viscous Working Fluids

Divya Thiagarajan
Purdue University

ANALYSIS AND DESIGN OF LUBRICATING INTERFACES IN EXTERNAL GEAR MACHINES FOR HIGH AND LOW VISCOUS WORKING FLUIDS

A Dissertation

Submitted to the Faculty

of

Purdue University

by

Divya Thiagarajan

In Partial Fulfillment of the

Requirements for the Degree

of

Doctor of Philosophy

May 2018

Purdue University

West Lafayette, Indiana

THE PURDUE UNIVERSITY GRADUATE SCHOOL
STATEMENT OF DISSERTATION APPROVAL

Dr. Andrea Vacca, Chair

School of Mechanical Engineering

Dr. Arezoo Ardekani

School of Mechanical Engineering

Dr. Monika Ivantysynova

School of Mechanical Engineering

Dr. Farshid Sadeghi

School of Mechanical Engineering

Approved by:

Dr. Jay P. Gore

Head of the School Graduate Program

To my grandfather, Mani thatha who believed that I would pursue a PhD years before I even knew it and to Appa, Amma and Karthick for always being part of this journey.

ACKNOWLEDGMENTS

First and foremost, I would like to thank my advisor, Prof. Andrea Vacca for no part of this research would have been possible without his vision, understanding and the countless discussions we have had over the last 5 years. His humility, passion for research and dedicated working style after years of academic success continue to inspire me and working with him has molded me as a successful researcher through my graduate student years. I would also like to acknowledge the continued guidance of Prof. Monika Ivantysynova and in sharing her expert thoughts and suggestions through our many interactions. I am grateful to Prof. Farshid Sadeghi and Prof. Arezoo Ardekani for not only being a part of my advisory committee, but also for offering two very high quality and unique classes at Purdue which have inspired me to pursue a research career in this field. I am also thankful for the technical guidance in many parts of this dissertation, from several industrial collaborators I have worked with during the course of my PhD.

My time at Maha lab will remain as a very cherished and memorable experience in my life, thanks to the many wonderful people I have met over the years, starting with my mentor, Sujan who helped me get started with the gap model. I would like to specially acknowledge the friendship of Matteo Pellegri and Meike Ernst who made Maha a second home for me. Countless hours I spent at the lab would not have been the same without the company of my lab mates over the years : Ram, Sidhant, Natalie, Rene, Matteo Fergnani, Hiral, Mrudula, Rituraj, Tom and many others. Any acknowledgement about Maha is incomplete without the mention of Susan Gauger who always goes the extra mile to help us and truly make us part of a big family. I would also like to thank Connie and Anthony for all the timely help they have done to make my graduate student life a much easier one.

My life in Lafayette (and West Lafayette) made me discover a home away from home, thanks to the life long friends I have made in town. For this, I would like to thank the company of Priya, Maria, Gaurav, Girija, Fabrizio, Shruthi Dasappa, Shruthi Kubatur and especially Ninad for making life outside the lab a very fulfilling experience.

I am also indebted to my long time friends who have become like family: Vasundhara, Sruthi, Gayathri and Guhan for patiently listening to all my frustrations in graduate school and for being a constant part of my life over all these years. I saved the best for the last in thanking my mom, dad and brother for their endless love and for being my strongest support in all my decisions in life, especially the ones during graduate school.

TABLE OF CONTENTS

Page

Page

Page

Page

Page

LIST OF TABLES

Table Page

LIST OF FIGURES

Figure Page

Figure Page

Figure Page

Figure Page

Figure Page

Figure Page

Figure Page

Figure Page

Figure Page

Figure Page

Figure Page

Figure Page

Figure Page

Figure Page

SYMBOLS

A	Area, m^2
a_r	Real contact area, m^2
a_{nom}	Nominal area, m^2
α	Coefficient of discharge
α_p	Pressure coefficient for viscosity, $Pa - l$
β_p	Pressure coefficient for density, $Pa - m^3/kg$
C_1	Cavitation Index
c_p	Specific heat capacity, J/kgK
C_p	Contact pressure coefficient, Pa
d	Wheelbase of external gear machine, m
δ	Roughness amplitude, m
e Eccentricity	
E	Young's modulus, Pa
E^*	Composite Young's modulus, Pa
η	Efficiency
$\mathbf{F}$	Force vector, N
$\mathbf{f}$	Body force vector, N
h_T	Gap compliance, m
H	Material hardness, Pa
H_Y	Non-dimensional hardness parameter
H_s	Hersey number
γ	Asperity aspect ratio
k	Thermal conductivity, W/mK
ξ, λ	Lame's coefficients, Pa
λ_x, λ_y	Autocorrelation lengths, m

Λ	Non-dimensional film parameter
m	Mass, kg
M	Moment, $N - m$
μ	Dynamic viscosity, $Pa - s$
μ_f	Friction Coefficient
n	Rotational speed, rpm
$\mathbf{n}$	Unit normal vector
$\mathbf{O}$	Order of magnitude
Ω	Area of the orifices, m^2
ω	Angular velocity vector, rad/s
p	Pressure, Pa
P	Power Loss, W
$\overline{P_c}$	Non-dimensional contact pressure
ϕ_x, ϕ_y	Pressure flow factors
ϕ_c	Contact factor
ϕ_s	Shear factor
$\phi_f, \phi_{fp}, \phi_{fs}$	Shear stress coefficients
Q	Flow rate, m^3/s
R	Outer radius of gears, m
R_q	RMS surface roughness, m
$\mathbf{r}$	Radius vector, m
ρ	Density, kg/m^3
ρ'	Non-dimensional Density
θ	Angle, $degrees$
t	Time, s
$\mathbf{T}$	Torque, Nm
T	Temperature, K
τ	shear stress, Pa
$\mathbf{u}$	Deformation vector, m

U	Speed, m/s
u	Velocity in X direction, m/s
v	Velocity in Y direction, m/s
V	Volume, m^3
$\mathbf{v}$	Cartesian velocity vector, m/s
ν	Poisson's ratio
X, Y, Z	Cartesian coordinates, m
ψ_v	Viscous dissipation, W/m^3
ψ_c	Frictional heat dissipation, W/m

ABBREVIATIONS

avg	average
bal	balance
b	bottom
c	contact
cav	Cavitating
ncav	Non-Cavitating
fc	frictional contact
d	drive gear
e	element
g	gear
i,j	indices
lat	lateral lubricating gap
loss	losses
leak	leakages
max	maximum
min	minimum
nFaces	total number of faces
rad	radial gap
ref	reference
rel	relief
sh	shear
t	top surface
th	theoretical
tot	total
tr	Turbulent resistance

var	variable
CAD	Computer Aided Design
CFD	Computational Fluid Dynamics
CLA	Center Line Average
CV	Control Volume
Dec.	Decreased
EGM	External Gear Machine
EHD	Elastohydrodynamic lubrication
FV	Finite Volume
FSI	Fluid Structure Interaction
GNI	Gap Non-uniformity Index
HP	High Pressure
Inc.	Increased
LB	Lateral Bushing
LP	Low Pressure
PDE	Partial Differential Equations
RMS	Root Mean Square
STL	Stereo Lithography
TS	Tooth Space
TSV	Tooth Space Volume
TEHD	Thermo-elastohydrodynamic lubrication
UD	Undeformed
3D	Three-dimensional
1	Driver Gear
2	Driven Gear

ABSTRACT

Thiagarajan, Divya Ph.D., Purdue University, May 2018. Analysis and Design of Lubricating Interfaces in External Gear Machines for High and Low Viscous Working Fluids. Major Professor: Andrea Vacca, School of Mechanical Engineering.

Lubricating interfaces represent a significant design constituent which contribute to the reliability and efficiency of many modern designs of gap compensated external gear machines (EGMs). However, the complex nature of the influence of fluid behavior in these interfaces on the structural and thermal effects of the solid components involved in the lubricating gap makes their design quite challenging. Moreover, the extensive range of applications currently available for EGMs warrant designs which can perform efficiently at extended range of operating conditions as well as with a comprehensive variety of working fluids. In order to improve the understanding of the physics in these lubricating gaps especially in gap compensated units, and thereby achieve virtual prototyping design tools for these conditions, the principal goal of this research is to extend the capabilities of the state of art numerical models for the lubricating interfaces in EGMs.

The present research addresses the design and analysis of the lateral lubricating interface between the lateral bushing and the gears in EGMs for critical operating points as well as for reference working fluids with significant differences in their viscosities which challenge the lubricating ability of the thin film interface. A novel mixed film-TEHD (Thermo-Elastohydrodynamic) model for the lateral lubricating gap was developed as a part of this research to capture the effects of such widely varying design parameters. Two different instances of experimental validation of this mixed film lubrication model were carried out for the reference cases of conventional oil based EGMs, namely with measured torque losses and drain leakage measurements. Furthermore, the capabilities of the lateral gap model are utilized in studying

the impact of the variations in surface finishes on the performance of a commercially available EGM chosen for this study, by considering lateral plate designs of varying surface roughness.

Additional contributions have also been made to the modeling of lateral gaps in EGMs to extend their capabilities, which include consideration of frictional contact forces between the lateral bushing and the housing for the first time. This research demonstrates the significance of considering the effect of friction on the performance of the lubricating gaps in gear pumps by using a reference case of an asymmetrically balanced EGM used for aerospace fuel injection applications. In addition, a mass conserving cavitation algorithm to account for the cavitating conditions in the lubricating interface was also integrated with the mixed lubrication model to improve the stability of the numerical predictions of the pressures in the lubricating gap.

Leveraging the design potential of the numerical tool developed in this research, designs to improve the lubrication performance of EGMs are presented in this work, which include surface shaping on the gears as well as achieving an optimal balance configuration in the lateral gap. These unique modifications along with the mixed lubrication model are then applied to a reference EGM case with water as its working fluid where the low viscosity of a fluid further adds to complexity in designing the lateral lubricating interface. A novel water based EGM prototype which can work at high pressures is thus proposed in this work, to implement and validate the proposed design approaches for the reference low viscous fluid. Furthermore, the present work also proposes certain unique variations to the common designs of oil-EGMs that need to be implemented in the prototype water hydraulic EGM to facilitate its practical implementation especially at high pressure operating conditions.

The methodologies and models developed in this research along with their proven fidelity using experiments could potentially serve as a design tool to formulate new efficient EGM designs for an extensive range of applications and working fluids.

1. INTRODUCTION

1.1 Introduction to External Gear Machines

External gear machines (EGMs) are an integral part of an extensive range of applications which includes aerospace, automotive, construction, agricultural and fluid handling industries. EGMs are especially popular in fluid power applications since they provide the most optimal solution for open circuit systems. The widespread use of these units are due to their compact sizes, good reliability and efficiencies, low costs and simplicity in manufacturing. Commonly found designs of EGMs in the market today are typically characterized by very few internal components to fully achieve their function of a positive displacement machines, both in the pumping and in the motoring modes of operation.

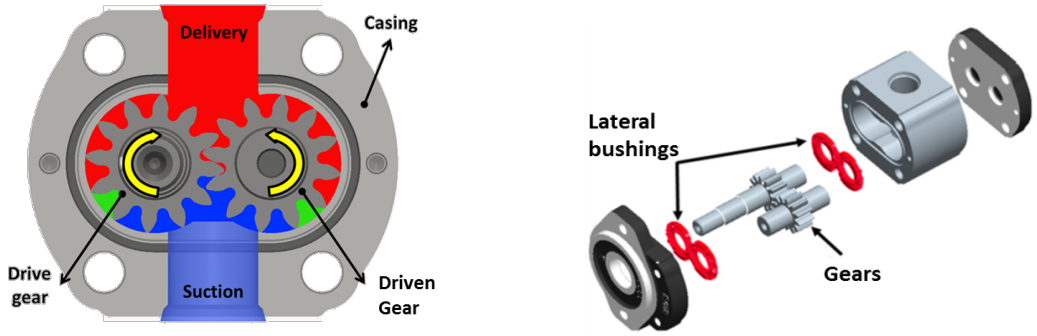

(a) (b)

Figure 1.1. (a) Schematic illustration of operation of a pressure compensated EGM which represents the displacement of the hydraulic fluid at low pressure near the suction port to the delivery port at high pressure, due to the meshing of the gears. The colors blue, green and red shown in the figure represent low, intermediate and high pressures of the fluid respectively. (b) Exploded view of the different internal components in an EGM.

The pumping operation of a typical EGM unit can be understood with the help of the illustration shown in Figure 1.1(a). Due to the meshing action of the driver and the driven gears, low pressure (LP) fluid at the suction side of the unit gets displaced as high pressure (HP) fluid at the delivery side. The external mechanical energy provided to the drive gear shaft at the inlet thus, gets converted to high pressure fluid energy at the outlet.

EGMs available currently in the market have options of having a gap compensation design that changes the lubricating gap configuration according to the operating conditions, with the help of design elements known as lateral bushings. Non gap compensated EGMs typically rely on designing appropriate gap clearances which work reasonably well across different operating conditions. The current research focuses primarily on gap compensated EGMs and Figure 1.1(b) shows the exploded view of the various internal components in a typical pressure compensated EGM unit. It can be seen from the figure that the driver and the driven gears are flanked by the lateral bushings on either side, which offer axial pressure compensation.

Lateral bushings constitute one of the key design components which influence the reliability and operating efficiency of an EGM. Common design elements in a lateral bushing are shown in Figure 1.2. In the side of the lateral bushing facing towards the gears, relief grooves are present as shown in Figure 1.2(a) which are responsible for preventing pressure peaks near the meshing zone and for timing of the connection between the fluid and the ports. The rear side of the bushing has the balance areas at high and low pressures (Figure 1.2(b)) which are separated by a seal. These balance areas are responsible for determining the performance of the lateral lubricating interface between the gears and the lateral bushings shown in Figure 1.3(a).

The lateral bushings in most EGM designs are free to float and are balanced by the combination of the pressure forces arising from the gap that pushes the bushing towards the gears (F_{IN} in Figure 1.3(b)) and an opposing force acting on the balancing areas on the bushing away from the gears (F_{OUT} in Figure 1.3(b)) and these constitute

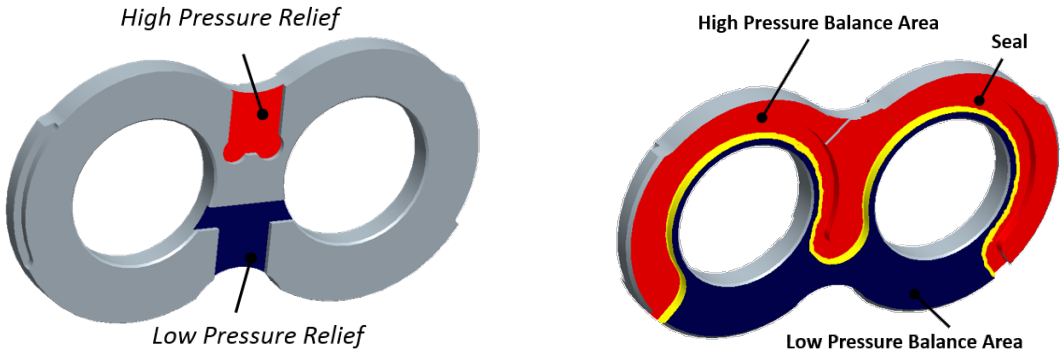

(a) (b)

Figure 1.2. (a) HP and LP relief grooves in the side of the lateral bushing facing the gears (b) HP (represented in red) and LP (represented in blue) Balance areas in the rear side of the lateral bushing.

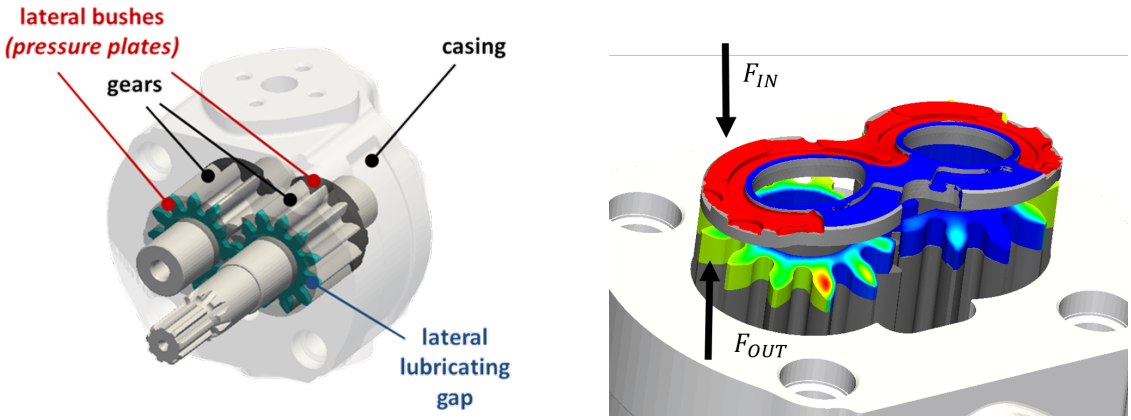

(a) (b)

Figure 1.3. Representation of (a) The lateral lubricating interface between the gears and the lateral bushings (b) Axial balance condition on the lateral bushing comprising of force F_{IN} from the HP and LP balancing areas, which pushes the bushing towards the gears and force F_{OUT} from the pressures in the lubricating gap that directs the bushing away from the gears.

an axial balance condition. This condition directly influences the behavior of the gap and thus, affects the reliability, operating efficiency and life of the EGM. This is due to the fact that an over balanced condition results in low gap heights in the lateral lubricating interface which causes increased wear on the components involved. On the other hand, an under-balanced condition indicates increased values of film thicknesses which results in increased lateral leakages from the gap. Thus, the lateral lubricating interface between the gears and the lateral bushings constitutes a significant design component of an EGM which needs to consider the complex physical phenomena involving structural, thermal, hydrostatic and hydrodynamic effects and is the main focus of the present research work.

In most EGM designs available currently in the market, provisions for journal bearing interfaces are made at the shaft of both the gears to support radial loads in the unit. Subsequently, these interfaces account for the radial movement of the gears which creates a radial lubrication gap between the gears and the casing as shown in red in Figure 1.4(a), along with the lateral gap. This interface mainly accounts for controlled casing wear to provide radial sealing in the unit. Although certain parts in this research include considerations from the radial gaps, the present research mainly focuses on modeling and analyzing the lateral lubricating interface.

Figure 1.4(b) and Figure 1.4(c) show the two commonly found designs of lateral bushings: pressure plate type and bearing block type. While both the designs of lateral bushings perform functions of axial pressure compensation, the bearing block additionally provides structural support to the shaft due to its integrated journal bearing interfaces. In the case of EGMs with the pressure plate type lateral bushing, the journal bearings are found in the casing and the outer covers of the unit. In addition, the lateral lubricating gap model implemented in this work has the ability to model both of these lateral bushing designs to predict the performance of the lateral gap. However, bearing block type designs warrant additional considerations due to frictional contact between the lateral bushing and the casing as shown in Figure 1.5, due to the substantial width of the bushing which can be neglected for the case of

pressure plate type designs. It can be seen from Figure 1.5 that the radial forces from the gear shaft on the journal bearing interface along with the differential fluid pressure force between the top and bottom of the lateral bushing lead to a frictional force between the bushing and the casing.

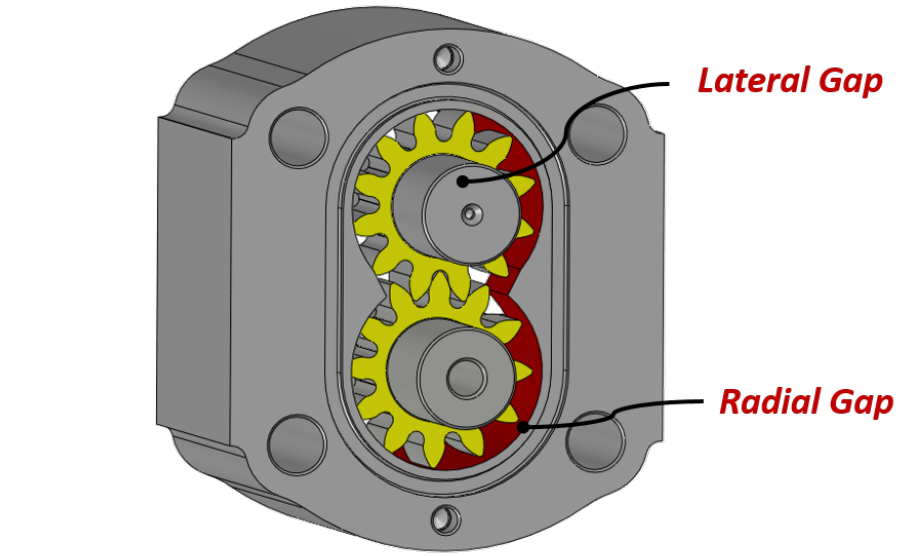

(a)

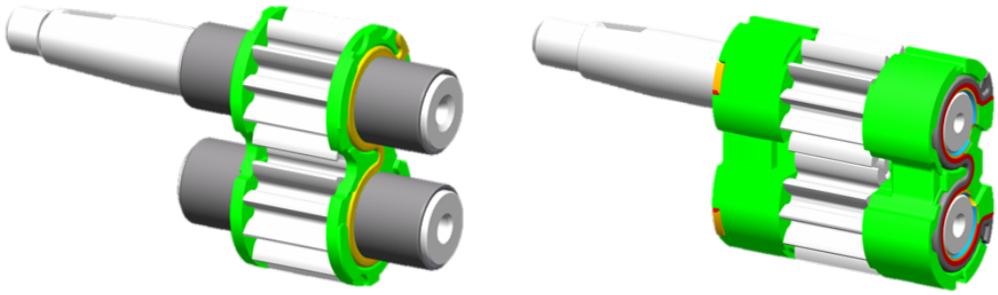

(b) (c)

Figure 1.4. (a) Representation of the lateral and the radial lubricating gaps present in EGMs. Lateral lubricating gap is highlighted in yellow while the radial gap is highlighted in red in the figure. (b) Pressure plate type lateral bushing (c) Bearing block type lateral bushing.

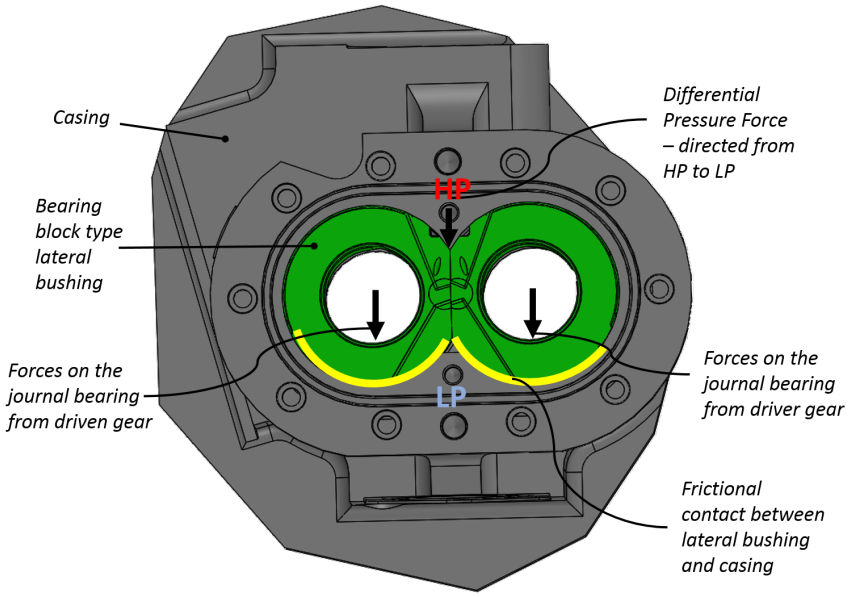

Figure 1.5. Illustration of the location of frictional contact (highlighted in yellow) between the lateral bushing and the gears along with the different radial forces which contribute to the total frictional force.

1.2 Research Motivation

Due to the extensive range of applications currently for EGMs, a variety of designs exist in the market. Many of these designs especially in the fluid handling industries use different kinds of fluids. However, such designs in the industries are usually conceived and developed based on expertise, empirical relationships and trial error prototyping which increases cost, time and efforts. Steps towards more efficient virtual prototyping using numerical tools are still in a relatively nascent stage, especially with respect to designing the lateral lubricating interface which is an integral design component of EGMs. Improperly designed lateral lubricating interface can result in increased wear on the bushing and the gears (as shown in Figure 1.6) which shows wear patterns on these components after several hours of operation, thereby indicating low fluid film thickness in the lateral gap. These conditions are specially sensitive due to

high fluid pressures in the lateral gap which cause considerable structural and thermal deformations of the gears and the lateral bushings along with axial forces which affect the fluid flow and consequently, influence the film thicknesses distribution in the gap (typically in the order of microns). Hence, due to the complexity of the physical phenomena of fluid-structure interaction in the lateral gap, an intricate numerical tool accounting for all its features needs to be developed.

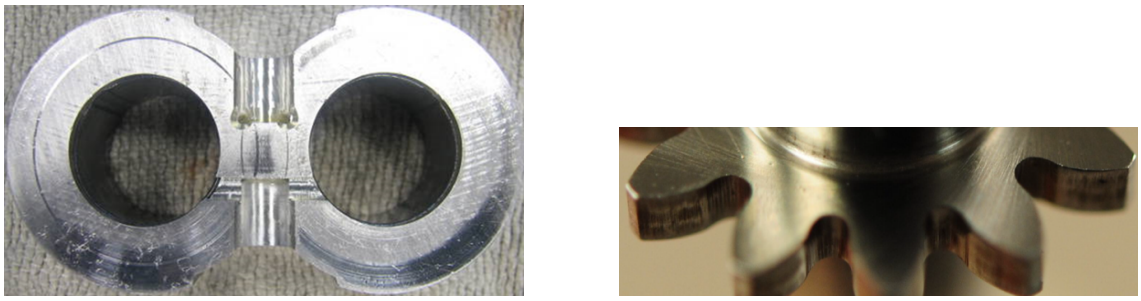

(a) (b)

Figure 1.6. Wear patterns found on the surfaces of (a) Lateral bushings (b) Gears, after several hours of operation.

Numerical modeling of the lateral lubricating interface in EGMs considering the rigid body tilt of the lateral bushing at different operating conditions was first studied by Hooke and Koc [1–3], Borghi et al. [4], Zecchi and Vacca [5]. Morgridge et al. [6] introduced EHD and simplified surface roughness effects for a lateral gap model on a single gear tooth.

The first comprehensive lateral lubricating gap model considering the coupled effects of the fluid, structural and thermal domains was presented in the work of Dhar and Vacca [7–9]. This model was also validated with the help of drain leakage measurements [7] as well as direct capacitive film thickness measurements [8]. The detailed experimental validation in these works indicate the importance of considering EHD as well as the hydrodynamic effects in the lateral gap in predicting accurately the lubrication performance of this interface. Although this is the most advanced

lateral gap model for EGMs in the current state of the art known to the author, there are some inherent limitations of this model which predominantly includes the assumption of a full film lubrication at all times which is also noted in Dhar [9].

At severe operating conditions of EGMs which include extreme operating pressures as well as speeds, this full film lubrication assumption where the surface features of the solid components are neglected becomes insufficient to accurately predict the behavior of the interface. The surface features also become increasingly important for working fluids with low viscosities where the lubrication ability of the interface becomes challenging. This results in lower film thicknesses in the interface when compared to higher viscous fluids, which are in the order of surface roughness heights. At these conditions, the surface features play a substantial role in sharing the high pressure loads in the gap, which directly influences the prediction of the film thickness as well as the related shear losses and leakages that are consequently important for predicting the performance of the entire EGM unit. This warrants mixed lubrication modeling where the surface topography of the interacting surfaces in the interface needs to be coupled with the fluid, structural and thermal effects in the gap. Moreover, due to the absence of a comprehensive mixed lubrication model which also accounts for the influence of surface features, the influence of varying surface roughness of the solid components on the lubrication performance has not been investigated before in the available literature for EGMs.

Mineral oil with a relatively high viscosity is the commonly used working fluid in EGMs for fluid power applications. Therefore, past works in modeling lubricating interfaces in EGMs have primarily focused on designs with oil as the working fluids. However, certain inaccuracies in these models still exist especially at severe operating conditions, which necessitates the need for a comprehensive gap model that also accounts for the interaction of the surface features in the lubricating gap. This is especially significant in predicting the performance of EGMs in applications such as power supply units in electro-hydraulic systems which supply flow on demand with varying speeds of the electric motors. The poor performance of pumping operation

of EGMs at low operating speeds is a limiting factor in these applications. The lubrication performance of these machines could potentially be improved with alternative design modifications. Introduction of micro surface shaping features on the gears was first shown to improve the efficiency of EGM units in Dhar [9], but experimental validation for these surface shaping designs is yet to be achieved. Optimizing the axial balance design as a potential design improvement was investigated in a previously published work of the author in Thiagarajan [10], with the help of an automated numerical algorithm integrated with a fluid structure interaction lateral gap model. Since this dissertation focuses on furthering the understanding of the lateral gap behavior, detailed description of this model is not present here. However, potentials of using this axial balance design tool in conjunction with the formulated gap model in this work are explored in this thesis.

It should also be noted here that cavitation in lubricating interfaces occasionally occurs in regions where the lubricating gap pressures drop below the saturation pressures of the working fluid. This phenomenon becomes especially prevalent at severe operating conditions of the EGM which are one of the main focus points of this research. In previous works that present the modeling of lubricating interfaces in EGMs, cavitation is considered in a simplified manner where the pressures are saturated to a constant value actively during the solution, whenever their values cross a preset threshold. However, in certain operating conditions such as the ones considered in this research, when a significant portion of the lubricating interface is under cavitation, the pressure saturation approach leads to numerical instabilities. Another significant drawback of this approach is that it is not a mass conserving one. Therefore, a numerically robust mass conserving model to handle possible cavitation in lubricating interfaces of EGM is necessary.

Furthermore, previous works in lubrication modeling of EGMs largely considered the use of thin lateral plate where the frictional contact of the plate with the casing (as shown in Figure 1.5) has a negligible impact on the overall performance. However, in the cases of a much thicker lateral bushing, the effect of friction needs to be considered

in the lubrication analysis. This research presents a new approach to consider the frictional contact of the bearing with the housing in an integrated manner with the FSI lateral gap model since this frictional force influences the movement of the lateral bushing which consequently affects the lubrication performance of the unit.

In addition, torque losses encountered in the operation of an EGM unit, is an important design factor since it influences the mechanical efficiency of the unit. A careful consideration of each of the contributing sources of torque losses is necessary for its accurate prediction since they are quite sensitive to varying operating parameters of the EGM design. Due to the complexity in predicting the torque losses, only empirical tools based on experimental data are presently available for this purpose and such experimental measurements are especially quite difficult to obtain while developing novel EGM designs. Numerical prediction of torque losses in EGMs without the need for reliable experimental measurements, has not yet been achieved in literature. It will be shown in this research that a broad consideration of the surface features along with the fluid and structural effects in the EGM unit, especially in the lubricating interfaces, is necessary to develop a numerical tool for predicting its torque losses.

The influence of the properties of working fluid on the lubrication performance of EGMs has never been studied before. Thus, the proposed advances in the numerical modeling as well as the novel design modifications could also potentially be investigated for a more lubrication challenging case of low viscous fluids. A detailed investigation into the design of EGMs under an extensive variation of viscosity of the working fluids is yet to be achieved in literature. Such a comprehensive study can advance the understanding and design methodologies of current state of the art EGMs and their applications.

1.3 Research Objectives

The objective of this dissertation is to formulate, implement and validate a numerical model for EGMs that can achieve the following goals,

1. To include the influence of surface asperities in sharing the high pressure loads in the gap and account for the change in the flow features as well as the hydrodynamic effects induced by the surface. The surface effects need to be coupled with the fluid structure and thermal interaction in the lateral lubricating interface to study its impact on the lubrication performance.

2. To investigate and predict the effect of varying surface roughness of the components on the functioning of the lateral lubricating interfaces.

3. To integrate a numerically stable mass conserving cavitation algorithm in the fully coupled elastohydrodynamic lubricating gap model.

4. To consider the frictional contact between the bearing block type lateral bushings and the casing in predicting the lubrication performance of the unit.

5. To utilize the lateral gap model to investigate novel design methodologies, such as introducing micro-surface shaping for improving the performance of lateral lubricating gap.

6. To propose a novel water-based EGM design to achieve good operating efficiencies and reliability at a wide range of operating conditions, while accounting for the lubricating difficulty due to the low viscosity of water.

7. To investigate the effects of varying viscosities of the working fluid on the overall performance of an EGM.

The lateral gap model in Dhar [9] forms the basis for the current work and the primary objective of this work lies in extending the capabilities and fidelity of this model as well as utilizing it for developing novel EGM designs. In order to test the

versatility of the proposed methodologies, reference fluids with viscosities that are very different from each other will be considered. This is due to the fact that an extended range of viscosities can critically affect the lubrication performance which can be used to demonstrate the applicability of the current work.

1.4 State of the Art

In this section, a detailed description of the available existing literature which is related to the most notable aspects of the current research study is presented.

1.4.1 Modeling of External Gear Machines

While a brief description of the state of the art numerical modeling of the lateral lubricating interfaces in EGMs has already been introduced in Section 1.2, this section presents the detailed description of these gap models as well as advances in modeling other EGM characteristics.

Numerical modeling of the lateral lubricating interfaces in EGMs have been achieved in several works of Koc and Hooke [1–3] and Borghi et al. [4] where the influence of the operating parameters in the EGMs including the tilt of the lateral bushings, on the performance of the lateral gap was studied. Furthermore, these authors also investigated the effect of designing different balance configurations of the lateral bushings in the lubrication performance. A FVM model for the lateral gaps considering the detailed meshing features of the gap domain was developed as part of a larger EGM simulation tool in the work of Zecchi and Vacca [5]. However, all of the aforementioned works assumed a fixed tilt of the lateral bushing or a constant clearance in the lateral gap, and neglected the structural and thermal effects in the gap. Morgridge et al. [6] published an EHD model for the lateral gap along with some surface roughness and profiling effects on a simplified model of a single gear tooth. The contribution of surface features to the load support in the gap as well as its influence in the fluid flow and solids in the gap were not considered in this work.

An EGM lateral gap model incorporating the hydrodynamic effects of the bushing was presented in Dhar and Vacca [11] as an integral part of comprehensive EGM simulation tool. The first fluid structure interaction (FSI) model of the lateral gaps, considering EHD and hydrodynamic effects while predicting film thickness was presented in the work of Dhar and Vacca [7] along with experimental validation using drain leakage measurements. This work confirms that EHD effects are indeed of paramount importance to correctly predict the lubricating film thickness in the EGM lateral gaps. Thermal deformation effects of the lateral bushings and the gears were fully coupled to this FSI-EHD lateral gap model and numerical prediction of the gap heights from this model was validated with indirect capacitive measurements of film thickness values in the work of Dhar and Vacca [8]. However, a comprehensive inclusion of surface features along with other physical phenomena in the prediction of the performance of the lateral gap in EGMs is yet to be developed. A novel model for predicting the performance of asymmetrically balanced EGMs where the performance of the two lubricating interfaces on either side of the gears are different from each other was presented for the first time in Thiagarajan et al. [10]. The frictional force model developed in this work for account for the contact between bushing and casing is integrated with the asymmetric gap model to predict the lubrication performance of a fuel injection pump for the first time in this research.

The analysis of flow delivered from an EGM was first studied with the help of graphical methods in the work of Beacham [12] and with simplified approaches in the studies of Bonacini and Carra [13], Manring and Kasaragadda [14]. The effects of designing various relief grooves and their profiles on the efficiency, pressure peaks and cavitation in EGMs by analyzing the fluid flow have been studied in the works of Casoli et al. [15]. Analysis of different forces acting on the moving parts of the machine with both analytical and numerical solutions have been presented by Ivantysyn and Ivantysynova [16] Falfari and Pelloni [17] and in Zardin and Borghi [18]. There have also been studies related to the flow field in EGMs using CFD applications by Wustmann et al.. [19], Simerics Inc [20], del Campo et al.. [21].

However, most of these works focused mainly on a carrying out detailed analysis on a specific aspect of operation of the EGMs. The development of the simulation tool HYGESim (HYdraulic GEar machine Simulator) focused on modeling accurately the various phenomena associated with the operation of an EGM to provide a complete simulation model of the machine. Formulation, development and experimental validation of HYGESim has been presented previously in the work of Vacca and Guidetti [22]. Since the present work involves using the various sub models in this larger framework of HYGESim, the model will be briefly discussed in Chapter 2.

1.4.2 Mixed Lubricating Modeling

The numerical modeling of the mixed lubrication regime and the influence of surface effects on lubrication performance has been studied widely in tribology for both conformal and non-conformal contact surfaces (Hamrock et al. [23], Spikes and Oliver [24]). Due to the complexity in coupling the interaction of the surfaces with the fluid film, numerous approaches in literature have been proposed which can be broadly divided as stochastic and deterministic (Spikes and Olver [24]). Deterministic modeling is a novel developing field which utilizes 3D idealized geometric representation of surfaces and has been a popular choice for line and point contacts (Zhu and Hu [25, 26]). Statistical representation of the surfaces is used in stochastic mixed lubrication modeling where the 2D lubrication assumption of Reynolds equation is still valid (Dowson [27], Hamrock [23]) and has been applied to many lubricating interfaces including conformal contact surfaces of journal bearing interfaces (Wang et al.. [28–30]). A basic comparison of the two different schools of approach was presented in Dobrica et al. [31], and in Wang and Zhu [32], a macro-micro combination of the two methods was proposed. However, in these works as well as in Wang et al. [30], Evans and Snidle [33] and de Kraker et al. [34], stochastic methods present a relatively simplified approach which are most appropriate for conformal contact surfaces such as the interface studied in the present work. Thus, mixed lubrication

modeling in the current work employs the average flow Reynolds equation for partial lubrication which was first presented in Patir and Cheng [35,36]. Further development to this approach was made in Wu and Zheng [37] and Meng et al. [38] where modified forms of the average Reynolds equation using a contact factor approach along with characteristic expressions for Gaussian distribution of surfaces were presented. These stochastic approaches are integrated into the present work.

The role of asperity contacts in sharing the lubricating loads has been widely studied in Greenwood and Williamson [39], Bowden and Tabor [40], Johnson [41], Harp and Salant [42], using various assumptions related to the orientation and distribution of the surface asperities. However, the work presented by Lee and Ren [43, 44] considering the effects of elastic plastic deformation to support loads is one of the most advanced numerical stochastic models for asperity contact according to the authors knowledge. A comprehensive mixed-TEHD model for journal bearing interfaces while considering the work of Lee and Ren [44] for asperity contact loads was presented in Wang et al. [28] and the approaches uses in this work have been integrated into the mixed-TEHD model for the lateral gaps in EGMs. It has also been suggested in the work of Martini et al. [45] that using advanced mixed lubrication models can aid in proposing design modifications to reduce the friction and thereby improving the lubrication performance of the interfaces under study, which is also one of the primary aims of this research.

Simplified models to include the importance of surface effects in hydraulic bearings and seals were presented in Yamaguchi and Matsuoka [46], Kazama and Yamaguchi [47], and for various lubricating interfaces in axial piston machines in Kazama [48] , Hashemi et [49], Fang and Shirakashi [50] and Wegner et al. [51]. Experimental work has also been performed in Kazama and Yamaguchi [52] to highlight the significance of surface roughness in thrust bearings in hydraulics. However, all these models utilize simplified analytical assumptions of surface features without considering any EHD or thermal effects which are shown to be quite significant in high pressure hydraulic applications (Pelosi and Ivantysynova [53] Zecchi [54], Schenk and Ivantysynova [55]).

To the best of the authors knowledge, comprehensive mixed lubrication modeling by including the aforementioned advances in tribology for coupling surface, fluid flow, structural and thermal effects such as the one presented in this work, has never been achieved before in EGMs.

1.4.3 Effects of Micro-Surface Shaping on Lubrication Performance

Micro surface shaping methods of different kinds were proven to improve lubricating abilities of several conformal tribological interfaces in the works of Nanbu et al. [56], Wang et al. [57], Krupka et al. [58]; Wang et al. [59], to name a few. Specifically, in positive displacement machines, the effect of surface shaping was shown to significantly lower the mechanical losses in axial piston machines by Ivantysynova, Baker [60]; Wondergem, Ivantysynova [61]; Chacon, Ivantysynova [62]. For EGMs, the only prior study on micro surface shaping was published by Morgridge et al. [6] where some improvements in the lubricating film were observed by introducing crowning in the end faces of the gears. Although this work indicated potential in using such profiles, other possible profiles were not explored and supported with experimental results.

The possibilities of promoting efficient EGM designs with novel surface shaping by adding linear sloping wedge and waved features on the gears, and shot peening effects on the gears as well as lateral bushings using a FSI-EHD model for the lateral gaps, were first demonstrated in the work of Dhar [9]. The application of the EHD lateral gap model along with an optimal axial balance procedure developed in Thiagarajan [10] was used in investigating optimal designs of wedge gears and were shown to reduce the mechanical losses from the gap in simulations. An experimental prototype to validate the numerical findings of adding of adding surface shaping is yet to be achieved. In this work, a modified surface shaping of a flat step and a wedge profile on the gear teeth is proposed and is experimentally validated using a prototype EGM with the same surface shaping.

1.4.4 Prediction of Torque Losses in EGMs

The evaluation of torque losses performed by several empirical models which were generated based on steady state experimental data, are available in literature for many different kinds of positive displacement machines. These models have been developed with increasing level of complexity, starting with the work of Wilson [63, 64] which included the first mathematical model for modeling the torque and flow losses for hydrostatic pumps and motors. Other research works such as Schlsser [65], Thoma [66], Hibi and Ichikawa [67], Zarotti and Nervegna [68], McCandlish and Dorey [69] and Ivantysyn and Ivantysynova [16] over the last few decades have extended the accuracy of these empirical models to predict both torque and flow losses in a hydrostatic unit. The work of Michael et al. [70] presents an analysis of EGM efficiency from experimental data based on Stribeck values.

However, all of these models are dependent on the availability of reliable experimental data which is also observed in the work of Manring [71] that notes the uncertainties in pump efficiency measurements. At the limit of the author's knowledge, currently there is no existence of an established approach which can comprehensively model all the torque and flow losses in an EGM without steady state measurement data. Furthermore, the aforementioned models do not account for special features such as changing configuration of the gears due to micro-motion along gear axis, which are specific to the case of EGMs.

The present work as part of validating the developed mixed-TEHD model for the lateral gaps, also presents a step towards utilizing a full numerical approach to predict the operation of EGMs, particularly related to the prediction of the torque losses without the necessity of using experimental data.

1.4.5 Low Viscous Working Fluids in High Pressure Hydraulics

The main driving goal of this research area is to investigate the use of water as a viable working fluid in high pressure applications since it has advantages of low

torque losses, low cost, being environment friendly and low risk of inflammability over oil. Although water as the major working fluid in hydraulic applications has inherent advantages over mineral oils, the low viscosity of water causes challenges in the lubrication performance especially in high pressure positive displacement machines. This remains as one of the principal barriers in the practical implementation of high pressure water hydraulics as an environment friendly, low cost and efficient alternative for novel applications in agriculture, food processing, medical applications etc. as described in Knight [72] and Krutz and Chua [73]. Though this research is primarily driven by water, the methods and tools developed here could be easily extended to applications using other low viscous fluids, such as fuel injection pumps in aerospace engines.

In the work of Spikes [74], the wear and fatigue problems that could potentially be associated with water is explained along with certain possible design techniques such using additives, compatible materials and surface shaping to overcome these issues. Such techniques have been successfully used to improve the performance of water lubricated journal bearings in Ravikiran and Bai [75] and Majumdar et al. [76].

There are quite a few works in literature which focus on numerical and analytical techniques to design water hydraulic components. Modeling and experimental validation of bearings in water hydraulic pumps and motors have been performed in the works of Wang and Yamaguchi [77]. Numerical simulation of slipper interfaces in water based axial piston machines have been studied by Kazama [48], Nie et al. [78] and Rokala [79]. However, all these works include simplified models without structural, thermal or surface effects integrated in them. Ernst and Ivantysynova [80] proposed surface shaping on the piston cylinder interface of axial piston machines to improve the performance of these units with water at high pressures ($\sim$ 300 bar) using an advanced TEHD model developed for these interfaces. However, no numerical model or verified design methodologies for high pressure water based EGMs exist in the current state of the art.

The present work aims to propose and validate such design techniques based on comprehensive numerical tools considering the various physical phenomena in the lateral lubricating gap of EGMs. Since the lateral lubricating interface is one of the major sources of power losses in the unit, it is the primary focus of the current work in designing water based EGMs. Furthermore, a novel radial compensation method is proposed in the prototype water based EGM developed as part of this work with a goal of reaching high operating pressures ($\sim$ 200bar). The methods developed for designing high pressure water based EGMs could potentially widen its current range of applications, while also extending these novel design methodologies for other working fluids with low viscosities.

1.5 Structure of the Dissertation

The organization structure of the remainder of this thesis is briefly outlined here in this section for the purposes of clarity. Details of the various reference cases and their specifications are listed in Table 1.1. The corresponding representation of their lubricating gap configuration is shown in Figure 1.7. Case 1A and Case 1B are typical EGMs used in mobile hydraulic machines which are quite similar to each other differing only in certain geometrical aspects, while Case 2 is an aerospace fuel injection pump and Case 3 represents the water-based EGM designed in this work.

Chapter 2 describes the state of the art simulation models developed prior to this work, that will be utilized in different parts of this thesis. Contributions made by the author to the modeling of lateral gaps will be presented in Chapter 3, which includes a detailed account of the implementation of mixed-TEHD model, cavitation modeling in the lubricating gaps and a model to account for the frictional contact between the bushing and the housing. Results from the simulations performed using the developments to the lateral gap model made in this research are discussed in Chapter 4 by using Case 1A. Numerical investigations are performed to analyze the different parameters used in the mixed-TEHD model along with analysis on the contribution of

Table 1.1.
Details of reference EGM cases used in this dissertation.

Case	**Balance type**	**Working Fluid**	**Lateral bushing type**	**No. of gear teeth**	**Displa-cement (cc/rev)**	**Maximum Operating Conditions**
Case 1A	Symmetric	Oil	Pressure plates	13	25	250 bar, 3000 rpm
Case 1B	Symmetric	Oil	Pressure plates	12	11.2	250 bar, 2500 rpm
Case 2	Asymmetric	Jet A fuel	Bearing Blocks	14	43	173 bar, 8000 rpm
Case 3	Symmetric	Water	Pressure plates	12	11.82	200 bar, 2000 rpm

surface asperities to the lubrication load support under severe operating conditions. Simulation results showing stable pressure fields in the lateral gap at these conditions after the implementation of the new cavitation algorithm, are also presented in this chapter.

In Chapter 5, the proposed novelty in modeling is validated by experiments through two different methodologies using torque losses and drain leakages, which are the primary parameters determining the performance of the lateral gap, by using a reference high viscous fluid (oil). The reference EGM identified as Case 1B is used for these validation studies. In addition, this chapter also presents the ability of the gap model to predict the effect of varying surface roughness on the functioning of the lateral lubricating interfaces. Two lateral plate designs belonging to Case 1B with a predetermined variation in surface roughness are chosen for the present study. The simulated predictions of the performance of the EGM from the developed

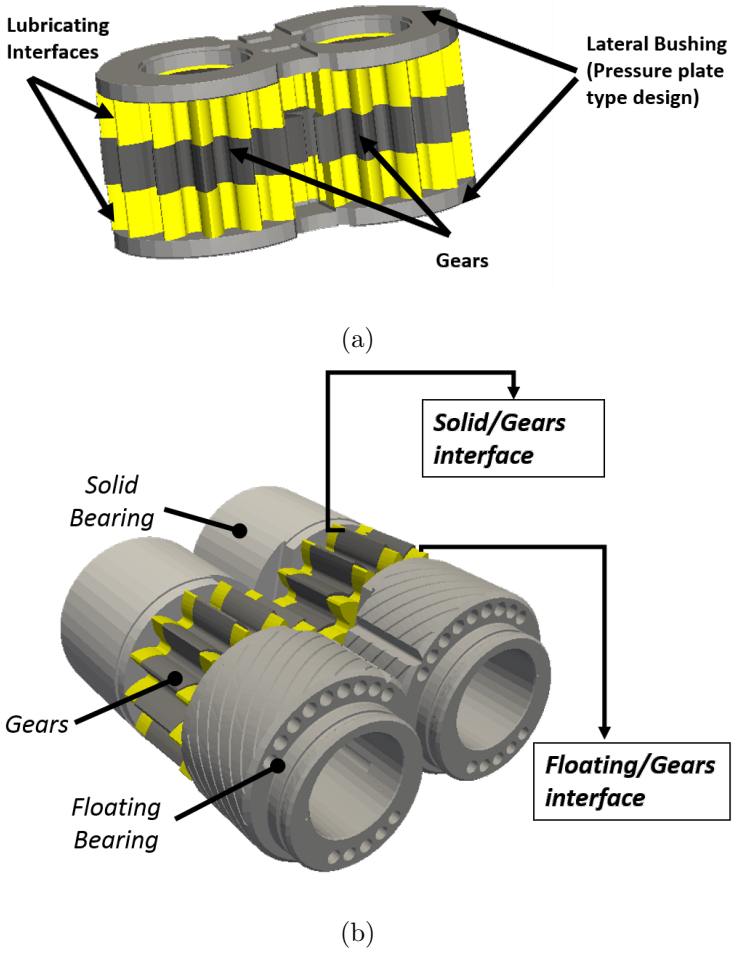

Figure 1.7. Representation of the lubricating interfaces in the reference cases used in this dissertation (a) Case 1A, Case 1B, Case 3 (b) Case 2.

mixed-TEHD model with the selected bushing designs are experimentally validated with corresponding lateral drain leakages measured directly from the reference unit. To demonstrate the ability of using a validated numerical model as a potential design tool, novel design methodologies to introduce micro-surface shaping for improving the performance of lateral lubricating gap will be experimentally validated on a prototype EGM for the case of oil in the subsequent Chapter 6.

After completing detailed validation for oil based EGMs, an asymmetrically balanced design of an external gear pump identified as Case 2 is used to to exhibit the

performance of the developed numerical model with low viscous working fluids (Jet A kerosene) and at high operating speeds $\sim$ 8000 rpm in Chapter 7. Furthermore, this chapter also demonstrates the influence of the adding a translational frictional force model on the bushing movements with the help of experimental measurements.

In Chapter 8, the design approaches of using micro-surface shaping effects and determining the optimal axial balance design by using an advanced mixed-TEHD lubricating gap model, will be applied to a more challenging and newer EGM design with another low viscous working fluid (water). It will also include proposing a novel EGM prototype (Case 3) which is suitable for working with water as the main hydraulic fluid. A novel radial compensation method is also proposed in this EGM prototype to achieve good operating efficiencies and reliability at a wide range of operating conditions while accounting for the lubricating difficulty due to the low viscosity of water. Finally, Chapter 9 presents a novel analysis to study the difference in lubrication performance between two reference high and low viscous fluids, which were chosen to be oil and water respectively.

2. OVERVIEW OF THE SIMULATION MODELS USED IN THE CURRENT RESEARCH

An overview of the existing simulation models developed prior to this research and used in the present work are discussed in this section. The analysis performed in this work primarily makes use of different sub-models in the multi domain simulation tool for EGMs, HYdraulic GEar Machine Simulator (HYGESim) [22] which was developed in the author's research team. A schematic representation of the structure of HYGESim along with the interaction between its different sub-models is shown in Figure 2.1. The simulation tool models and predicts the various features associated with the operation of an EGM which includes fluid flow behavior through the different TSVs, radial micro-motion of the gears and radial balance of forces as well as the effects of the fluid structure interaction in the lateral lubricating interface. This is achieved through interfacing between the different sub-models that constitute HYGESim in a manner outlined in Table 2.1.

A brief description of the different modules in HYGESim is presented in this section. The lateral lubricating gap module which comprehensively accounts for the flow features, structural and thermal effects in the lubricating interfaces between the lateral bushing and the gears, is the central component in this research. Thus, the description in this section focuses more on the state of the art details of this lateral gap model.

2.1 HYGESim Simulation Tool

In the present section, a description of three sub models of HYGESim, namely the fluid dynamic model, the geometric model and the model for journal bearings which are primarily used in this research along with the lateral gap model are presented.

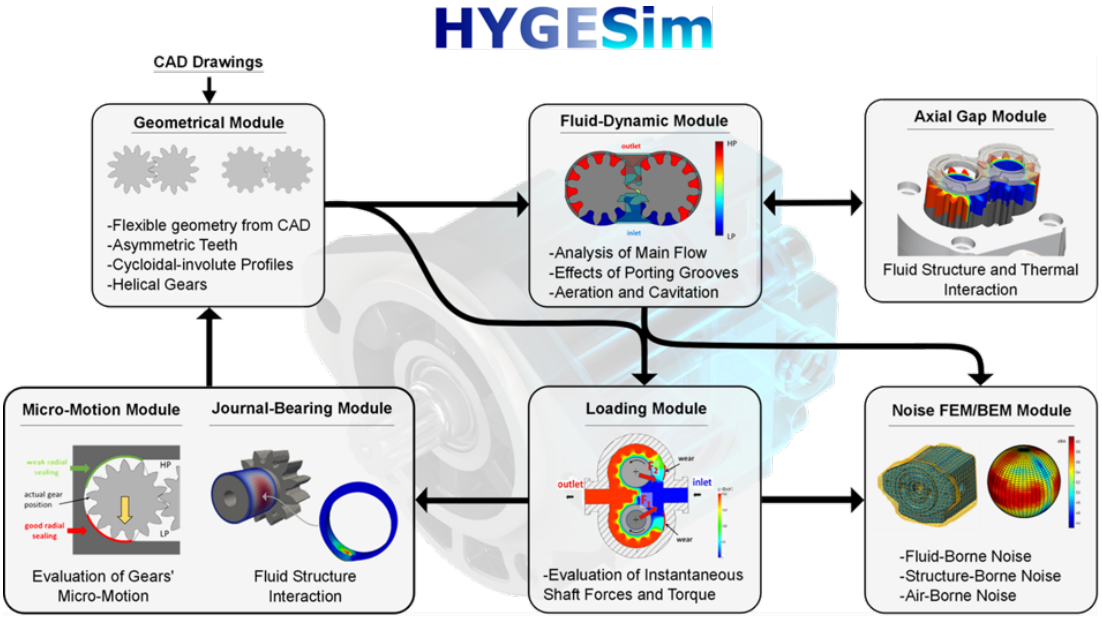

Figure 2.1. Framework of the simulation tool HYGESim and it submodules.

While the fluid dynamic model, developed inside the LMS Imagine Lab AMESim [81] environment with custom and standard component libraries in C++ language, is responsible for the simulation of flow through the TSVs, the geometric model evaluates the radial motion of the gears with the help of a standalone application. The CFD model for the journal bearing interfaces which has been developed using C++, OpenFOAM [82] and GSL [83] estimates the flow features associated with these interfaces.

2.1.1 Fluid Dynamic Model

A lumped parameter approach is used to solve for the internal fluid flow in the various TSVs in the fluid dynamic module of HYGESim. The EGM is divided into multiple control volumes (CVs) as shown in Figure 2.2. The TSVs which also form a part of the classified CVs are shown in the same figure for both the driver and driven

Table 2.1.
Summary of information exchanged between the different sub-models of HYGESim.

Submodel	**Input**	**Output**
Geometric Model	CAD drawings, $\mathbf{e_1}$, $\mathbf{e_2}$ from journal bearing model	Information about flow connection geometries to fluid dynamic and loading model, A_{TS} and x_{TS}, y_{TS} to axial gap model
Fluid dynamic model	Information from geometric model, $Q_{leak-lat}$ from lateral gap model	p_{TSV} to the lateral gap, loading and noise model
Loading model	p_{TSV} from fluid dynamic model	$\mathbf{F_{R1}}$, $\mathbf{F_{R2}}$ forces to journal bearing and pressure forces to noise model
Journal Bearing Model	$\mathbf{F_{R1}}$, $\mathbf{F_{R2}}$ from loading model	$\mathbf{e_1}$, $\mathbf{e_2}$ to geometry model
Lateral Gap Model	p_{TSV} from fluid dynamic model, A_{TS} and x_{TS}, y_{TS} from geometric model	$Q_{leak-lat}$ to the fluid dynamic model

gears. The pressure (p) in each CV as a function of time is modeled using the laws

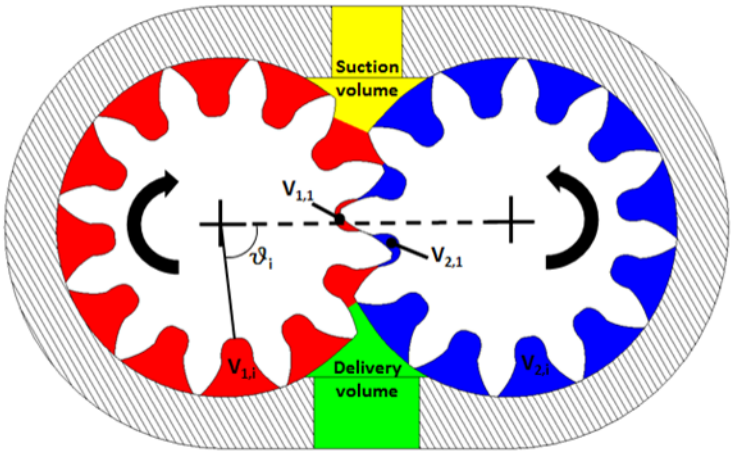

Figure 2.2. Illustration of the control volumes used in HYGESim along with the angular sign convention used in the model.

of conservation of mass along with the equations for the fluid flow in the following manner,

$$\frac{dp_j}{dt} = \frac{1}{V_j}\frac{dp}{d\rho}_{p=p_j} \cdot \left[\sum \left(\dot{m}_{in,j} - \sum \left(\dot{m}_{in,j} - \rho|_{p=p_j} \left(\frac{dV_j}{dt} \right) \right] \right(\tag{2.1}$$

The fluid aeration and cavitation effects are considered in the term $\frac{1}{V_j}\frac{dp}{d\rho}_{p=p_j}$ which represents the effective bulk modulus of the mixture of fluid with air and vapor bubbles. A transient approach is used for evaluation of gas and vapor fraction in different control volumes, details of which are described in [84]. Basically, the main fluid properties (density, viscosity, bulk modulus) are evaluated assuming a continuum given by a mixture of liquid, incondensable gas (undissolved air bubbles), vapor. Incondensable gas is generated below the saturation pressure (assumed atmospheric, in this research), with proper gas transport equations. The asymptotic value is given by the Henry-Dalton law and vapor is generated in case the pressure falls below the vapor pressure.

The flow through two TSVs is modelled as a turbulent orifice with the help of the following equation for the flow rate ($\dot{m}$) where Ω_{ij} is the parameter indicating the throat area connection between the two CVs under consideration,

$$\dot{m_{i,j}} = \frac{p_i - p_j}{|p_i = p_j|}.\rho|_{p=p_j}.\alpha.\Omega_{ij}\sqrt{\frac{2(p_i - p_j)}{\rho|_{p=\overline{p_{ij}}}}} \tag{2.2}$$

2.1.2 Loading Model

The pressure and contact forces acting on the gears are evaluated numerically in the HYGEsim model [22] by calculating the flow through the orifice connections. The resultant radial forces and torque acting on the driver (Gear 1) and driven gears are illustrated in Figure 2.3 while considering forces acting along both the X and Y directions. The pressures evaluated from the fluid dynamic model (Equation (2.1)) are used to obtain the pressure forces acting on the X and Y directions using the following equations, where Ω_{yz} and Ω_{xz} are the TSV projection areas and ϑ denotes the angle of rotation [22],

$$\overrightarrow{f_x}(\vartheta) = p_i(\vartheta).\Omega_{yz}\vartheta)\overrightarrow{i_x} \tag{2.3}$$

$$\overrightarrow{f_y}(\vartheta) = p_i(\vartheta).\Omega_{xz}\vartheta)\overrightarrow{i_y} \tag{2.4}$$

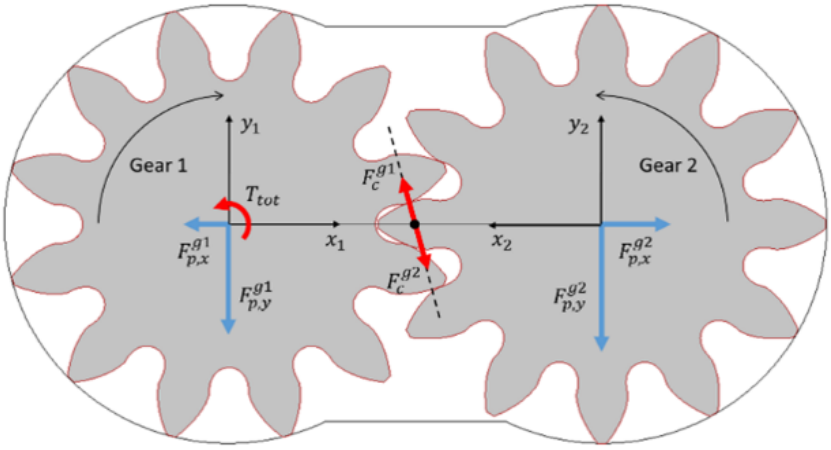

Figure 2.3. Balance of the different forces acting on the gears in an EGM with a zoomed in view of the contact and the frictional contact forces.

The pressure forces acting on all the TSVs can be added to obtain the resultant instantaneous pressure forces $\overrightarrow{F^g_{p,x}}(\vartheta)$ and $\overrightarrow{F^g_{p,y}}(\vartheta)$ acting along X and Y directions respectively. The line of action of these pressure forces: $X(\vartheta)$ and $Y(\vartheta)$ can be evaluated using the geometrical configuration shown in Figure 2.3. The total torque needed to be applied at the shaft of the drive gear can thus be estimated with the help of the forces acting on the gear using the following equations where T_p is the torque applied at the center of each gear,

$$T_p(\vartheta) = \overrightarrow{F^g_{p,x}}(\vartheta).X(\vartheta) + \overrightarrow{F^g_{p,y}}(\vartheta).Y(\vartheta) \tag{2.5}$$

The total torque required at the drive shaft of the pump depends on the contact force ($\overrightarrow{f_c}$) originating from the meshing of the gear teeth as well as the torque on the drive gear due to the pressure forces (T_d) as shown in Figure 2.3. Thus, the total torque evaluated in this model has all the losses related to the turbulence resistance through the orifices and is given by the following equation, in which R_d is the outer radius of the drive gear and α is the pressure angle of the gear profile,

$$T_{tot} = T_d + f_c.R_d.cos\alpha \tag{2.6}$$

The interaction between the fluid dynamic model and the FSI model for the lateral gaps is important in the present work since this primarily results in setting the pressure boundary conditions in the computational domain of the lateral gap which includes the various TSVs along with the suction and the delivery ports. The co-simulation approach developed in Vacca et al. [85] involves the interaction between the FSI model and the fluid dynamic model where the exchange of pressure-leakage information between these two models occurs iteratively until convergence is reached. An instance of pressures in a TSV as it travels through one revolution from LP port to HP port along with the delivery pressure at the HP port is shown in Figure 2.4. It must be noted that the angular sign convention shown in this figure is identical to that indicated in Figure 2.2. As it can be observed from the figure, the pressures are varying according to the angle of rotation of the TSV, and this leads to variable

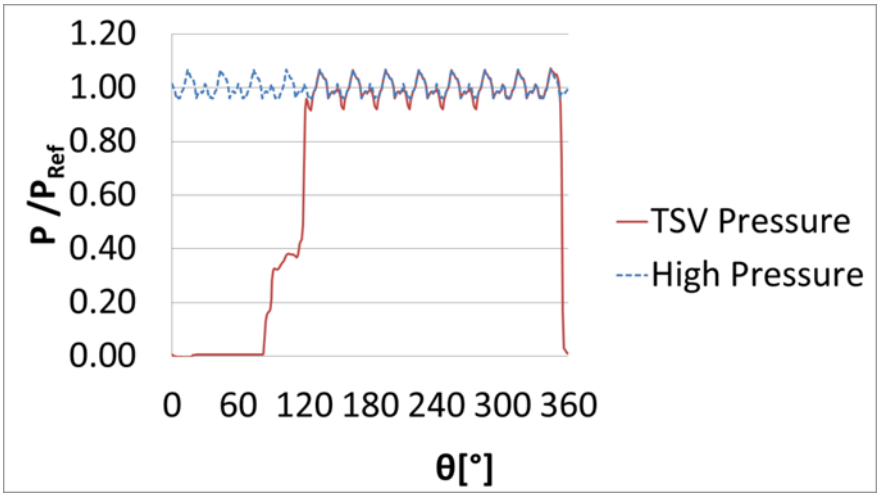

Figure 2.4. Typical pressure in a TSV and at the delivery (high pressure) port as predicted by HYGESim. This example of the pressure plot corresponds to the design of Case 1A.

loads on the lubricating interface. Detailed description of the implementation of the fluid dynamic model along with its experimental validation can be found in Vacca et al. [22].

2.1.3 Model for Journal Bearing Interfaces

Radial gap interfaces (as shown in Figure 1.4) are present in typical designs of EGMs due to the four journal bearing interfaces between the shafts of the gears and bearing block type of lateral bushings. A CFD model for these interfaces [86] has been developed using C++, OpenFOAM [82] and GSL [83] in the author's research team. This model has also been coupled with the lumped parameter module of HYGESim to exchange forces and eccentricity information at the interface as described schematically in Figure 2.1. The instantaneous radial forces acting on each gear are evaluated from the lumped parameter model along with the line of action of these forces. The total radial load on the gears consists of contributions from the contact

force (F_c^g) as well as the pressure forces in the x and y directions [86] which are acting on each gear as shown in the equation below,

$$\overrightarrow{F_{load}^g} = \overrightarrow{F_{px}^g} + \overrightarrow{F_{py}^g} + \overrightarrow{F_c^g} \tag{2.7}$$

It is also assumed that the forces acting on each gear is supported by both its journal bearing interfaces equally. The pressures in this interface are solved by using the form of Reynolds equation [23] in Cartesian coordinates since the curvature of such a thin gap film can be neglected as shown below,

$$\left(\frac{-\rho h^3}{12\mu}\right)\left(\nabla p\right) + \frac{\rho \mathbf{v_b}}{2}.\nabla(h) + \rho \mathbf{v_b}.\nabla(h_b) + \rho\frac{\partial h}{\partial t} = 0 \tag{2.8}$$

The discretized FV fluid mesh for this interface is represented in Figure 2.5. A radial force balance is also performed on the gears iteratively with the evaluation of the pressure distribution in the interface to solve for the eccentricities and the radial micro motion of the gears. Further details related to the implementation and validation of the journal bearing gap model in HYGESim can be found in [86].

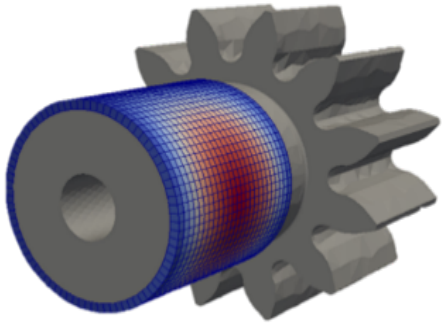

Figure 2.5. Representation of the FV fluid mesh used in the journal bearing interface and the numerically evaluated pressure distribution at the interface [86] (example refers to Case 1A).

2.1.4 Geometric Model

The geometric model is responsible for the calculation of several relevant geometrical areas of volumes for input to both the lateral gap model as well as the fluid dynamic model and this interaction was documented earlier in Table 2.1. The equations (Equation (2.1) and Equation (2.2)) introduced to model the flow between the TSVs in the fluid dynamic model require the knowledge of the volumes of the TSVs as well as the area of the connections between them.

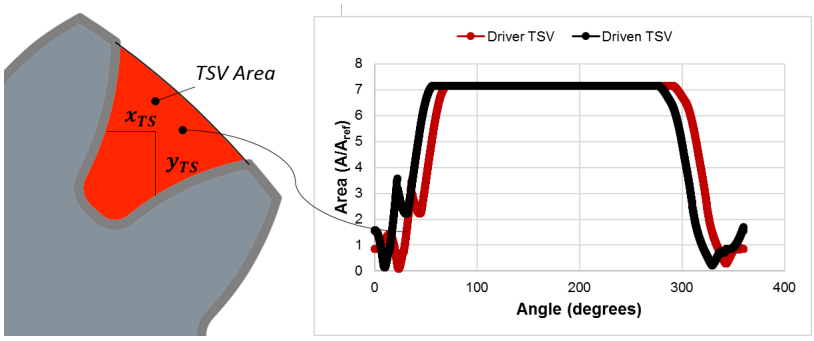

Figure 2.6. An instance of the area encompassed by a tooth space volume (A_{TS} shown in red), corresponding to Case 1A, with the centroids of the area marked as x_{TS} and y_{TS} and a plot of a driver and driven tooth space area as it goes through a revolution, which is used as an input to the force balance solver of the lateral gap model.

Since these are based on the actual CAD drawings of EGMs, the geometric model, and consequently the whole procedure, can work for any given geometry of EGMs (for example, relief groove designs, teeth profiles etc.). The typical outputs from the geometric model which include the TSV areas of the gears as they undergo one revolution are shown in Figure 2.6. The TSV area information is, in particular, provided to the FSI model and is used to estimate the forces acting on the bushing which is used both to calculate the force balance on the bushing as well as to calculate its deformation. Evaluation of these forces on the lateral bushing and the related elastic deformation will be described in the next section. Further information related

to the implementation of the geometric model in the framework of HYGESim and the various connections between the fluid volumes can be found in [87].

2.2 Thermo-Elastohydrodynamic Model of the Lateral Lubricating Gaps

The TEHD model for the lateral lubricating gaps in EGMs is part of the central focus of the research and hence the details related to the implementation of this model will be elaborated in this section. However, the model outlined in this section is the previously developed version of the TEHD model for the lateral gaps [9] which assumes a regime of full film lubrication at all times. Chapter 3 will discuss the formulation and implementation of a mixed film−TEHD version of the lateral gap model which is the novelty in the present work. The results from this research presented in the subsequent sections of this dissertation also include results from the full film lubrication model, primarily for the purposes of comparison. Furthermore, it is also necessary to outline the details of the full film model since it forms the basis for the implementation of the mixed lubrication model.

The FSI-TEHD model of the lateral lubricating gaps in EGMs has been developed as an independent application using the programming language C++ and was linked with open source libraries like OpenFOAM [82] for FV discretization of PDEs and linear system solving, GSL [83] for multidimensional root-finding and spline interpolation. An illustration of the lateral gap model previously developed with the full film lubrication assumption along with the interaction between the different sub-models are shown in Figure 2.7. The interfacing of the different sub-models in the TEHD model is shown in Table 2.2.

The TEHD model is primarily composed of the following sub-models, each of which will be explained in the subsequent sections in this chapter,

- *Preprocessor and mesh generator* : Finite volume meshing of the fluid film geometry and the solid components.

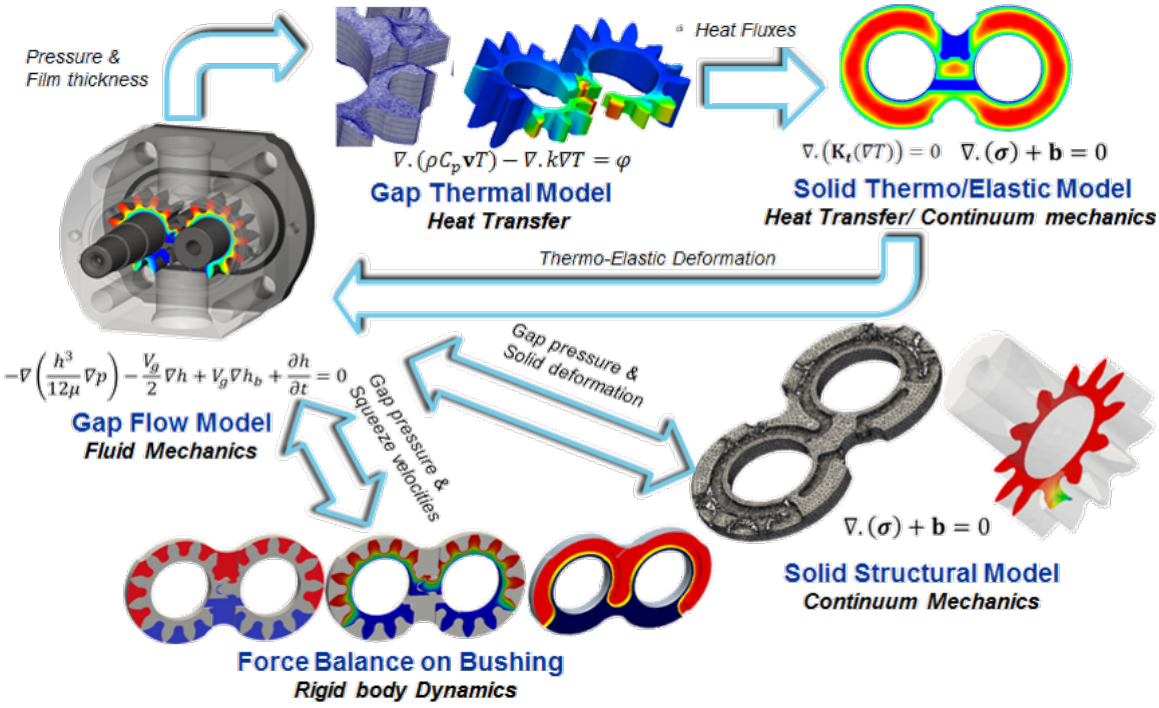

Figure 2.7. Schematic representation of the full film lubrication TEHD model for the lateral lubricating gaps [9].

- *Interface with HYGESim Fluid Dynamic Model* : Sets the pressure boundary conditions on the fluid film mesh.
- *Gap Flow Model* : Finite volume solver for the main constitutive equations for the fluid.
- *Solid Structural Model* : Finite volume solver for the main constitutive equations for the solids i.e. the gears and the lateral bushings.
- *Force Balance Model* : Accounts for the static balance of forces and moments acting on the lateral bushings.
- *Gap Thermal Model* : Finite Volume solver for the energy equation and the associated constitutive equations for the temperature fields in the gears and the lateral bushings

Table 2.2.
Summary of information exchanged between different sub-models in the TEHD model.

Submodel	**Input**	**Output to other sub-models**
Gap Flow Model	Squeeze velocities from force balance model, elastic deformation from structural model, thermo-elastic deformation from thermo/elastic model	Pressures to thermal model, structural model, force balance model
Force Balance Model	Pressures from gap flow model	Squeeze velocities to gap flow model
Structural Model	Pressures from gap flow model	Elastic deformation to gap flow model
Thermal Model	Pressures from gap flow model	Temperatures to Thermo/Elastic Model
Thermo-Elastic Model	Temperatures from thermal model	Thermo-Elastic deformation to gap flow model

2.2.1 Mesh Generation

Generation of Fluid Mesh : A mesh generation module for creating the mesh for the fluid domain was developed in C++ as part of the preprocessing for the FSI model [9]. FV meshes for the fluid domain of the lateral gap are generated in this module after starting from the CAD drawings of the gears and the lateral bushings for the EGM under study. This lends to flexibility and robustness of the model since any given design of an EGM can be simulated with relative ease. While the fluid

mesh is generated using the CAD of the gears, the computational domain for the lubricating gap must also account for its interaction with the relief grooves in the lateral bushing. Since the lubrication assumption is not valid in the regions where the grooves are associated with the gap domain and uniform pressures are present in these regions, these must be eliminated from the gap computational mesh. Thus, a two dimensional (with a single cell in the third dimension) FV mesh consisting of 6 node prism elements of the gears are created using the open source GMSH libraries. Then the mesh created is rotated by the appropriate step in order to create the base FV domain of dynamic meshes. The intersection of the relief groove geometry with this base domain is performed, where all cells of the finite volume mesh that are either inside or cut by the relief grooves are removed and the boundaries of this cut region are smoothened. Subsequently, a dynamic gap mesh with a varying configuration due to the cutting of the relief grooves at each desired time step is obtained. An instance of the gap mesh and the intersection with the relief grooves is shown in Figure 2.8.

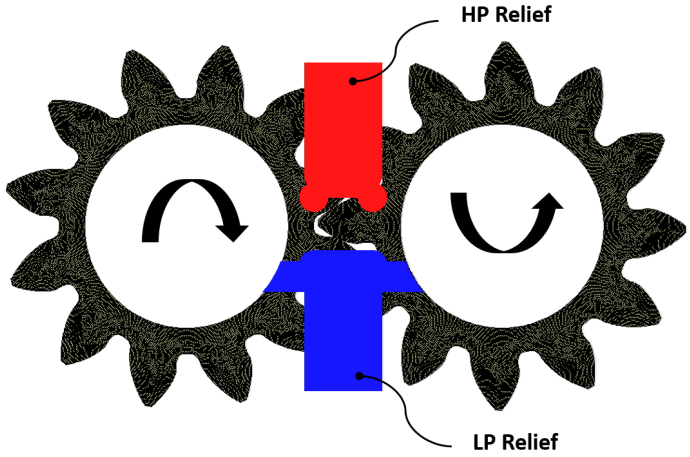

Figure 2.8. FV computational fluid mesh (∼120000 cells) for the lateral gap in Case 3 shown along with its interaction with the HP and LP Relief Grooves.

Generation of Solid Meshes : The mesh generation for the solids is relatively simple when compared to the generation of the fluid mesh, since the geometry of the

meshes remains constant. Three dimensional FV meshes (shown in Figure 2.9) for the solids are generated using the commercial code ANSYS [88]. Tetrahedral meshes for the solid components were chosen since this allowed for the most automated and fastest meshing solution, with the meshes conforming to the geometry very accurately. While the lateral bushing mesh remains static with respect to the rotation of the shaft, mesh of the gears is rotated at the specified angular velocity of the pump using a simple rotational coordinate transformation for all the cells in the gear mesh which is given by the following equations,

$$x_{new,i} = x_{old,i}cos(\theta) - y_{old,i}sin(\theta) \tag{2.9}$$

$$y_{new,i} = x_{old,i}sin(\theta) + y_{old,i}cos(\theta) \tag{2.10}$$

The coupling of the solid and the fluid domains is one of the key aspects of the FSI model and this requires transferring of information between the fluid mesh and the two solid meshes. This is accomplished by numerically linking the three meshes by using an inverse distance weighted interpolation method.

(a) (b)

Figure 2.9. Figure showing the solid meshes in Case 3 of (a) Lateral bushing Pressure plate type design ($\sim$ 43000 cells) and (b) Gears ($\sim$ 89000 cells).

2.2.2 Interface with the Fluid Dynamic Model

The interaction of the lateral gap model with the fluid dynamic model of HYGESim was outlined earlier in Section 2.1.1. There is a two-way interaction between the two models when they exchange pressure-leakage information to set the boundary conditions at the various interfaces of the gap domain which include those in the meshing region and those outside this region, as shown in Figure 2.10. This co-simulation approach is performed in a similar manner to the one published in [85]. Apart from setting the pressure boundary conditions, the FSI model is also provided with the variable areas and centers of mass of the TSVs as the gear rotates over the entire revolution by the geometric model of HYGESim which was outlined earlier in Section 2.1.4.

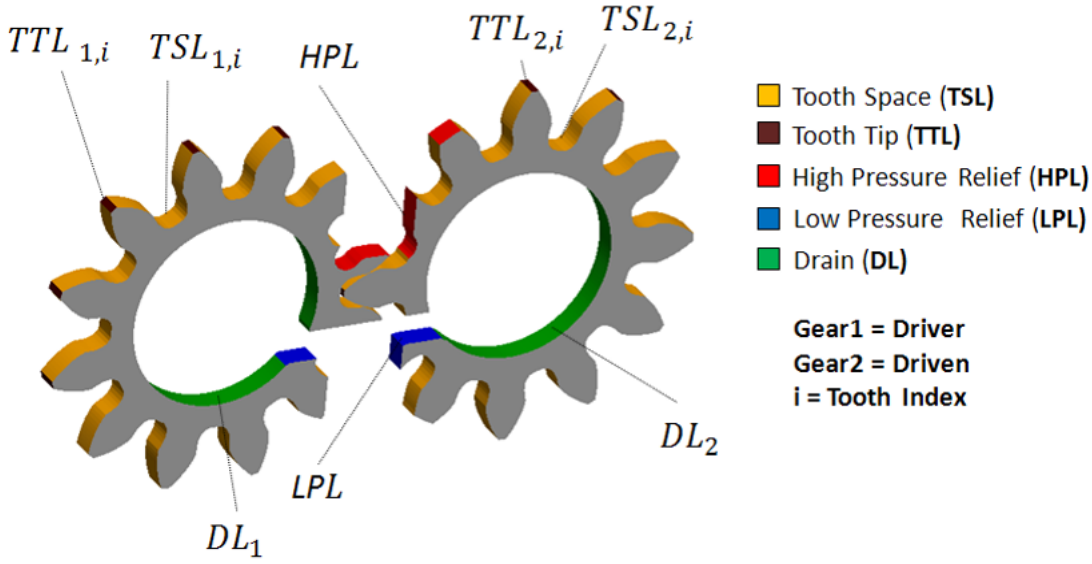

Figure 2.10. The lateral gap and interfaces along which the FSI and the HYGESim fluid dynamic model which interact with each other, corresponding to Case 1A.

2.2.3 Gap Flow Model

The pressures and the fluid flow in the lateral lubricating gap is solved with the help of the Reynolds equation which is derived from the well-known Navier Stokes equations using certain simplified assumptions which are suitable for this case [23]. Since the current section focuses on detailing the implementation of the full film TEHD model for the lateral gap which was previously developed, the form of Reynolds equation explained here is applicable only for the assumption of the presence of a fully developed fluid film at all times of operation. For the purposes of modeling the lateral lubricating gap in EGMs, the common form of Reynolds equation [23] has been modified to model deformation features in both the surfaces involved, namely the gears and the lateral bushings [9]. Therefore, the modified form of the Reynolds equation derived exclusively for EGMs is given as follows and the detailed derivation of this equation can be found in the work of [9].

$$\nabla . \left(\frac{-\rho h^3}{12\mu}\right)\left(\nabla p\right) + \frac{\rho \mathbf{v_b}}{2}.\nabla(h) + \rho \mathbf{v_b}.\nabla(h_b) + \rho\left(\frac{\partial h_t}{\partial t} - \frac{\partial h_b}{\partial t}\right) = 0 \tag{2.11}$$

In Equation (2.11), $h = h_t - h_b$ represents the gap heights in the lubricating interface. In the geometry being used in the current case (shown in Figure 2.11) the velocity of the upper surface $\mathbf{v_t} = 0$ since the lateral bushings are stationary. The lower surface corresponds to the lateral surface of the gears and rotates with a velocity $\mathbf{v_b} = \mathbf{v_g}$.

A finite volume solver for the Reynolds equation was implemented in an application developed in C++ while leveraging the field handling and operating capabilities of OpenFOAM [82]. The pressure is solved for using a Preconditioned Conjugate Gradient algorithm, with a Diagonalized Incomplete Cholesky preconditioner. Chapter 3 of this work outlines the details of the implementation of a modified form of the Reynolds equation for mixed lubrication modeling and this section has further detailed description related to the gap flow model.

Fluid properties modeling associated with the dependence of the working fluids density and viscosity on the pressures in the lubricating gap domain also need to be

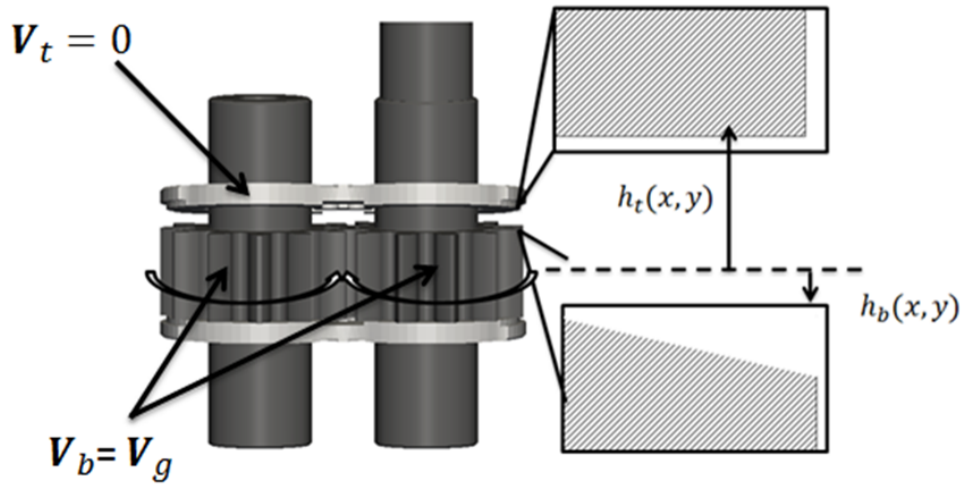

Figure 2.11. Figure explaining the terms in the Reynolds equation for the current case with height of the top surface as h_t and bottom surface as h_b where $h = h_t - h_b$. The rotational speed of the gears is v_b and the lateral bushing is fixed with v_t [9].

accounted in the gap flow model. Since the present work broadly considers two very different fluids, the fluid properties of each working fluid need to be handled in a different manner. The reference high viscous fluid considered in this work is the ISO 46 mineral oil, for which the following relations are available in [16].

$$\rho = \rho_0(1 + \beta_p(p) - \beta_T(T)) \tag{2.12}$$

$$\mu = \mu_0(e^{\alpha_p p} + e^{-\alpha_T T}) \tag{2.13}$$

A low viscous fluid considered in this work is tap water and the fluid properties for modeling this working fluid was derived in the present work using standard experimental data [89]. Details of the derivation of these relations are presented in Appendix A of this dissertation.

2.2.4 Determination of Gap Heights and Squeeze Velocities

The geometry of the lateral gap is a plane when solid deformations are not considered, and therefore can be fully determined considering the 3 points that are shown in Figure 2.12. Using the gap height information stored at the points T0, T1 and T2, the gap height for an arbitrary point in the domain can be calculated using the following equations,

$$h_{UD}(x,y) = x\frac{2h_{T2} - h_{T1} - h_{T0}}{2(d+R)} + y\frac{h_{T1} - h_{T0}}{2R} + \frac{h_{T0} + h_{T1}}{2} \tag{2.14}$$

The information about the squeeze velocities is also stored at the three points as shown in Figure 2.12, and the resultant squeeze velocity at an arbitrary point is given by,

$$\frac{\partial h_{UD}(x,y)}{\partial t} = x\frac{2\frac{\partial h_{T2}}{\partial t} - \frac{\partial h_{T1}}{\partial t} - \frac{\partial h_{T0}}{\partial t}}{2(d+R)} + y\frac{\frac{\partial h_{T1}}{\partial t} - \frac{\partial h_{T0}}{\partial t}}{2R} + \frac{\frac{\partial h_{T0}}{\partial t} + \frac{\partial h_{T1}}{\partial t}}{2} \tag{2.15}$$

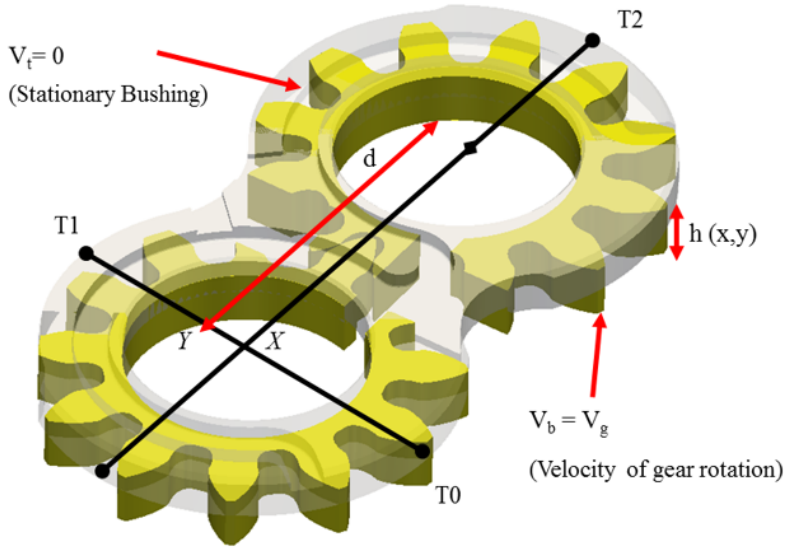

Figure 2.12. Figure showing the lubricating gap (in yellow) between the lateral bushing (transparent view) and the gears.

2.2.5 Structural Model

The structural components of the lubricating interface: gears and the lateral bushings experience high pressure loads and deformation which is expected to be in the EHD lubrication regime. Thus, the deformation of the solid components is modeled using a finite volume stress/deformation solver and hence, the gap model fully couples the effects of both solid and fluid domains. Using the formulation described in Jasak and Weller [90], the elasticity equation may be written in a form amenable to a segregated FV solution (shown in Equation (2.16)) and the resulting discretized linear system was solved using a geometric multi-grid solver.

$$\nabla.[(2\xi + \lambda)\nabla\mathbf{u}] + \nabla.[\xi(\nabla\mathbf{u})^T + \lambda\mathbf{I}tr(\nabla\mathbf{u}) - (\xi + \lambda)\nabla\mathbf{u}] = -\rho\mathbf{f} \tag{2.16}$$

Detailed discussion of the different criteria behind developing and formulating this FV deformation solver have been validated and published in [9]. In the same work, different constraints applied on the lateral bushing for calculating its deformation have been discussed. For all the results presented in this work, a LP constraint on the lateral bushing has been used wherein the lateral bushing is assumed to be pressed against the casing on the low pressure side, unless mentioned otherwise. [9] also shows that simulation results obtained using the LP constraint has the closest prediction to the corresponding experimental results. On the other hand, a simplified symmetry constraint has been used for evaluating the deformation of the gears for a symmetrically balanced EGM. Further details pertaining to the evaluation of the deformation of the lateral bushings and the gears using an off-line technique using the influence matrix approach is also explained in [9].

2.2.6 Gap Thermal Model

The thermal effects on the fluid flow in the lateral gap is accounted in the TEHD model by primarily solving for the temperature distribution in the lubricating gap

using the following form of the energy equation, assuming full film lubrication at all times [9],

$$\nabla.(\rho C_p \mathbf{v} T) - \nabla.k\nabla T = \psi_v \tag{2.17}$$

The first term on the left of the energy equation is the convection term and represents the transport of enthalpy with the fluid flow, while the second term on the left of the equation represents the diffusion of temperature across the fluid domain. The last term is the source term which indicates the viscous dissipation that is modeled using the following simplified equation [9],

$$\psi_v = \mu\left[\frac{dv}{dz}\right]^2 + \mu\left[\frac{du}{dz}\right]^2 \tag{2.18}$$

It must be noted that this source term represents only the viscous dissipation through the fluid film. However, it will be explained later in Chapter 3 that in the case of mixed film lubrication conditions, the source term also includes energy dissipation due to the near solid to solid contact of the surface asperities.

A 3D mesh for the lubricating gap was created [9] to solve for the temperature in the energy equation due to the fact that the dissipation function needs to be evaluated in the Z direction as well. An instance of this 3D mesh for the gap at a given time step is shown in Figure 2.13, where a 2D mesh with 6 node prism elements was extruded with $\sim$ 10 to 20 cells in the direction of the gap height. Further details related to the implementation of the gap thermal model can be found in [9].

2.2.7 Solid Thermo-Elastic Model

The heat generated in the fluid film due to viscous dissipation is transferred to the solid components in the gap, which are the gears and the lateral bushings. The increase in heat dissipation causes thermal deformation in these solid components which is calculated using the equation outlined in Equation (2.16). The various boundary conditions used for determining the temperatures of the solids and the solution scheme adopted for solving this heat transfer problem are detailed in the

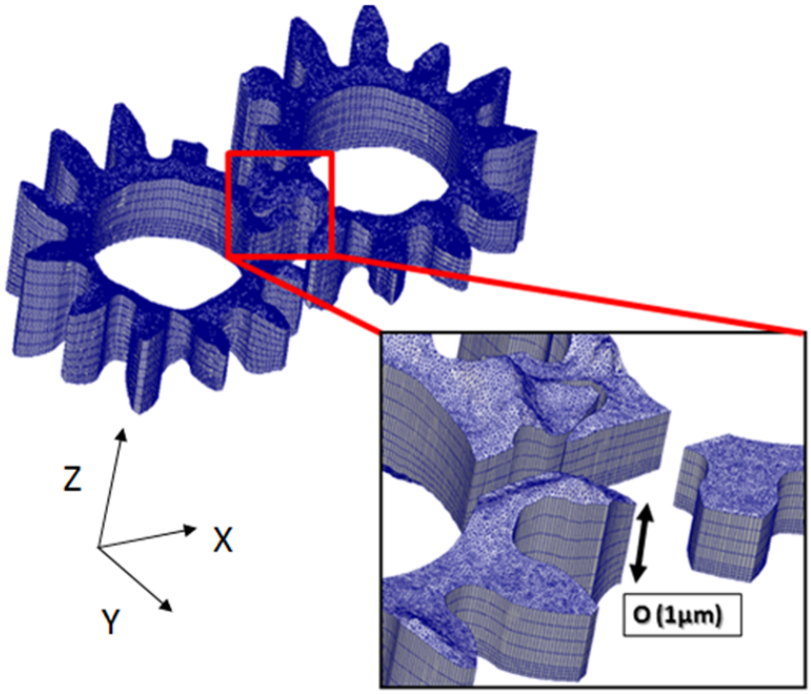

Figure 2.13. The 3D finite volume mesh created for thermal modeling on the lateral gap for Case 1A. The gap thickness is scaled up by 10000 to be visible. Inset shows mesh detail along with typical thickness length scale [9].

work of [9]. The resulting thermal deformation of these solids along with their elastic deformation are evaluated using the methodology outlined in Section 2.2.5. This source of deformation also contributes to updating the film thickness in the lubricating gap domain (h) and this is indicated by the final film thickness equation in the lateral gap as follows,

$$h_{TEHD} = h = h_{EHD} + \delta h_{LB_T} + \delta h_{g,T} \tag{2.19}$$

2.2.8 Force Balance Solver

In a steady state operation of an EGM, a static force equilibrium condition exists on the lateral bushing and for this reason, a force balance solver is integrated in

the lateral lubricating gap model. These force balance conditions define what is known as the 'axial balance' of a pressure compensated EGM. Accurate evaluation of these forces is important to determine both the hydrodynamic and hydrostatic effects which influence the prediction of the lubrication performance in the lateral gap. This section summarizes the different forces acting on the lateral bushing, and the detailed discussion of these forces and their implementation in the model can be found in the works of [9]. The forces presented here are primarily classified into those acting on the balance side of the lateral bushings which are directed towards the gears and the cumulative addition of the forces directed away from the gears. It must be noted here that an additional force due to asperity contact arises in the mixed lubrication model for the lateral gaps which also contributes to the force balance on the lateral bushing, and this will be discussed in the subsequent Chapter 3.

Forces Acting Towards the Gears : In most pressure compensated designs of lateral bushings, high pressure and low pressure balance areas separated by a seal which is present on their rear side (as shown in Figure 2.14(b)). The forces acting on the balance areas are evaluated with the help of the following equations and they are directed towards the gears in the lateral gap,

$$F_{Bal} = p_{HP} A_{HP,Bal} + p_{LP} A_{LP,Bal} \tag{2.20}$$

The point of application of the resultant balance force is calculated using the centers of mass of the high and low pressure balance areas with the help of the following equations,

$$X_{Bal} = \frac{F_{HP,Bal} X_{HP} + F_{LP,Bal} X_{LP}}{F_{Bal}} \tag{2.21}$$

$$Y_{Bal} = \frac{F_{HP,Bal} Y_{HP} + F_{LP,Bal} Y_{LP}}{F_{Bal}} \tag{2.22}$$

Forces Acting Away From the Gears : Certain different components of force on the lateral bushing act in the direction away from the gears and results in lifting the bushing against the balancing force. This sub-section briefly describes the various forces which collectively constitute these lifting forces for the bushing.

The high pressure and the low pressure at the relief grooves (as shown earlier in Figure 2.14(a)) in the lateral bushing respectively constitute the pressure forces which contribute to the force balance condition. At any given angle of rotation, the pressures acting on these relief grooves can be obtained from the fluid dynamic model as discussed earlier in Section 2.1.1. The resultant forces acting on the bushing due to the relief grooves can be evaluated using the following equations,

$$F_{Rel} = p_{HP} A_{HP,Rel} + p_{LP} A_{LP,Rel} \tag{2.23}$$

The distribution of pressures in the different TSVs on the lateral bushing also comprises the force balance on the lateral bushing and is illustrated in Figure 2.14(c). The pressures in the TSVs can be obtained from the interface of the gap model with the fluid dynamic model of HYGESim as explained earlier in Section 2.1.1 and the corresponding forces acting on the TSV areas can be evaluated with the help of the following equation,

$$F_{TSV} = \sum_{i}^{n_t} p_i A_i \tag{2.24}$$

The point of action of these forces is assumed at the center of each TSV and this information along with the TSV areas are obtained from the geometric model which was detailed earlier in Section 2.1.4.

The final force which constitutes the axial balance condition on the lateral bushing is the force due to the pressures evaluated by the Reynolds equation in the gap computational domain. A typical pressure distribution in the lubricating gap is shown in Figure 2.14(d). Since the gap domain is discretized using an FV mesh, the resultant force must be calculated using the pressures in the individual cells and also the areas of the individual cells.

$$F_{TSV} = \sum_{i}^{nFaces} p_i A_i \tag{2.25}$$

The 'axial balance' condition in the lateral bushing is achieved when the two opposing forces on the lateral bushing constitute a static force and moment equilibrium at every instantaneous position of the gears when a steady state operation of the

EGM is assumed. The balance of the system of these forces acting on a pressure plate type lateral bushing was shown earlier in Figure 1.3.

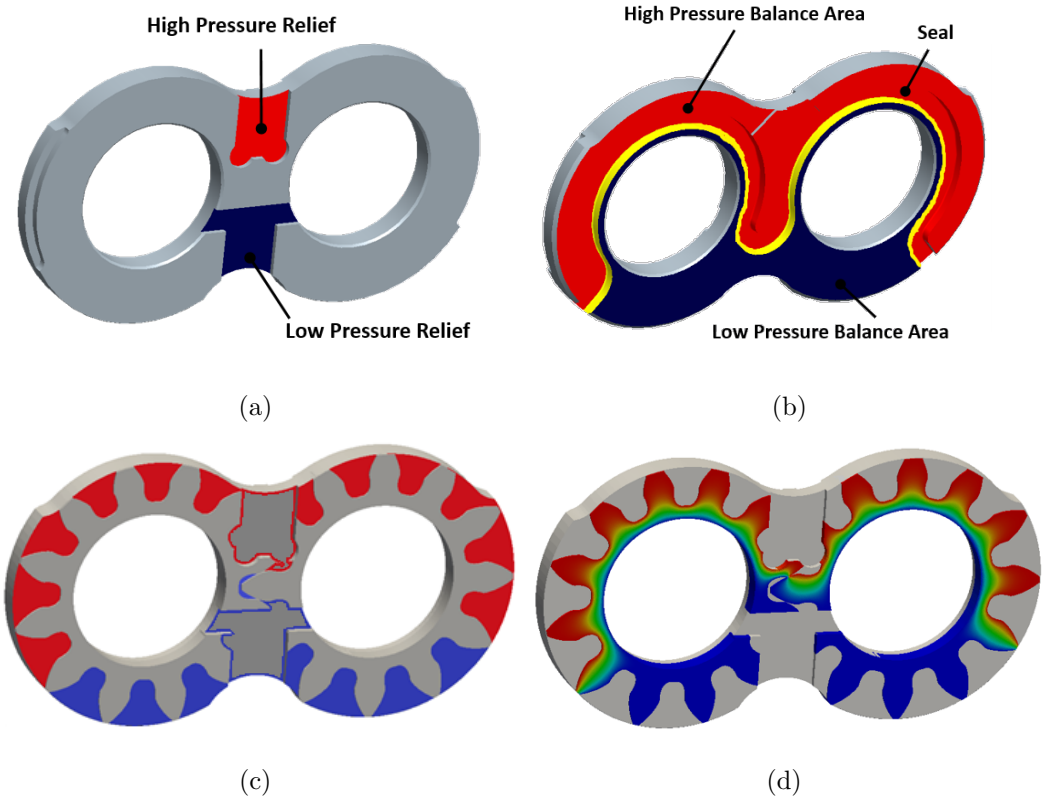

Figure 2.14. The pressures acting on the lateral bushing (example from Case 1B) from the (a) Relief grooves (b) Pressure compensating balance areas (c) TSVs and (d) The lateral lubricating gap [9].

Since for a particular iteration the values of F_{Bal}, F_{Rel} and F_{TSV} are based on inputs to the FSI model, the above conditions of static equilibrium are fulfilled by the solution of the pressure in the gap. Therefore, for every iteration in the progress of the algorithm, a value of the resultant force from the lubricating gap F_{Gap} must be found which fulfills the necessary conditions for static equilibrium of the lateral bushing. Thus, the hydrodynamic effects necessary to fulfill the axial balance condition are determined iteratively between evaluating the pressures in the gap domain and the evaluation of its squeeze velocities. Thus, the evaluation of the micro-motion of the

lateral bushing along with the associated structural and thermal effects is completed using the force balance solver. Further details related to the implementation of this solver and the numerical scheme adopted for the entire TEHD gap model can be found in the work of [9].

2.2.9 Calculation of Lateral Leakages from the Gap

The evaluation of the lateral leakages from the lubricating gap is a significant post processing result which is obtained from the converged simulations of the TEHD model. Leakages from the lateral gap are useful in determining performance of a given EGM design as it is an important constituent of its volumetric efficiency. It should be also observed here that these equations for the leakages are valid only for the full film lubrication regime.

The velocity field in the lubricating gap is obtained from the FSI model and the details of the derivation for the following equations can be found in [9].

$$u = \frac{1}{2\mu}\frac{\partial p}{\partial x}(z^2 - z(h_t + h_b) + h_t h_b) - \frac{z u_g}{h_t - h_b} + \frac{h_t u_g}{h_t - h_b} \tag{2.26}$$

$$v = \frac{1}{2\mu}\frac{\partial p}{\partial y}(z^2 - z(h_t + h_b) + h_t h_b) - \frac{z v_g}{h_t - h_b} + \frac{h_t v_g}{h_t - h_b} \tag{2.27}$$

The velocity field obtained from the above expressions can be integrated to give the leakage flow rate Equation (2.28) and the power losses due to leakages from the lubricating gap can thus be found using Equation (2.29).

$$Q_{leak} = \sum_i \left(\iint_{A_i} \right(v_i . n_i dA \tag{2.28}$$

$$P_{loss,leak} = Q_{leak} \mathbf{\Delta p} \tag{2.29}$$

2.2.10 Calculation of Shear Stresses on the Gear Surface

Computation of the shear stresses acting on the gear surface is also a post-processing feature in the lateral gap and this evaluation is important in determining

the viscous shear losses which directly influence the hydro-mechanical efficiency of an EGM. The shear stress equations presented in this section are valid only when a full film is present at all times and a modified equation for both the leakages and the shear stresses will be presented in Chapter 3 of this dissertation.

The shear stresses due to fluid viscosity are calculated on the surface of the gears and represent a form of power loss from the lubricating gap for the EGM. Considering the gears to be aligned along the XY plane with the Z axis being normal to the gear lateral surfaces, the shear stresses on the gear surface are given by,

$$\tau_{zx} = \mu \frac{\partial u}{\partial z} \tag{2.30}$$

$$\tau_{zy} = \mu \frac{\partial v}{\partial z} \tag{2.31}$$

From the assumptions detailed in [9], the shear stresses on the surface of a gear can be described as a function of the pressure field and the gear velocity.

$$\tau_{zx} = -\frac{h}{2}\frac{\partial p}{\partial x} - \frac{\mu u_g}{h} \tag{2.32}$$

$$\tau_{zy} = -\frac{h}{2}\frac{\partial p}{\partial y} - \frac{\mu v_g}{h} \tag{2.33}$$

In the above equations u_g and v_g are two components of the velocity vector obtained from the angular speed of the gear. This results in a torque that opposes the motion of the gears as stated in Equation (2.34) where i is summed over the cells in the FV domain.

$$\mathbf{T} = \sum_i \left(A_i(\mathbf{r_i} \times \tau_\mathbf{i}) \right. \tag{2.34}$$

Thus the power loss associated with fluid viscous friction can be calculated as,

$$P_{loss,shear} = T.\omega \tag{2.35}$$

2.3 Automatic Numerical Procedure for Finding Optimal Axial Balance

The design of the 'axial balance' condition for an EGM design is a very delicate process which needs to comprehensively consider the hydrostatic and hydrodynamic

effects in the lateral gap. An over-balanced condition implies that the fluid film thicknesses in the lateral gap are very low which results in increased losses due to viscous shear and could result in potential wear on the gears and the lateral bushings. On the other hand, very high film thicknesses in the gap indicate an under-balanced condition which can result in increased leakages from the gap and this can compromise the volumetric efficiency of the EGM. Since, the axial balance design is such a delicate design process, an optimal solution needs to be determined which can carefully consider both the aforementioned opposing sources. An optimal axial balance design is thus critical for ensuring reliability, good operating efficiency and life of an EGM.

Design of axial balance is usually achieved by designing the balance areas on the lateral bushing (as illustrated in Figure 1.2) since this is the only component in the force balance condition (discussed earlier in Section 2.2.8) which can be controlled by the designer. A fully automatic numerical optimization procedure for optimizing the axial balance in EGMs was developed in the works of [10,91] as part of an application in C ++ using open source resources such as OpenFOAM [82], GSL [83] and Linux shell scripting. A flowchart outlining the numerical algorithm used in this procedure is shown in Figure 2.15.

The flowchart in Figure 2.15 shows that for a range of operating conditions provided at the input of the procedure, the algorithm first generates an initial set of designs by varying the design parameters. Objective functions for each of the designs in the current set are then evaluated using the FSI-EHD model for the lateral lubricating gaps. Depending on the evaluation of the objective functions, a direct search method [10, 91] is implemented in an iterative manner to determine the optimal balance design in this multi-objective optimization procedure against a preset convergence criterion. Further details related to the formulation and implementation of this numerical algorithm for different EGM designs can be found in [10, 91].

Two design parameters are selected to define the balance area for each design in the optimization procedure. The first variable is the high pressure balance area A (as highlighted in red in Figure 2.16) and the Y coordinate of the point of application

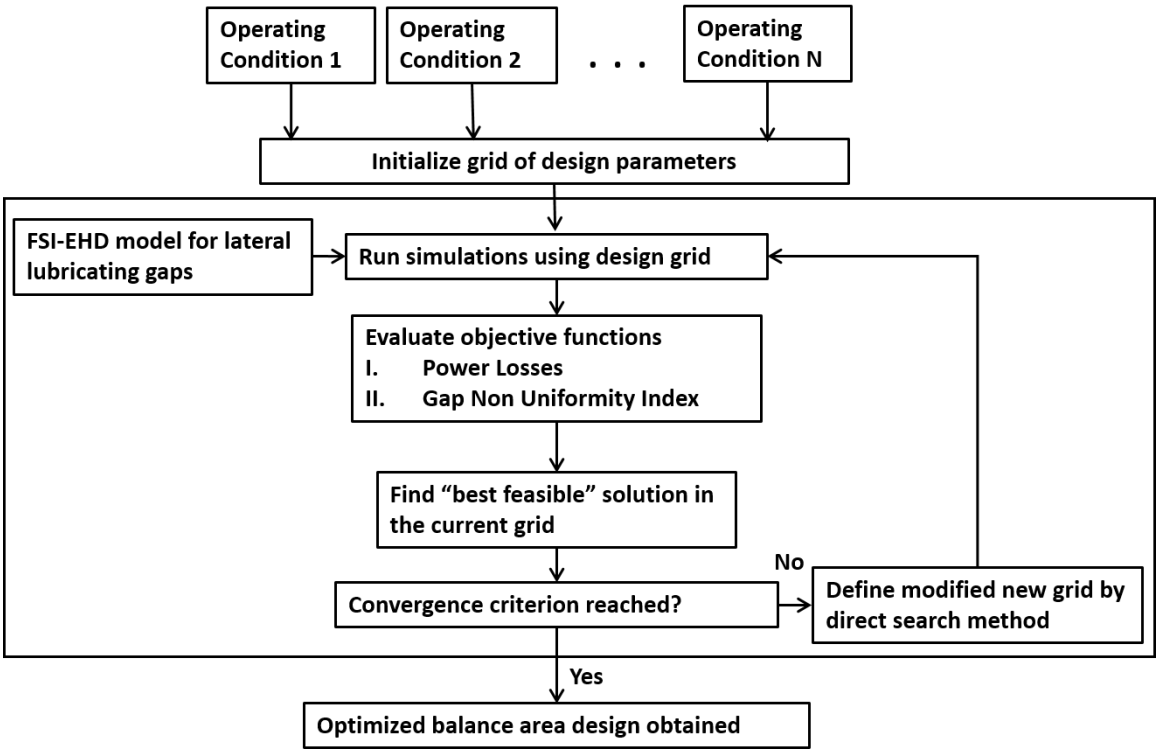

Figure 2.15. Algorithm used in the numerical procedure for designing the optimal axial balance of EGMs [10].

of the resultant force which acts on the high pressure balance area. The reasons for selecting these parameters can be explained with the help of Figure 2.16. It can be observed that the high pressure force acting on the balance side of the lateral bushing can be reduced to a single equivalent resultant force which has a single point of application (point **P** shown in Figure 2.16). Therefore, the balancing force and moment arising from rear side of the lateral bushing can be fully defined by the point of application of the resultant force and the value of the balance area A. By varying A and Y (Y coordinate of point **P**), the forces and moments acting on the lateral bushing also vary.

The objective functions used in the optimization procedure can be primarily classified into the total power loss from the lateral gap and a factor defined as the Gap Non-uniformity Index (GNI) [10, 91]. The power losses in the total gap arise from

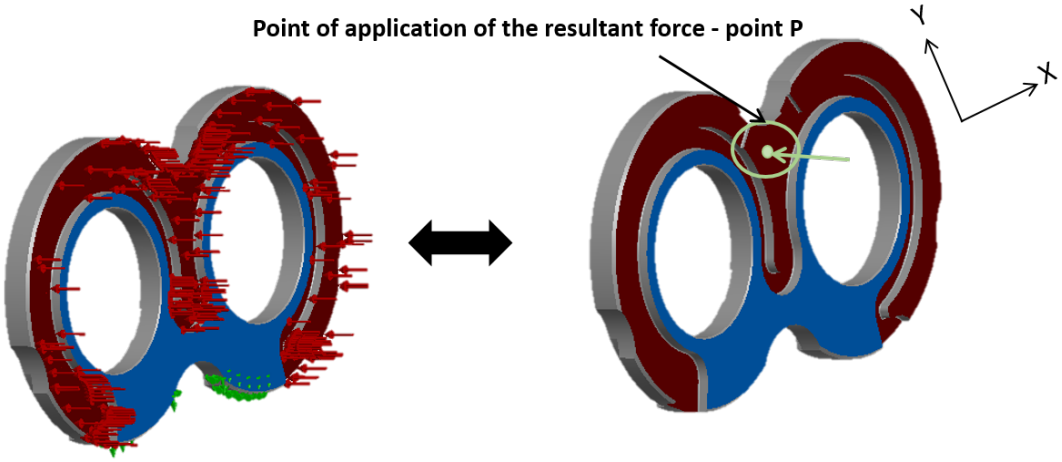

Figure 2.16. (a) Uniform pressure force acting on the balance area of the lateral bushing (shown here is the pressure plate type design in Case 1A) subject to the constraint on the LP side (shown in green). (b) Equivalent resultant force and its point of application on the lateral bushing [92].

the lateral leakages and the shear stresses on the surface of the gears, both of which can be evaluated using the equations described earlier (Equation (2.29) and Equation (2.35)).

The GNI parameter was defined to account for the orientation of the lateral bushings while designing the axial balance. It is desired that the lubricating gap is not tilted towards a particular direction and the orientation of the lateral bushings with respect to the gears is quite uniform across the lateral gap. The GNI parameter indicates the number of non-uniformities in the lateral gap by using a statistical approach with the help of the following equation,

$$GNI = \frac{h_{max} - h_{min}}{2h_{avg}} \tag{2.36}$$

It can be observed that if the GNI for a design under consideration is high, it translates to the fact that the lubricating interface between the lateral bushing and the gears in this design has a higher number of non-uniformities and may have undesirable regions of contact. Thus, evaluating the GNI as an objective function of the

optimization procedure gives a satisfactory measure of the orientation and uniformity of the lubricating gap for a given design of balancing areas in the lateral bushing.

Thus, the numerical procedure developed for obtaining an optimal axial balance design considers the objective functions for the power losses from the lateral gap as well as its non-uniformities for each input operating condition. Consequently, this results in a multi-objective problem to obtain an optimal solution and is solved in an iterative manner concurrently by using the lateral gap model according to the numerical scheme shown in Figure 2.15.

3. CONTRIBUTIONS TO MODELING LUBRICATING INTERFACES

In this chapter, significant contributions made to the numerical modeling of lateral lubricating gaps in EGMs in this dissertation are outlined. While the first part of this chapter comprehensively details the gap model accounting for the mixed lubrication regime occurring at extreme operating conditions of the EGM, its following section discusses the implementation of an improved model for handling occurrence of cavitation phenomenon in the lateral lubricating gaps. Contributions to the lateral gap modeling also include the implementation of a structural solver capable of handling lateral bushings and gears which constitute more than one material in their construction, thereby extending the range of component designs that can be explored using the gap model. The last section presents a module capable of accounting for the friction between the casing and a bearing block type lateral bushing and its influence on the lubricating performance of the machine, as introduced previously in 1. Details related to the model implementation are presented here, while simulation results from these models are presented in the subsequent chapters.

3.1 Mixed-TEHD Model for the Lateral Lubricating Gaps

In the present section, a novel mixed − Thermoelastohydrodynamic model developed as an integral part of this research work is presented. Although a full film lubrication regime is the desired mode of operation for positive displacement machines, mixed lubrication regime occurs at certain extreme operating conditions and with fluids possessing poor lubricating properties such as the low viscous fluids considered in the present research. Mixed lubrication represents a lubrication phenomenon where the surface features play a significant role along with the fluid film in evaluating the various features in the lubricating gap. This becomes especially significant when

the film thicknesses in the lubricating gap are in the same order of magnitude as the surface roughness of the surfaces involved in the interface. In such cases, the load supported in the interfaces which is one of the chief functions in any lubricating gap, especially for the ones present in positive displacement machines, is supported both by the fluid film as well as the surface asperities. Thus, the modeling of mixed lubrication regime becomes substantial in EGMs where the load support in the lubricating interfaces directly influences the operating efficiency of the unit.

An overview of the mixed-TEHD model for the lateral lubricating gaps in EGMs along with the depiction of the interaction between the different sub-models is shown in Figure 3.1. While the elastic deformation solver and the thermo-elastic deformation solver remains identical to the ones described for the full film lubrication TEHD model described earlier in Section 2.2.5 and Section 2.2.7, the other sub-models are adapted to model film lubrication along with the addition of a sub-model for solving asperity contact. These additional changes in the mixed-TEHD model are highlighted below and are explained in detail in the rest of the sections in this chapter.

- *Fluid flow solver* : Solves the average flow Reynolds equation for partial film lubrication which also reduces to the conventional Reynolds equation at full film conditions.

- *Asperity Contact Solver* : Evaluates the load support offered by the surface asperities by considering their elastic plastic deformation features.

- *Force Balance Solver* : Evaluates the force equilibrium on the lateral bushing by additionally including the contact force due to the surface asperities.

- *Gap Thermal Solver* : Solves the energy equation in the gap by additionally including the asperity contact heat dissipation.

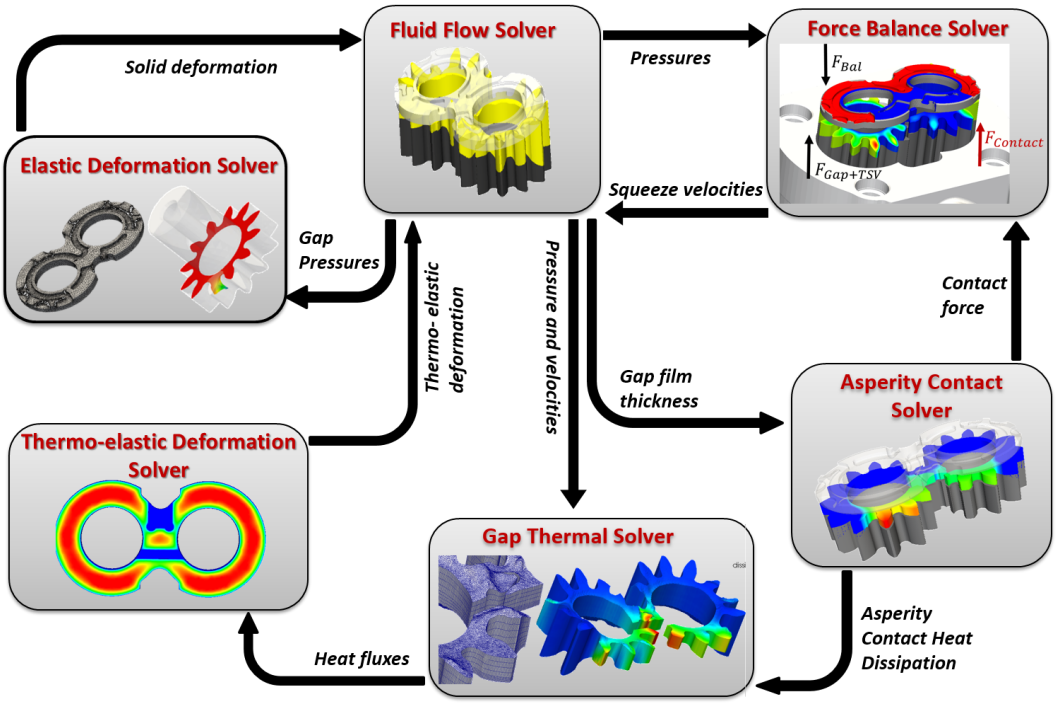

Figure 3.1. Schematic overview of the mixed - TEHD model for the lateral gaps in EGMs.

3.1.1 Definition of Surface Topography Features

In order to fully comprehend the details related to the implementation of the mixed lubrication model, certain definitions specifically related to the surface topography which influence the lubrication performance need to be presented in this section. Different kinds of measurement devices along with their standard reference measurement lines can be found in [23]. This section, however focuses on the definitions of standard surface parameters based on such available measurements for a given surface under study. Broadly, two prominent parameters are widely used in tribology to define the surface features [23] from the surface topography measurements using a stylus instrument, namely the centerline average (CLA) which is denoted by the parameter R_a and the root mean square (RMS) which is indicated by the parameter R_q. The mean line of the surface profiles as obtained from the measurements (represented in

Figure 3.2) is chosen as the reference line according to the mean or M system [23]. It is assumed in the M system that the mean line runs perfectly parallel to the surface profile and the surface area above and below the mean line of the profile remains the same.

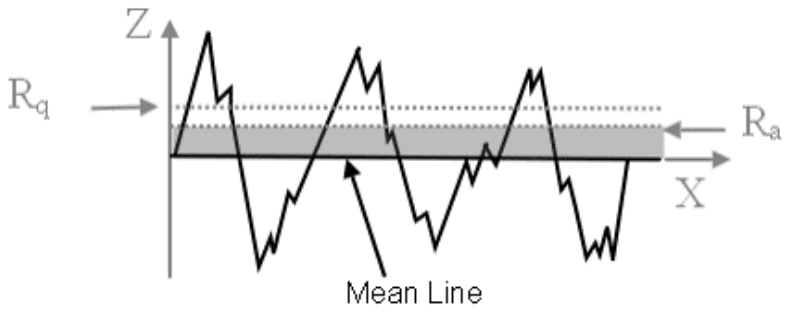

Figure 3.2. Figure representing the parameters R_a and R_q for a given surface topography measurement along with the reference M line.

The surface parameter R_a represents the arithmetical mean deviation from the mean M line of the profile. From a given sample set of surface measurements in the Z direction (z_i) along the X direction as indicated in Figure 23, R_a can be evaluated with the help of the following equation where N represents the number of measurements in the sample,

$$R_a = \frac{1}{N}\sum_{i=1}^{N} |z_i| \tag{3.1}$$

R_a represents the averaging of the given surface data (represented in Figure 3.2) and thus, it is sensitive enough to differentiate surfaces with different shapes and varying ratios between its peaks and valleys [23, 93]. However, this parameter is not sufficient enough to define a surface since it does not indicate the magnitude of deviation from the mean line.

R_q represents the standard deviation of the surface and with the help of given sample set of surface measurements, it can be evaluated by using the following equation,

$$R_q = \left(\frac{1}{N} \sum_{i=1}^{N} |z_i|^2 \right)^{1/2} \tag{3.2}$$

R_q has the capability to capture the variation in distributions of the surface valleys and peaks. Since R_q directly represents the standard deviation or the RMS of the surface profile, it is believed in literature [23, 93] to be more accurate than R_a. Although both the parameters have inherent inaccuracies [23] and need additional surface parameters to fully define a profile, R_q is chosen in this research work to characterize the considered surfaces for the sake of simplicity.

3.1.2 Determination of the Mixed Lubrication Regime

Lubrication regimes can be broadly divided into full film, mixed film and boundary regimes depending upon the thickness of the fluid film and the influence of the surface roughness features on the lubrication performance. While full film lubrication defines a consistent lubricating film of reasonably high thicknesses at all times which is solely responsible for the lubricating ability of the interface, boundary lubrication regime has considerable surface asperity contact and the lubricating film does not play any role in the lubrication performance. Mixed lubrication regime is the intermediate phenomenon where both the surface features and the lubricating film directly influence the lubricating behavior of the interface.

Although all the lubrication regimes have been extensively studied over the past few decades [24, 94], the exact bounds between each regime has never been rigorously defined in literature [24]. This is primarily due to the complexity in defining the exact regions where either the fluid film or the surface asperities cease to influence the lubricating gap. As a result, only certain approximate analytical tools are available to simplify the definition of the different regimes and two of these tools are discussed in the following sub-sections.

Analytical Dimensional Film Parameter : An analytical expression which relates a dimensional film parameter Λ and the surface roughness value R_q of the two surfaces involved in the lubricating interface, approximately helps in distinguishing the different possible regimes of lubrication [23]. This non-dimensional film parameter Λ can be defined as follows where h_{min} in the expression is the minimum film thickness in the lubricating interface,

$$\Lambda = \frac{h_{min}}{\sqrt{R_{q,a}^2 + R_{q,b}^2}} \tag{3.3}$$

Using the aforementioned film parameter, the distinction between the various lubrication regimes has been derived [23] and are listed in Table 3.1. It can be observed from the table that an additional elastohydrodynamic (EHD) lubrication regime which considers the structural deformation of the surfaces due to the pressures in the gap is defined between the hydrodynamic and mixed regimes. It must be noted that the EHD regime modeled in the existing full film lateral gap model for EGMs is very close to the limits of the mixed lubrication regime. This reasoning can be used to further drive the motivation to include mixed film modeling for the present case.

Table 3.1.
Distinction of the various lubrication regimes according to the dimensionless film parameter Λ.

Lubricating regime	**Limits of film parameter Λ**
Hydrodynamic lubrication	$5 \leq \Lambda < 100$
Elastohydrodynamic lubrication	$3 \leq \Lambda < 10$
Mixed lubrication	$1 \leq \Lambda < 5$
Boundary lubrication	$\Lambda < 1$

In order to simplify the non-dimensional parameter in terms of actual values of film thicknesses to understand the significance and onset of the mixed lubrication regime in EGMs, $R_{q,a}$ and $R_{q,b}$ have both been assumed at a value of 0.5 μm, which is usually

around the expected surface roughness values achieved at the end of surface finishing treatments for most lateral bushings and gears currently available in the market. The corresponding values of Λ and h_{min} (in μm) were evaluated and a plot between these two values are shown in Figure 3.3. It can be observed from the plot and the corresponding values in Table 3.1 that even for values of h_{min} in he order of 2 μm, the effects of mixed lubrication become prominent and needs to be incorporated in the modeling. Such film thickness values are quite typical in the operation of EGMs as observed in the works of [9, 10].

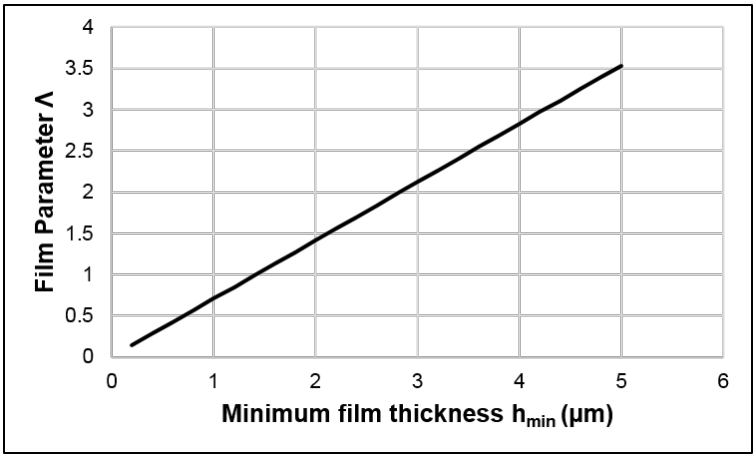

Figure 3.3. Plot representing the relationship between h_{min} and Λ.

Stribeck Curves : The popular Stribeck curves obtained through experiments performed on journal bearings have been widely used in tribology literature [23] to understand the different regimes of lubrication. The curve is plotted between the coefficient of friction (μ_f) and a dimensionless Hersey number (H_s) (or the lubrication parameter) which is defined with the help of the dynamic viscosity of the fluid (μ), operating pressure (p) and rotational speed (ω) as follows,

$$H_s = \frac{\mu\omega}{p} \tag{3.4}$$

The Stribeck curve showing the effects of operational parameters as represented by H_s on the coefficient of friction is shown in Figure 3.4 along with the ranges for the different lubrication regimes.

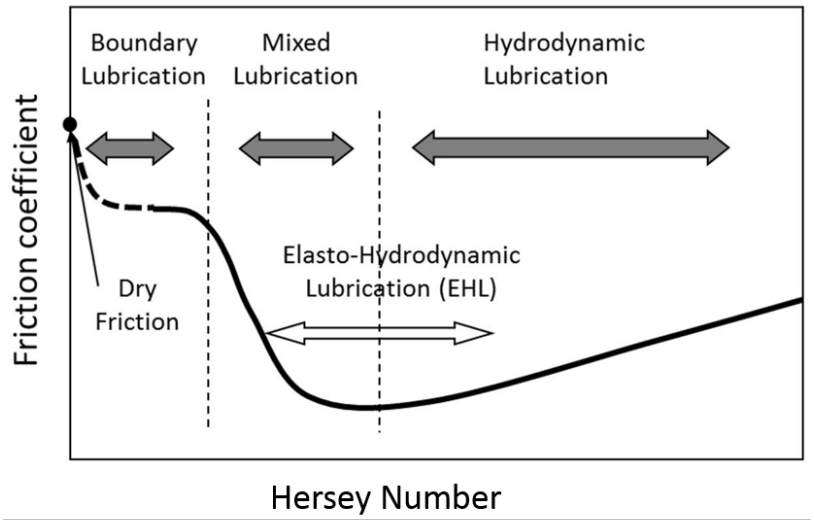

Figure 3.4. Representation of the Stribeck curve along with the indicated lubrication regimes.

It must be noted from Figure 3.4 that as the value of H_s decreases, the effect of the fluid film on the lubricating gap also decreases and surface features need to be accounted in the gap model. For a given operating speed and pressure, a lower viscous fluid will have higher chances of mixed lubrication than a working fluid with higher viscosity. Since one of the chief goals of this research involves modeling of working fluids with extreme values of viscosities, a generic lubricating gap model which is capable of modeling both full film and mixed lubrication needs to be developed. The formulation and implementation of such a model is detailed in the subsequent sections in this chapter.

3.1.3 Average Flow Reynolds Equation

The average flow Reynolds equation is a modified form of the Reynolds equation originally developed for full film lubrication (Equation (2.11)). This equation which was first developed in the work of [35, 36] has been used widely in many partial lubrication models which were outlined earlier in Section 1.4.2. In this equation, the average hydrodynamic pressure resulting from both the surface features as well as the fluid film in the lubricating interface is evaluated. The average flow Reynolds equation uses a statistical approach to determine the asperity effects on the lubricant flow through the gap. First, a local film thickness function h_T is defined as the gap compliance with the help of the roughness amplitudes δ_1 and δ_2 of each of the surfaces respectively as follows,

$$h_T = h + \delta_1 + \delta_2 \tag{3.5}$$

The roughness amplitudes defined as the mean deviation from the center line for each of the surfaces as shown in Figure 3.5. In all the cases simulated in this work, surfaces with Gaussian distribution of asperity heights with zero mean is assumed. Thus, δ_1 and δ_2 in this work represent the standard deviations of the surfaces respectively. Although, alternative and more complex definitions are available for the gap compliance in [94], the above simplified approach is found to be suitable enough for conformal contacts [34] such as the one in the present study. The value of h for the case of EGMs can be determined from the Equation (2.14) as stated earlier while considering both surface and thermal effects. The form of average flow Reynolds equation as presented in [37] to solve the average pressure in the gap is given as,

$$\frac{\partial}{\partial x}\left(\phi_x \frac{h^3}{12\mu}\frac{\partial p}{\partial x}\right) + \frac{\partial}{\partial y}\left(\phi_y \frac{h^3}{12\mu}\frac{\partial p}{\partial y}\right) = \frac{U_1 + U_2}{2}\left(\frac{\partial h_T}{\partial x} + \frac{\partial h_T}{\partial y}\right) + \frac{U_1 - U_2}{2} R_q \left(\frac{\partial \phi_s}{\partial x} + \frac{\partial \phi_s}{\partial y}\right) + \frac{\partial h_T}{\partial t} \tag{3.6}$$

ϕ_x,ϕ_y and ϕ_s are called as the flow factors which are functions of statistical parameters of the participating surfaces and the film thicknesses in the lubricating gap [36]. ϕ_x and ϕ_y accompany the Poiseuille terms in the Reynolds equation which represent

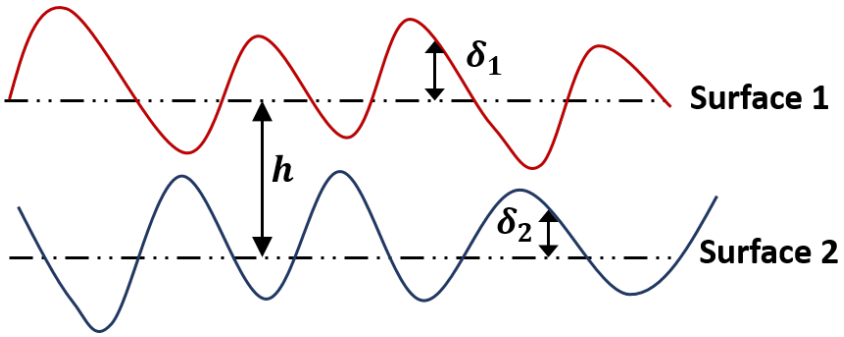

Figure 3.5. Figure representing the physical interpretation of the numerical gap compliance function.

the flow driven by pressure and thus, are called the pressure flow factors in the X and Y directions respectively. ϕ_s is called the shear flow factor [94] and is associated partially with the Couette flow which is also referred to the shear flow. When compared to the traditional Reynolds equation for full film lubrication (defined in [23]), it can be observed from Equation (3.6) that an additional shearing term $\frac{U_1-U_2}{2}R_q\left(\frac{\partial\phi_s}{\partial x}+\frac{\partial\phi_s}{\partial y}\right)$ is present which accounts for the shearing flow due to the surface roughness. For smooth surfaces, $R_q = 0$ removes the shearing term from the equation and all the other flow factors at the limit of full film lubrication reduces the average flow Reynolds equation to the corresponding conventional one for full film [36].

The flow factors are obtained by evaluating the ratio between the flows through rough (with a defined surface topography) and smooth surfaces which are otherwise identical [35]. A Gaussian distribution of the surface heights for both the gears and the lateral bushings have been assumed for the all the results presented in this research. This assumption has been found to be reasonable in several mixed lubrication models [28, 30] and is also observed in more than 90 percent of the finished surfaces [93].

The values for the flow factors for a normally distributed surface were evaluated in [37] and represented with the help of the parameter h/R_q where the film thickness h is non-dimensionalized with the help of the surface roughness R_q. These purely

statistical relationships are used in the present work and is elaborated in Appendix B of this dissertation.

Additional assumptions have been made for the case of EGMs to derive a form of the average flow Reynolds equation which is suitable for the present work. The surfaces of the gears and the lateral bushings are assumed to be isotropic which implies that the surface properties along the X and Y directions are identical. Since the lateral lubricating gap constitutes rotational surfaces, the expected wear on both the X and Y directions are not very different from each other. Thus, the asperity aspect ratio is $\gamma = \frac{\lambda_x}{\lambda_y} = 1$ which consequently makes the pressure flow factors ϕ_x and ϕ_y identical to each other. A simplified differential relationship between the gap compliance h_T (defined earlier in Equation (3.5)) and the local film thickness h was defined in [37] by introducing a contact factor ϕ_c as follows,

$$\partial h_T(x,t) = \phi_c \partial h(x,t) \tag{3.7}$$

A composite roughness parameter R_q is defined for the lateral gap which considers the surface roughness R_{q1} andR_{q2} of the lateral bushing and the gears respectively according to the following equation which have been used in the work of [30],

$$R_q = \sqrt{R_{q1}^2 + R_{q2}^2} \tag{3.8}$$

Using different values of the composite roughness parameters allows the flexibility in the present mixed lubrication model to simulate Gaussian distribution surfaces with different R_q.

A modified form of the average flow Reynolds equation for EGMs has been derived using the assumptions made earlier while deriving the full film Reynolds equation for EGMs (Equation (2.11)) and by adapting the generic average flow Reynolds equation (Equation (3.6)) and Equation (3.7) for the contact factor to incorporate the deformation of both the surfaces. Thus, the Reynolds equation for simulating partial film lubrication in EGMs can be obtained as follows,

$$\nabla . \quad \phi_x \left(\frac{-\rho h^3}{12\mu} \right) \left(\nabla p \right) + \phi_c \frac{\rho \mathbf{v_b}}{2} . \nabla(h) + \phi_c \rho \mathbf{v_b} . \nabla(h_b) + \phi_c \rho \left(\frac{\partial h_t}{\partial t} - \frac{\partial h_b}{\partial t} \right) + R_q \frac{\mathbf{v_b}}{2} \frac{\partial \phi_s}{\partial x} = 0 \tag{3.9}$$

The flow factors can be first determined with the film thickness information in the lateral gap in the time step being evaluated according to the formulas listed in Appendix B. Using the values of the flow factors and the film thicknesses, the average pressure in the lateral gap due to both the surface and the fluid film can be evaluated.

3.1.4 Asperity Contact Solver

The asperity contact solver constitutes one of the most significant features in the mixed lubrication model developed for the lateral gaps. This is owing to the fact that the contact of the surface asperities influences the load support in the lubricating interface. When the film thickness in the gap reaches the limit of mixed lubrication regime as defined earlier in Section 3.1.2, the interaction of the asperities from both the gears and the lateral bushing share a portion of the total load in the lubricating gap with the fluid film.

In order to evaluate the effects of asperity interactions on the lubrication performance, a rough surface contact model proposed in the work of [44] is used in the present research. This contact model assumes that the surface asperities experience a combination of elastic and plastic deformation, and numerical contact simulations were performed for surfaces with different surface roughness and material properties. Empirical relationships between the gap compliance and the resulting contact pressure were formulated after a series of numerical simulations using regression and are purely based on the statistical surface and material properties of the associated surfaces. The non-dimensional relationship between the gap compliance and the contact pressure from the asperities as obtained from [44] is defined with the help of the following fourth order polynomial in terms of the non-dimensional contact pressure ($\overline{P_c}$) which is the unknown in the equation,

$$\frac{h_T}{R_q} = \exp \quad \sum_{i=0}^{4} \left(\overleftrightarrow{\gamma_G}[G_i]\overrightarrow{H_Y})\overrightarrow{P_c^i} \right) : when\ \overline{P_c} < H_Y \tag{3.10}$$

$$\frac{h_T}{R_q} = 0 : when\ \overline{P_c} \geq H_Y \tag{3.11}$$

In equations Equation (3.10) − (3.11), H_Y indicates the non-dimensional material hardness defined in [44] according to the following equations, where H is the material hardness, E^* is the composite Youngs modulus of both the surfaces as defined by Equation(3.13) and λ_y is the statistical auto-correlation length of the surface which is related to the frequency of horizontal distribution of the asperities. λ_y indicates the horizontal distance along the surface at which any two points on the surface are independent of each other and in the present case, a value of λ_y larger than the RMS surface roughness is assumed.

$$H_Y = \frac{2H\lambda_y}{\pi E^* \sigma} \tag{3.12}$$

$$E^* = 2\left[\frac{1-\nu_1^2}{E_1} + \frac{1-\nu_2^2}{E_2}\right]\Bigg(\tag{3.13}$$

In the above equation for the equivalent Youngs modulus for both the surfaces, E_1 and E_2 represent the Youngs moduli for both the surfaces respectively while ν_1 and ν_2 are their Poisson ratios respectively. $\overline{P_c}$ represents the non-dimensional contact pressure which is defined by the following equations,

$$\overline{P_c} = \frac{P_c}{C_p} \tag{3.14}$$

$$C_p = \frac{\pi E^* R_q}{2\lambda_y^*} \tag{3.15}$$

$\overrightarrow{\gamma_G^T}$ and $\overrightarrow{H_Y^T}$ are the parametric matrices which are defined empirically by [44] as follows,

$$\overrightarrow{\gamma_G^T} = [1, \gamma^{-1}, \gamma^{-2}, \gamma^{-3}] \tag{3.16}$$

$$\overrightarrow{H_Y^T} = [1, H_Y^{-1}, H_Y^{-2}, H_Y^{-3}] \tag{3.17}$$

Since the occurrence of elastic plastic deformation for the asperity contact is assumed in the model, the resulting contact area which contributes to the load support is permanently altered from the nominal area (a_{nom}) which is available in the gap domain. This permanent alteration of the surfaces in the lubricating gap is also observed as wear patterns in the lateral bushing after operation, which is noted in the work of [9] and shown earlier in Figure 1.6. The non-dimensional relationship between

this altered area (a_r) which will be referred to as the real contact area and the contact pressure is given as follows,

$$\frac{a_r}{a_{nom}} = \exp \quad \sum_{i=0}^{4} \left(\overleftrightarrow{\gamma_A}[A_i]\overrightarrow{H_Y})\overrightarrow{P_c^i} \right) : when \overline{P_c} < H_Y \tag{3.18}$$

$$\frac{a_r}{a_{nom}} = 1.0 : when \overline{P_c} \geq H_Y \tag{3.19}$$

$\overrightarrow{\gamma_A}$ represents the parametric matrix for the real contact area evaluations and is evaluated with the help of the following expression,

$$\overrightarrow{\gamma_A^T} = [1, \gamma^1, \gamma^2, \gamma^3] \tag{3.20}$$

The values of the parametric matrices used in this work is referred from the work of [44] and the actual values of these matrices can be found in this cited article.

The contact pressure in the lubricating interface is solved for each cell in the FV mesh of the computational domain with the help of Equation (3.10) − (3.11) after obtaining the current film thicknesses in the gap from the gap fluid flow model. Since Equation (3.10) represents a fourth order polynomial in terms of the unknown $\overline{P_c}$, an iterative secant method [99] is used to solve for the non-dimensional contact pressure. Using these values of $\overline{P_c}$ at the end of convergence, the real contact area using Equation (3.18) − (3.19) is evaluated for each cell in the gap mesh. It must be observed here that all the contact calculations are dependent solely on the surface topography and the material properties of the associated surfaces and are independent of other features in the lubricating gap.

All the contact conditions performed in this sub-model are found to be invoked close to the limit of the mixed lubrication regime when defined as $\frac{h_T}{R_q} = 1.5$. This criterion for estimating the onset of the influence of the surface asperities on the lubrication regime was found to be reasonable in the works of [28].

Figure 3.6 shows the instances of contact calculations in the asperity contact sub-model by representing the different evaluated parameters in the lateral gap which are the gap film thickness (shown in Figure 3.6(a)), contact pressure (shown in Figure 4.2(a) and the resulting contact area (shown in Figure 4.2(b)) as estimated by

the asperity contact model. The highlighted regions in Figure 3.6 indicate the parts of the gap domain where the contact calculations were performed as a result of the aforementioned contact criteria. It must be noted from these figures that the rest of the gap domain is unaffected by this contact model and are present under the full film lubrication regime.

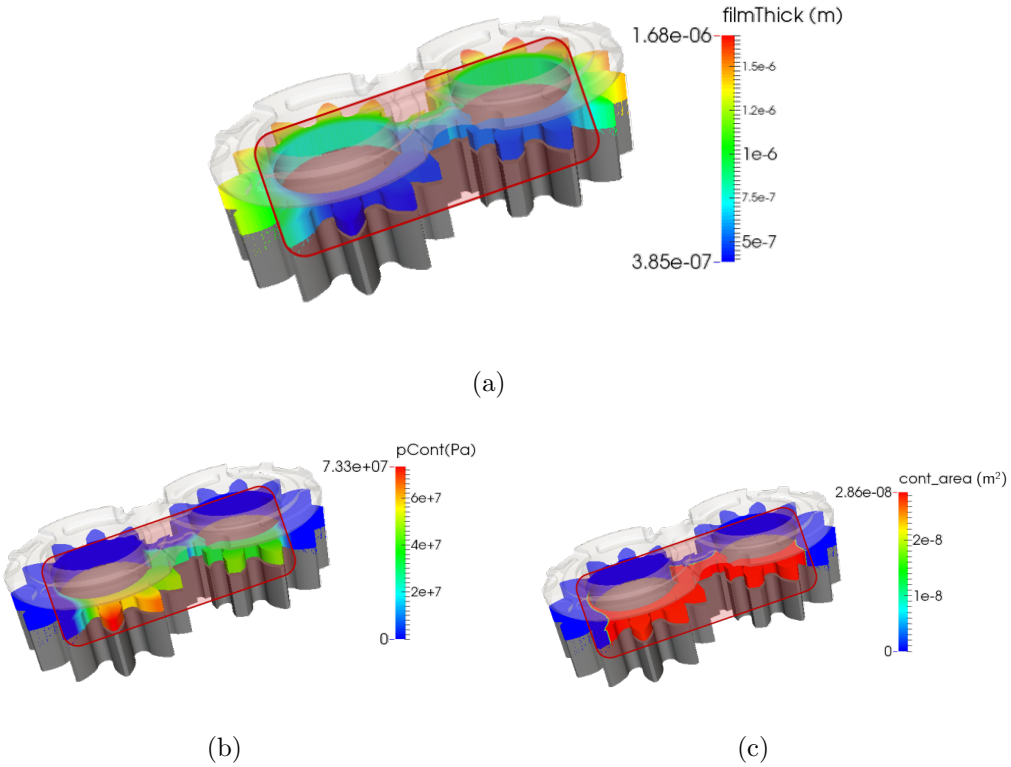

Figure 3.6. Representation of the contact calculations in the asperity contact sub model (example for Case 1B) (a) Gap film thickness distribution (b) Evaluated contact pressure (c) Evaluated contact area.

3.1.5 Force Balance Solver

The force balance solver in the mixed-TEHD lubrication model includes all the forces from the full film model described in Section 2.2.8 and an additional contact

force due to the contact pressure evaluated from the asperity interactions. Since all the other forces have already been outlined in Section 2.2.8, this sub-section only contains the description of the contact force which is exclusively added for the mixed lubrication model.

The contact pressures and the real contact area (represented in Figure 3.6) evaluated from the asperity contact sub-model contribute to the contact forces which is consequently evaluated only at those faces where the contact conditions imposed on the model is attained. The contact forces are evaluated through a cumulative addition of all contact pressures and the corresponding real contact area as follows,

$$F_{contact} = \sum_{i}^{nFaces} \Big(p_{c-i} a_{r-i} \tag{3.21}$$

It can be observed from the above equation that although the formula is applied to all the faces in the computational gap, the contact pressures are non-zero only at the contact regions. The point of application of the contact force can be obtained with the help of the following equations,

$$X_{contact} = \frac{\sum_{i}^{nFaces} p_{c-i} a_{r-i} X_i}{F_{contact}} \tag{3.22}$$

$$Y_{contact} = \frac{\sum_{i}^{nFaces} p_{c-i} a_{r-i} Y_i}{F_{contact}} \tag{3.23}$$

In the force balance solver, instantaneous squeeze velocities of the bushing which contribute to the hydrodynamic effects in the lateral gap are determined at the points $T0$, $T1$ and $T2$ (as shown in Figure 2.12) using Powells multidimensional root finding method from GSL libraries [83], in order to satisfy the force and moment equilibrium contributed by all the components of forces on the lateral bushing.

3.1.6 Gap Thermal Model

The temperature in the lubricating gap along with the imposed boundary conditions (as outlined in Section 2.2.6) are solved using the form of the energy equation

using the full film lubrication assumption. However, for the case of the mixed lubrication regime, it was noted in the work of [28] that the source term in the energy equation needs to be modified to include the effect of heat dissipation when the asperities from the two surfaces are in close proximity with each other at the limit of the contact criterion. The modified form of the energy equation implemented in the mixed-TEHD model is represented below,

$$\nabla.(\rho C_p \mathbf{v} T) - \nabla.k\nabla T = \psi_t \tag{3.24}$$

The source term ψ_t is composed of two different sources for heat dissipation which are the viscous dissipation through the fluid film ψ_t (as represented in Equation (2.17)) and the heat dissipation through the asperity contact. The contribution of these two sources to the total source term is represented as follows,

$$\psi_t = \frac{\psi_v dV_e + \psi_c dA_e}{dV_e} \tag{3.25}$$

In the above equation, dV_e represents the differential volume in the element and dA_e indicates the discretized surface area of the cell [28]. The frictional heat per unit area is represented by ψ_c and is computed using the friction coefficient μ_f with the help of the following equation,

$$\psi_c = \mu_f p_c U \tag{3.26}$$

The friction coefficient for the asperity contact is presently assumed at 0.1 which was also in the same order of values assumed for journal bearing interfaces in [30,34]. It must be noted here that the asperity contact heat dissipation is calculated only at the regions where the contact pressures are non-zero. In full film lubrication conditions, the energy equation reduces to the form stated in Section 2.2.6.

3.1.7 Evaluation of Shear Stresses

The work of [36] derive an average stress expression for the shear stresses from the same domain used for obtaining the average flow Reynolds equation. Additional

correctional factors used in this equation to account for the disturbance in the velocity fields due to the roughness of the surfaces and the mean shear stress ($\overline{\tau_{zx}}$,$\overline{\tau_{zy}}$) for a generic lubricating interface are given by the following equations,

$$\tau_{zx} = -0.5 * \phi_{fp}(h_t - h_b)\frac{\partial p}{\partial x} - \left(\frac{\mu(\phi_f - \phi_{fp})u_g}{h_t - h_b}\right)\Bigg(\tag{3.27}$$

$$\tau_{zy} = -0.5 * \phi_{fp}(h_t - h_b)\frac{\partial p}{\partial y} - \left(\frac{\mu(\phi_f - \phi_{fp})v_g}{h_t - h_b}\right)\Bigg(\tag{3.28}$$

The shear stress correction factors ϕ_f, ϕ_{fs}, ϕ_{fp} are purely dependent on the surface distribution of the lubricating interface. Since a Gaussian distribution is assumed in this work, the non-dimensional equations for these factors have been derived in the work of [37] and their expressions are listed in Appendix B of this work. The resultant torque and power losses due to the shear stress can be obtained using the same equations listed for full film lubrication in Section 2.2.10.

3.1.8 Evaluation of Leakages

The average flow Reynolds equation (Equation (3.9)) is derived from the assumption that there is a disturbance in flow when the roughness in the surface becomes significant [35]. This equation is originally derived from the average flow equation in the X and Y directions after introducing the factors for rough and smooth surfaces as follows where $\overline{p}$ is the average pressure in the interface,

$$q_x = -\phi_x\frac{h^3}{12\mu}\frac{\partial \overline{p}}{\partial x} + \left(\frac{U_1 + U_2}{2}\right)\overline{h} + \left(\frac{U_1 - U_2}{2}\right)R_q\phi_s\Bigg(\tag{3.29}$$

$$q_y = -\phi_y\frac{h^3}{12\mu}\frac{\partial \overline{p}}{\partial y} \tag{3.30}$$

However, for the case of EGMs, the deformation of both the surfaces need to be considered and by integrating the velocity fields and using the equations indicated in Equation (2.26) − (2.27), the equation for leakages can be obtained as listed in [95]. A differential boundary element of the desired region is considered for deriving the leakages as shown in Figure 3.7.

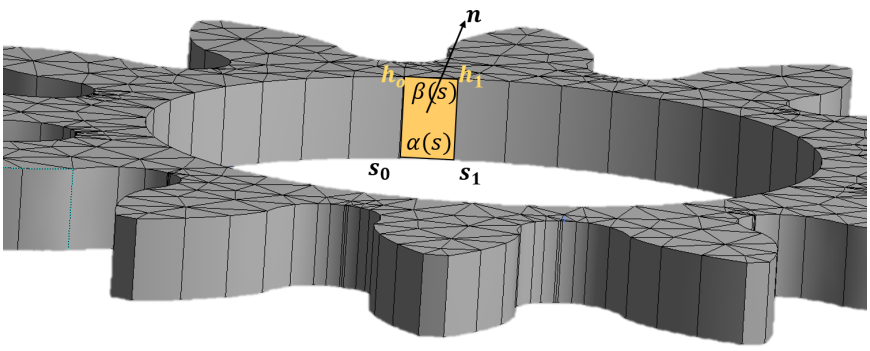

Figure 3.7. Representation of the differential boundary elements used for deriving the leakages.

An integral equation for the leakages can be obtained by integrating the velocity fields along the normal to the face of the differential element (as shown in Figure 3.7) in the following manner,

$$Q_{leak_i} = \int_{s_0}^{s_1} ds \int_{\alpha(s)}^{\beta(s)} (un_x + vn_y)dz \tag{3.31}$$

$$s_0 = 0, s_1 = \delta, \alpha(s) = 0, \beta(s) = h_0 + \frac{h_1 - h_0}{s_1 - s_0}s \tag{3.32}$$

After performing the same evaluations and by comparing the flow factors for the terms in Equation (3.29) − (3.30), the following equation for evaluating the leakages in mixed lubrication conditions was derived,

$$\begin{aligned} Q_{leak} = \sum_{i}^{nFaces} \Bigg[& -\frac{-\delta_i}{48}\left(\phi_x\left(n_{1i}\frac{1}{\mu}\frac{\partial \overline{p}}{\partial x}_i + n_{2i}\frac{1}{\mu}\frac{\partial \overline{p}}{\partial y}\right)\right. \\ & (-4h_b^3 + 6h_{1i}h_b^2 + 6h_{0i}h_b^2 - 4h_{1i}^2h_b - 4h_{0,i}^2h_b - \\ & 4h_{0i}h_{1i}h_b + h_{0i}^3 + h_{0i}^2h_{1i} + h_{0i}h_{1i}^2 + h_{1i}^3) + \\ & \left. R_q\phi_s\frac{\delta_i(h_{0i} + h_{1i} - 2h_b)}{4}(un_1 + vn_2)\right] \end{aligned} \tag{3.33}$$

The leakages in the lateral gap can thus be evaluated as part of the post-processing routines by using the values of the converged pressure fields and the resultant velocity fields.

3.1.9 Numerical Scheme for Mixed-TEHD Lateral Gap Model

A flowchart representing the iterative scheme adopted for solving and coupling the different sub-models outlined in the mixed-TEHD gap model is shown in Figure 3.8. It can be observed from the flowchart that the all the sub-models outlined in Sections 3.1.3 − 3.1.6 interface with each other in an iterative manner while exchanging information across each other as summarized in Figure 3.1.

An initial guess for the film thickness at the three points pictured in Figure 2.12 is made at the beginning of the algorithm. Using the film thickness distribution in the computational domain, the various flow factors required to implement the mixed film model are evaluated using the non-dimensional relationships listed in Appendix B. Subsequently, the average flow Reynolds equation is solved to obtain the average pressure in the gap. This allows the evaluation of velocity fields in the gap and thus, by solving the energy equation in the 3D fluid mesh (as detailed in Section 2.2.6), the temperature in the lateral gap can be obtained. The fluid properties can then be updated using the various relationships presented in this work for each working fluid considered. Since the thermal effects do not vary as dynamically as the structural effects, the deformation of the solids due to these effects are evaluated only every revolution. In these steps, the temperature fields in the gap are used to evaluate the resultant heat fluxes at the lateral bushings and the gears. Subsequently, the thermo-elastic deformation of the solids is evaluated after solving the applied temperature on the solids through the diffusion equation. This deformation loop is performed iteratively until a converged pressure is achieved according to a preset criterion.

At the end of the thermo-elastic coupling, the asperity contact sub-model is invoked to evaluate any possible contact pressure and the corresponding contact area in the event that that the contact condition is achieved. Then, the force balance model solves for the static force equilibrium on the lateral bushing and repeats the entire numerical scheme until the final squeeze velocities determining the tilt of the bushing is obtained. The resultant squeeze velocities are then integrated to find the new tilt

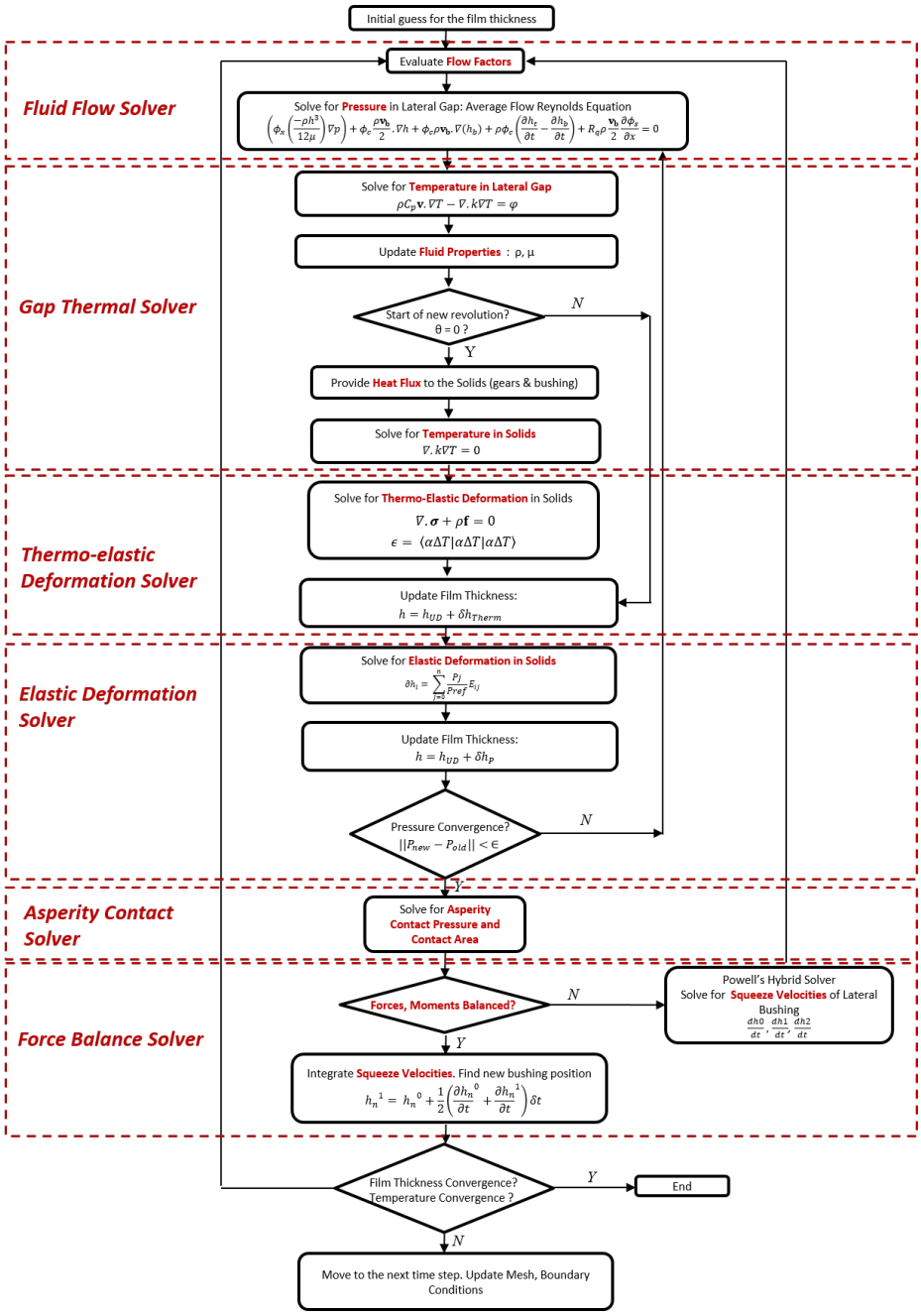

Figure 3.8. Flowchart representing the numerical scheme implemented in the mixed-TEHD model for the lateral lubricating gaps in EGMs. The flowchart also shows the coupling of the different sub-models constituting the mixed-TEHD model and the manner in which they interact with each other.

of the bushing. The entire scheme is iterated for every angular step in the computational domain until a steady state convergence in terms of both the film thickness and temperatures in the lateral gap are obtained.

3.2 Cavitation Modeling in Lateral Lubricating Gaps

The most commonly used numerical technique to handle cavitation conditions in lubricating gaps (as introduced earlier in Chapter 1) is the Reynolds condition or the Swift-Steiber model [96] where the pressures in the gap are saturated to a constant value actively during the solution, whenever their values cross a preset threshold. This approach was also used in the lubricating gap modeling in hydraulic machines of axial piston type [53–55] and in external gear machines for lateral gaps in the work of [9]. However, using a simplified approach such as the Reynolds conditions in severe operating conditions, can lead to numerically unstable pressure distribution shown in Figures 3.9(b) and 3.9(b). Unrealistic pressure peaks and valleys can be seen in these figures, which were found to occur typically at low gap height regions in the gaps. This necessitates a numerically stable mass conserving cavitation algorithm which is implemented for the first time in EGMs in the present research.

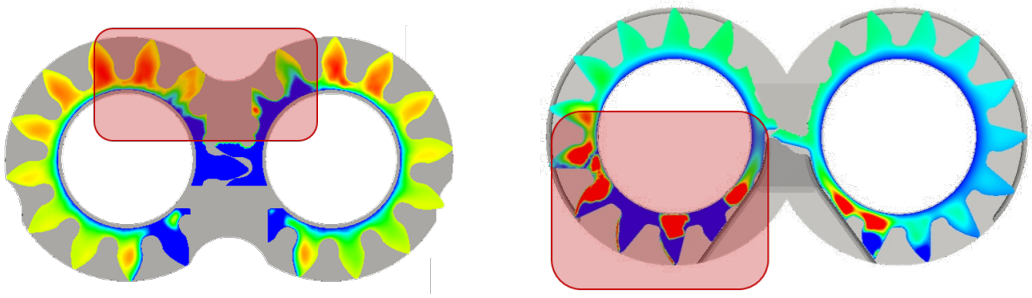

(a) (b)

Figure 3.9. Instances of numerical instabilities in predicting pressure distribution in the lateral lubricating gaps at relatively heavy cavitation regions.

3.2.1 Modeling Approach

A mass conserving cavitation model as proposed in Payvar and Salant [97] and in Shi and Salant [98], which follow a modified implementation of the Jakobsson-Floberg-Olsson (JFO) boundary conditions, is implemented in the current mixed-TEHD lateral gap model. According to this approach, the lubricant forms defined separations between the fluid film and the cavitation zones, with the formation of air pockets in the cavitation zones. Since only a fraction of the lubricant occupies the total lubricating gap, density in the cavitation zones are lower than the fluid film density. The JFO model essentially predicts the onset and shape of the cavitation regions with defined boundaries alongside the fluid film, without considering complex bubble dynamics. Such a simplified approach is necessary in order to smoothly integrate with the current lateral gap model where other coupled complex effects are already present.

In the work of [98], an universal cavitation Reynolds equation as described in Equation (3.34) is proposed, which is valid in both fluid film and cavitation regions.

$$\frac{\partial}{\partial x}\left(\frac{h^3}{\mu}\frac{\partial p}{\partial x}\right)+\frac{\partial}{\partial y}\left(\frac{h^3}{\mu}\frac{\partial p}{\partial y}\right)\Bigg(=U_g\frac{\partial}{\partial x}\left(\frac{\partial \rho' h}{\partial x}\right)\Bigg(+U_g\frac{\partial}{\partial y}\left(\frac{\partial \rho' h}{\partial y}\right)\Bigg(+\frac{\partial \rho' h}{\partial t} \tag{3.34}$$

In the above equation, the non-dimensional density $\rho' = \rho_{cav}/\rho_{ncav}$ where ρ_{cav} corresponds to the density in the fluid film and ρ' refers to the density in the cavitation region. The cavitation conditions are determined with the help of a cavitation index C_1 which basically acts as switch function between 0 and 1 that correspond to non-cavitating and cavitating regions respectively. The definition of the cavitation index is presented in Equations (3.35) and (3.36).

$$\rho < \rho_{cav} : C_1 = 0 \tag{3.35}$$

$$p < p_{cav} : C_1 = 0 \tag{3.36}$$

Thus, by using this cavitation index, the values of density and pressure in the lubricating gap can be defined with the help of the following equations,

$$\rho = C_1\rho_{ncav} + (1 - C_1)\rho_{cav} \tag{3.37}$$

$$p = C_1 p_{ncav} + (1 - C_1) p_{cav} \tag{3.38}$$

It must be noted that in Equation (3.38), p_{cav} and p_{ncav} correspond to the pressures in the cavitating and non-cavitating regions respectively.

3.2.2 Cavitation Algorithm

The cavitation model described in the previous section was integrated with the FSI lateral gap model according to the algorithm described in the flowchart in Figure 3.10.

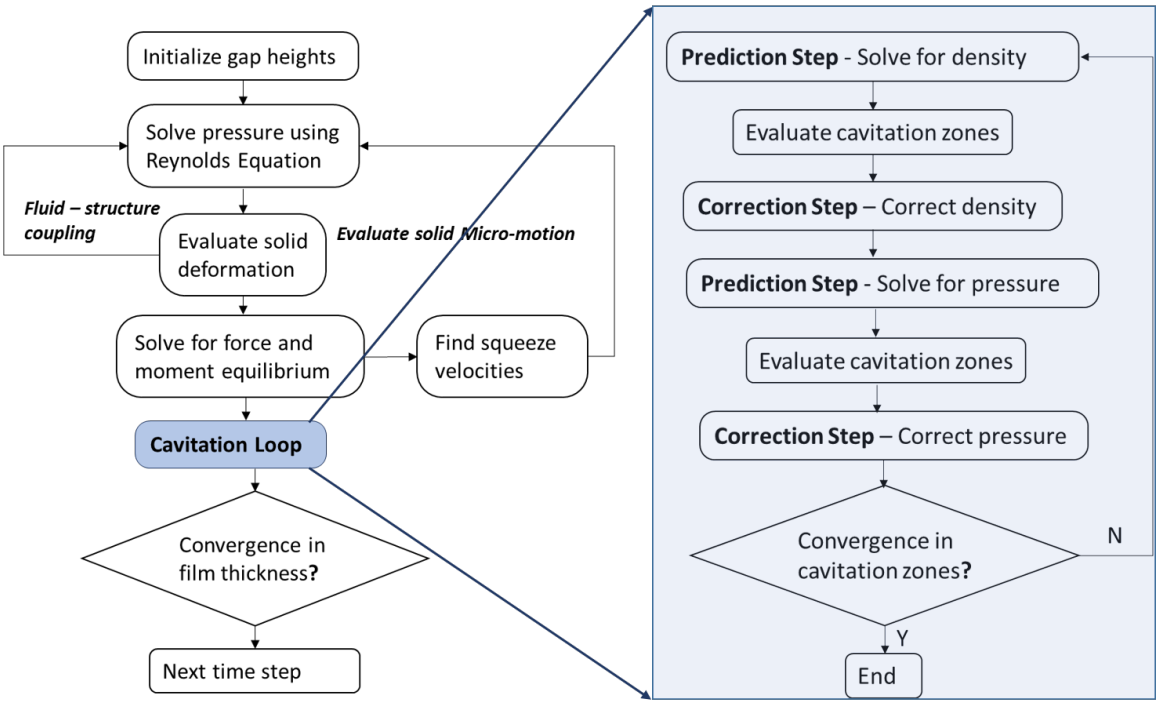

Figure 3.10. Flowchart representing the implementation of cavitation model in the FSI model for the lateral lubricating interfaces in EGMs.

It can be seen from the flowchart that the cavitation loop highlighted in blue can be solved at the end of the force balance evaluation. This has been implemented in the interest of reducing computational time, since fast dynamic changes in pressures

were not observed at the other loops in a given iteration for an angular step. Thus, the cavitation loop is performed only once in each angular iteration of the FSI model. Several steps are embedded within the cavitation loop as shown in Figure 3.10, which includes prediction and correction steps for both pressure and density. During the prediction steps, the universal Reynolds equation in Equation (3.34) is solved successively for pressure as well as density. The correction steps follow Equation (3.37) and Equation (3.38) for correcting density and pressure respectively. Following the evaluation of the density in the prediction step using the universal Reynolds equation, the cavitation indices at each computational element are evaluated using Equation (3.35). The values of cavitation index are then used to correct the density distribution in the lubricating interface and also serve as indicators for the cavitating and non-cavitating regions. Similar prediction and correction steps are also followed for the evaluation of pressures. The density and pressure evaluations are performed successively until a convergence is reached for the location of the cavitation zones, which marks the end of the cavitation algorithm. Detailed discussion on the simulation results obtained after implementing the cavitation algorithm can be found in Chapter 4.

3.3 Implementation of Multi-material Structural Solver

The structural solvers presented in the previous section as well as in Section 2.2.5 are limited by their ability to handle bushings and gears made of only material. This limitation arises from the constitution of the FVM based OpenFOAM solver used for this model. Moreover, FEM based methods for solving structural deformation are more commonly used in literature and are known to be more reliable than FVM solvers. To extend the capability of the lateral gap model to explore designs with more than one material in their physical constitution, this section describes the implementation of a fully automated algorithm to generate the off line influence matrices for lateral bushings and gears. This algorithm utilizes the FEM based ANSYS [88]

static structural solver in conjunction with Matlab to evaluate the different rows of the influence matrix.

The process of generating an Influence Matrix for each solid component was automated according to the flowchart shown in Figure 3.11 by using scripting commands from ANSYS Mechanical APDL and programming with MATLAB. ANSYS static structural module was the main structural solver used for evaluating the solid deformation. It can be seen from the flowchart in Figure 3.11 that the first step in this algorithm involves manually setting up the ANSYS structural solver with the appropriate FEM mesh and applying loads from the constant pressure regions. Using the APDL input file from this setup, a MATLAB code is used to identify and record the information related to the gap interface where we need to evaluate the structural deformation. This information is used to apply unit loads iteratively on each element of the gap interface and automatically run corresponding structural simulations in ANSYS. These simulation results are then used in the same MATLAB code to evaluate the corresponding deformation on all the gap elements.

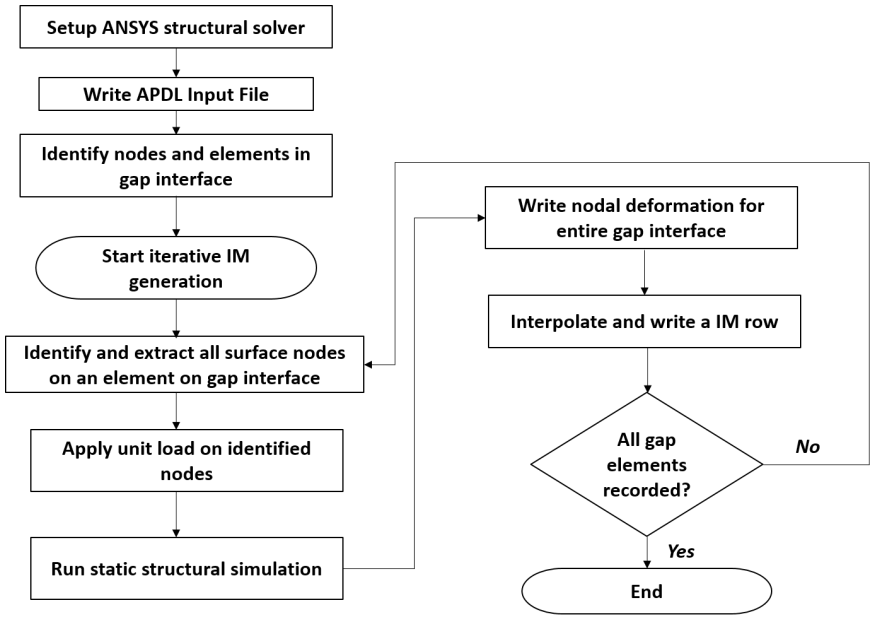

Figure 3.11. Flowchart used for Influence Matrix generation using ANSYS structural solver.

At the end of the automation algorithm, an inverse weighted interpolation scheme shown in Equation (3.39) and Equation (3.40) is used to interpolate the nodal deformation values from the FEM solver into corresponding element cell centers as required by the FVM based lateral gap solver.

$$u_e(x) = \frac{\sum_{i=1}^{6} w_i(x) u_i}{\sum_{i=1}^{6} w_i(x)} \tag{3.39}$$

$$w_i(x) = \frac{1}{d(x, x_e)} \tag{3.40}$$

In the above equations, u_e corresponds to element deformation, u_i corresponds to nodal deformation, w_i refers to the weighting function and $d(x, x_e)$ implies the distance of each node from the element cell center. It should be noted here that this automated algorithm can also be used as a single material solver since interfacing with the ANSYS solver leverages all the capabilities of the ANSYS structural module.

3.4 Modeling of Friction Between Casing and the Lateral Bushing

A significant contribution in this dissertation is the addition of a frictional force model for the first time, to the FSI lateral gap model to account for the effect of radial forces acting on bearing block type lateral bushings as discussed earlier in Chapter 1. This model has been fully integrated with the force balance solver which was presented earlier in Section 2.2.8 and is utilized only when frictional forces arising between the bearing block type designs of bushings and the housing.

The radial forces acting on the lateral bushing contribute to a frictional force which restricts its movement as shown in Figure 3.12. These radial forces comprise of the fluid pressure forces acting on the LP area at the bottom of the bushing and the forces from the journal bearing interface between the shaft and the bushing. It is important to account for this frictional force as a variation with operating conditions as well as with the micro-motion velocities of the bushing in the force balance model.

The Stribeck curve as modeled in [99] has been used to account for the variation of translational friction force with velocities of the floating bearing. The analytical

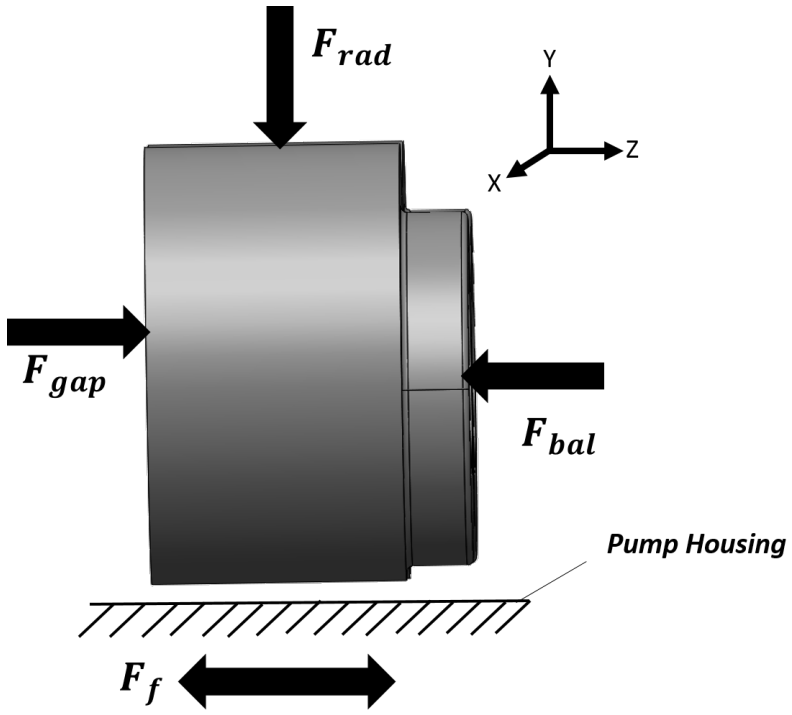

Figure 3.12. Illustration of the different radial forces acting on the floating bearing and their resulting frictional force at the contact with pump housing using the lateral bushing design from Case 2.

expression for the Stribeck curve has been represented graphically in Figure 3.13 along with the various parameters used in the model. The most significant parameters used in this model are highlighted in this figure where various parts of the curve are separated as Stribeck, Coulomb and viscous friction respectively.

The physical phenomena of a rigid body overcoming static friction and moving to a dynamic friction range at higher velocities are captured by the different sections of the model, as represented in the equation below, between frictional force F and the rigid body velocity v which in this case corresponds to the velocity of the lateral bushing,

$$F = \sqrt{2e}(F_{brk} - F_C) \cdot \exp\left(-\left(\frac{v}{v_{St}}\right)^2\right).\frac{v}{v_{St}} + F_C.\tanh\left(\frac{v}{v_{Coul}}\right) + fv \qquad (3.41)$$

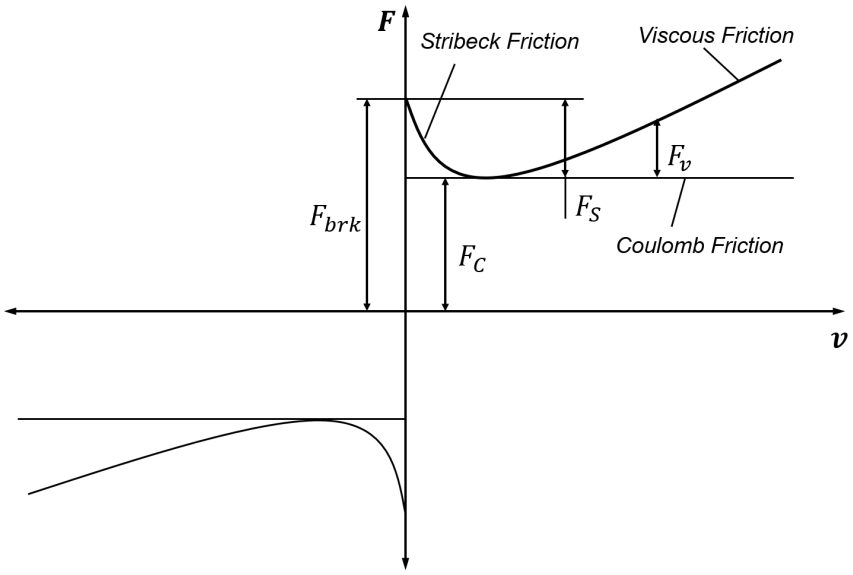

Figure 3.13. Representation of a Stribeck curve with different parameters for variation of frictional force with velocities.

F_C in the above equation corresponds to the Coulomb frictional force which considers the static frictional force experienced by the body and is represented with the help of the following equation,

$$F_C = sgn(v) \cdot \mu_f((p_{HP} - p_{LP}) * Area_{LP} + F_{Rd} + F_{Rs}) \tag{3.42}$$

In Equation (3.42), the forces F_{Rd} and F_{Rs} are radial forces from the journal bearing as computed directly from the fluid dynamic model of HYGESim for each operating condition used for simulations. p_{HP} and p_{LP} are high and low pressures respectively which depend on the operating condition used in the simulation, while $Area_{LP}$ is the LP area on the bottom side of the floating bearing.

Table 3.2 lists the remaining parameters used in the frictional force model and the details of their implementation. It must be noted here that the values of μ and v_{brk} are the only assumptions in the model and these values are reported in the results sections along with the corresponding simulations. Thus, the frictional force evaluated from

Equation (3.41) is used in conjunction with the force balance model along with the other forces to solve for force and moment equilibrium conditions.

Table 3.2.
Description of various parameters used in the Stribeck curve model.

Parameters	**Description**
F	Friction force
F_C	Coulomb friction
$F_{brk} = 2.5 * F_C$	Breakaway friction
v_{brk}	Breakaway friction velocity
$v_{St} = v_{brk}\sqrt{2}$	Stribeck velocity threshold
$v_{coul} = \frac{v_{brk}}{10}$	Coulomb velocity threshold
v	Relative velocity
f	Viscous friction coefficient
μ_f	Static friction coefficient

It must be noted here that for evaluating the friction forces, the floating bearing is modeled in a simplified manner where it can have only one degree of freedom of motion along the axial direction i.e. to and away from the gears. The velocity at the location defined by h_0 on the undeformed gap plane (shown earlier in Figure 2.12) is used in Equation (3.41) to evaluate the corresponding variation in frictional forces. These computed frictional forces are subsequently used in the force equilibrium calculations to evaluate the translational position of the floating bearing which satisfies the equilibrium conditions.

4. SIMULATION RESULTS: REFERENCE EGM CASE 1A WITH OIL AS THE WORKING FLUID

In this section, simulation results obtained from the mixed-TEHD model explained in Chapter 3 using a high viscous fluid are presented. The reference working fluid used for this purpose is the ISO 46 hydraulic oil with a density at 50°C and at atmospheric pressure, as 851 kg/m^3 and dynamic viscosity at the same reference conditions as 0.026 $Pa-s$. The relationship between the different fluid properties for this reference fluid which are represented in Equation (2.12) − (2.13) is used in all the simulations presented here. Since the primary aim of the mixed-TEHD model which is one of the chief original contributions of the present work, is to predict the physics of the lateral lubricating gap in mixed lubrication conditions, the results presented in this section focus on such conditions. The corresponding performance of the full film model at these conditions is also examined and compared to the results from the mixed film model. In addition, the last part of this chapter presents the impact of using the cavitation algorithm discussed in Section 3.2.

4.1 Results from the Mixed-TEHD Lateral Gap Model

For the purposes of comparing the results from the mixed and the full film lubrication models for the lateral gap, a reference EGM Case 1A (described in Chapter 1) was chosen. The lateral bushings are composed of aluminum alloy and are of a pressure plate type design, while the material of the gears is hardened steel. Capacitive film thickness measurements to validate the full film gap model were performed on this reference EGM design in the work of [8].

Figure 4.1 compares the gap film thickness and the corresponding pressure distribution in the lateral gap between the mixed film and the full film models at a

moderate pressure of $p/p_{ref} = 0.25$ and a low speed of 300 rpm where mixed lubricating conditions are likely to occur and where $p_{ref} \sim \mathbf{O}(300bar)$. It is noted here that the results presented in this section are normalized to protect confidential information related to the EGM.

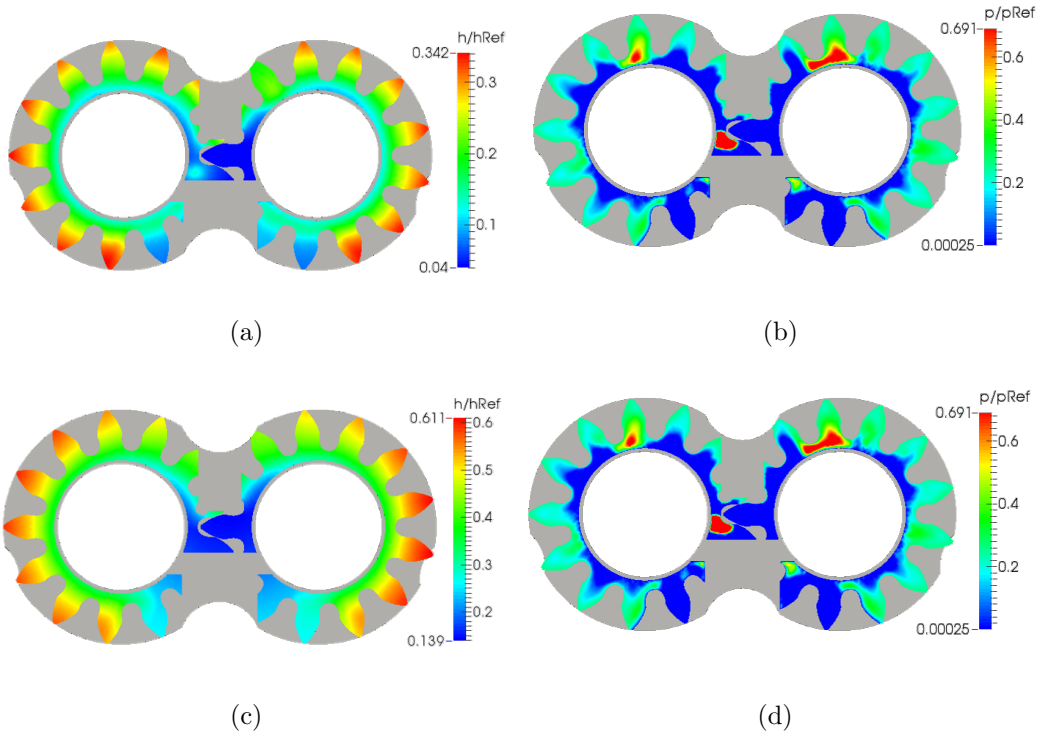

Figure 4.1. Representation of the results in the lateral gap at $p/p_{ref} = 0.25$ and 300 rpm (a) Full Film model - Gap film thickness (b) Full Film model - Pressure distribution (c) Mixed Film model - Gap film thickness (d) Mixed Film model - Pressure distribution.

Figure 4.1(a) and Figure 4.1(b) represent the gap film thickness and pressure distribution respectively from the full film model, while the corresponding film thickness and pressures as predicted by the mixed film model are shown in Figure 4.1(c) and Figure 4.1(d) respectively. The gap heights are normalized using $h_{ref} \sim \mathbf{O}(3\mu m)$ and a surface roughness value of $R_q = 0.5\mu m$ is used for the mixed lubrication model. It must be observed here that in this condition, the low film thickness regions which

correspond close to contact conditions are observed in the meshing zone of the gears from both the models (with reference to Figure 4.1(c) and Figure 4.1(d)). Although the spatial orientation of the gap from both the models are quite similar to each other, the actual values of the film thicknesses are significantly different from each other which can be observed from the maximum and minimum gap heights from the plots. These values predicted by the mixed lubrication model are almost two times higher than those obtained from the full film model. This is mainly due to the fact that such a large centralized region of low film thickness increases the load support from the asperities and thus, increases the contact forces from a centralized point of application which subsequently increases the gap heights and the load support from the interface.

The prediction of the pressure distribution from the interface is quite different from both the models especially with respect to the localized pressure peaks. Since the average flow Reynolds equation predicts the gap pressures averaged across both the fluid film and the asperities, localized peaks are observed lesser from the mixed film model which are quite representative of the real EGM operation. Thus, the full film model fails to capture these effects of load sharing by the asperities under such mixed lubrication conditions.

The effects of load sharing by the asperities that is accounted in the mixed lubrication model can be understood from the plots shown in Figure 4.2(a) which show the non-dimensional contact pressure as calculated from Equation (3.10) − (3.11) and the normalized contact area in the computational domain for the same operating condition shown in Figure 4.2(b). It can be noted from these plots that the contact pressure and the contact area are highest around the meshing zone which has the region of low film thickness in Figure 4.1(c) and non-existent where the contact conditions are not met.

Figure 4.3 shows the plots of the various flow factors obtained from the mixed lubrication model (for the same operating point shown in Figure 4.1) which are essentially non-dimensional factors obtained from the expressions listed in Appendix B.

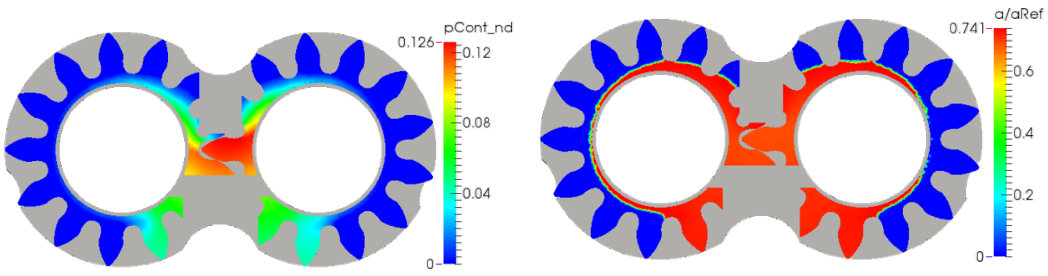

(a) (b)

Figure 4.2. Figure showing the results in the lateral gap from the mixed lubrication model at $p/p_{ref} = 0.25$ and 300 rpm (a) Non-dimensional contact pressure (b) Normalized contact area.

It must be noted that the factors ϕ_x, ϕ_c and ϕ_s are used in the average flow Reynolds equation (Equation (3.6)) while the other three factors are exclusively for the shear stress equations in Equation (3.27) − (3.28). It can be seen from Figure 4.3(a) and Figure 4.3(b) that the factors ϕ_x and ϕ_c directly complement the film thickness plots shown in Figure 4.1. These factors are closer to 1 at regions of higher film thickness due to the presence of a full film regime at those regions, while having a value which progressively becomes lower than 1 with decreasing film thickness. The spatial variation of shear factor ϕ_s instead of its actual value, is the primary term in the average flow Reynolds equation accounting for the shearing of two rough surfaces and is dependent on the sliding velocities of the surfaces. Since this is a low speed operating condition, the variation in ϕ_s is not quite significant in this case as shown in Figure 4.3(c).

The flow factors used in the torque loss equations are shown in Figure 4.3(d) − Figure 4.3(f). In Equations (3.27) − (3.28) for the shear stress, it is observed that the terms ϕ_f and ϕ_{fs} are part of the same term and complement each other. Thus, the distribution of these factors shown in Figure 4.3(d) and Figure 4.3(f) respectively are complementary to each other. ϕ_{fp} is expected follow a direct correlation with the

film thickness (Appendix B) and this is reflected in the plot shown in Figure 4.3(e) as well.

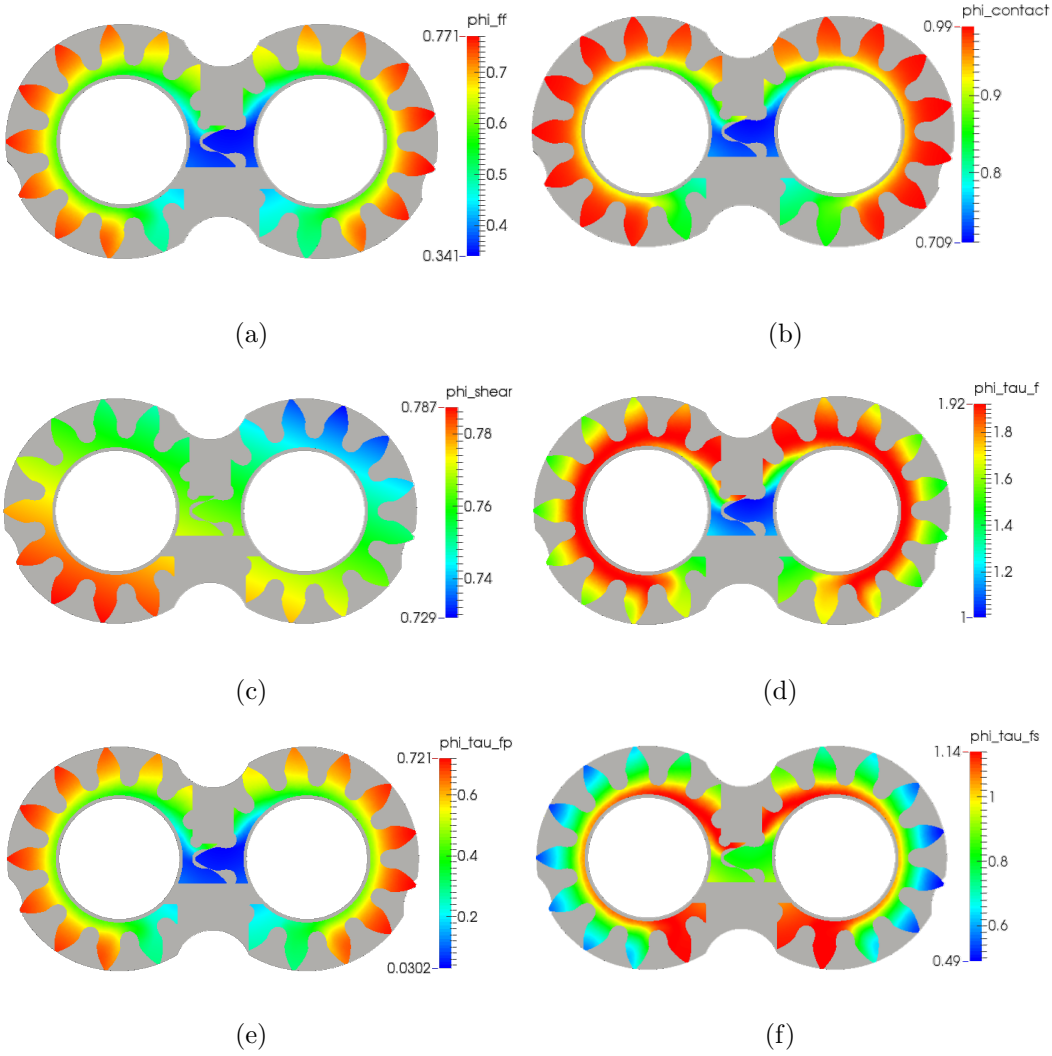

Figure 4.3. Plots of the different flow factors in the lateral gap domain from the mixed lubrication model at $p/p_{ref} = 0.25$ and 300 rpm (a) ϕ_x (b) ϕ_c (c) ϕ_s (d) ϕ_f (e) ϕ_{fp} (f) ϕ_{fs}.

In order to complete the comparison between the mixed and the full film lubricating models, the gap film thickness plots from these models are presented at other operating conditions in this section. The results obtained from both the models at an operating point of $p/p_{ref} = 0.25$ and 400 rpm is shown in Figure 4.4. In this case, the

spatial orientation of the gap film thickness predicted by each of the models is quite different from each other. The simplified saturation of the low film thicknesses at a constant value in the full film model propagates through the domain as it can be seen around the meshing zone in Figure 4.4(a), whereas the mixed film model evaluates more realistic film thicknesses as shown in Figure 4.4(b) by considering the effect of the surface asperities. It can also be observed that the minimum film thickness is higher in the predictions from the mixed film model when compared to the full film model.

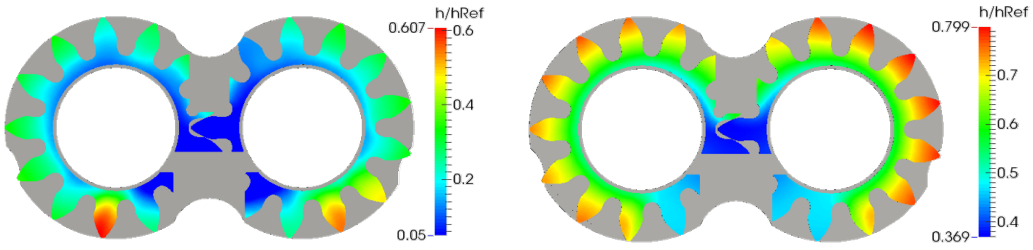

(a) (b)

Figure 4.4. Film thickness distribution in the lateral gap at $p/p_{ref} = 0.25$ and 400 rpm from (a) Full Film model (b) Mixed Film model.

Similar observations can also be made for the results shown for the operating condition $p/p_{ref} = 0.25$ and 500 rpm (shown in Figure 4.5) where the full and mixed film predictions of the gap height distribution as well as its values were quite different from each other.

However, under instances which are closer to full film lubrication conditions as defined by the contact condition and other criteria listed in Appendix B, the mixed lubrication model converges to the full film model which was one of the key goals of creating a comprehensive lateral gap model that can simulate a wide range of lubrication regimes in EGMs. In order to illustrate this instance, Figure 4.6 shows

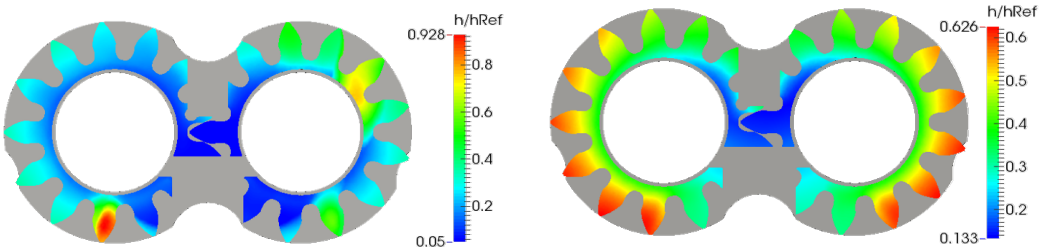

(a) (b)

Figure 4.5. Film thickness distribution in the lateral gap at $p/p_{ref} = 0.25$ and 500 rpm from (a) Full Film model (b) Mixed Film model.

the gap film thickness from both the models at $p/p_{ref} = 0.15$ and 1000 rpm where the predictions from both the models are almost identical to each other.

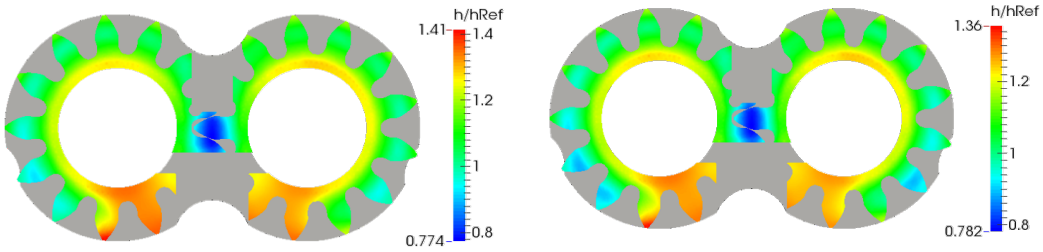

(a) (b)

Figure 4.6. Film thickness distribution in the lateral gap at $p/p_{ref} = 0.15$ and 1000 rpm from (a) Full Film model (b) Mixed Film model.

Another instance of encountering operating conditions closer to full film lubrication conditions is shown in Figure 4.7 where gap film thickness results from both the models at an operating point of $p/p_{ref} = 0.1$ and 1000 rpm are shown to have an identical spatial orientation, but actual values of the gap heights differ slightly from each other.

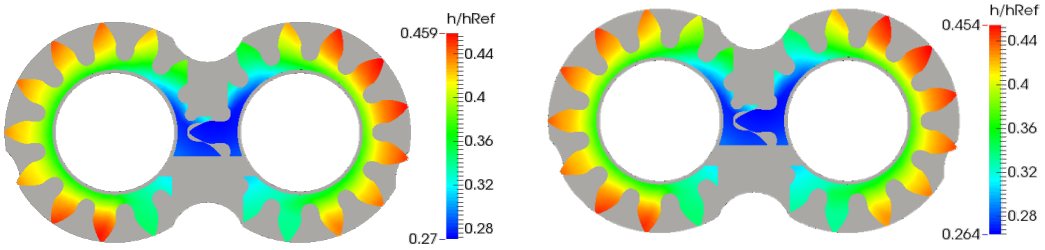

(a) (b)

Figure 4.7. Film thickness distribution in the lateral gap at $p/p_{ref} = 0.1$ and 1000 rpm from (a) Full Film model (b) Mixed Film model.

The previously presented results of gap film thickness results were all presented at a single instant of time, and such a gap height distribution varies across different angular instances due to the variation in the hydrodynamic and hydrostatic effects in the gap. In order to verify that the mixed film model captures these effects in the entire operation of the EGM similar to the previously validated full film model, the values of film thicknesses at any given point were averaged at steady state for an entire revolution (360°) using the following formula,

$$h_{avg} = \frac{\sum_1^{360} h}{360} \tag{4.1}$$

The average film thickness was then normalized with $h_{avg} \sim \mathbf{O}(2e^{-6}\mu m)$ once steady state convergence was obtained with both the mixed and full film models. Figure 4.8 shows such plots obtained from both the models at an operating condition of $p/p_{ref} = 0.4$ and shaft speed of 2000 rpm where predominantly full film lubrications were observed.

It can be seen from the plot that the average spatial orientation of the gap predicted by both the mixed and the full film models are quite similar to each other, although the maximum film thickness from the mixed film model is slightly higher than the full film model at this condition. The regions of high film thickness and low film thicknesses predicted by both the models are almost identical to each other.

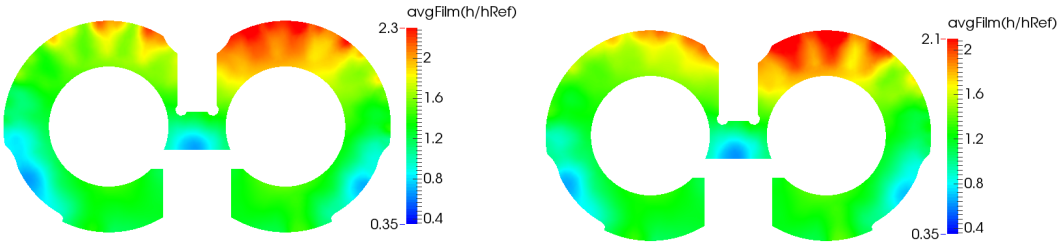

(a) (b)

Figure 4.8. Average film thickness plots obtained at $p/p_{ref} = 0.4$ and 2000 rpm for (a) Full Film model (b) Mixed Film model.

These plots which consider the full revolution of the EGM, further support the conclusion that in this particular EGM design at nearly full film conditions, both the models predict similar spatial orientation of the lateral gap.

As explained earlier in Section 3.1.2, a clear border between the different lubrication regimes is quite difficult to define and some differences between the prediction from full and mixed film are present, especially near these conditions as shown in Figure 4.7. Since, the prediction of torque losses and the drain leakages from the gap are quite sensitive to the values of the gap heights (Equations (3.27) – (3.28), Equation (3.33)), Table 4.1 tabulates the predictions of these parameters from both the models for all the operating conditions presented so far in this section.

All the torque losses and the leakages reported here are averaged over the last converged revolution at the end of each simulation. It can be seen from the table that in the first three operating conditions where more instances of mixed lubrication were observed, the parameters predicted by both the models are quite different from each other. This is especially true for the leakages since from Equation (3.33), it is evident that the leakages are directly proportional to the cube of the gap heights and thus is more sensitive to its changes than the torque losses. This is also quite significant in the near full film lubrication conditions (the last two operating conditions) where the differences observed in leakages are more prominent than the torque losses. For this

Table 4.1.
Torque losses and Leakages in the lateral gap predicted by the full and mixed film model a various operating conditions.

p/p_{ref}, rpm	**Torque loss** (Nm)		**Leakages** (lpm)	
	Full Film	Mixed Film	Full Film	Mixed Film
0.25, 300	0.70	0.21	6.17e-06	4.14e-05
0.25, 400	0.52	0.26	4.12e-05	1.03e-04
0.25, 500	0.81	0.34	1.43e-04	7.88e-05
0.15, 1000	0.64	0.64	1.37e-03	1.28e-03
0.1, 1000	0.77	0.77	4.18e-05	3.50e-05

reason, this work attempts to validate the mixed-TEHD model using both torque loss and leakage measurements, which will be presented in Chapter 5.

4.2 Contribution of Asperities and Fluid Film to Load Support

In this section, the relative influence of the surface asperities and the fluid film in supporting the loads in the lubricating gap are examined. In this study, a fixed gap height was set in the lateral gap to test the performance of the asperities and the fluid film at each input gap height. The total force from the gap used to support the loads consists of the hydrodynamic force from the fluid film and the contact force originating from the asperities.

Figure 4.9 shows the variation of the total force predicted by the gap model at different fixed gaps ($F_{ref} = \mathbf{O}(10000N)$) at an operating condition of $p/p_{ref} = 0.4$ and 300 rpm, along with the contribution from hydrodynamic and contact forces for a surface roughness value of $R_q = 0.5\mu m$. As the gap heights decrease progressively into more dominant mixed lubrication regimes (as defined by the contact condition), the contact forces from the asperities increases exponentially (Equation (3.10)), while the contribution from the fluid film decreases steadily. Thus, at very low gap heights,

the participation of surface asperities in the total load support cannot be neglected and a dedicated model such as the mixed film model presented in this work is necessary for accurate performance predictions. It should also be noted that since a considerable variation in the film thicknesses is expected in the lateral gap during the EGM operation owing to the hydrodynamic effects, it is quite convenient to have a comprehensive model such as the present one, which reduces to full film assumptions at higher gap heights.

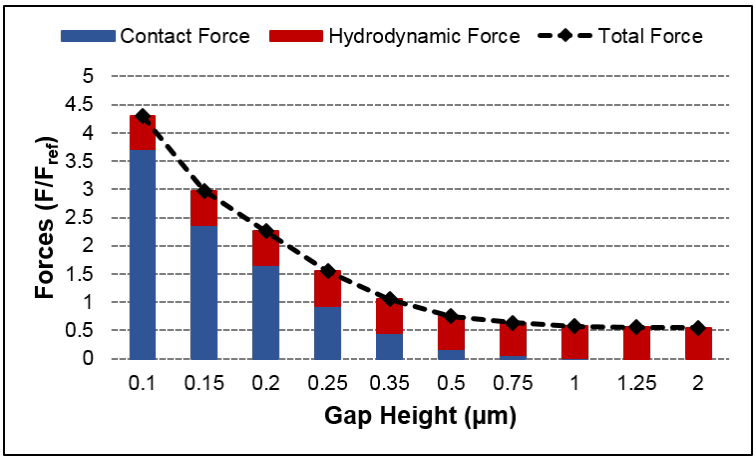

Figure 4.9. Relative contribution of surface asperities and fluid film to the total load support for $R_q = 0.5\mu m$.

A comparison of the total forces experienced in the lateral gap at different fixed gap heights for three different values of R_q is shown in Figure 4.10. It can be observed from this plot that the lowest tested $R_q = 0.1\mu m$ resembles nearly smooth surfaces, thus indicating minimal contribution from the asperities as seen in the magnitude of the total forces at low gap heights. Furthermore, the total gap forces increase with increasing R_q at lower gap heights, implying that higher contact forces push the lateral plate further away from the gears at these conditions. These findings directly agree with the experimental measurements later reported in Section 5.3.2, where higher leakages were observed for a plate with higher R_q.

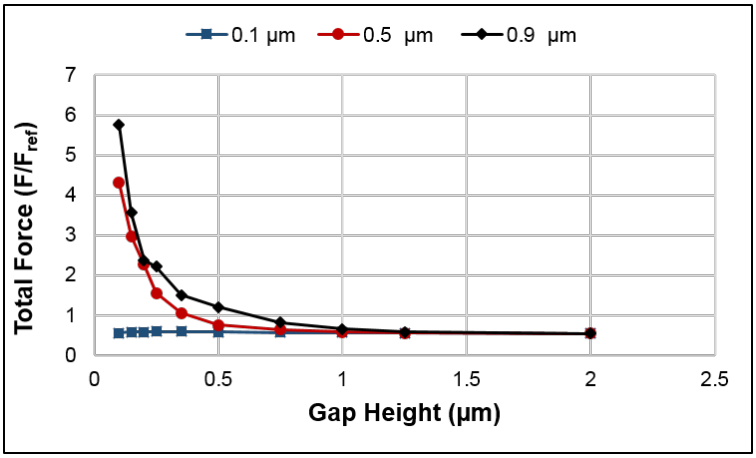

Figure 4.10. Total forces predicted by the mixed-TEHD model for different surface roughness R_q.

4.3 Results from the Cavitation Model

The cavitation algorithm has been integrated with the FSI lateral gap model according to the details in Section 3.2. The objectives of the cavitation model was to predict numerically stable pressure distribution in the lubricating interface while following a mass conserving algorithm. To demonstrate the effectiveness of this algorithm, the same prototype external gear machine (Case 1A) used in presenting the results for the previous sections of this chapter has been used with a very low speed operating condition of 300 rpm and a delivery pressure of $p/p_{ref} = 0.4$. The cavitation model was first integrated with the full film lubrication model to demonstrate its capabilities without the additional effects due to mixed lubrication. Figure 4.11 shows the pressure and film thickness results from the full film model without the new cavitation algorithm, when the minimum pressures were merely saturated to a threshold value. Unrealistic pressure peaks and valleys can be observed in Figure 4.11(a) arising from the presence of very low film thickness regions (shown in Figure 4.11(b)) which prompt repeated saturation of pressures due to insufficient fluid film, thus leading to cavitating conditions in the interface.

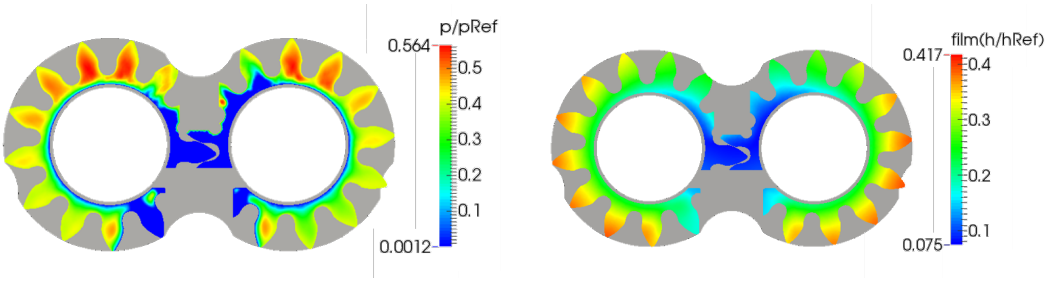

(a) (b)

Figure 4.11. Results with full film model without new cavitation algorithm obtained at $p/p_{ref} = 0.4$ and 300 rpm showing (a) Gap pressure (b) Film thickness.

However, with the addition of the new cavitation algorithm to the full film model, improved stability in the pressure distribution predictions can be seen in the lubricating interface as depicted in the results plotted in Figure 4.12(a). A consequent increase in the gap height prediction is also observed in Figure 4.12(b) with the implementation of the cavitation algorithm due to the variation observed in the pressure predictions.

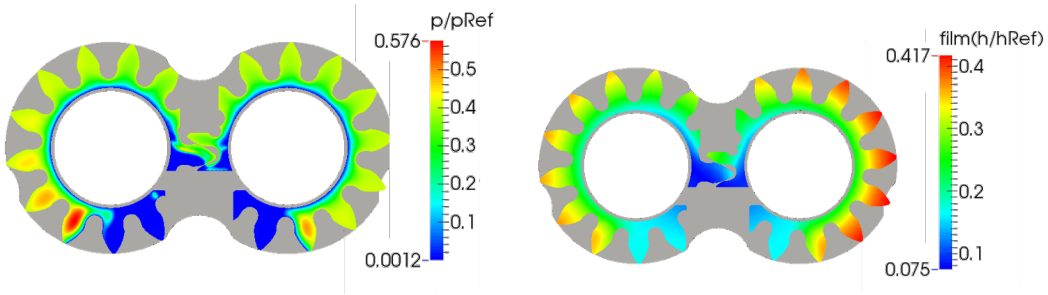

(a) (b)

Figure 4.12. Results using cavitation algorithm integrated with the full film model obtained at $p/p_{ref} = 0.4$ and 300 rpm showing (a) Gap pressure (b) Film thickness.

With the implementation of the cavitation algorithm with the mixed film model, only slight changes in the film thickness predictions can be observed in the results presented in Figure 4.13 . This is due to the fact that that the implementation of the cavitation algorithm increased the minimum film thicknesses beyond the mixed lubrication regime thus prompting the mixed film model to reduce to the full film model.

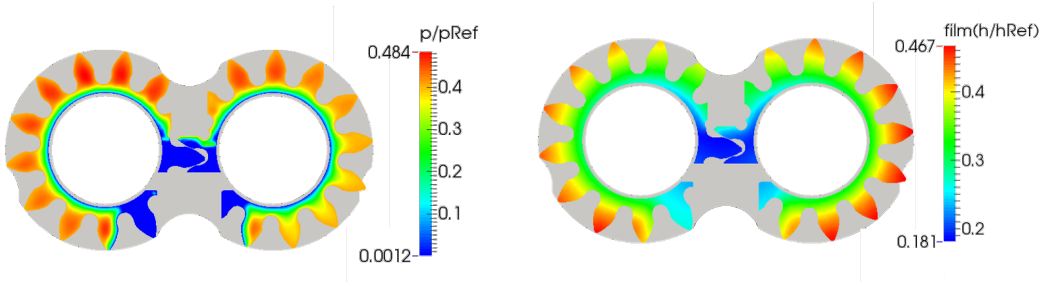

(a) (b)

Figure 4.13. Results using cavitation algorithm integrated with the mixed film model obtained at $p/p_{ref} = 0.4$ and 300 rpm showing (a) Gap pressure (b) Film thickness.

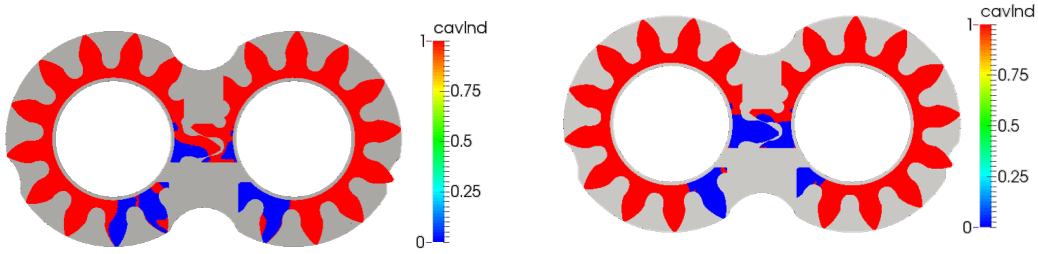

(a) (b)

Figure 4.14. Distribution of cavitating regions indicated by the cavitation index as observed with (a) Full film model with cavitation (b) Mixed film model with cavitation.

To demonstrate the mass conserving capability of the cavitation algorithm, Table 4.2 shows the normalized error in evaluating the total leakages entering and leaving the computational gap domain. The leakages are evaluated at all the patches in the fluid domain boundaries as represented earlier in Figure 2.10, by using the appropriate leakages equations described earlier for the full film and mixed film models. The error term Q_{net}/Q_{dRef} was evaluated by dividing the sum of all the flow entering and leaving the boundaries Q_{net} with Q_{dRef} which has the same order of magnitude as the value of drain leakages for this condition. It can be seen from the values in the table that the overall error in leakages are lower due to the lower film thicknesses encountered in the gap at these conditions.Nevertheless, a reduction in the total error of the leakages is observed with the addition of the cavitation and mixed film models by almost an order of magnitude if the error in the full film model without cavitation algorithm is compared to the other two models.

Table 4.2.
Normalized error in total flow (Q_{net}/Q_{dRef}) in the lateral gap as computed by the different lateral gap models presented in this section.

Net leakages from Full Film w/o cavitation model	**Net leakages from Full Film with cavitation model**	**Net leakages from Mixed film with cavitation model**
0.185	0.044	0.028

However, it should be noted from the pressure distributions shown in Figure 4.13(a), that significant changes can be observed with the combination of the cavitation algorithm and the mixed film model. This indicates that the effect of the average flow Reynolds equation which accounts for the surface features in predicting the pressure distribution is still significant in influencing the predictions in the lubricating gaps. Utilizing the mixed film model with the cavitation algorithm thus becomes significant

in accurately capturing the effects of the surface features in contributing to load support as well as provide numerically stable pressure distribution results. Figure 4.14(a) and Figure 4.14(b) show the distribution of the cavitating regions indicated by the cavitation index C_1 as predicted by the full film and mixed film models respectively. The blue regions in these plots with $C_1 = 0$ indicates the presence of cavitation and significant variations can be seen across the mixed and full film models which supports the earlier emphasis on the necessity of using the cavitation algorithm in conjunction with the mixed film model.

5. EXPERIMENTAL VALIDATION: REFERENCE EGM CASE 1B WITH OIL AS THE WORKING FLUID

In this chapter, efforts to perform an experimental validation of the predictions obtained from the mixed-TEHD lateral lubricating gap is presented for ISO VG46 hydraulic fluid which is the reference high viscous fluid in the current work. In the first part of this section, studies performed to verify the various assumptions used in the mixed lubrication model are presented to demonstrate the fidelity of the developed gap model. After validating the assumptions used in the model with the help of commercially available EGMs, two different investigations were performed to validate the mixed lubrication model with experiments conducted at Maha Fluid Power Research Center, Purdue University. The first study presented here for this purpose is with torque losses in EGMs, while the second study involves validating against measured drain leakages from the lateral lubricating interfaces. In both the studies, the corresponding predictions from both the mixed and full film lubrication lateral gaps are compared with experimental measurements to validate the performance of the mixed lubrication model at different operating conditions.

5.1 Verification of Mixed-TEHD Model Assumptions

In the current study, detailed surface profile measurements were carried out on lateral plates of varying surface roughness to validate important assumptions made in the stochastic based mixed-TEHD model as outlined earlier in Chapter 3. Specifically, studies to validate the assumptions that surface asperity heights follow a Gaussian distribution and that the surface properties are isotropic with respect to the X and Y directions on the plane are presented in this section. Two kinds of lateral plates (marked as 1 and 2 in Figure 5.1) belonging to the reference EGM were used for the

purposes of this study, with plate 2 having the nominal surface finish (commercial design) and additional finishing operations have been performed on plate 1 for obtaining a smooth surface. Two lateral plates of each of these designs have been used in the same reference EGM (Case 1B) for testing the influence of varying surface roughness on the units performance and these results are presented later in Section 5.3.2.

Figure 5.1. Sample lateral plates belonging to the same reference EGM with varying surface roughness.

Profile measurements were performed on the lateral surfaces facing the gears in all the test plates using a Surftest SJ-500 Mitutoyo stylus profilometers. Six different linear directions (represented in Figure 5.2) are defined on each lateral plate, along which the profilometer runs were completed.

An instance of surface profile height measurements (with $z_{ref} = \mathbf{O}(1\mu m)$) for plate 2 is shown in Figure 5.3 with an evaluation length of $\mathbf{O}(2.5mm)$ and ~ 5100 profile heights.

Analysis of recorded profilometer measurements is necessary for understanding the nature of the surface profiles as well as for determining inputs to the mixed-TEHD model. Thus, the various statistical parameters such as centerline average (R_a), root mean square (R_q), skewness (R_sk) and kurtosis (R_{ku}) are reported in this work. Standard definitions of R_a and R_q which were presented earlier in Section 3.1.1 are used to determine the general distribution of the surfaces, R_sk and R_{ku} as defined in Equations (5.1) $-$ (5.2) are used to determine the quality of the peaks and valleys

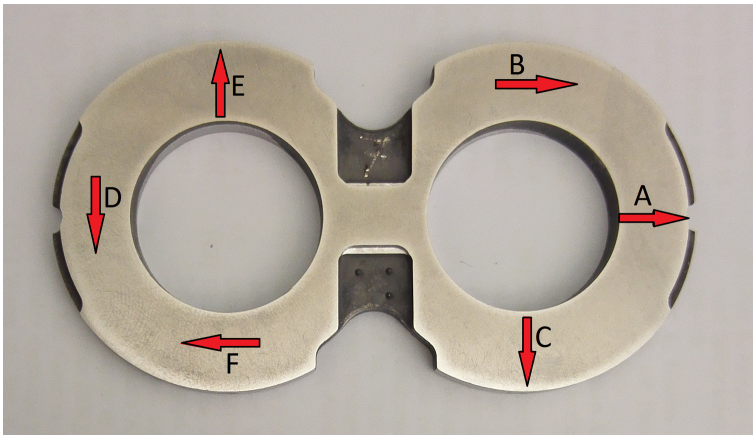

Figure 5.2. Various profilometer directions defined on the lateral plate.

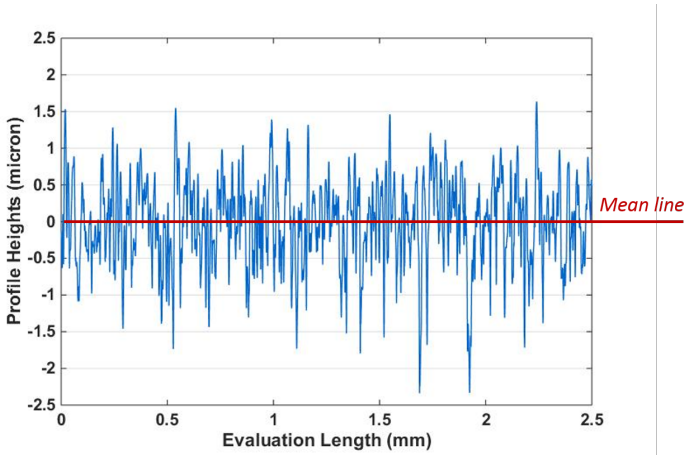

Figure 5.3. Sample profilometer measurements for lateral plate 2.

of the surface asperities. Skewness (R_{sk}) is an indication of the tendency of the profile to favor either peaks or valleys. Kurtosis (R_{ku}) is a measure of the sharpness of the probability density of the profile. Detailed definitions and use of these various parameters can be found in Hamrock et al [23].

$$R_{sk} = \frac{1}{N{R_q}^3} \sum_{i=1}^{N} {z_i}^3 \tag{5.1}$$

$$R_{ku} = \frac{1}{N{R_q}^4} \sum_{i=1}^{N} {z_i}^4 \tag{5.2}$$

Table 5.1 presents a summary of all the parameters as an average over the six directions (shown in Figure 4) for both the lateral plates chosen for study. It can be noted that that plate 2 has higher R_a and R_q values than plate 1 which is expected due to the additional smoothing processes that were performed on plate 1. It is also interesting to note that the R_{sk} and R_{ku} values for plate 2 are quite close to zero, which indicates the absence of any sharp peaks or valleys with respect to the mean line. However, in the case of plate 1, R_{ku} is high which indicates a sharp peak in the distribution. In this case, the value of R_{sk} is also considerably negative, indicating sharp valleys. This could be explained by the fact that since most surface heights in plate 1 are quite close to the mean line, small deviations or scratches could amplify the value of the skewness parameter.

Table 5.1.
Summary of statistical surface parameters for plates 1 and 2.

Plate	R_a/R_{aRef}	R_q/R_{qRef}	R_{sk}	$R_{k\mu}$
Plate 1	0.18	0.28	-1.123	13.005
Plate 2	0.96	0.41	-0.269	0.214

It must be noted here that the mixed-TEHD model assumes that the surface profiles follow a Gaussian probability distribution and the parameter R_q is used to define each surface profile distribution. To verify this assumption of the gap model, the probability distribution of the profile measurements is compared against an equivalent Gaussian distribution which is defined with the help of the following equation,

$$p(z) = \frac{1}{\sigma\sqrt{2\pi}} \exp\left[-\frac{1}{2}\left(\frac{z-\mu}{\sigma}\right)^2\right] \tag{5.3}$$

In Equation (5.3), μ and σ represent the mean and standard deviation of the measurement under consideration. Figure 5.4(b) shows probability distribution of

the surface profile heights across the six measurement directions for plate 2 as plotted against its equivalent Gaussian distribution. It can be noted that actual measured profile heights fit very closely to a perfect Gaussian distribution, thus verifying one of the major assumptions of the mixed-TEHD model.

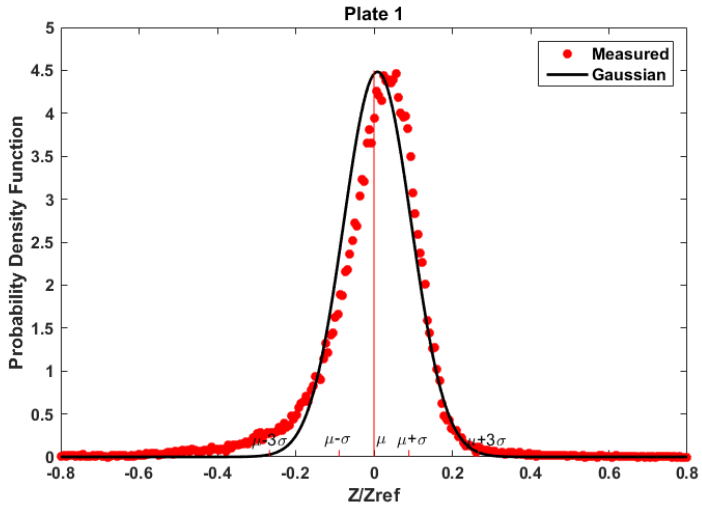

(a)

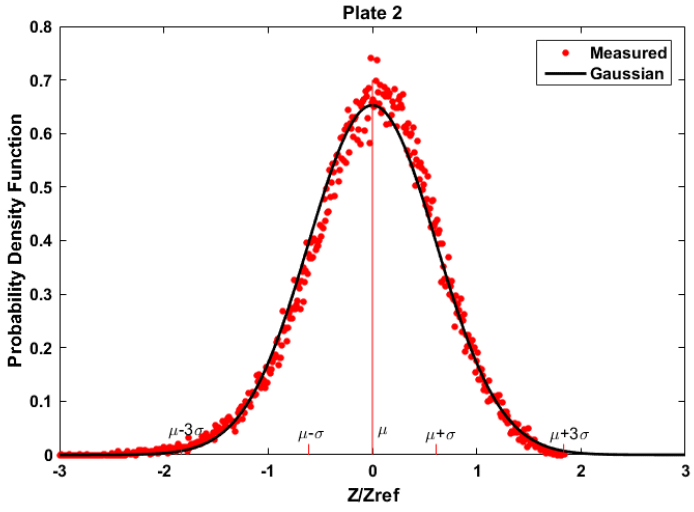

(b)

Figure 5.4. Comparison of probability distribution of measured surface profile heights over an equivalent Gaussian distribution for (a) Plate 1 (b) Plate 2.

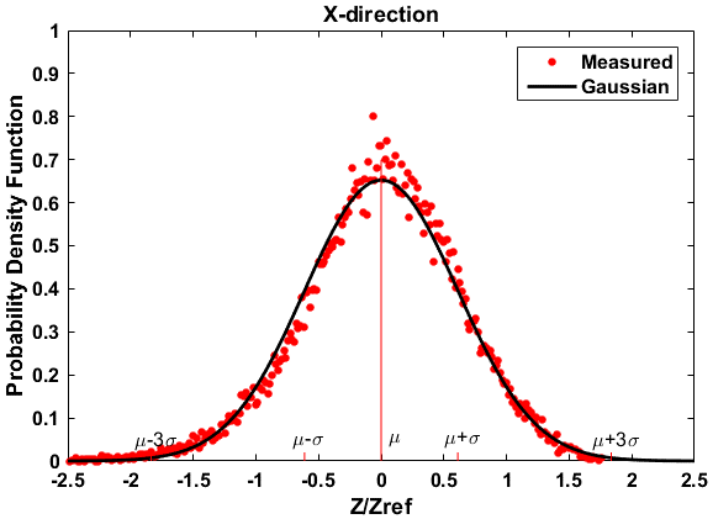

(a)

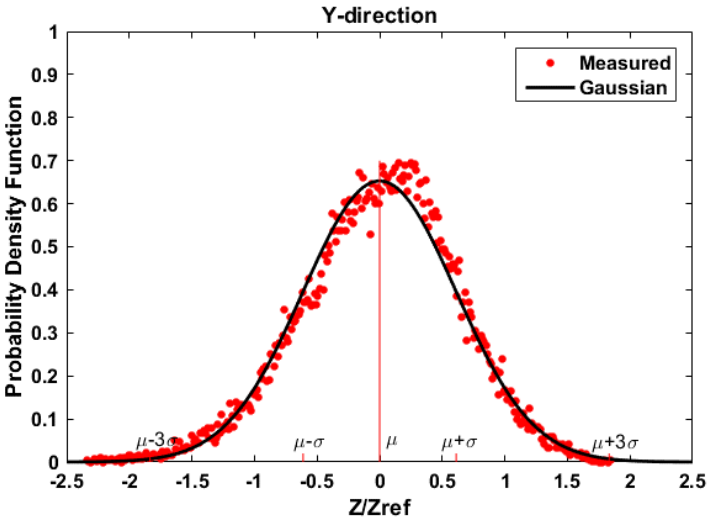

(b)

Figure 5.5. (a) Probability distribution plot for plate 2 along X − direction as an average of profile heights along A, B and F measurement directions. (b) Probability distribution plot for plate 2 along Y − direction as an average of profile heights along C, D and E measurement directions.

A similar probability distribution plot for plate 1 (shown in Figure 5.4(a)) also matches closely with an equivalent Gaussian distribution. The mixed film model

also assumes that the properties of the surface are identical in both horizontal and vertical directions. This isotropic assumption of the model is verified by plotting probability distribution plots for each direction for plate 2 as shown in Figure 5.5(a) and Figure 5.5(b). Each plot is generated after averaging the profile heights along 3 measurement directions (as indicated earlier in Figure 5.2) in each direction.

It can be inferred from Figure 5.4(a) - Figure 5.5(b) that the Gaussian distribution is a reasonable assumption across each of the directions. Moreover, the value of $R_q/R_{qRef} = 1.222$ along X direction is quite close to the corresponding value $R_q/R_{qRef} = 1.224$ along Y direction, thus demonstrating the isotropic nature of the surfaces. Thus, the conclusions obtained in this section lend confidence to the use of the mixed-TEHD model in predicting the lubrication performance of the reference EGM while accounting directly for the measured roughness values.

5.2 Experimental Validation with Torque Losses in EGMs

While this section is primarily intended to validate the mixed-TEHD lateral gap model, this research effort also supplements the contribution of a novel approach to numerically estimate the various torque losses encountered in EGMs. One of the major challenges in the different detailed numerical models developed for EGMs (Chapter 1) which have not been addressed yet in literature, is the prediction of the hydro-mechanical efficiency (often referred as torque efficiency). In many design cases, the hydro-mechanical efficiency is an important design parameter which needs to be evaluated to assess performance requirements during the early design phases. The hydro-mechanical efficiency (η_{hyd}) of a positive displacement unit can be defined with the following equation [100] where T_{ideal} and T_{real} are the ideal and actual torque required to operate the hydrostatic unit,

$$\eta_{hyd} = \frac{T_{ideal}}{T_{real}} * 100 \tag{5.4}$$

The present work shows how the cumulative torque losses predicted by the different numerical sub-models for a reference EGM at various operating conditions align at a good approximation with experimental measurements of the torque losses.

5.2.1 Source of Torque Losses

The ideal torque (T_{ideal}) is the theoretical torque which is required to operate an ideal EGM when there are zero losses encountered in the operation and can be defined with the help of the following equation [100] where V_i represents the derived swept volume [100] of the unit under consideration,

$$T_{ideal} = \frac{\Delta P * V_i}{2\pi} \tag{5.5}$$

Losses in the torque applied to the drive gear in a real EGM unit originate from different sources which can be theoretically decomposed into several terms according to the following equation for the actual torque (T_{real}) [16],

$$T_{real} = T_{ideal} + T_{s\mu} + T_{s\rho} + T_{sp} + T_{sc} \tag{5.6}$$

The losses contributed by the viscous friction in the different lubricating interfaces is represented by $T_{s\mu}$. There are primarily two different kinds of lubricating gaps present in typical EGMs, namely the lateral gap existing between the gears and the lateral bushings and the radial gap which exists between the gears and the casing. The two kinds of lubricating interfaces typically found in an EGM were represented earlier in Figure 1.4(a) in a simplified manner. A simplified approach to estimate the effect of the pump operating parameters and the loss term $T_{s\mu}$ is described in [16]: when the film thicknesses in the lubricating interfaces are constant and assuming laminar flow conditions, these losses are directly proportional to the operating speed of the unit (n),

$$T_{s\mu} = \frac{K_\mu * \mu * n}{h} \tag{5.7}$$

where h is the gap height of the lubricating interface and μ represents the viscosity of the working fluid. K_μ denotes the constant of proportionality in the torque loss relationship with speed.

$T_{s\rho}$ represents the torque losses arising from the turbulent resistances due to the fluid flow through the internal connections in the different fluid volumes in an EGM unit. As described in [16], a rough expression for $T_{s\rho}$ can be provided by assuming a proportional relationship between the velocities in turbulent orifices connections and the overall flow rate. With this simplification, these kind of losses follow a second order relationship with operating speed as shown in Equation (5.8), where ρ is the density of the working hydraulic fluid while K_ρ characterizes the constant of proportionality.

$$T_{s\rho} = K_\rho * \rho * n^2 \tag{5.8}$$

T_{sp} indicates the pressure dependent torque losses which originate from the parts in a positive displacement machine where there are instances of dry friction [16]. These losses are directly proportional to the operating pressure [16] and can be represented with the help of the following equation where K_p is the proportionality is constant,

$$T_{sp} = K_p * \Delta P \tag{5.9}$$

In the case of EGMs, the sources of T_{sp} arise from the frictional forces due to the contact of the driver and the driven gears.

$T_{s\mu}$, $T_{s\rho}$ and T_{sp} are significant sources of torque losses for EGMs and can be evaluated using the different numerical models described in Chapter 2. All other kinds of torque losses which are independent of the operating conditions can be cumulatively represented by T_{sc}. These losses are usually influenced by pre-loaded stresses on the assembly seals and springs [16]. T_{sc} is assumed to be generally negligible in the case of EGMs and for the present study.

5.2.2 Numerical Estimation of Torque Losses

The various sources of theoretically expected torque losses can be evaluated numerically using the simulation models described earlier in Chapter 2 and Chapter 3. The viscous friction losses from the lateral and the radial lubricating gap can be obtained using the same set of equations described in Section 2.2.10 for the full film model (for both lateral and radial gaps) and Section 3.1.7 for the mixed film model (only lateral gaps), and can be individually categorized as T_{sh-lat} and T_{sh-rad}. It must be noted here that there are totally two lateral lubricating and four journal bearing interfaces in the reference EGM considered for this research work and thus, the torque losses computed using the relationships in the aforementioned sections are added accordingly.

The losses due to turbulent resistances primarily arise from the orifice connections though the EGMs which are modeled in the fluid dynamic model of the EGM. The total torque calculated from this model is represented in Equation (2.34), Using this evaluated torque, the torque losses solely due to turbulence resistance flow through the orifices can be obtained from the following equation after obtaining T_{ideal} from Equation (5.5) for a given operating condition,

$$T_{tr} = T_{tot} - T_{ideal} \tag{5.10}$$

The evaluation of torque losses due to frictional contact forces between the gears are modeled in a simplified manner by assuming a spur gear transmission efficiency from the driver to the driven gear due to the inherent frictional losses present at the contact of the gear teeth. These mechanical losses are directly dependent on the gear profiles as well as the load of the EGM unit which are the delivery pressures at the outlet. Thus, the torque losses due to the mechanical transmission from the driver to the driven gear can be modeled using the following equation where $T_{p-driven}$ is the torque applied on the driven gear shaft due to the pressure forces (evaluated using Equation (2.34)),

$$T_{fc} = \frac{(1 - \eta_{mech-g})}{\eta_{mech-g}} * T_{p-driven} \tag{5.11}$$

where T_{fc} represents the torque losses contributed by the frictional contact forces and η_{mech-g} represents the inherent mechanical efficiency of the gears which can be evaluated using simplified gear efficiency formulas found in [101]. In the present study, the value of η_{mech-g} is assumed to be 94 % which is in the lower end of the range of general mechanical efficiencies for spur gears with profiles similar to the ones used with the reference EGM in this work. However, future work in this research can potentially include a more accurate tool to predict these frictional torque losses at the contact of the gears.

Thus, the numerically evaluated torque losses can be cumulatively added with the help of the following equation to obtain the total torque loss for an EGM design at a given operating condition,

$$T_{loss-n} = T_{sh-lat} + T_{sh-rad} + T_{tr} + T_{fc} \tag{5.12}$$

5.2.3 Simulated Results of Individual Torque Losses

The numerical models for estimating the different torque losses described in the previous section were used to calculate the losses for different operating conditions. All the results presented in this section are evaluated for three different shaft speeds of 1000 rpm, 1500 rpm and 2000 rpm for a range of operating pressures in a reference EGM Case 1B. The actual values of the torque loss and pressure values have been normalized for confidentiality reasons using $T_{ref} \sim \mathbf{O}(1Nm)$ and $p_{ref} \sim \mathbf{O}(100bar)$.

Figure 5.6(a) shows the simulated torque losses from the four journal bearing interfaces in the reference EGM unit. The torque losses are plotted against different delivery pressures in the unit for each operating speed under consideration. It can be seen that while these viscous shear losses from the bearing increases with increasing pressure, they also show a direct proportional behavior with operating speed as theoretically defined earlier in Equation (5.7). Thus, the constant trend of viscous losses increasing linearly with operating speed observed numerically is in agreement with the theoretical relationship. With increasing pressures, the radial pressure forces

acting on the gears increase and thus results in reduced gap heights in these bearing interfaces which subsequently results in increased torque losses.

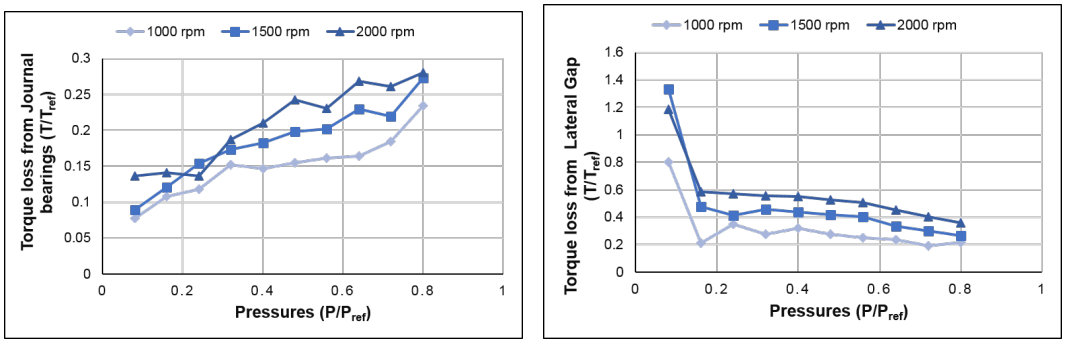

(a) (b)

Figure 5.6. Numerically simulated torque losses in the reference EGM unit for different operating conditions at the (a) Journal bearing interfaces and (b) Lateral lubricating interfaces.

Similarly, the torque loss contribution from the viscous shear in the lateral gap is plotted for different operating conditions in Figure 5.6(b). It can also be observed that the torque loss variation with operating speed follows trends similar to the theoretical relationship in Equation (5.7). However, unlike the trends of torque loss with pressure noted in the journal bearing, the viscous shear loss from the lateral gap decreases with increasing pressure.

The torque losses contributed by the flow through the turbulent resistance in the different orifice connections as evaluated for various operating conditions are shown in Figure 5.7(a). It is observed from this plot that there is a quadratic variation of this kind of torque loss with speed, which is in line with what was anticipated with Equation (5.8). However, there is no notable variation of this loss with the operating pressures and the loss seems to remain almost independent of the pressures.

Figure 5.7(b) shows the variation of the torque losses due to the frictional contact forces for the selected operating conditions. It is noted from this plot that these frictional forces are only dependent on the delivery pressures of the EGM unit and

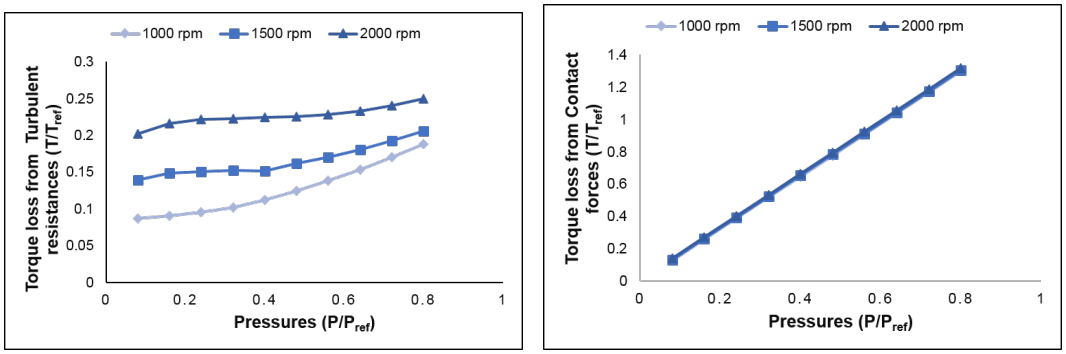

(a) (b)

Figure 5.7. Numerically simulated torque losses in the reference EGM unit for different operating conditions due to the (a) Turbulent resistances and (b) Contact forces.

are independent of the varying operating speeds. These numerically observed trends of this torque losses are in accordance with the relationship predicted by Equation (5.9) due to the fact that the contact forces between the gears increase with increasing operating pressures.

It can be observed from the magnitudes of the numerically predicted sources of torque losses in Figure 5.6 and Figure 5.7 that the largest contributor of the torque losses arises from the frictional contact between the gears at higher pressures (p/p_{ref}>0.5) while the lateral gap losses are the dominant source of torque losses at lower pressures.

5.2.4 Experimental Measurements of Torque Losses

In order to validate the numerically predicted torque losses presented in the previous section with experimental losses, steady state measurements were performed on the reference EGM unit at the author's research lab. The reference external gear pump was characterized at different operating conditions in terms of both shaft speed and delivery pressure by measuring delivery flow rate, input torque required at the

drive shaft and the various temperatures associated with inlet and outlet of the unit. Figure 5.8(a) shows a picture of the test rig used in the experiments reported in the current study along with the reference EGM unit mounted on it.

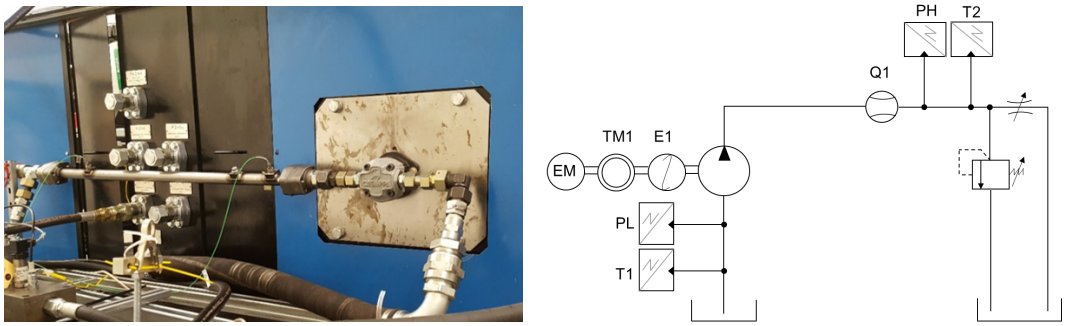

(a) (b)

Figure 5.8. (a) Setup of the test rig used for the experimental validation of the torque losses in the reference EGM unit. (b) ISO schematic of the hydraulic circuit used in the experiments.

The ISO schematic hydraulic circuit implemented in the experimental test rig is shown in Figure 5.8(b) Table 5.2 shows the details of the different sensors and components which are used for the measurement data. The input torque applied at the drive shaft of the pump (as measured by torque meter TM1 shown in Figure 5.8) represents the actual torque T_{real} and the torque loss can be obtained by subtracting the theoretically expected torque for an ideal machine (T_{ideal}). Thus, the torque loss at different operating conditions can be evaluated with the help of the measured input torque available from the readings of the torque meter TM1.

The ideal expected torque T_{ideal} is dependent on the measured derived displacement of the unit according to Equation (5.5). Since T_{ideal} is critical for evaluating the torque losses accurately, the derived displacement from the experiments can be calculated using the Toet method [102] and ISO 8426 method [103]. However, both of these available methods to calculate the derived displacement of positive displacement machines do not completely capture inherent features of EGMs such as the

Table 5.2.
Details of the different sensors and components used in the experimental test rig.

Symbol	**Type**	**Specifications**
EM	Electric Motor	ABB, 4-quadrant electric motor: 93.2 kW
T1, T2	Resistive thermocouple	Omega K-Type, Scale: 50 - 200 C
PH	Piezo-resistive pressure sensors	WIKA, Scale : 0 - 250 bar
Q1	Flow meter	VSE, Scale: 0.05 - 150 l/min
TM1	Torquemeter	HBM T10FS, Scale: 0 - 500 Nm
E1	Optical speed measurement system	HBM T10FS, Scale: 0 - 15000 rpm

effects of radial micro-motion of the gears. As described in [22], the interaxis distance between the gears centers depends on the operating pressure and speed. These interaxis variations affect the actual volumetric capacity of the unit. By keeping this in mind, it appears evident how the Toet method fails in capturing these features since it assumes no dependence on the units geometrical features with pressure. On the other hand, the ISO 8426 method does not take into account the variation of volumetric efficiency with shaft speed.

Due to these inconsistencies in the aforementioned methods, the present work uses numerically calculated values of the displacement as predicted from HYGESim, which comprehensively accounts for the different possible micro-motions along with the flow evaluations at any given operating condition. For each of the operating conditions

reported in this paper, the displacement of the unit was obtained from HYGESim and is summarized in Figure 5.9(a) where each curve represents the variation of normalized displacement against different pressures for a given operating speed. It can be observed from the plot that the displacement increases with increasing pressure and decreases with increasing speed. The Toet method accounts for the variation of displacement only with speed whereas the ISO method captures the dependence of displacement on pressure. However, it is noted from the numerically calculated values that although both speed and pressure have an effect on the displacement, the actual variation in the magnitude of displacement was not substantial.

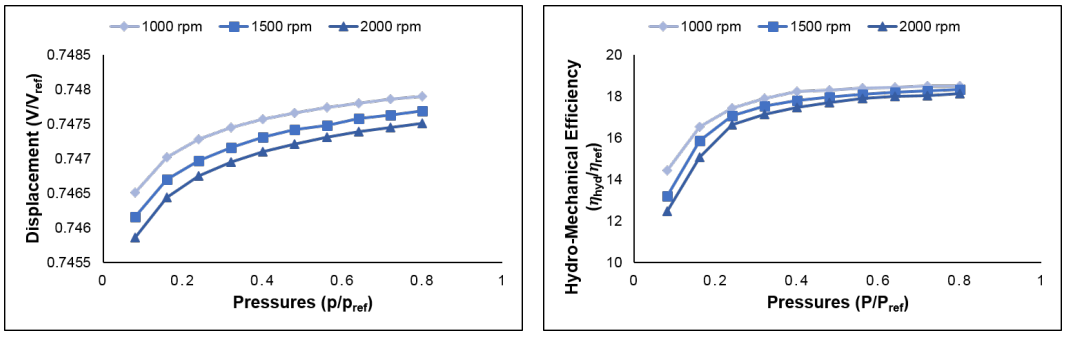

(a) (b)

Figure 5.9. (a) Numerically calculated values of displacement at different operating conditions for a reference EGM unit. (b) Normalized hydro-mechanical efficiency as measured by experiments for different operating conditions.

The hydro-mechanical efficiency (η_{hyd}) defined earlier in Equation (5.4) is now calculated with help of the experimental measurements. Normalized values of hydro-mechanical efficiency with the help of η_{ref} (for the reasons of confidentiality) are plotted for different operating conditions in Figure 5.9(b). It can be observed from the plot that the hydro-mechanical efficiency decreases with increasing speed which is due to the trends explained in the earlier section, where all the individual sources of torque losses increase with increasing speed (except for frictional contact forces which

are independent of speed). It can also be noticed that the efficiency is lower at lower pressures.

5.2.5 Validation with Numerically Predicted Torque Losses

The torque losses measured at the different operating points are compared to the cumulative prediction of the losses from different sources as represented in Equation (5.12). Since the primary aim of this effort is to compare and validate the performance of the mixed and full film lubrication models, the lateral gap losses (T_{sh-lat}) alone are calculated from both the models separately and used along with Equation (5.12) to compare experimentally measured losses. Thus, in all the results represented here, the simulated losses with full film model represents the torque losses calculated by using the T_{sh-lat} evaluated from the full film lateral gap model. A similar representation with the mixed film model evaluates just the T_{sh-lat} using the mixed model, while all the other sources of losses remain identical for both the comparisons. A composite surface roughness value of $R_q = 0.9\mu m$ was used in the mixed lubrication model.

Figure 5.10 − Figure 5.14 show the comparison of the torque losses between experimentally measured losses, simulated losses using the full film gap model and the simulated losses using the mixed film model at operating speeds of 700 rpm, 900 rpm, 1000 rpm, 1500 rpm and 2000 rpm respectively for a range of operating pressures.

It can be observed from the plots that both the simulated losses with mixed and full film gap models predict quite closely to the experimental losses at all pressures p/p_{ref}>0.3. At lower pressures, the mixed lubrication model predicts better than the full film model. This is primarily due to the fact that the magnitude of the contribution of losses from the lateral gap model is greater at lower pressures (as shown in Figure 5.6). Thus, the torque loss prediction is more sensitive at lower

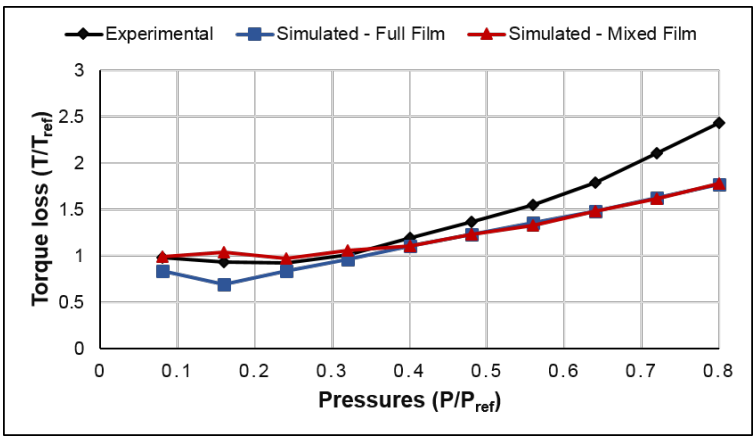

Figure 5.10. Comparison of torque losses between experimental measurements and the simulating losses using the full film and mixed film models respectively at an operating speed of 700 rpm.

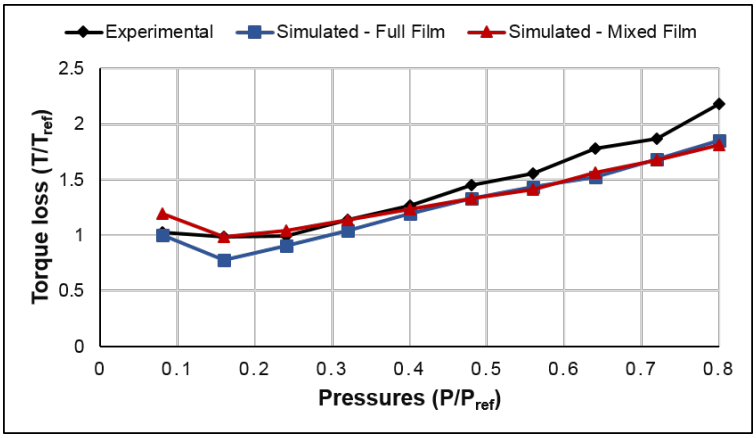

Figure 5.11. Comparison of torque losses between experimental measurements and the simulating losses using the full film and mixed film models respectively at an operating speed of 900 rpm.

pressures where the contribution from the lateral gap is higher than the rest of the sources of losses.

The aforementioned reasoning can be supported by comparing the instances of gap film thickness plots in the lateral gap from the full and mixed film models at the

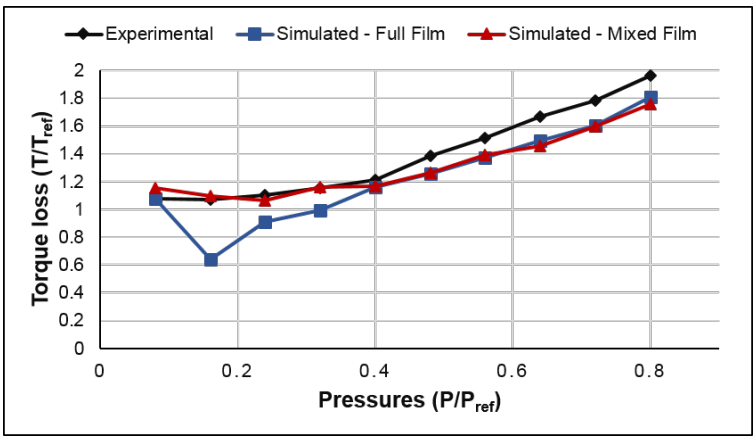

Figure 5.12. Comparison of torque losses between experimental measurements and the simulating losses using the full film and mixed film models respectively at an operating speed of 1000 rpm.

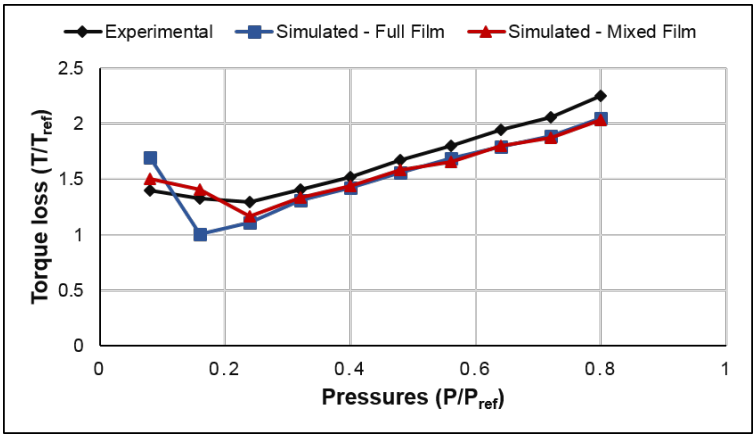

Figure 5.13. Comparison of torque losses between experimental measurements and the simulating losses using the full film and mixed film models respectively at an operating speed of 1500 rpm.

operating speed of 700 rpm and at pressures of $p/p_{ref} = 0.16$ and $p/p_{ref} = 0.8$ in Figure 5.15 and Figure 5.16 respectively.

It can be observed from Figure 5.15 that the regions of low and high film thicknesses along with the values of maximum and minimum gap heights are different between the predictions of the full and mixed film models respectively. This is owing

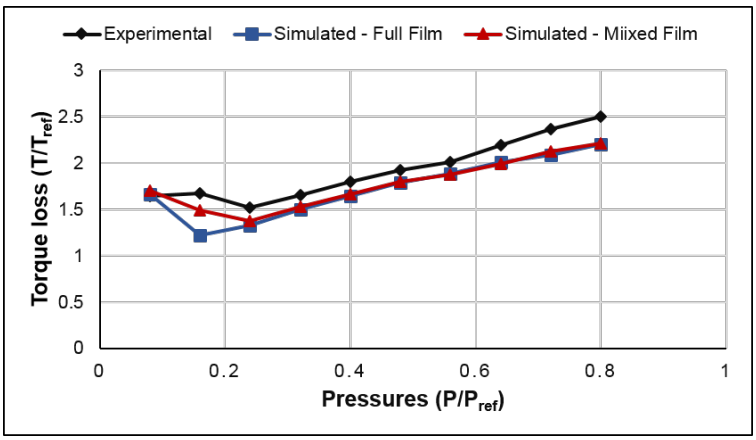

Figure 5.14. Comparison of torque losses between experimental measurements and the simulating losses using the full film and mixed film models respectively at an operating speed of 2000 rpm.

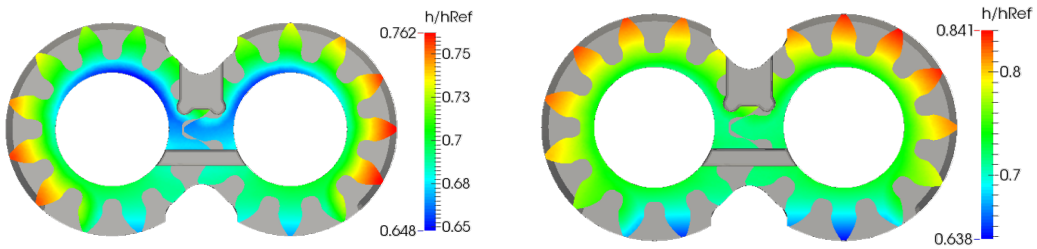

(a) (b)

Figure 5.15. Gap film thickness distribution in the lateral gap at $p/p_{ref} = 0.16$ and 700 rpm from (a) Full Film model (b) Mixed Film Model.

to the fact that the hydrodynamic effects of the contact force and its point of application can affect the tilt of the lateral bushing. Due to a resulting lower minimum film thickness and its distribution, the torque loss prediction is higher in the mixed film model.

Although instances of mixed lubrication conditions are also observed in the high pressure condition shown in Figure 5.15 which results in varying gap heights, the contribution from this interface to the total torque loss is lower. Furthermore, due to

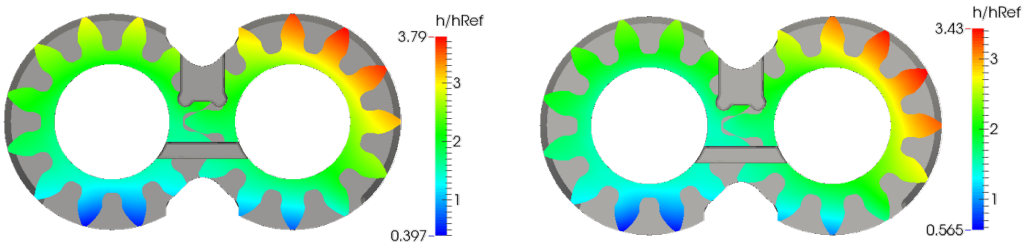

(a) (b)

Figure 5.16. Gap film thickness distribution in the lateral gap at $p/p_{ref} = 0.8$ and 700 rpm from (a) Full Film model (b) Mixed Film Model.

the presence of relatively higher gap heights, the difference between the actual values of the shear losses predicted by the two models are not very different from each other. Thus, in all the plots shown in Figure 5.10 − Figure 5.14, the effect of the mixed lubrication model in predicting the losses is more dominant at lower pressures. In addition, it must be noted that an increased deviation of the total predicted torque losses from the experimental losses exists at the lower speeds of 700 rpm and 900 rpm, especially at higher pressures. This could potentially be due to the presence of possible mixed film conditions in the journal bearing interfaces at these operating points which are currently not modeled and the simplified assumptions which are presently used for modeling the losses due to the contact between the two gears.

It can be concluded from the present study that the numerical prediction of the torque losses conforms closely to the experimental losses at a wide range of operating conditions. This study also validates the predictions of the mixed lubrication model developed in this study and thus further supports the necessity to have such a robust lateral lubricating gap model which can model the influence of the interface on the performance of the unit at an extensive range of operating points.

5.3 Experimental Validation with Drain Leakages

Although the prediction of the mixed lubrication model was verified with experimental torque losses in the previous section, this approach is quite limited since the actual contribution of the lateral gap to the total losses being measured is lower at quite a few operating conditions. Thus, another attempt to validate the mixed lubrication model at more operating points should include measuring a quantity which is exclusively related with only the lateral gap. This enables the validation efforts to be more sensitive to the prediction from the lateral gap model. In this section, the drain leakages which are directly related to the lateral gap are measured and the predictions from the full and mixed film lubricating gap models are compared to estimate the performance the newly developed mixed film model.

The direct relationship between drain leakages and the gap height can be obtained from Equation (3.33) as follows,

$$Q_{drain} \propto h^3 \tag{5.13}$$

The above expression indicates that the leakages from the lateral gap are quite sensitive to the gap heights which can aid in distinguishing the two lateral gap models at severe mixed lubricating conditions. Drain leakage measurements has already been used to validate the full film lateral gap model in EGMs in the work of [9]. The reference EGM used in the present study is identical to the one used in this previously performed work and thus, the modeling assumptions used in this work are similar to the former work. This is especially concerning the structural constraint used on the lateral bushing to evaluate its deformation and it was concluded that constraining the bushing at the LP side was the most feasible option.

The Case 1B EGM used for this study was a prototype with a specially designed outlet for drain leakages which could flow through the casing as shown in Figure 5.17(a). The configuration of the lateral pressure plate along with the seal is shown in Figure 5.17(b) and it can be seen that the seal (highlighted in yellow) completely isolates the drain interface (marked in dashed red line) [9], which aids

positively in capturing just the lateral leakages which is the primary aim of these measurements. A graduated cylinder with an accuracy of 1 mL was used in the experiment by recording the leakages for a consistent amount of time at different operating points. The ISO schematic hydraulic circuit for the test setup is shown in Figure 5.18(a) and the notations for the different elements used can be seen in Table 5.2.

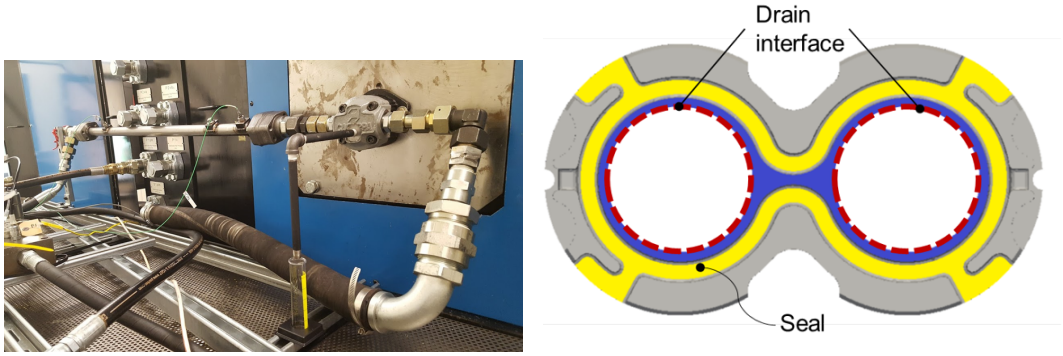

(a) (b)

Figure 5.17. (a) Setup of the experimental test with the special prototype EGM and a graduated cylinder for measuring drain leakages (b) Configuration of the balance side of the lateral pressure plate used in the prototype EGM used in the measurements with the drain interface marked in red.

5.3.1 Validation of Gap Model with Drain Leakages

In this section, measured drain leakages are used to compare against the corresponding simulated predictions from the mixed-TEHD model. Experimental measurements were conducted for a range of operating pressures from $p/p_{ref} = 0.08$ to $p/p_{ref} = 0.8$ at different operating speeds of 500 rpm, 1000 rpm, 1500 rpm and 2000 rpm. It must be noted here that a wider range of operating conditions were considered for the present study when compared to the former work in [9]. Figure 5.18(b) shows the measured drain leakages plotted against the delivery pressures for all the

tested operating speeds. It is observed that there is a strong correlation of leakages with the pressures as they increase steadily at higher pressures. However, there is only a marginal increase in the leakages with increasing speed. The values of leakages and pressures have been normalized for the sake of confidentiality.

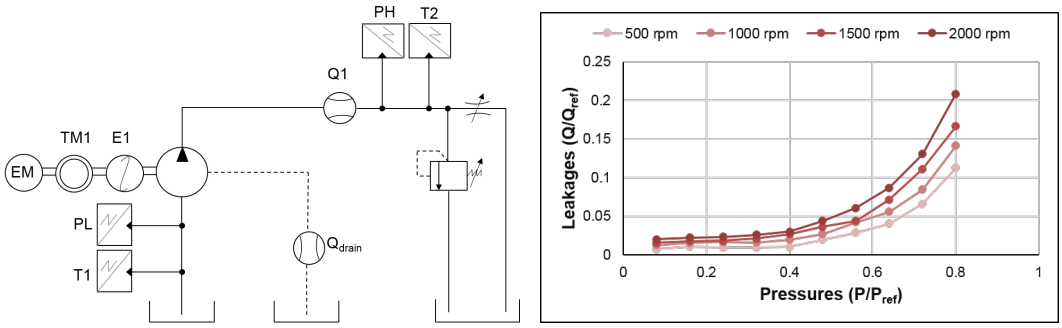

(a) (b)

Figure 5.18. (a) ISO hydraulic circuit for the experimental setup used for measuring drain leakages (b) Measured drain leakages plotted for different operating conditions.

Figure 5.19 shows the comparison of the experimental drain leakages at an operating speed of 500 rpm with the corresponding results obtained from simulating the lateral interface using the full and mixed film lubricating gap models. It can be seen from the plots that the two models predict quite closely to the experimental measurements for pressures up to p/p_{ref}>0.7. At higher pressures, the mixed film model is closer to the experiments than the full film model indicating a dominant mixed lubricating condition. This can be supported by observing film thickness plots predicted by the two models in Figure 5.20 at 500 rpm and $p/p_{ref} = 0.72$. The surface roughness for the mixed-TEHD model was set at $R_q = 0.5\mu m$.

In Figure 5.20, there is a considerable difference in the high and low film thickness predicted by the full film gap model and this results in sharp contact region near the suction side which indicates mixed lubrication conditions. Although the spatial orientation of the gap predicted by the mixed film model remains similar, such a

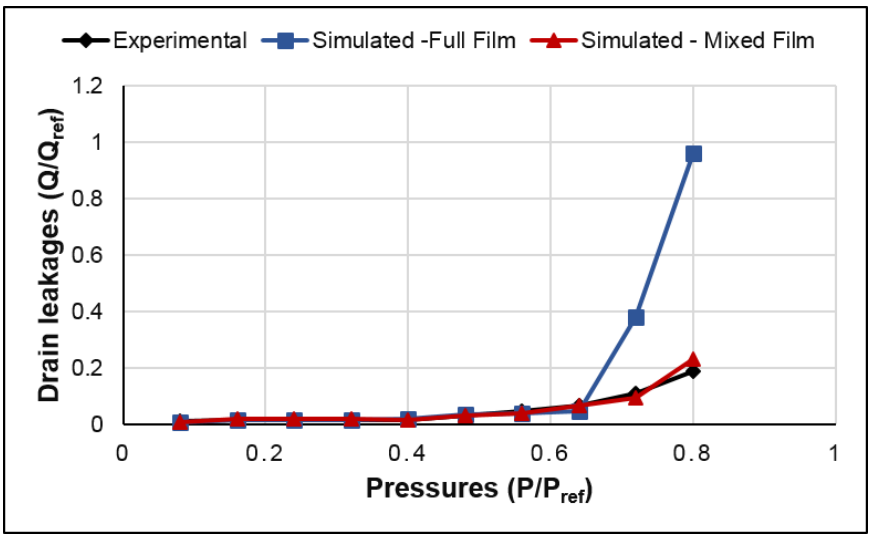

Figure 5.19. Comparison of measured drain leakages with the simulated ones from the full and mixed film models at an operating speed of 500 rpm.

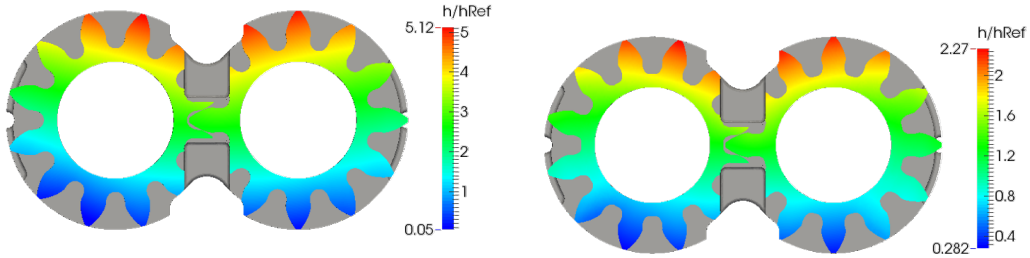

(a) (b)

Figure 5.20. Film thickness distribution in the lateral gap at 500 rpm and $p/p_{ref} = 0.72$ as predicted by (a) Full Film model (b) Mixed Film model.

considerable difference between the gap height values is not present. While the highest film thickness predicted by the mixed film model are lower than the corresponding prediction from the full film model, the minimum gap height is higher. This is due to the additional load sharing by the surface asperities which prevents any sharp contact

regions. Thus, the leakages predicted by the mixed film model is lower than the full film model and this is supported by the corresponding experimental measurements.

The comparison of the experimental measurements of leakages with the full film and mixed film models for operating speeds of 1000 rpm, 1500 rpm and 2000 rpm are shown in Figure 5.21 - Figure 5.23.

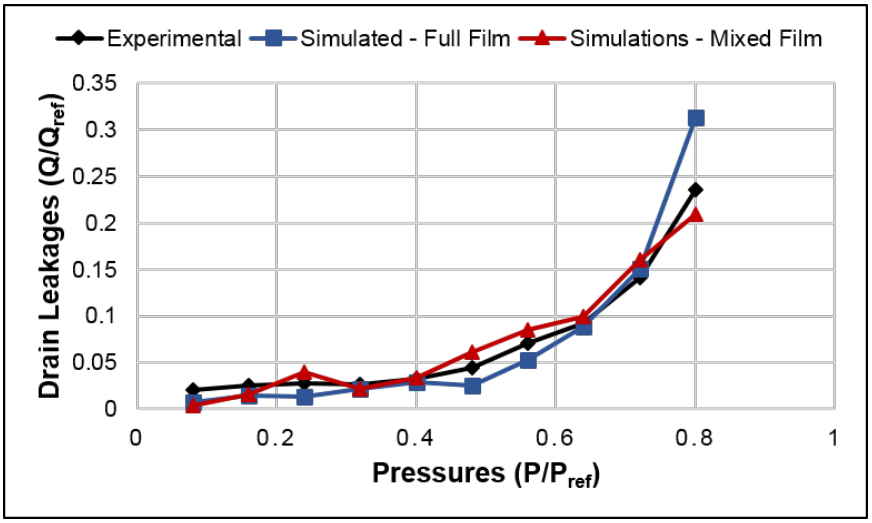

Figure 5.21. Comparison of measured drain leakages with the simulated ones from the full and mixed film models at an operating speed of 1000 rpm.

It can be seen from the plots that while the trends predicted by both the lateral gap models are identical to the experimental values, certain differences exist between them. At higher pressures, these differences are more dominant due to the presence of higher gap heights and consequently higher leakages. This difference is especially significant due to the cubic relationship between gap heights and leakages (Equation 5.13). These reasons can be supported by the gap film thickness plots obtained for the same operating speed of 1500 rpm, but at different pressures $p/p_{ref} = 0.8$ and $p/p_{ref} = 0.56$ in Figure 5.24 and Figure 5.25 respectively.

While in the operating condition at higher pressure shown in Figure 5.24, the magnitudes of the gap heights predicted by the two models are quite different from

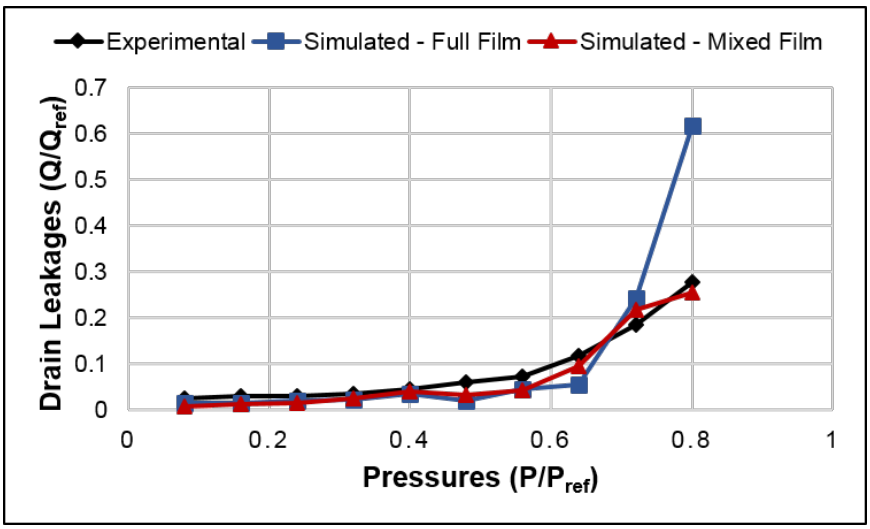

Figure 5.22. Comparison of measured drain leakages with the simulated ones from the full and mixed film models at an operating speed of 1500 rpm.

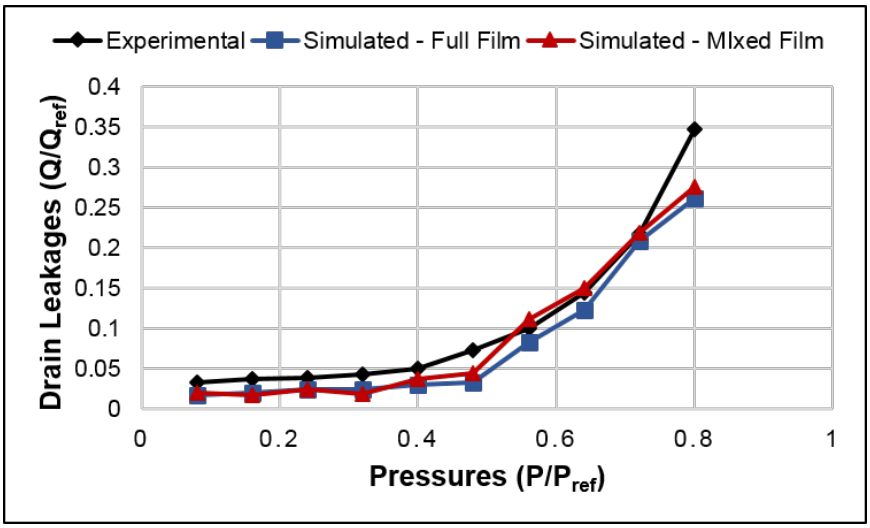

Figure 5.23. Comparison of measured drain leakages with the simulated ones from the full and mixed film models at an operating speed of 2000 rpm.

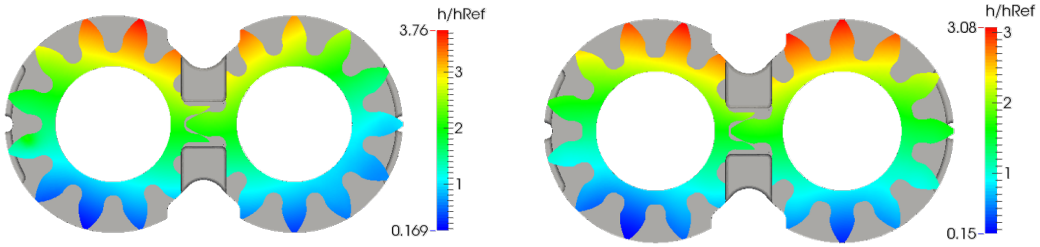

(a) (b)

Figure 5.24. Film thickness distribution in the lateral gap at 1500 rpm and $p/p_{ref} = 0.8$ as predicted by (a) Full Film model (b) Mixed Film model.

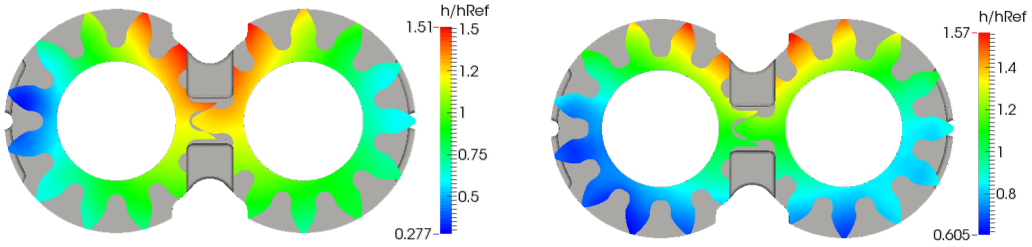

(a) (b)

Figure 5.25. Film thickness distribution in the lateral gap at 1500 rpm and $p/p_{ref} = 0.56$ as predicted by (a) Full Film model (b) Mixed Film model.

each other which results in substantial variation in the leakages predicted by the models at this operating condition as shown in Figure 5.22. Though some instances of mixed lubrication are also noticed in the operating condition in Figure 5.25, the actual variation in the maximum gap height is not very different for the two models, although there is an increase in the minimum gap height prediction from the mixed film model. Although this does not result in a dominant variation in the leakages as

seen in Figure 5.22, the prediction from the mixed lubrication is still closer to the experimental measurements.

It is also significant to analyze the torque losses from the lateral gap for this EGM design which is different from the reference design used to validate the torque losses in the earlier section (Section 5.2). Increased instances of mixed lubrication conditions were found at lower pressures in the EGM design used for torque loss validation earlier (Section 5.2), while such conditions are more dominant at higher pressures in the EGM presently used for leakage validation.

Figure 5.26 shows the plot of the normalized torque losses in the lateral gap for different operating pressures and a shaft speed of 1500 rpm for the EGM design used in the present section. It can be seen that the differences in torque losses between the full film and mixed film models are not significant except at $p/p_{ref} = 0.8$ where the mixed film model predicts a higher torque loss. This is also correlated with the drain leakage plots where the deviation between the two models is more significant at this operating point. However, due to the cubic relationship between leakages and gap heights (Equation (5.13)), the deviation in leakages is more significant. It must also be noted that the differences between the torque predictions exist at other operating points, indicating that some instances of contact conditions do exist at these points as the gap heights get close to the order of surface roughness in the gap. Thus, in order to obtain an accurate prediction of the performance of the lateral gap, surface features need to be considered at all simulation points.

From the above investigation on the torque losses, it can be observed that it is difficult to generalize the occurrences of mixed lubrication conditions based solely on the operating parameters, since these are quite dependent on the specific EGM design and its balance configurations.

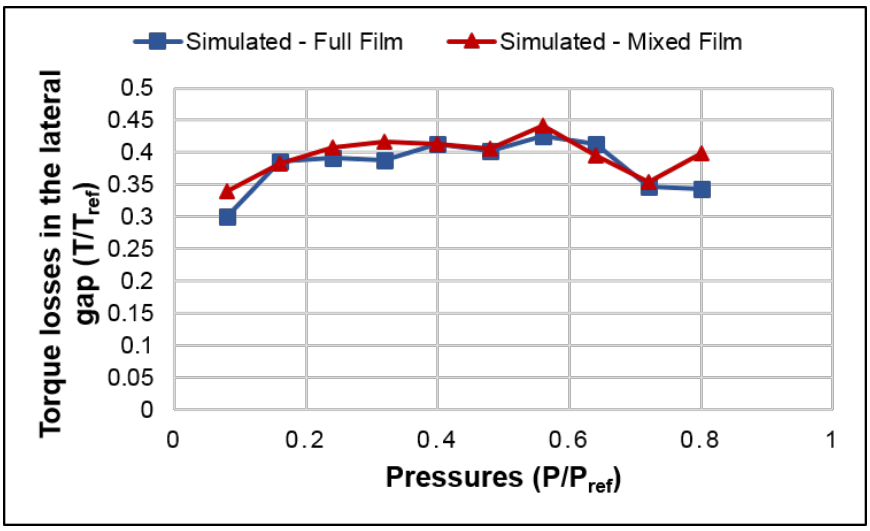

Figure 5.26. Comparison of measured drain leakages with the simulated ones from the full and mixed film models at an operating speed of 1500 rpm.

5.3.2 Influence of Varying Surface Roughness on Lubrication Performance

The experimental setup for measuring the drain leakages from the specially modified prototype EGM was used to test the influence of varying surface roughness of the lateral plate on the unit's performance with respect to the lateral gap. The lateral plates marked as plate 1 (with fine finishing) and plate 2 (with coarse finishing) as reported in Section 5.1 were used individually to test the performance of the EGM. It must be noted here that the two lateral plates of each of these designs have been used in the same reference Case 1B EGM for testing the units performance for all the results presented in this work. The measured leakages for plates 1 and 2 at different measured pressures (where $p_{ref} = \mathbf{O}(100bar)$) for operating speeds of 300 rpm, 400 rpm, 1000 rpm and 2000 rpm respectively in Figure 5.27 − Figure 5.30. It can be seen from all the plots that the lateral leakages from the plate with higher R_q is consistently higher than the design with lower R_q. This can be attributed to the reasoning that the surface asperities have a higher contribution to the lubrication load support at mixed

lubrication conditions in the case of the coarser lateral plate. With increased surface roughness, there are increased chances of the gap heights being in a similar order of magnitude, which consequently results in higher contact forces from the asperities. These forces push the plates further away from the gears, thereby accounting for the increased leakages observed experimentally in Figure 5.27 – Figure 5.30. It is also noted that the measured leakages increase with increasing operating speed, which is consistent with the expected trends.

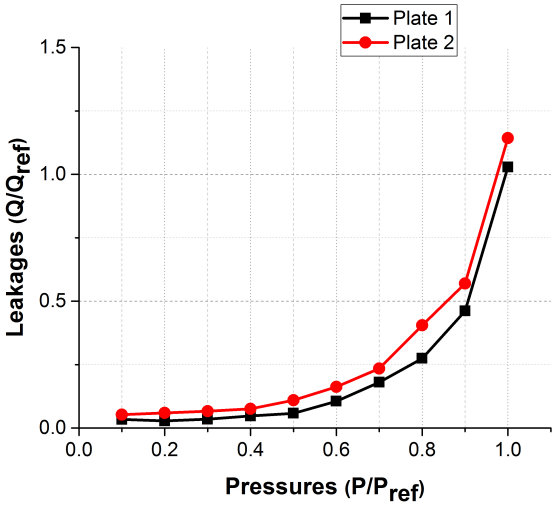

Figure 5.27. Measured drain leakages for plates 1 and 2 for various pressures at shaft speed 300 rpm.

Surface profilometer measurements (similar to the methods used in Section) were performed on the lateral plates after running the experiments to study the influence of the running the pump under the aforementioned operating conditions. Two lateral plates belonging to plate 1 and plate 2 designs were present in the reference pump on its either sides at the flange and end cover ends respectively. Table 5.3 compares the R_a/R_{aRef} R_q/R_{qRef} values before and after the experiments for all the plates used in this study. It can be seen from this table that for plate 2, the roughness values measured after experiments were lower than the corresponding values before the ex-

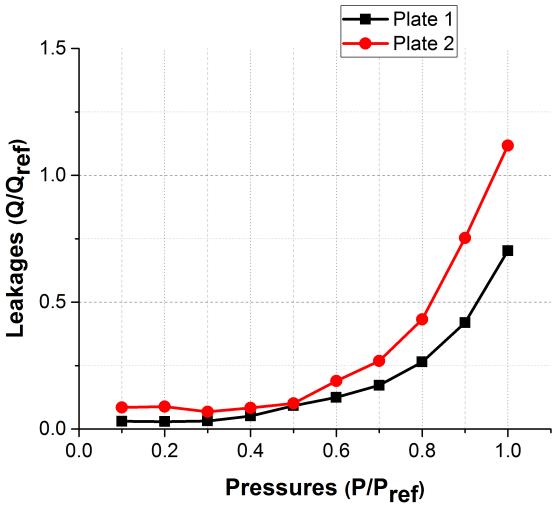

Figure 5.28. Measured drain leakages for plates 1 and 2 for various pressures at shaft speed 400 rpm.

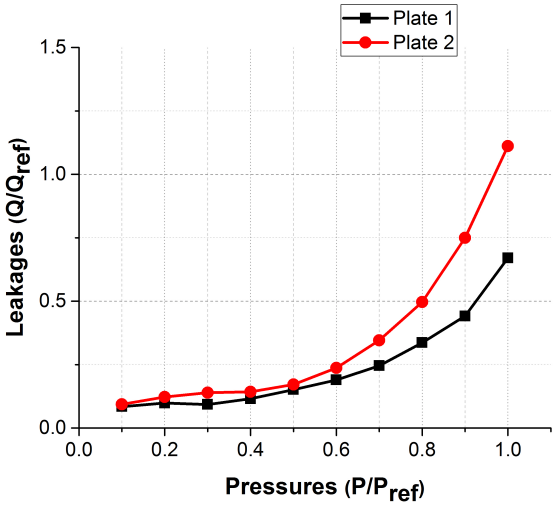

Figure 5.29. Measured drain leakages for plates 1 and 2 for various pressures at shaft speed 1000 rpm.

periments, thus indicating that the roughness asperities were smoothened during the pump operation due to the asperity contact. However in the case of plate 1, the

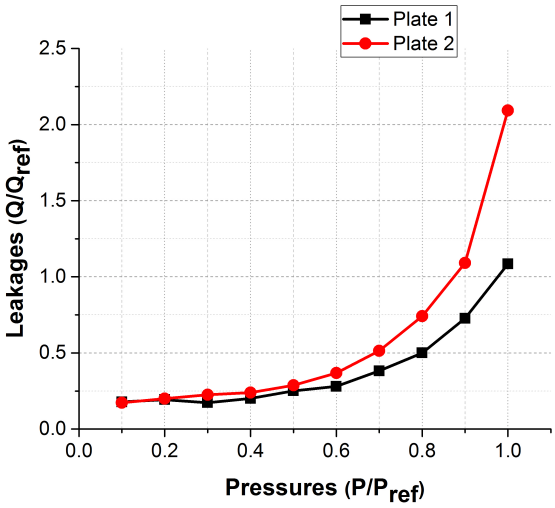

Figure 5.30. Measured drain leakages for plates 1 and 2 for various pressures at shaft speed 2000 rpm.

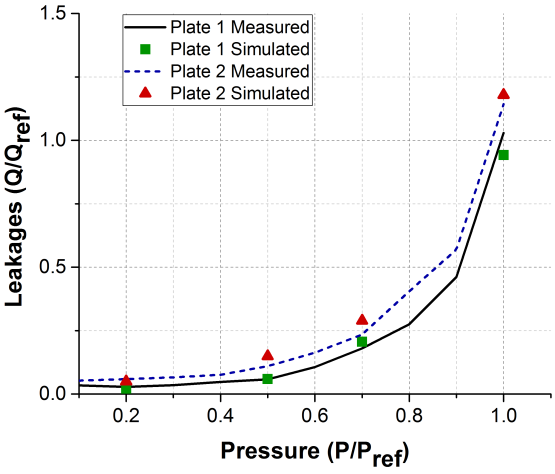

Figure 5.31. Comparison of simulated and measured drain leakages for plates 1 and plate 2 at operating speed of 300 rpm.

roughness values were increased slightly after the operation. This could be attributed to the nearly smooth surface of plate 1 which affects the accuracy of the measure-

ments. The six directions considered in the plate measurements could possibly be insufficient to capture the small changes in surface roughness encountered during the experiments. While future research directions could include possible improvement in the measurement techniques, this novel study still proves the significance of considering surface features in analyzing and designing the lubrication performance of EGMs.

Table 5.3.
Summary of measured changes in surface roughness values of various lateral plate designs used in experiments.

Parameters	**Plate 1 (Flange)**	**Plate 1 (Cover)**	**Plate 2 (Flange)**	**Plate 2 (Cover)**
R_a/R_{aRef} (before test)	0.18	0.2	0.96	0.9
R_a/R_{aRef} (after test)	0.22	0.26	0.94	0.88
R_q/R_{qRef} (before test)	0.28	0.34	1.22	1.18
R_q/R_{qRef} (after test)	0.3	0.4	1.2	1.14

Comparison of the drain leakage measurements from plates 1 and 2 with the simulations from mixed-TEHD model was performed in a manner similar to Section 5.3.1.In Figure 5.31, a comparison of the simulated and the experimental leakage measurements for plates 1 and 2 are presented for various pressures at an operating speed of 300 rpm. The comparison reveals that the model predicts quite closely to the trend followed in the experiments with increasing pressures for both the plates. Furthermore, the model consistently predicts higher leakages for a higher value of R_q (in plate 2) when compared to plate 1 owing to the increased load support from the

asperities as discussed in Section 4.2. It is also interesting to note here that a higher difference in leakages between the two plates is observed at higher pressures from both the simulations as well as experiments. This can be attributed to the reasoning that higher pressures increase the chances of mixed lubrication for the reference EGM design, which consequently increases the contact forces from the asperities.

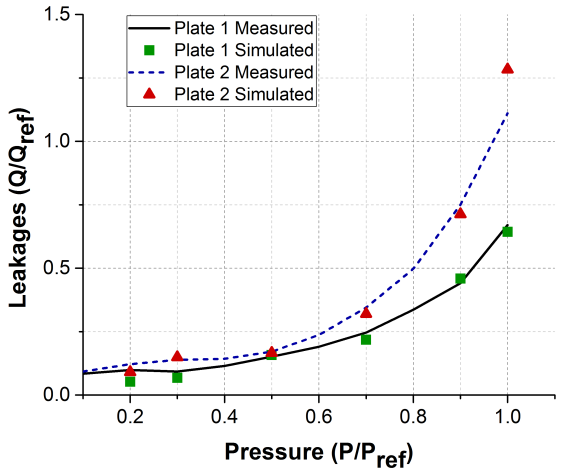

Figure 5.32. Comparison of simulated and measured drain leakages for plates 1 and plate 2 at operating speed of 1000 rpm.

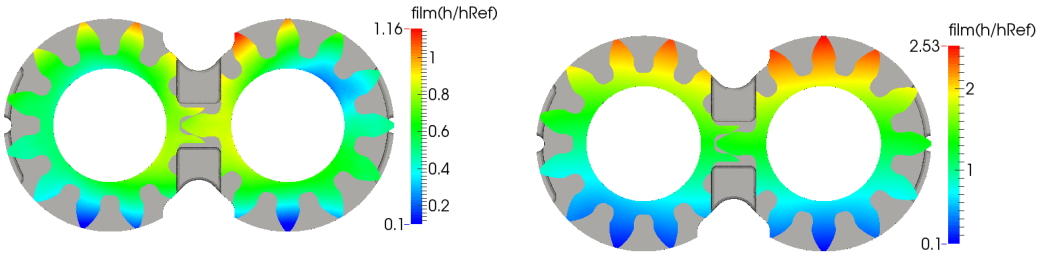

(a) (b)

Figure 5.33. Gap film thickness plot at $p/p_{ref} = 0.7$ and 1000 rpm speed for (a) Plate 1 (b) Plate 2.

A similar comparison of the measured and the predicted leakages from the gap model at a shaft speed of 1000 rpm is shown in Figure 5.32, where the leakage trends observed in the experiments for both the variation in surface roughness as well as pressures are captured in the model results. It is also noted here that there is a larger variation in leakages between plates 1 and 2 at higher pressures. This can be supported with the help of film thickness plots shown in Figure 5.33(a) and Figure 5.33(b) ($h_{ref} = \mathbf{O}(3\mu m)$) at $p/p_{ref} = 0.7$ at 1000 rpm for both plates 1 and 2. It can be seen from Figure 5.33(b) that a higher film thickness region is found near the delivery side for plate 2 owing to the higher contact forces from the asperities in the low film thickness regions near the suction. On the other hand, such load support from the asperities is lower in plate 1 where nearly smoother surfaces are present. It should also be noted in Figure 5.33(a) and Figure 5.33(b) that the contact forces and the surface roughness effects change the configuration of the gap heights at the interface and consequently vary the drain leakage values as observed in the experimental measurements.

Experimental studies performed in this chapter indicate that the influence of surface effects in the lubrication performance of the lateral gap is an important factor for designing EGMs. However, the extent of the influence of these effects can vary depending on the operating parameters as well as the various parameters related to the EGM design itself. Thus, a comprehensive lateral gap model which can account for both mixed and full film lubrication conditions, such as the one developed in this work, can potentially be a useful tool for designing efficient and reliable EGMs.

6. SURFACE SHAPING TO IMPROVE LUBRICATION PERFORMANCE OF EGM REFERENCE CASE 1B WITH OIL AS THE WORKING FLUID

Addition of micro-surface shaping effects especially on the lateral surface of the gears have been shown to improve the lubrication performance of lateral gaps in EGMs in the works of [9, 92] for the reference high viscous working fluid (ISO VG46 hydraulic oil). Specifically, it was shown in these works that adding a linear sloping wedge on the lateral surface of each gear tooth on its either side (as represented in Figure 6.1(a)) was shown to reduce the torque losses from the lateral lubricating gap. However, in the present thesis, it is also proposed that adding a flat step along with a wedge profile on the surface of the gears (as indicated in Figure 6.1(b)) has the potential to further reduce the torque losses. This section presents simulation results from the lateral gap model supporting these claims and a corresponding experimental validation of these numerical findings using Case 1B EGM prototype with a step and wedge profile designed on each of its gear teeth.

6.1 Simulations Results from the Lateral Lubricating Gap Model

An extensive study related to the selection of the optimal axial balance design for different wedge depths in the case of the wedge only design has been shown earlier in [92]. In the present study, a modified surface shaping is designed where the linear sloping wedged region does not start at the root of the gear teeth and instead follows a flat region from the root of the tooth, resulting in a step and wedged surface as shown in Figure 6.2(a) for a single gear tooth. Figure 6.2(b) represents this surface shaping with the step and wedge when extended to the entire domain of the lubricating gap. The amount of step region along with the maximum wedge depth can be varied, resulting in different surface shaping designs.

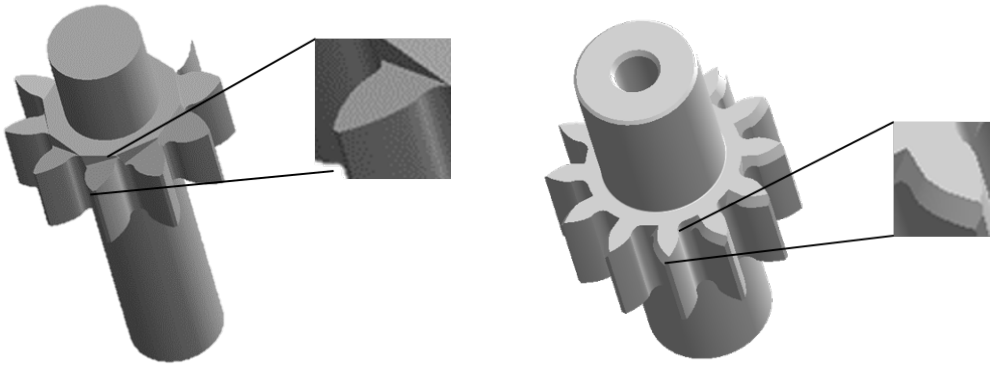

(a) (b)

Figure 6.1. (a) Linear sloping wedge surface shaping in the order of microns to the surface of the gears (b) A step and wedge profiling (order of microns) on the lateral surface of the gears. (Exaggerated for clarity).

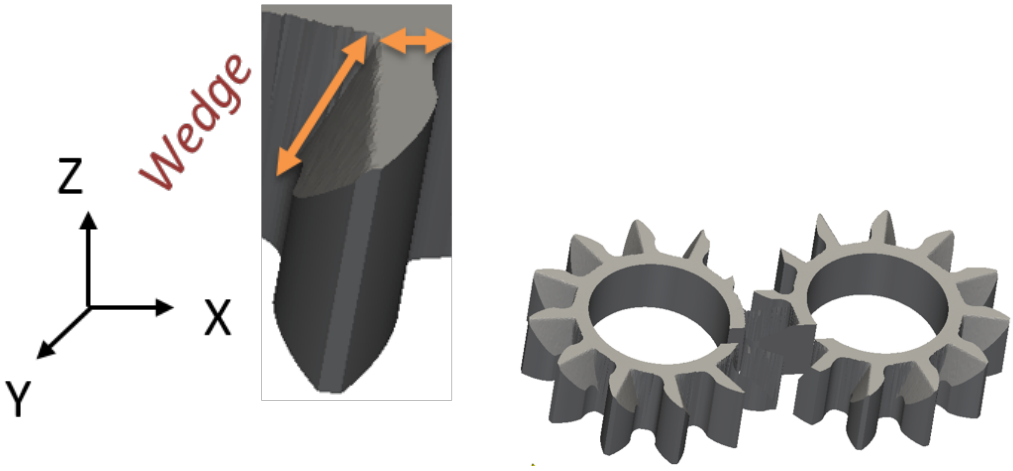

(a) (b)

Figure 6.2. Representation of lubricating gap domain for the step and wedge surface shaping as concerned with (a) Single gear tooth (b) Entire lubricating gap domain (exaggerated for visual representation).

A representation of performance of the step and wedge gears is compared to the linear wedge only gears as well as the nominal design in terms of the total torque losses from the lateral gap, as predicted using the equations described in Section 2.2.10, across three different operating conditions with shaft speed 2000 rpm and delivery pressures at $p/p_{ref} = 0.2$, 0.6 and 1.2. In this comparison shown in Figure 6.3, the total power losses from the lateral gap is calculated and compared to the nominal EGM design, a design with 1 μm linear wedge only, design with 50 % step and 1 μm wedge and lastly, a design with 50 % step and 10 μm wedge.

Figure 6.3 shows that the lubrication performance of the step and wedged gears with a 1 μm wedge depth, is only marginally better than the wedged gears with the same wedge depth in terms of the power losses. A maximum of $\sim$ 14 % reduction of the losses was observed at the operating condition of $p/p_{ref} = 1.2$ and 2000 rpm when the step and wedged gears with 1 μm is compared with the wedge gears of the same wedge depth. The comparison in Figure 6.3 also shows that the performance of the 10 μm wedge and 50 % step is found to be superior to the 1 μm wedge depth and 50 % step gears as well as the only linear wedge gears across all operating conditions considered for this comparison. The maximum improvement in the power losses was about 50 % when compared to the linear wedge only design and this is observed at $p/p_{ref} = 0.2$ and 2000 rpm.

6.2 Experimental Validation of Step and Wedged Surface Shaping

The projected benefits of adding the wedge micro shaping to the surface of the gears in conventional designs of EGMs through simulations were experimentally validated by testing the step and wedge surface shaping design on the reference EGM Case 1 with displacement 11.2 cc/rev (12 teeth). Step and wedge design is chosen owing to the ease of manufacturing of higher wedge depths as compared to the linear wedge only design, which maximizes the advantages of the proposed surface shaping design (as shown in Figure 6.1(b)). A maximum wedge depth of 10 μm with close to

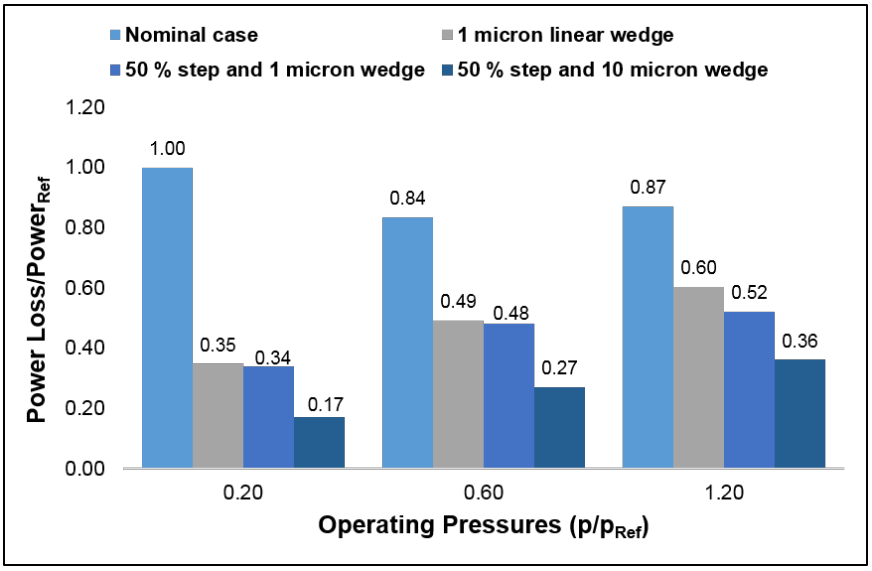

Figure 6.3. Comparison of the normalized total power losses in the lubricating gap between step and wedge, wedge and nominal gear designs at different operating pressures.

50 % step was manufactured on either surface of the two gears, ensuring that the direction of the inclination of the wedge in each gear was favorable to the corresponding direction of rotation of both the drive and the driven gears respectively.

Steady-state characterization tests on both the standard and the prototype EGM with wedged gears were performed using an experimental test setup similar to that shown in Figure 5.8(a). Torque measurements at different operating conditions were performed to evaluate advantages of the prototype in terms of torque losses. The tests were performed by using the same reference pump, by only replacing the gears. The same lateral bushings (thus maintaining same balance areas) were utilized for both experiments, hence reproducing similar comparison conditions as shown in Figure 6.3.

Reference operating conditions for the comparisons are defined by shaft speeds of 1000 rpm, 1500 rpm and 2000 rpm across a range of outlet pressures from $p/p_{ref} =$ 0.08 to 0.8 in increments of $p/p_{ref} = 0.08$. Any reduction in the viscous losses offered by the wedged gears would directly result in reduced input torque when compared

to the nominal design, since all other factors affecting the torque losses in a positive displacement machine are kept the same in this experiment.

Figure 6.4 − Figure 6.6 shows the comparison of the input torque measured for the operating conditions outlined earlier for wedged and nominal design of the gears. It can be observed from these plots that there is a consistent reduction in the input torque required to drive the external gear pump using the wedged gears across an extensive range of tested operating conditions, when compared against the corresponding nominal design of the same prototype. Specifically, at higher outlet pressures greater than $p/p_{ref} = 0.56$ at all the operating speeds, the wedged gears were found to further reduce the input torques required to drive the external gear pump. Thus, the prototype with 50 % step and 10 μm maximum wedge depth surface shaping was found to improve the performance of the external gear pump by experimentally proving the reduction in the torque losses. Hence by extension, the concept of wedged surface shaping to improve the mechanical efficiency of EGMs was experimentally validated with the help of this study.

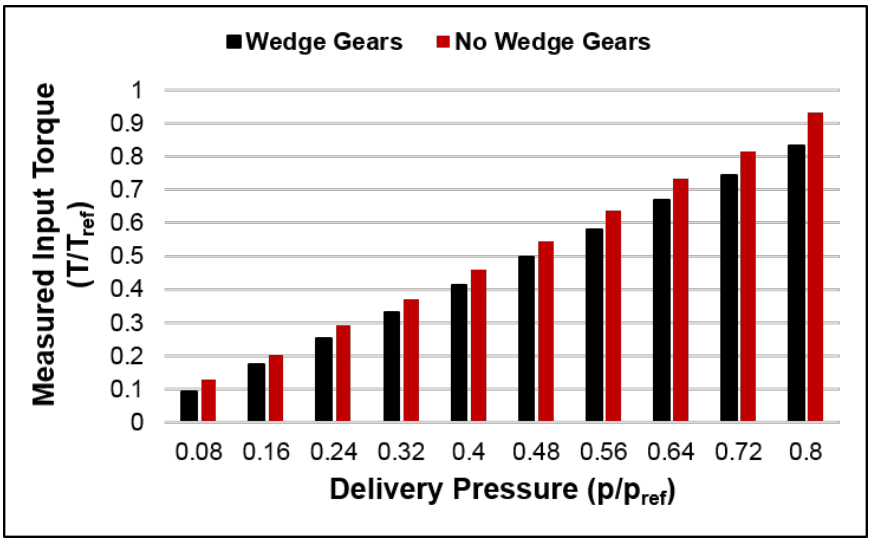

Figure 6.4. Input torque measured for wedged gears and the nominal gears for shaft speed 1000 rpm.

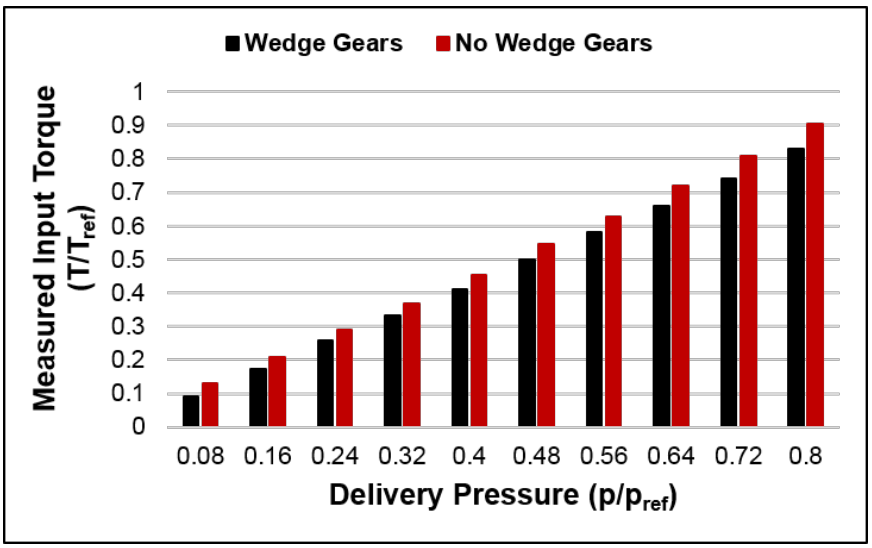

Figure 6.5. Input torque measured for wedged gears and the nominal gears for shaft speed 1500 rpm.

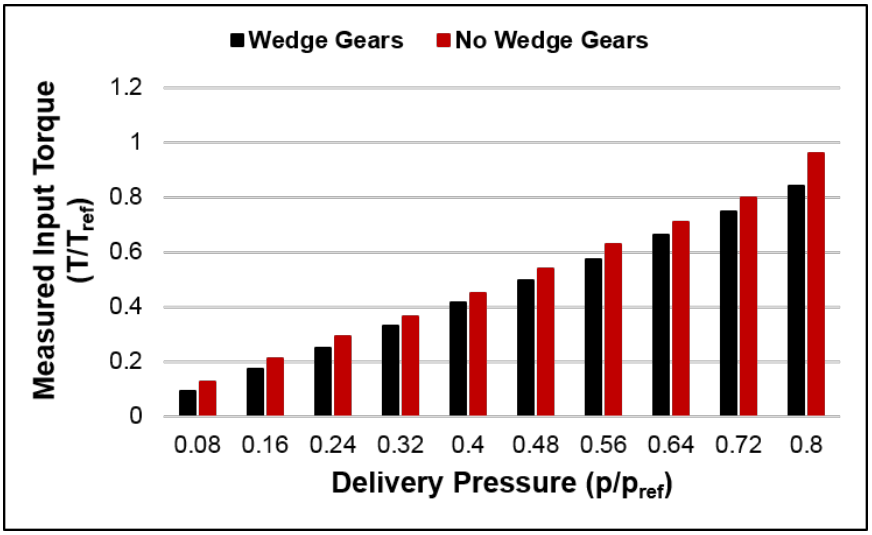

Figure 6.6. Input torque measured for wedged gears and the nominal gears for shaft speed 2000 rpm.

Therefore in the study presented in this section, it was confirmed with the help of experimental validation on a prototype EGM that introducing a properly designed

step and wedge surface shaping on the surface of the gears can aid in reducing the torque losses, which subsequently results in improved lubrication performance in the case of reference high viscous fluid. To the best of the authors knowledge, the idea of introducing wedged surface shaping or other micro surface shaping designs on the gears to improve the hydro-mechanical efficiency of EGMs has never been manufactured and validated before, due to the intricacy in designing and studying its effects on the complex phenomena associated with the lateral lubricating gap. However, with the help of advanced numerical tools such as the FSI-EHD lateral lubricating gap model and the axial balance optimization procedure, such a delicate design process is simplified. Using these findings and numerical tools, such novel designs will also be explored in Chapter 8 for improving the performance of EGMs for working fluids with low viscosity where designing a lubricating interface is quite challenging.

7. ANALYSIS OF LUBRICATING INTERFACES IN CASE 2 WITH JET A FUEL AS THE MAIN WORKING FLUID

In this chapter, Case 2 of a commercially available external gear pump (EGP) used in aerospace engines for fuel injection application is considered (specifications described in Chapter 1), to demonstrate the significance of the developed models in this research when applied to a low viscous working fluid. While Chapter 8 discusses the applications of the numerical lateral gap model with another low viscous fluid, water using a conventionally designed EGM, the current chapter considers an asymmetrically balanced EGP design with Jet A working fluid which has viscosity values close to that of water.

In asymmetrically balanced designs, the two lubricating interfaces on either side of the gears perform differently from each other. Therefore, the driver and the driven gears have unbalanced lateral forces acting on them, which result in the axial movement of these gears. A lubricating gap model for asymmetrically balanced EGM accounting for the variation of performance between the two interfaces along with the micro-motion of the gears has been studied in [10]. This asymmetric gap model along with the frictional modeling described in Section 3.4 is utilized in the current work to investigate the performance of an aerospace fuel injection pump. Moreover for the first time, the work presented in this chapter demonstrates the implementation of a frictional force model to account for the influence of radial forces acting on the lateral bushing which affect the lubricating performance of the EGP. Typically, in pressure compensated designs of these pumps, the lubricating interfaces perform important functions like bearing high pressure loads and sealing against leakages, similar to that of reference pumps used in the previous sections, that directly affects the units operating efficiencies.

Figure 7.1 shows a transparent view of the different components in the reference pump and the lubricating gaps under study are highlighted with the help of a red box. It must be noted that the reference pump has two different stages and only the performance of the highlighted components is considered in the current study. Two lubricating interfaces are present between each of the lateral bushings and their respective side of the gears as shown earlier in Figure 1.7(b). The lateral bushing indicated as floating bearing is responsible for providing the axial pressure compensation at different operating conditions while the net forces in the EGP push the other bushing (indicated as solid bearing) towards the end of the casing. This is because the rear side of the solid bearing has low pressure fluid (as shown in Figure 7.2(b)) which results in pressing itself against the covers of the EGP. On the other hand, the floating bearing shown in Figure 7.2(a) has the HP and the LP areas separated by an O ring seal. Consequently, the floating bearing is the only axial balancing element in the reference design, which leads to a condition referred to as an asymmetrically balanced system. The two lateral lubricating interfaces between the gears and the respective lateral bushings in such a system, are here onwards designated as floating/gears and solid/gears interface as indicated in Figure 1.7(b).

The frictional force acting between the floating bearing and the housing (as explained earlier in Chapter 1 in Figure 1.5) influences the movement of the floating bearing which consequently affects the lubrication performance of the unit.

Experiments to demonstrate the influence of these frictional forces by measuring the floating bearing position at each operating condition were performed in this research, which will be shown later in Section 7.1. The experiments were conducted by successively varying the outlet pressures in consistent steps at a constant operating speed, while starting at the lowest outlet pressure and increasing to the highest pressure and tracing the same experimental path again from highest to the lowest outlet pressure. While retracing the same experimental path from the highest to the lowest outlet pressure after reaching the highest pressure, the measured position of the floating bearing was different at each outlet pressure when compared to the pre-

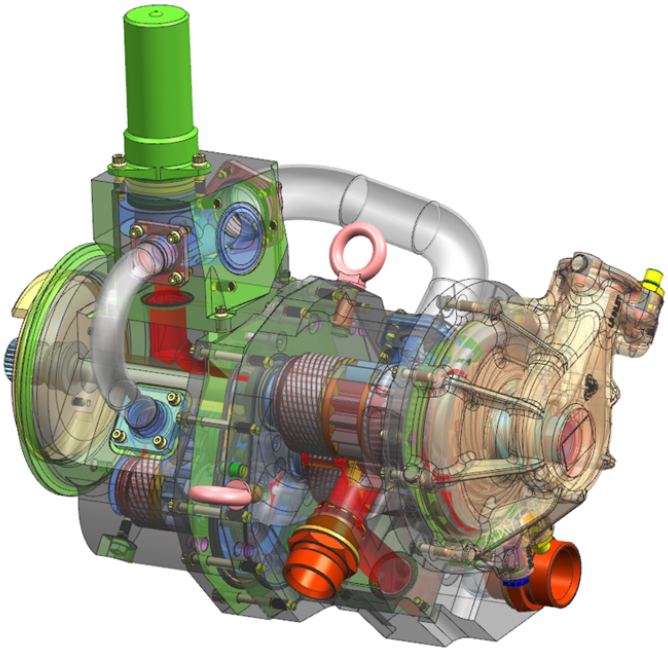

Figure 7.1. Overview of the reference fuel pump used in the current study and location of the lubricating interfaces is highlighted in red.

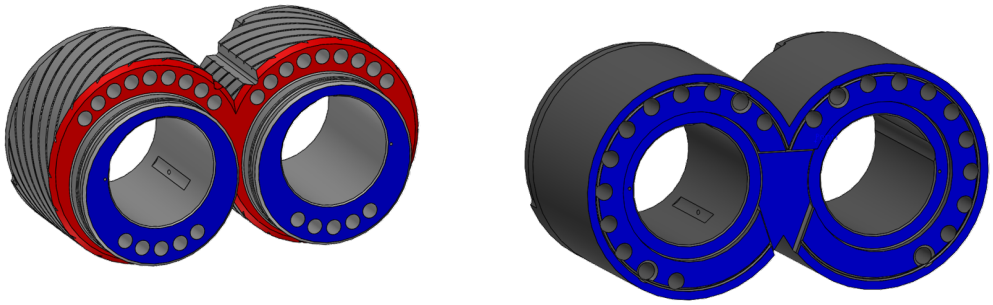

(a) (b)

Figure 7.2. Areas of the lateral bushings with high pressure (highlighted in red) and low pressure (highlighted in blue) fluids shown for (a) Floating bearing (b) Solid bearing.

vious measurement at the same pressure obtained while increasing from the lowest to highest pressures. This resulted in a hysteresis of the floating bearing position as shown in a qualitative plot using Figure 7.3, where the orange and blue points represent the position of the floating bearing at the same pressure, but approached with different preceding outlet pressures. The frictional forces acting on the floating bearing are strongly dependent on the starting position of the bearing at each operating condition, since the friction is dominant enough to influence and restrict the motion of the bearing. Thus, different starting positions due to different preceding pressures result in varying resulting position of the floating bearing.

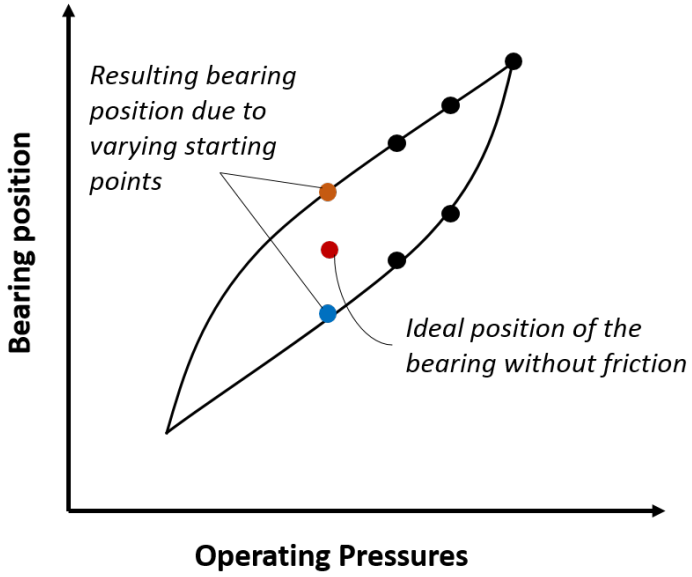

Figure 7.3. Qualitative representation of the "hysteresis" phenomenon of the floating bearing position experienced during the experimental measurements

In the current study, the effect of the frictional contact of the floating bearing with the housing is considered in an integrated manner with the FSI lateral gap model. Details of the asymmetric gap model used for this work can be found in [10]. It must be noted here that only the isothermal parts of the model (fluid flow solver, structural solver and force balance solver with the frictional force model) along with

the assumption that the floating bearing and the gears are restricted to translating only along the axial direction are used for the scope of this study. Predictions from the simulation model are then compared with experimental measurements of the floating bearing position, which also confirm the substantial effect of friction on the performance of the reference EGP under study. After detailing the effects of the FSI gap model with the frictional effects, this chapter also describes the experimental setup used for recording the performance of the EGP unit and validating the simulated gap results.

7.1 Experimental Analysis

Experimental measurements were performed in an instrumented prototype of the reference pump design for a wide range of operating speeds ($n/n_{ref} = 0.11 - 0.94$ with $n_{ref} = \mathbf{O}(10000rpm)$) and outlet pressures ($p/p_{ref} = 0.025 - 0.9$ with $p_{ref} = \mathbf{O}(3000psi)$) using Jet A1 fuel as the main working fluid with the help of a dedicated fuel pump test rig, at the Rolls Royce Center, Birmingham, United Kingdom. The ISO schematic circuit of the experimental test rig is shown in Figure 7.4 along with a simplified representation of the internal components of the reference pump. Various data related to the temperatures on the pump components as well as the fuel, pump outlet flow, outlet and inlet pressures as well as pressures on the different components were monitored using appropriate sensors and recorded during controlled experimental testing. The experimental setup allowed control of fluid temperatures in the system as well as continuous monitoring of internal pressures and temperatures of the pump components, to ensure the consistency of the recorded measurements especially with respect to the hysteresis behavior explained in the previous section. Although several data points were acquired for full characterization of the reference pump, only the acquisition of the floating bearing position data is reported in this paper for respecting the scope of the current work. Eddy current sensor (Micro-Epsilon EU05(65) with accuracy 0.05 μm) mounted on the back of the pump

casing (as shown in Figure 7.4) was used to measure the floating bearing position during the pump operation.

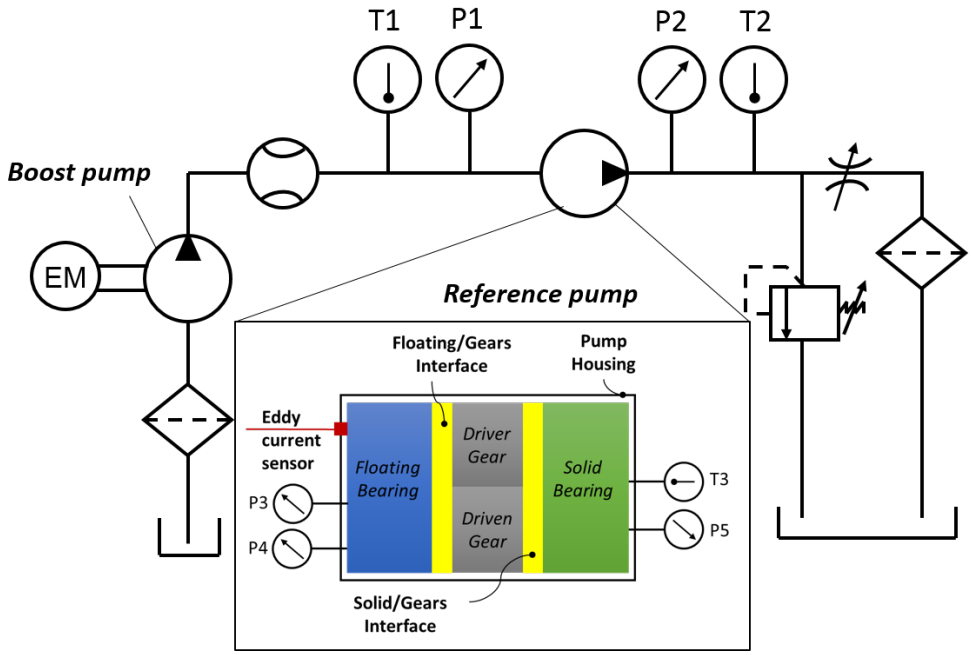

Figure 7.4. ISO hydraulic circuit of the experimental setup used along with a schematic representation of location of the eddy current sensor on the instrumented prototype to measure the floating bearing position in Case 2.

The experiments were conducted by successively varying the outlet pressures in steps of $p/p_{ref} = 0.1$ at a constant operating speed, while starting at the lowest outlet pressure and increasing to the highest pressure, followed by tracing the same experimental path again from highest to the lowest outlet pressure. Steady state monitored data was recorded at every outlet pressure tested during the experimental campaign and the measured outlet pressures at speed of $n/n_{ref} = 0.55$ is shown in Figure 7.5(a). Similar experimental methodology was used at other operating speeds, while the range of outlet pressures tested were different at each speed.

To compare the simulated results using the FSI lateral gap model, the input operating conditions of pressure and speed to the gap model were similar to the one

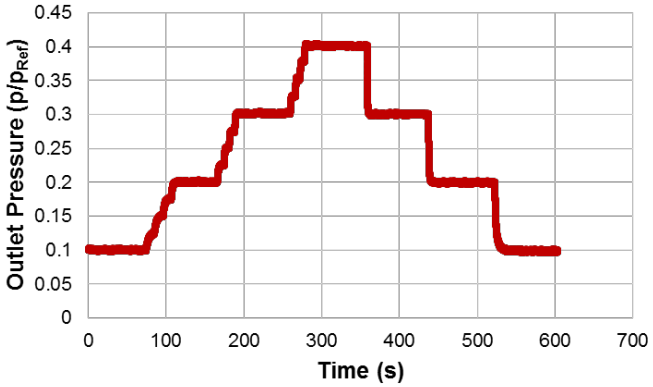

(a)

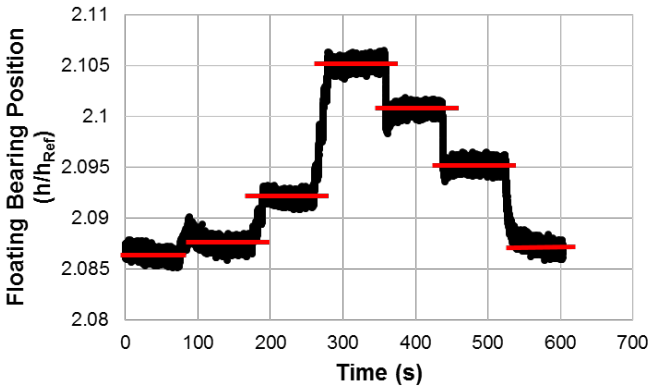

(b)

Figure 7.5. (a) Measured outlet pressures at a constant speed of $n/n_{ref} = 0.55$ while varying the outlet pressures from $p/p_{ref} = 0.1$ to $p/p_{ref} = 0.4$ in steps of $p/p_{ref} = 0.1$. (b) Corresponding measured bearing position at each operating condition The straight red lines represent the mean position of the bearing at each recorded operating pressure.

used in experiments. The starting gap heights at each operating delivery pressure in the lateral gap simulations were obtained from the converged floating bearing position from the previous operating pressure.

Due to the complexities involved in directly using the measured floating bearing positions since the location of the sensor is susceptible to deformation, it becomes quite difficult to track the direct location of the sensor from the model predictions.

To overcome these issues and compare the experimental results with simulations, relative position of the floating bearing is evaluated with respect to the minimum outlet pressure at a given measured speed with the help of Equation (7.1).

$$h_{rel,exp} = h_{exp} - h_{min,exp} \tag{7.1}$$

The rigid body position of the floating bearing can be directly obtaining from the tracking point h_0 (shown earlier in Figure 2.12) in the lateral gap simulations at each operating condition. The position of the floating bearing relative to its position at the starting outlet pressure can be obtained from the following equation,

$$h_{rel,sim} = h_0 - h_{min,0} \tag{7.2}$$

7.2 Simulation Results and Validation

The current section presents the results obtained from FSI lateral gap simulations to demonstrate the effect of frictional forces on the lubrication performance of the fuel injection pump. Certain modeling assumptions have been used for performing the simulations which include restricting the motion of the floating bearing, driver and driven gears to only the axial direction, thereby allowing only one degree of freedom for each of the solid components.

7.2.1 Simulations at a Constant Operating Speed of $n/n_{ref} = 0.55$

In the first set of simulations, the operating speed was kept constant at $n/n_{ref} = 0.55$ while the outlet pressures were varied at $p/p_{ref} = 0.1$, $p/p_{ref} = 0.2$, $p/p_{ref} = 0.3$ and $p/p_{ref} = 0.4$ successively, before retracing the path and reducing from $p/p_{ref} = 0.4$ to $p/p_{ref} = 0.1$ in steps of $p/p_{ref} = 0.1$ to complete the simulation cycle in a manner similar to experiments described in Section 7.1. Table 7.1 summarizes the various parameters and their corresponding values used in the first set of simulations. It must be noted here that the values of friction coefficient and breakaway velocity were assumed.

Table 7.1.
Parameters used in the simulations at operating speed of $n/n_{ref} = 0.55$.

Parameters	**Values**
Starting gap height	$h/h_{ref} = 0.33$
Starting pressure	$p/p_{ref} = 0.1$
Inlet pressure	$p/p_{ref} = 0.037$
Friction coefficient	0.025
Breakaway velocity	$v/v_{ref} = 0.32$
Outlet pressures	$p/p_{ref} = 0.1$,$p/p_{ref} = 0.2$, $p/p_{ref} = 0.3$, $p/p_{ref} = 0.4$
Operating speed	$n/n_{ref} = 0.55$

A starting gap height of $h/h_{ref} = 0.33$ was assumed for the starting outlet pressure of $p/p_{ref} = 0.1$ and the gap film thickness results at this operating condition for both the lubricating interfaces are shown in Figure 7.6. The gap heights obtained at convergence at $p/p_{ref} = 0.1$ are then used as starting gap heights at $p/p_{ref} = 0.2$, which in turn are successively used in $p/p_{ref} = 0.3$. This pattern of passing gap height information then continues to $p/p_{ref} = 0.4$ followed by $p/p_{ref} = 0.3$, $p/p_{ref} = 0.2$ and $p/p_{ref} = 0.1$. The film thickness distribution for these operating conditions are shown in Figure 7.7 - Figure 7.12. It is observed from these plots that, as the gap height information is passed along successive simulations, the film thickness increases with increasing pressure. Furthermore, the gap heights in the second leg of these simulations are higher for a given outlet pressure since the starting gaps are higher from higher input outlet pressures. It must be noted that all the film thickness plots presented in this section have been normalized using $h_{ref} = \mathbf{O}(3\mu m)$ for confidentiality reasons.

The relative positions of the floating bearing at different operating pressures in both the legs of this set of friction simulations are computed using Equation (7.1)

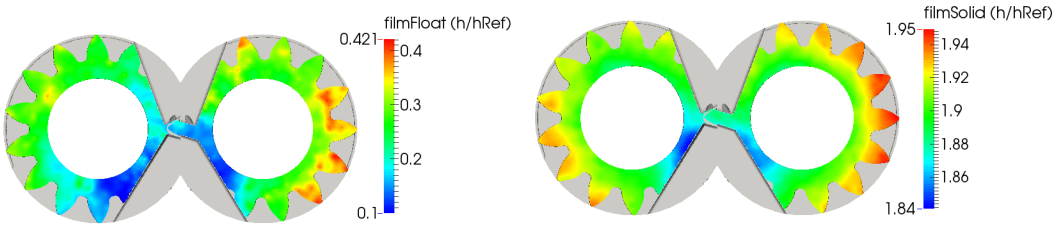

(a) (b)

Figure 7.6. Film thickness distributions in first leg of friction simulations at $n/n_{ref} = 0.55$ and $p/p_{ref} = 0.1$ in (a) Floating/Gears Interface (b) Solid/Gears Interface.

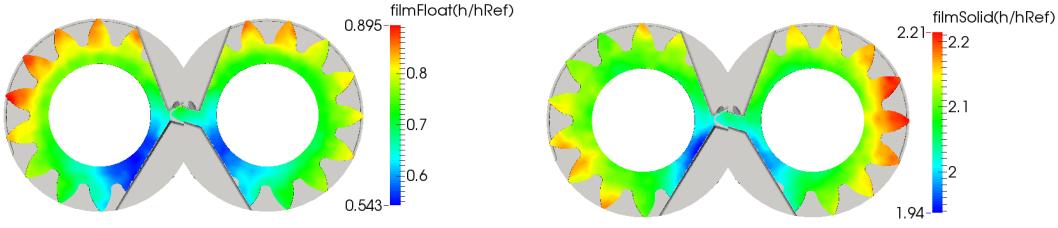

(a) (b)

Figure 7.7. Film thickness distributions in first leg of friction simulations at $n/n_{ref} = 0.55$ and $p/p_{ref} = 0.2$ in (a) Floating/Gears Interface (b) Solid/Gears Interface.

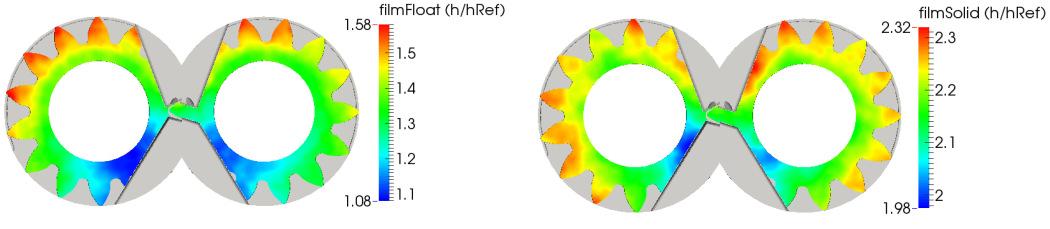

(a) (b)

Figure 7.8. Film thickness distributions in first leg of friction simulations at $n/n_{ref} = 0.55$ and $p/p_{ref} = 0.3$ in (a) Floating/Gears Interface (b) Solid/Gears Interface.

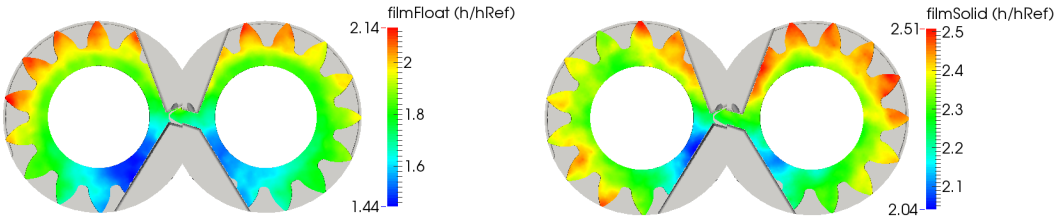

(a) (b)

Figure 7.9. Film thickness distributions in first leg of friction simulations at $n/n_{ref} = 0.55$ and $p/p_{ref} = 0.4$ in (a) Floating/Gears Interface (b) Solid/Gears Interface.

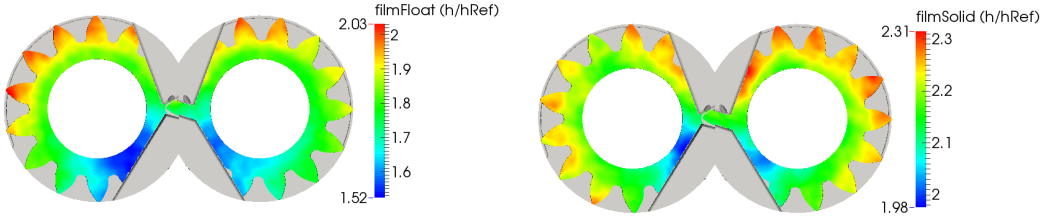

(a) (b)

Figure 7.10. Film thickness distributions in second leg of friction simulations at $n/n_{ref} = 0.55$ and $p/p_{ref} = 0.3$ in (a) Floating/Gears Interface (b) Solid/Gears Interface.

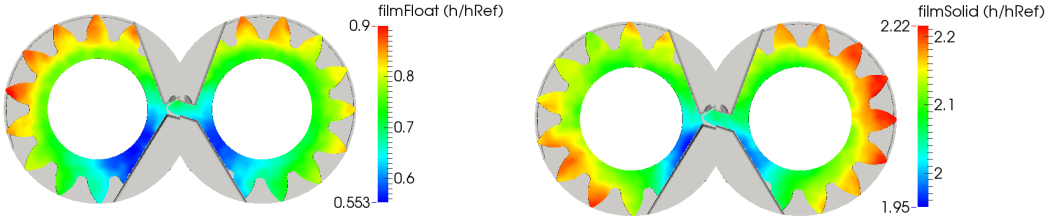

(a) (b)

Figure 7.11. Film thickness distributions in second leg of friction simulations at $n/n_{ref} = 0.55$ and $p/p_{ref} = 0.2$ in (a) Floating/Gears Interface (b) Solid/Gears Interface.

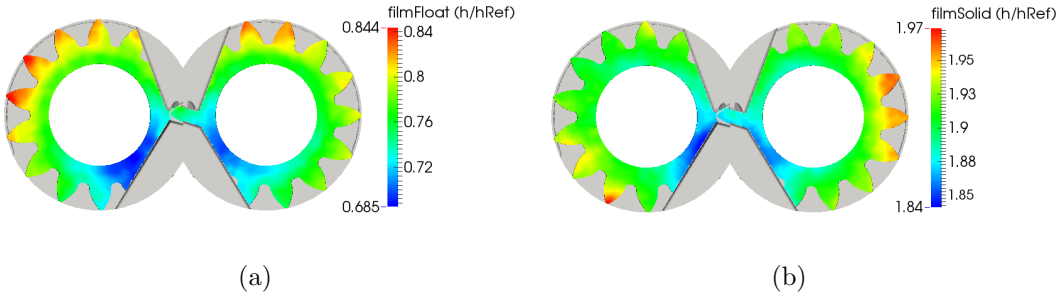

(a) (b)

Figure 7.12. Film thickness distributions in second leg of friction simulations at $n/n_{ref} = 0.55$ and $p/p_{ref} = 0.1$ in (a) Floating/Gears Interface (b) Solid/Gears Interface.

– (7.2) and the comparison plot is shown in Figure 7.13. It can be seen from this plot that the simulated positions of the floating bearing match closely with the experimental measurements. This result also implies that the lateral gap model (with frictional forces) can predict the hysteresis change in bearing position as the experiments progress over different operating pressures.

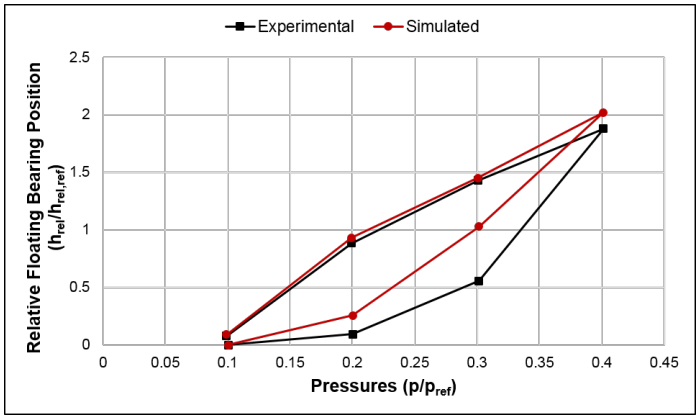

Figure 7.13. Comparison of experimental and simulated predictions of relative floating bearing position at $n/n_{ref} = 0.55$ set of friction simulations.

7.2.2 Simulations at a Constant Operating Speed of $n/n_{ref} = 0.78$

The second set of friction simulations was performed with operating speed of $n/n_{ref} = 0.78$ with the corresponding parameters and its values as listed in Table 7.2. The strategy of passing gap height information across successive runs similar to the first set of simulations is used. It must be noted that the value of the friction coefficient is changed for this set of simulations.

Table 7.2.
Parameters used in the simulations at operating speed of $n/n_{ref} = 0.78$.

Parameters	**Values**
Starting gap height	$h/h_{ref} = 0.33$
Starting pressure	$p/p_{ref} = 0.3$
Inlet pressure	$p/p_{ref} = 0.05$
Friction coefficient	0.009
Breakaway velocity	$v/v_{ref} = 0.32$
Outlet pressures	$p/p_{ref} = 0.3$, $p/p_{ref} = 0.5$, $p/p_{ref} = 0.8$
Operating speed	$n/n_{ref} = 0.78$

Figure 7.14 shows the comparison of predicted and experimental floating bearing positions at the second set of operating conditions. It can be seen that while the model captures the trend of the bearing movement, it has a higher deviation at higher pressures ($p/p_{ref} = 0.8$) which could be due to the possible increased deformation at sensor tracking location on the floating bearing during experiments.

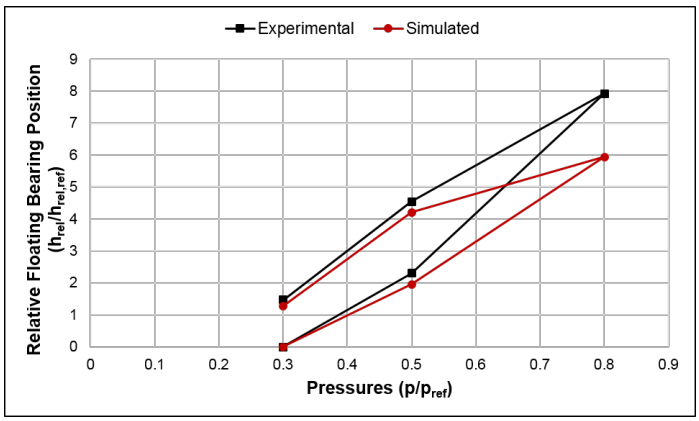

Figure 7.14. Comparison of experimental and simulated predictions of relative floating bearing position at $n/n_{ref} = 0.78$ set of friction simulations.

7.2.3 Simulations with Consistent Friction Model Parameters

To find an equivalent value of friction coefficient and breakaway velocity which work for both sets of simulations, efforts were taken to understand the behavior of the friction equation in Equation (3.41). Figure 7.15(a) and Figure 7.15(b) show the analytical variation of frictional force with velocities using independently varying values of μ_f and v_{brk} respectively. It can be understood from these plots that the frictional forces increase with increasing v_{brk} and decreasing μ_f. With this understanding, the objective was to determine the same values of μ_f and v_{brk} which predict closely the position of the floating bearing at both operating speeds presented in this section. It must also be noted here that the values of forces and the velocity have been normalized with $F_{ref} = \mathbf{O}(1000N)$ and $v_{ref} = \mathbf{O}(0.005m/s)$ respectively.

After investigating different values of friction model parameters, simulations at different pressures for both $n/n_{ref} = 0.55$ and $n/n_{ref} = 0.78$ are reported in this section with values of $\mu_f = 0.008$ and $v/v_{ref} = 1.29$. Figure 7.15(a) and Figure 7.15(b) show the relative bearing positions predicted by simulations and experiments with the updated model parameters at operating speeds of $n/n_{ref} = 0.55$ and $n/n_{ref} = 0.78$

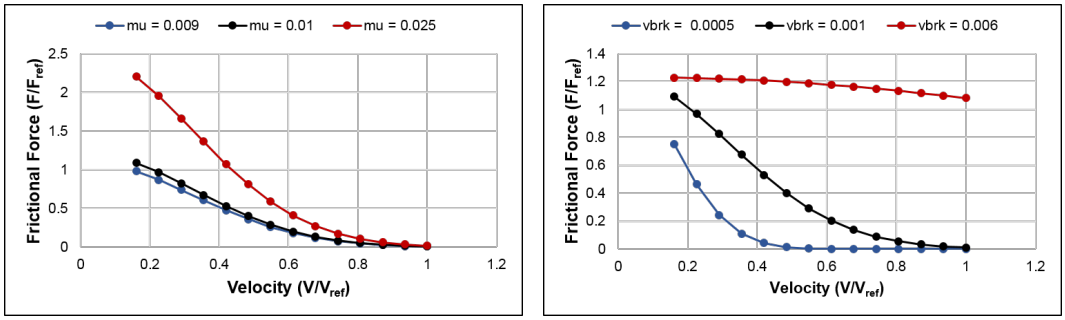

(a) (b)

Figure 7.15. (a) Analytical variation of frictional force with velocity for varying μ_f at $v_{brk}/v_{brk-ref} = 0.32$ (b) Analytical variation of frictional force with velocity for varying v_{brk} at $\mu_f = 0.01$.

respectively, while all other simulation parameters remain consistent with Table 7.1 and Table 7.2. It can be seen from these plots that while the predicted bearing position matches closely to experimental values at $n/n_{ref} = 0.55$, the deviation from experiments is quite significant at $n/n_{ref} = 0.78$, especially at the highest pressure of $p/p_{ref} = 0.8$. Reasons for this deviation could include possible higher deformation of the sensor affecting measurements at higher pressures and further investigation could be carried out in future to improve the current model predictions at these higher pressures. However, it is still important to note that the lateral gap model can predict the bearing position trends at these higher pressures and is quite reliable at lower pressures and lower speeds.

7.2.4 Effect of Varying Nose Pressures

A study has been conducted to understand the effect of varying pressures on the nose region found at the back of the floating bearing (highlighted in blue in Figure 7.2(a)) at different operating pressures and speeds. In all the cases presented in this section, the values of $\mu_f = 0.02$ and $v/v_{ref} = 0.32$ have been consistently used with a starting gap height of $h/h_{ref} = 0.67$. The tested operating conditions were

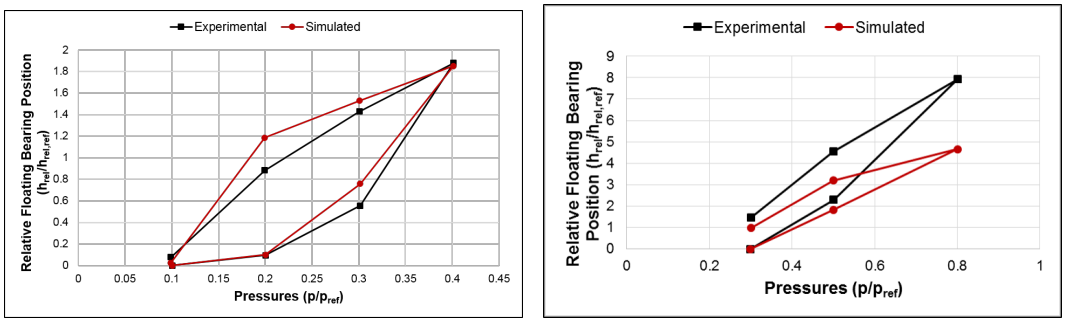

(a) (b)

Figure 7.16. (a) Comparison of experimental and simulated predictions of relative floating bearing position at $n/n_{ref} = 0.55$ set of friction simulations with $\mu_f = 0.008$ and $v/v_{ref} = 1.29$ (b) Comparison of experimental and simulated predictions of relative floating bearing position at $n/n_{ref} = 0.78$ set of friction simulations with $\mu_f = 0.008$ and $v/v_{ref} = 1.29$.

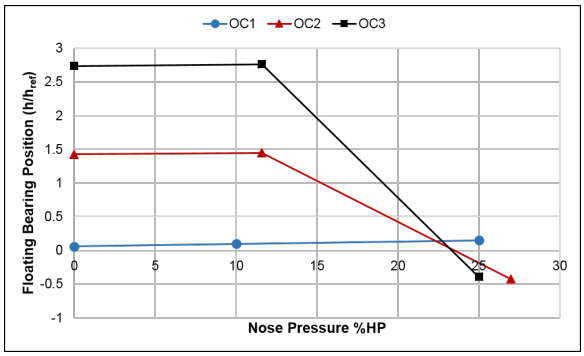

Figure 7.17. Effect of varying nose pressures on the position of the floating bearing at different operating conditions.

OC1 as $p/p_{ref} = 0.3$ outlet, $p/p_{ref} = 0.05$ inlet, $n/n_{ref} = 0.78$, OC2 as $p/p_{ref} = 0.1$ outlet, $p/p_{ref} = 0.037$ inlet, $n/n_{ref} = 0.55$ and OC3 as $p/p_{ref} = 0.05$ outlet, $p/p_{ref} = 0.0015$ inlet, $n/n_{ref} = 0.11$. The resulting floating bearing position evaluated at h_0 with the aforementioned three operating conditions with varying percentage of HP of nose pressure has been shown in Figure 7.17. It can be seen from the

plot that the nose pressure has minimal influence at higher pressures and higher speeds, while it dominantly influences the bearing position at lower speeds and lower pressures. This can be attributed to the fact that the radial forces are higher are higher operating pressures and speeds, implying the more dominant effect of the friction force as opposed to the nose pressure forces. Thus, the effect of frictional forces becomes a very important consideration that needs to be accounted for at these conditions and this reasoning is supported by this study.

7.3 Use of Multi-material Structural Solver

In this section, the FEM based structural solver explained in Section 3.3 is utilized to demonstrate the effect of a multi material floating bearing on the lubrication performance of the unit. The floating bearing in the reference EGM under study in this section is composed of two different materials as highlighted in Figure 7.18 with the help of green and red colors. The component highlighted in red corresponds to a lead bronze alloy, whereas the component of the bearing highlighted in green is made of aluminum.

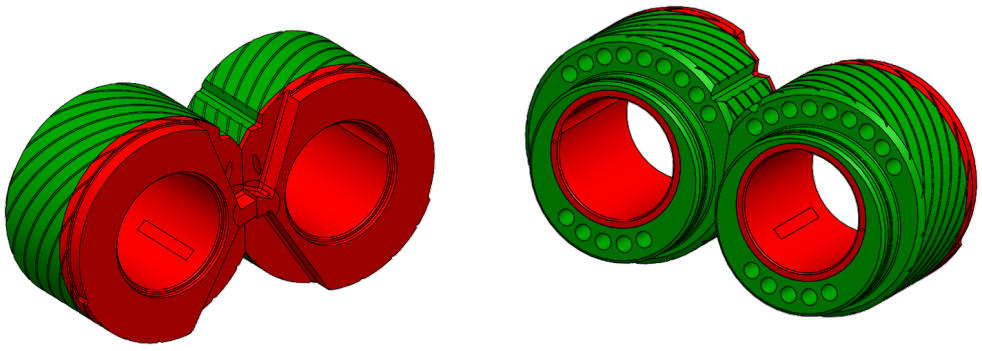

(a) (b)

Figure 7.18. Figure highlighting the distinct materials present in the floating bearing (a) Side of the floating bearing facing the gears (b) Side of the floating bearings facing away from the gears.

The friction model along with other simulation parameters used in the previous section is also used here to demonstrate the effect of using two materials on the floating bearing. It must be noted here that the solid bearing has its back face fixed as the structural constraint for evaluating deformation, while the LP side at the bottom of the floating bearing is used as a fixed constraint for the structural solver. The operating conditions used for presenting the simulation results in this section are $p/p_{ref} = 0.2$ outlet, $p/p_{ref} = 0.037$ inlet, $n/n_{ref} = 0.55$. While the material configuration shown in Figure 7.18 is used to demonstrate the multi-material solver results, the floating bearing with a full composition of lead bronze alloy is used to compare the results from the single material structural solver.

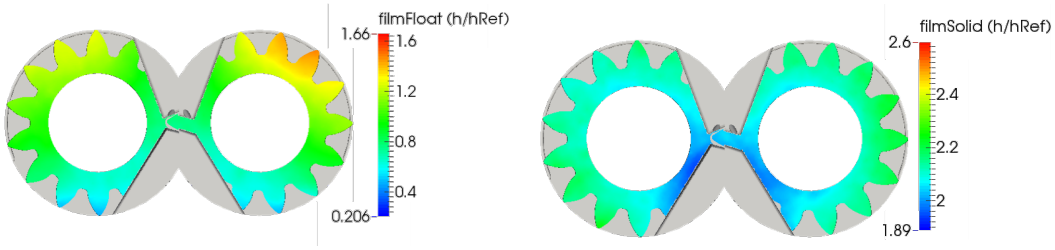

(a) (b)

Figure 7.19. Film thicknesses predictions using the single material solver in (a) Floating/Gears Interface (b) Solid/Gears Interface.

Figure 7.19 and Figure 7.20 show the simulation results obtained from the gap module when single and multi-material solvers with the aforementioned conditions, are used respectively. The plot legends used for both the figures are kept the same to highlight the differences between the two structural solvers. It can be observed that the magnitude and variation of deformation is higher for the multi-material solver than the single material solver. This can be attributed to the change in the outer component of the floating bearing which has lower density that causes higher deformation in the multi-material case. However, it should be noted that the spatial

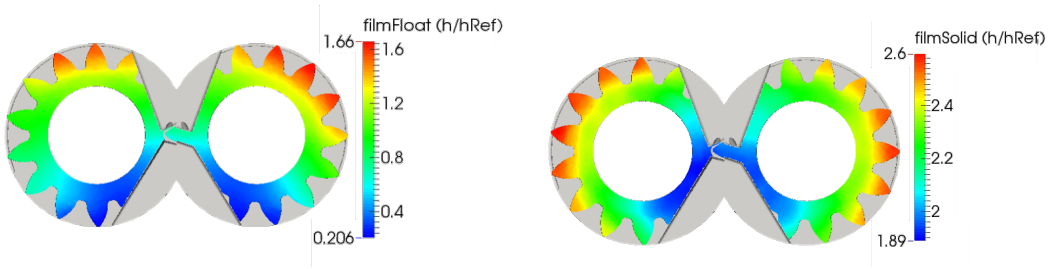

(a) (b)

Figure 7.20. Film thicknesses predictions using the multi-material solver in (a) Floating/Gears Interface (b) Solid/Gears Interface.

orientation of the deformation remains largely the same for both the cases, since it arises mainly from the application of the structural constraint to the solid component.

8. DESIGN OF LUBRICATING INTERFACES FOR WATER AS THE WORKING FLUID

In this chapter, design methodologies for improving the performance of the lateral lubricating interface in EGMs having a working fluid with low viscosity are presented. The reference fluid used for this purpose is tap water and the fluid properties used in the analysis are listed in Appendix A. The benefits of using water as a potential hydraulic working fluid were outlined in Chapter 1. However, owing to the fact that the viscosity of water is about 30 times lesser than that of oil, lubrication performance especially related to the load support in the interface, is quite challenging to design. Additionally, this section investigates the different approaches previously proposed to improve the performance of oil based EGMs such as optimizing the axial balance [92] and adding micro-surface shaping on the gears as outlined in Chapter 6. Furthermore, this chapter also explores the design of a prototype water hydraulic EGM to accommodate the different design challenges associated with using water as the main working fluid.

8.1 Results with Optimized Axial Balance

The reference EGM design Case 3 was chosen as the starting point for designing EGMs with water as the working hydraulic fluid. In order for the design to be compatible with water, aluminum alloy was chosen as the material for the lateral bushing, while gears were made of stainless steel. Two different operating conditions are used in all the studies presented in this section which includes one at a delivery pressure $p/p_{ref} = 0.8$ and shaft speed of 2000 rpm and the other reference condition at a pressure of $p/p_{ref} = 0.32$ and 1000 rpm speed. In this manner, fairly extreme operating conditions of high pressure with high speed and low pressure with low speed

are counted as references. Selection of such operating conditions have proven to be a reasonable assumption to analyze the axial balance of EGMs in [92].

The lateral gap interface of the reference EGM design was simulated using the mixed film model at the two reference operating conditions with tap water as the working fluid. The resulting film thickness plots are shown in Figure 8.1. No additional modifications were made to the existing design in the plots shown in Figure 8.1. It can be seen that low film thickness region is present near the suction side of the drive gear in both the conditions while higher gap heights can be found near the delivery side of the driven gear, which indicates increased tilt and non-uniformities in the gap. The higher gap heights encountered here also results in higher lateral leakages from the gap.

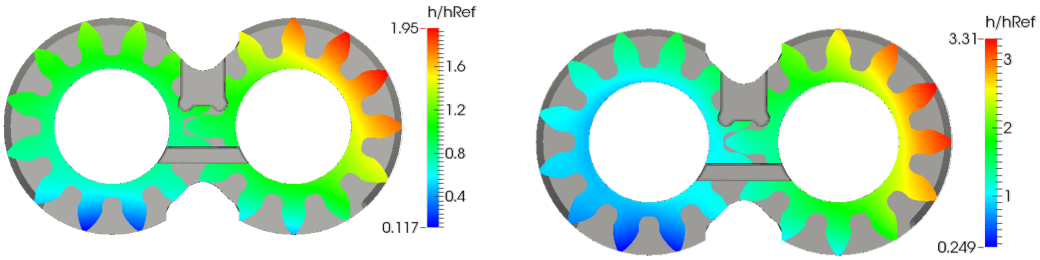

(a) (b)

Figure 8.1. Gap film thickness distribution with the nominal reference EGM design at (a) $p/p_{ref} = 0.32$, 1000 rpm (b) $p/p_{ref} = 0.8$, 2000 rpm.

The axial balance optimization procedure detailed in Section 2.3 was used to determine the optimal balance area of this design considering both the reference operating conditions. The objective functions used were the power losses in the gap due to shear stress and leakages as well as its non-uniformities. The results for film thickness from the optimization procedure are shown in Figure 8.2. The optimal design parameters were determined by the algorithm to be at $A/A_{ref} = 1.016$ and $Y/Y_{ref} = 1$ which implies that the optimal balance area is higher than the

corresponding starting area, while the point of application of the force remains the same for both the original and the optimal balance configurations.

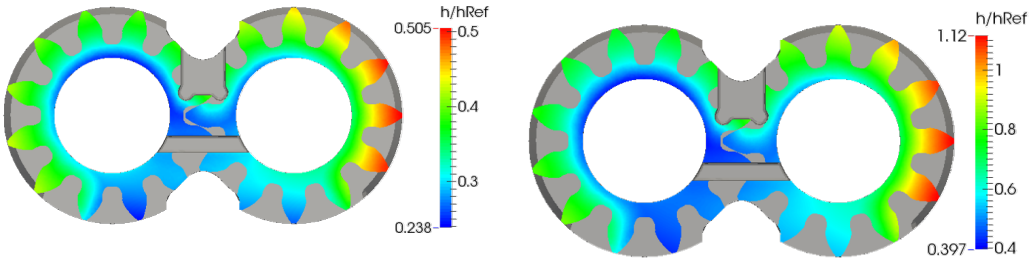

(a) (b)

Figure 8.2. Gap film thickness distribution with the optimal balance area design at (a) $p/p_{ref} = 0.32$, 1000 rpm (b) $p/p_{ref} = 0.8$, 2000 rpm.

It can be observed visually from nominal and optimal designs that the maximum gap height has reduced considerably (resulting in lower leakages) and the minimum gap height has increased, thereby avoiding any sharp contacts in the gap. It is more useful to look at the comparison between the power losses and the GNI, between the two designs at each of the operating conditions as shown in Table 8.1. It can be seen that there is a substantial reduction in the leakages and the non-uniformities for the optimal design.

Although, there is an increase in shear losses, the actual values of these losses are already low enough for water due to its low viscosity and thus, does not contribute much to the performance of the gap making it one of the advantages of using water as a hydraulic fluid. Furthermore, since this is a multi-objective problem, compromises between the different parameters need to be made while obtaining the optimal design.

However, the optimal balance area is not feasible to design on the existing lateral bushing since it is much higher than the reference area and thus, for designing a feasible balance, additional modifications such as surface shaping need to be introduced which is investigated in the subsequent sections of this chapter.

Table 8.1.
Comparison of different objective functions between optimal and reference balance area designs.

Operating Condition p/p_{ref}, rpm	**Power loss due to viscous shear**	**Power loss due to lateral leakages**	**Gap Non-Uniformity Index**
0.32, 1000	Increased by 57.71 %	Decreased by 97.73 %	Decreased by 55.22 %
0.8, 2000	Increased by 41.57 %	Decreased by 98.74 %	Decreased by 44.35 %

8.2 Results with Surface Shaping Effects

Since optimizing only the balance area of the reference design (which is primarily a change in the hydrostatic effects) is not sufficient to result in a feasible design of the lateral bushing for water-based EGMs, additional design parameters need to be considered. Micro-surface shaping effects such as wedged gears (detailed in Chapter 6) were shown to improve the performance of oil-based EGMs by introducing additional hydrodynamic effects and hence, this section investigates the possibilities of adding these effects to water-based EGMs.

8.2.1 Results from Adding Linear Wedge Shaping

A linear sloping wedge of 1 μm was added to the lateral surface of the gears in the reference design and the results obtained at the two reference operating conditions are shown in Figure 8.3. Furthermore, the axial balance procedure was applied on this design in a similar manner to Section 8.1 to obtain an optimal balance design with the wedge gears and the corresponding gap film thickness results in Figure 8.4.

The optimal design point was evaluated by the procedure at $A/A_{ref} = 1.006$ and $Y/Y_{ref} = 0.956$.

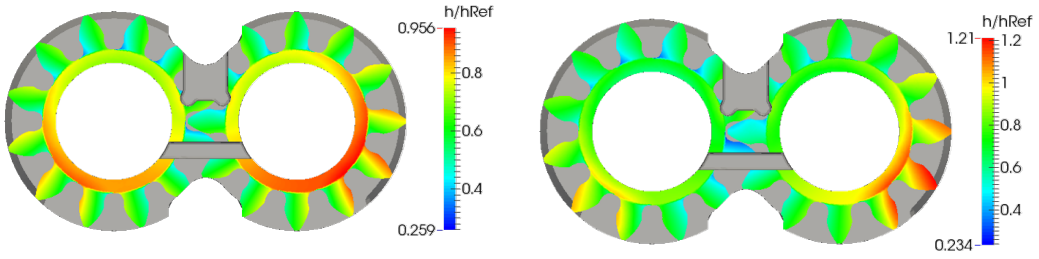

(a) (b)

Figure 8.3. Gap film thickness distribution with nominal balance area and 1 μm linear wedge design at (a) $p/p_{ref} = 0.32$, 1000 rpm (b) $p/p_{ref} = 0.8$, 2000 rpm.

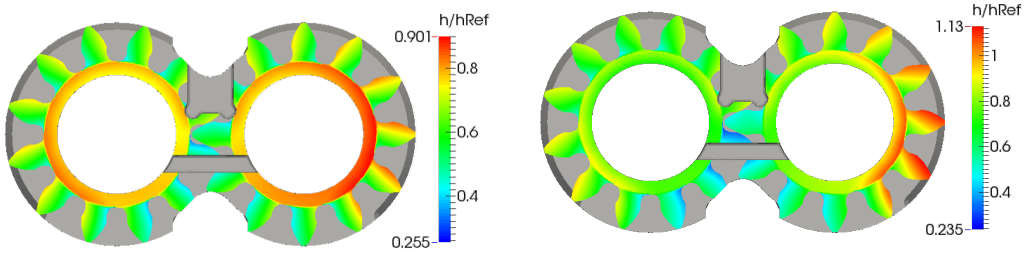

(a) (b)

Figure 8.4. Gap film thickness distribution with 1 μm linear wedge design and its optimal balance area at (a) $p/p_{ref} = 0.32$, 1000 rpm (b) $p/p_{ref} = 0.8$, 2000 rpm.

It can be seen from the gap film thickness distribution in Figure 8.3 that by just adding the wedge gears in the gap, the spatial orientation as well as the gap height values have improved with respect to the nominal reference design as shown earlier in Figure 8.1. Furthermore, optimizing the balance area for the design of the wedge

gears preserves most of the orientation of the gap (Figure 8.4) and is quite close to the reference design. Table 8.2 details the actual performance of both the designs with respect to each other and the optimal design with respect to the nominal design without the wedge gears.

Table 8.2.
Comparison of different performance parameters between wedge gears with nominal and optimal balance designs and with reference nominal EGM design.

Operating Condition, p/p_{ref}, rpm	**Comparison of wedge gears with optimal balance area wrt to wedge gears with nominal balance area**			**Comparison of wedge gears with optimal balance area wrt to wedge gears with nominal balance area**		
	Power loss due to viscous shear	Power loss due to lateral leakages	GNI	Power loss due to viscous shear	Power loss due to lateral leakages	GNI
0.32, 1000	Inc. by 57.71 %	Dec. by 97.73 %	Dec. by 55.22 %	Inc. by 43.17 %	Dec. by 76.25 %	Dec. by 49.16 %
0.8, 2000	Inc. by 41.57 %	Dec. by 98.74 %	Dec. by 44.35 %	Inc. by 49.30 %	Dec. by 97.15 %	Dec. by 42.98 %

It can be seen from Table 8.2 that only marginal differences in the objective functions exist between the two balance area designs of the wedge gears. However, the non-uniformities in the gap were reduced in the optimal design for the wedge gears when compared with its nominal balance. On the other hand, the optimal balance of the wedge gears shows a significant improvement over the reference EGM design

especially in terms of leakages and the non-uniformities in the gap and is quite close to the results obtained from just optimizing the balance area without any surface shaping effects Table 8.1. In spite of increase in the shear losses due to the lower viscosity of water, the performance of the lateral gap is still in the acceptable total operating efficiency.

Furthermore, the balance area obtained in this design is quite close to the nominal starting area which also makes the lateral bushing design feasible for practical implementation. Thus, it can be concluded from this study that a combination of design modifications using both hydrostatic and hydrodynamic effects can be used for improving the lubricating performance of water-based EGMs.

8.2.2 Results from Adding Step and Wedge Shaping

In Chapter 6, it was shown that adding a profile of a flat step followed by a linear wedge can help in further improving the lubrication performance of oil-based EGMs which was also supported with experimental results. A similar attempt has been employed for water-based EGMs in this section where a micro-surface shaping profile of 30 % step followed by 1 μm wedge is added to the lateral surface of the gears on its either side. The gap film thickness results after adding these shaping effects to the reference EGM design from both the reference operating conditions are shown in Figure 8.5. A comparison of the performance of this design against the previously analyzed designs having wedge gears (with optimal balance) and the reference design is presented in Table 8.3.

While the gap film thickness plots show similar trends to the wedged gears, the comparison with the power losses shown in Table 8.3 reveal significant differences between the two designs. Though the shear losses that are less significant for water have been reduced with the help of the step and wedge gears, there is an increase in non-uniformities and the leakages when compared with the wedge only gears. How-

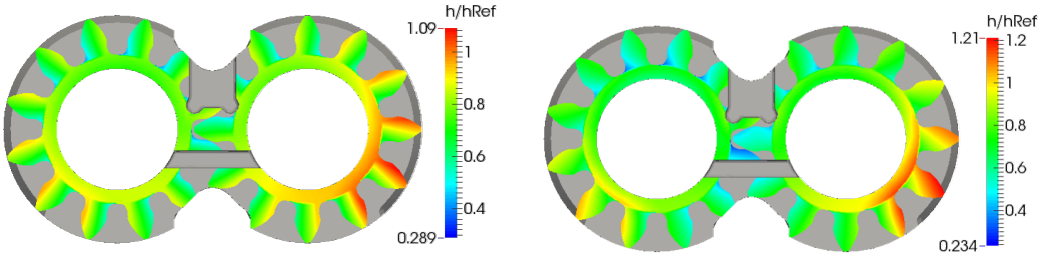

(a) (b)

Figure 8.5. Gap film thickness distribution with 30% step 1 μm wedge design at (a) $p/p_{ref} = 0.32$, 1000 rpm (b) $p/p_{ref} = 0.8$, 2000 rpm.

Table 8.3.
Comparison of the performance of the step and wedged gears with respect to the wedge gears (with optimal balance) and the reference design.

Operating Condition, p/p_{ref}, rpm	**Comparison of step wedge gears wrt to wedge gears with optimal balance area**			**Comparison of step wedge gears wrt to nominal design**		
	Power loss due to viscous shear	Power loss due to lateral leakages	GNI	Power loss due to viscous shear	Power loss due to lateral leakages	GNI
0.32, 1000	Inc. by 24.52 %	Inc. by 18.52 %	Inc. by 5.97 %	Inc. by 24.70 %	Dec. by 70.85 %	Dec. by 46.04 %
0.8, 2000	Dec. by 22.84 %	Inc. by 29.54 %	Inc. by 11.02 %	Inc. by 34.28 %	Dec. by 95.96 %	Dec. by 35.92 %

ever, the step and wedge gears still outperform the reference design by a considerable margin, which makes it a potential option for designing water-based EGMs.

The potentials of improving the lubrication performance in water based EGMs using different design modifications along with the necessary numerical tools has been established in this section. These principles can be potentially used in the practical implementation of a water hydraulic EGM operating at high pressures, which is yet to be achieved in the present state of the art work in this field.

8.3 Design of a Prototype Water Hydraulic EGM

The previous section presented methodologies for designing the lateral lubricating interface in water-based EGMs, which remains the most challenging design component. However, in order to validate these proposed designs experimentally, a prototype water hydraulic EGM needs to be developed since such an EGM is not available currently in the market. This is primarily owing to the reasons that the practical implementation of a high pressure water hydraulic EGM is difficult due to the challenging lubricating abilities of water. While the lateral lubricating gap could be potentially designed using the proposed methods in the previous sections, the radial gap (shown in Figure 1.4(a)) also needs to be well designed for a good and reliable operation of the unit. The low viscosity of water can potentially affect the radial gap especially at higher pressures, leading to increased radial leakages and wear on the EGM casing.

A novel radial compensation approach to improve the performance of the journal bearing interfaces and consequently, the radial gap by using external roller bearings has been proposed in this work. Due to the introduction of these additional bearings, certain features of a standard EGM (typically used for hydraulic oils) warrant design modifications. Thus, a prototype design of a water hydraulic EGM with goals of operating at high pressures is presented in this work. While practical realization of

this prototype has not been achieved in the current work, future directions of this research could include experimentally testing of this water hydraulic EGM.

8.3.1 Novel Radial Compensation Method

The journal bearing interfaces in many designs of currently available pressure compensated EGMs are responsible for the radial movement of the gears which results in the break-in of the casing as determined by the lubricant film in the journal bearings [22,86]. This break-in of the casing caused by the radial force F_r ensures sealing in the radial gap as shown in Figure 8.6 and this is controlled by the radial load support in the journal bearings. However, due to the low viscosity of water, radial load support which is sufficient enough to offer good radial sealing (as shown in Figure 8.6) may not be present. This radial sealing is quite challenging to design and thus, external load support due to roller bearings is introduced in the prototype water hydraulic EGM.

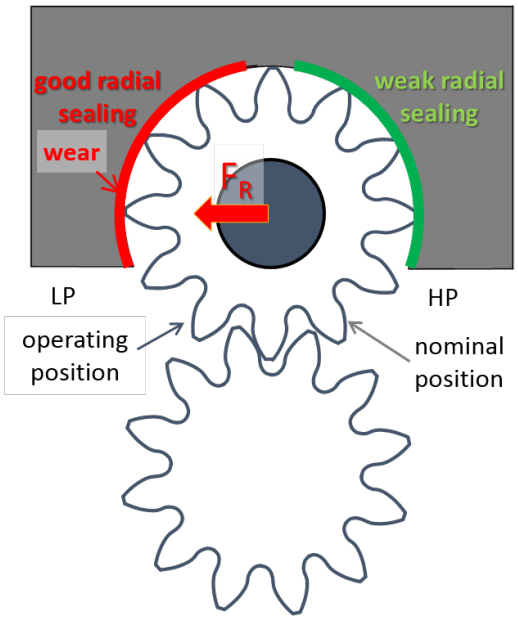

Figure 8.6. Illustration of radial sealing effects in EGMs.

A variety of roller bearings are available currently in the market and are designed for a wide range of applications [104]. However, in the present prototype, certain design constraints are applied on the selection of the roller bearings since they need to be compatible with operation of the EGM. The present application requires four roller bearings for all the interfaces in the unit, which must be compact enough to fit in the assembly of the EGM. Furthermore, the chosen roller bearing must be self-lubricated and not require any external supply of lubricant, since such a supply might affect the pumping operations. A radial load carry capacity of $\sim 15kN$ is desired for each roller bearing, since such radial loads are experienced in similar sized oil-based EGMs.

Grease operated needle roller bearings (as shown in Figure 8.7(a)) were chosen for this purpose due to their advantages of being one of the most compactly available roller bearings and their ability to offer high radial supports. The diameter to length ratio in most of the needle bearings is very small, in the range of 0.1 0.4 which contributes to their compact size and they require a low grade grease for their operation [104]. In Figure 8.7(b), it can be seen that the rollers directly act on the shaft raceways through the enclosed presence of grease and the entire unit is protected by an outer cage. The ends of the roller bearings are usually partially sealed to prevent the grease from escaping to the environment.

In the present prototype, four drawn cup type needle roller bearings with open ends (INA HK2020−2RS) are chosen. Each of the four roller bearings weighs 23 g with a basic static load rating of 20.1 kN and a dynamic load rating of 12.7 kN which fits the design requirement of the present EGM.

Since the proposed needle bearings are grease lubricated and open ended, it is necessary to avoid interference between the working grease and the main hydraulic fluid in the EGM. To overcome this problem, shaft seals are proposed to be present at the ends of all the roller bearings used in the unit. A typical shaft seal used in such roller bearings is shown in Figure 8.7(b), where an outer cylindrical covering is present to provide the required fit to the housing, along with an elastomer sealing lip which

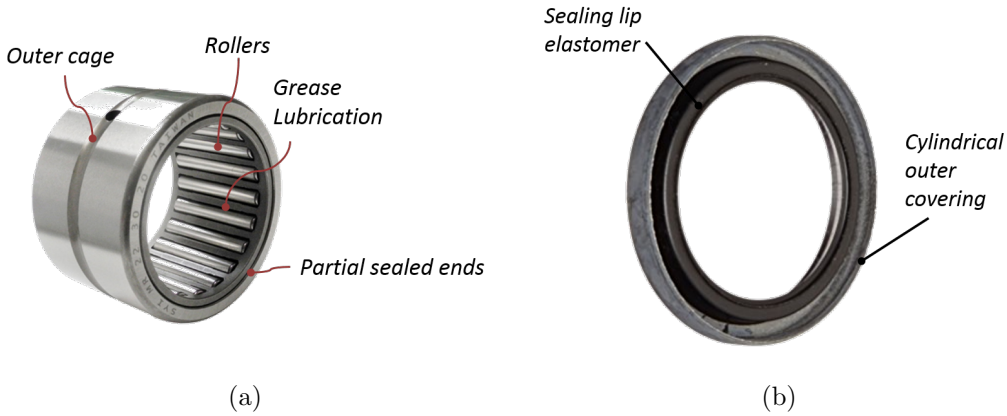

(a) (b)

Figure 8.7. Typical components illustrated in (a) Needle roller bearing (b) Shaft seal.

seals the lubricant dynamically in the bearing against leaking to the environment. In the present application, eight shaft seals from INA sealing rings for the needle roller bearings (INA SD20X26X4) are chosen to seal both the ends of each of the four needle roller bearings.

8.3.2 Design of the Radial Compensation Block

An external radial compensation method is designed with the help of the radial load support offered by the needle roller bearings for the water hydraulic prototype EGM. An external radial compensation block (as shown in Figure 8.8(b)) is designed with the roller bearings press fit into it along with the sealing rings at its ends. Grooves are added to the suction side of the block which are highlighted in blue in Figure 8.8(a) to ensure that the roller bearings are always operated at low pressures.

The design setup of the compensation block placed on either side of the gears along with the lateral plates for the axial pressure compensation is shown in Figure 8.9. As the radial block moves radially towards the low pressure side, the gears also move radially (as shown in Figure 8.6) to cause break-in wear on the casing. The amount of casing wear is controlled by the clearances allowed in the assembly of

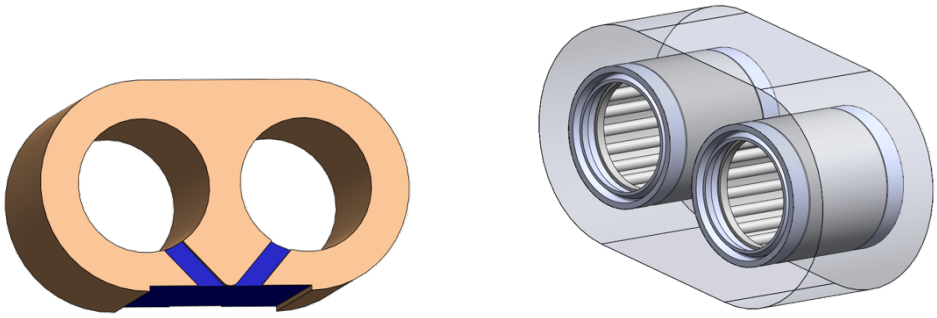

(a) (b)

Figure 8.8. Design of the radial compensation block (a) Front side of the block with LP grooves (b) Radial block with roller bearings and shaft seals.

the compensation block as well as the load support offered by the bearings. In order to prevent the radial compensation block from interfering with the axial pressure compensation by the lateral plates, the diameter of the block is made bigger and a three-piece design of the EGM is proposed which will be explained in the subsequent section.

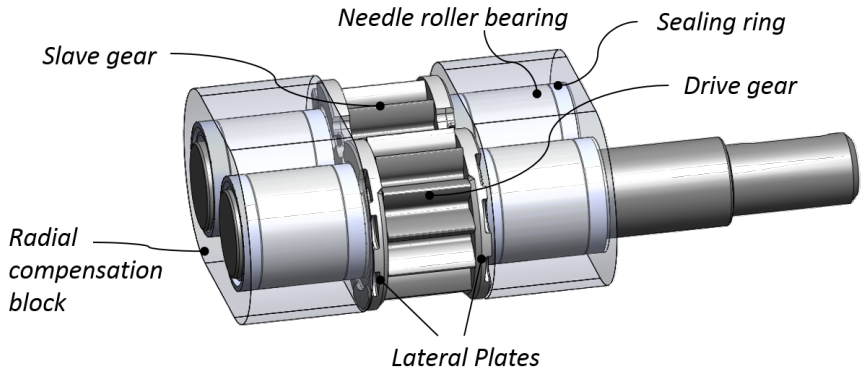

Figure 8.9. Setup of the components of the radial compensation block along with the gears and the lateral plates in the prototype EGM.

8.3.3 Elements of Prototype Water Hydraulic EGM

A three-piece EGM design is proposed for the present prototype, primarily in order to ensure that the radial and axial compensation methods do not interfere with each other. An overview of the proposed prototype along with its transparent view to reveal the arrangements of its different elements is shown in Figure 8.10.

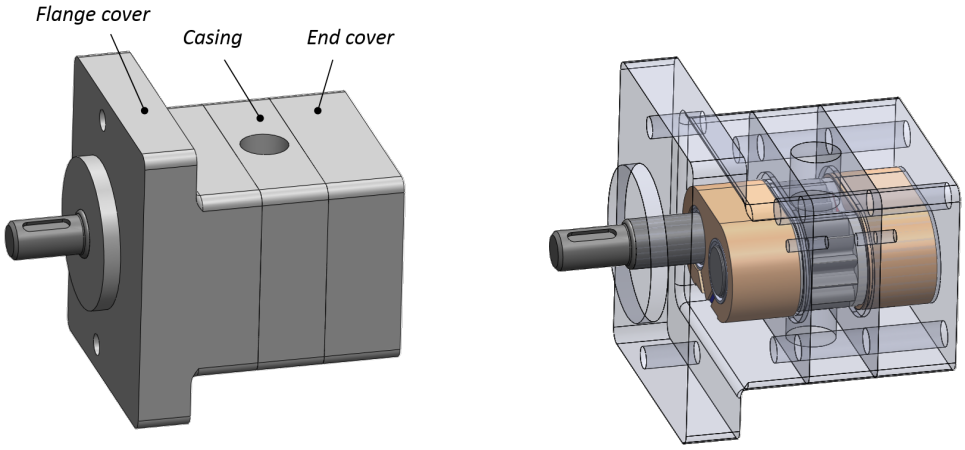

(a) (b)

Figure 8.10. Design of the radial compensation block (a) Front side of the block with LP grooves (b) Radial block with roller bearings and shaft seals.

In the proposed design, the flange and the end cover elements (shown in Figure 8.10) contain each of the radial compensation blocks while the casing encloses the gears and the lateral plates. The gears are proposed to be made of stainless steel while all the other components in the prototype are made of aluminum in order to be compatible with the pumping operation with water. The configuration of the assembly bolts used in the prototype can also be seen in the transparent view of the EGM in Figure 8.10. It must be noted that slots are present on the flange and end covers to offer a controlled break-in process by allowing radial movement of the block.

A pre-determined manufacturing clearance (in the order of microns) will have to be allowed between the block and its corresponding seat in the covers for this purpose.

9. COMPARISON OF LUBRICATION PERFORMANCE BETWEEN HIGH AND LOW VISCOUS FLUIDS

In this chapter, a comparison is drawn between the performances of the reference high and low viscous fluids in the lateral lubricating gaps in EGMs. ISO VG46 hydraulic mineral oil and water are the two reference working fluids considered in this study. First, this section presents an investigation into the effect of viscosity of the fluid on the lubrication regime in EGMs for these reference fluids. In addition, the impact of the strong change in viscosity of the fluid from oil to water, is evaluated in terms of their resulting power losses in the lateral gap and the contribution from the individual sources of these power losses.

9.1 Significance of Operating Parameters on the Lubrication Regime

In order to comprehensively account for the performance of the lubricating interface under operating parameters such as operating speed, operating pressure and properties of the working fluid, it is convenient to develop a reference study to understand these effects. Stribeck curves presented in Section 3.1.2 are a popular tool for understanding the influence of the aforementioned factors on the kind of lubrication regime at the interface especially for those present in journal bearings. The non-dimensional Hersey number defined in Equation (3.4) accounts for the influence of these factors on the friction encountered in the lubricating gap as shown in Figure 3.4. However, it is quite difficult to develop a similar theoretical tool for studying the lubricating interfaces in EGMs since an equivalent friction coefficient is rather challenging to define in this case. In the case of EGMs, the torque losses evaluated from the lateral gap model are the closest parameter representing the friction in the interface. In order to demonstrate the effects of the operating parameters including

the working fluid on the lubrication performance, a non-dimensional parameter for the viscous shear has been formulated as part of the current research work. This non-dimensional viscous shear (T_{nd-sh}) can be expressed the help of the following relationship which depends on the actual shear loss at an operating condition (τ_{sh}) having units of Pa, the dynamic viscosity of the fluid (μ) with units as $Pa-s$ and the operating speed of the EGM (ω) in rad/s,

$$T_{nd-sh} = \frac{\tau_{sh}}{\mu\omega} \tag{9.1}$$

The ideology behind the definition of a novel non-dimensional parameter exclusively for the case of EGMs was to compare the effect of friction in the lateral lubricating interface for working fluids with significantly different values of viscosities such as the reference fluids considered in this work. In such cases, the actual values of the torque losses under the influence of such varying values of viscosities are significantly different from each other and fail to make a fair comparison with the same operating parameters. Furthermore, the shear stresses in EGMs are primarily dependent on the Couette term rather than the Poiseuille term in the torque loss equation (Equation (3.27) (3.28)) as observed in literature [9]. Since the Couette term is dependent on the viscosity and the sliding velocity of the surfaces, this non-dimensional parameter closely represents the friction coefficient for the lubricating interface.

To demonstrate the relationship between this non-dimensional parameter and the various operating parameters, the reference EGM Case 1B was chosen for the simulations conducted in this study with the original balance area configuration on the bushing. The reference working fluids were chosen as ISO VG46 hydraulic oil (which was the same fluid used in the earlier results presented in this section) and water whose fluid properties are listed in Appendix A. It must be noted that the reference viscosities used to non-dimensionalize the shear stress were 0.0261 $Pa-s$ for the oil and 0.000891 $Pa-s$ for water, which are least two orders of magnitude different from each other. Simulations were performed using the mixed-TEHD model for both the fluids at different operating speeds ranging from 200 rpm to 2000 rpm and at operating pressures of 80 bar and 200 bar.

Figure 9.1(a) shows the plot of T_{nd-sh} against the operating speed for both oil and water at an operating pressure of 80 bar. It can be seen that this non-dimensional viscous shear is consistently higher for water than oil at all the tested operating speeds for this pressure. Although the actual values of the torque losses are lower for water owing to its much lower viscosity compared to oil, non-dimensionalizing the torque losses using the values of viscosity indicates that the chances of mixed lubrication regime initiating in water is higher than oil. This can also be supported from the percent contact area shown in Figure 9.1(b). The occurrences of contact in the case of water is higher than that of oil at all the tested conditions. It can be noted that the regions of contact area which indicate that the film thicknesses are in the order of surface roughness at each condition, supports the corresponding non-dimensional shear which is also higher with the increased contact area. This is owing to the reasoning that with increased low gap heights in the contact area, the corresponding viscous shear losses also increase. The increased instances of such contact conditions thus implies a strong presence of a mixed film regime that warrants the implementation of a mixed lubricating model in this work. It is also observed that the non-dimensional shear reduces at higher speeds and at higher viscosities indicating a close behavior to the original Stribeck curves shown earlier in Section 3.1.2.

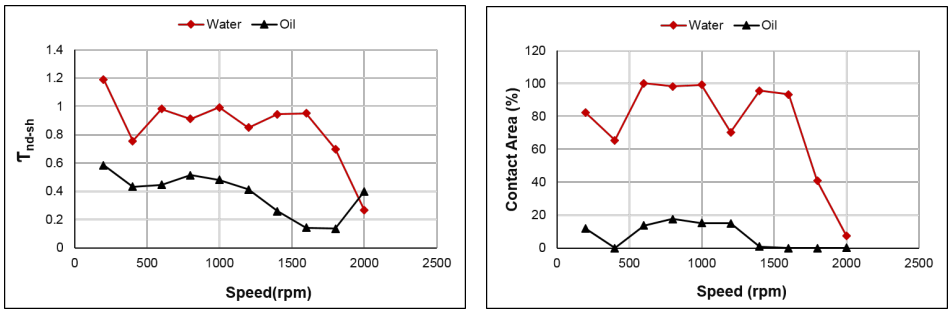

(a) (b)

Figure 9.1. Plots showing (a) The T_{nd-sh} against different operating speeds at 80 bar for water and oil and (b) The corresponding % of contact area (right) obtained from the mixed-TEHD model.

The aforementioned observations made using the T_{nd-sh} parameter can be further supported from the gap film thickness plots at selected operating conditions for the sake of brevity. Figure 9.2 shows the gap film thickness plots for water and oil at the same operating pressure of 80 bar and a speed of 800 rpm. The film thicknesses encountered in the case of oil is higher than that of water. Consequently, the contact conditions are encountered more frequently in the case of water and this fact is also confirmed from the contact area plots in Figure 9.1(b).

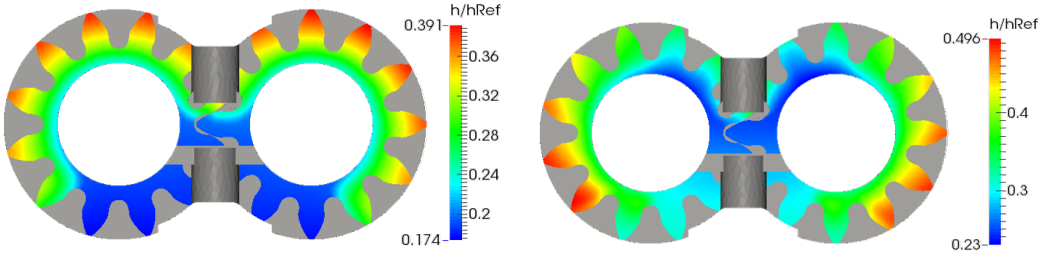

(a) (b)

Figure 9.2. Gap film thickness distribution predicted by the mixed lubrication model at 80bar, 800 rpm for (a) Water (b) Oil.

Figure 9.3 shows the distribution of gap heights at the same operating speed of 80 bar and a higher speed of 2000 rpm. It can be observed from the plots that the gap heights encountered in these cases are higher than at the lower speed operating condition shown in Figure 9.2 and thus, the instances of contact are also lower.

However, it is interesting to note here that the hydrodynamic tilt for water is stronger in this case as it can be noted from the increased non-uniformities in the gap between high and low gap heights seen in Figure 9.3. Although this method can be useful in predicting the lubrication regime in the EGMs, in order to design the lateral gap to yield a good operating performance, torque losses remain insufficient to be solely used a fitness function for determining the lubricating performance. Additional considerations such as the objective functions defined earlier in Section 2.3

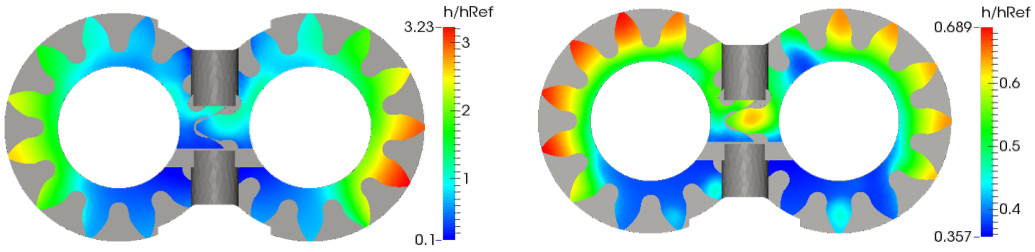

(a) (b)

Figure 9.3. Gap film thickness distribution predicted by the mixed lubrication model at 80bar, 2000 rpm for (a) Water (b) Oil.

need to be included to comprehensively design the lubricating gap for a challenging working fluid such as water due to its lower viscosity. Thus, a comprehensive mixed-lubrication model which can account for the complex physical phenomena occurring in the lubricating gap along with the optimization procedure detailed in Section 2.3 is essential to design an especially challenging lubricating interface with water.

A similar comparison between water and oil using T_{nd-sh} has been made at a higher operating pressure of 200 bar and is shown in Figure 9.4(a). In this case, higher values of the non-dimensional viscous shear are observed for both the fluids at all the tested operating conditions. The corresponding contact area are also similar to each other except at higher speeds, where oil has a lower value of T_{nd-sh} than water. This observation directly correlates with the trends predicted by the Stribeck curve where at higher pressures/loads, there is a greater tendency towards mixed lubrication while there is an opposing trend with increasing speeds. Thus, the attempt of this study to create a numerical formulation to predict the influence of the operating parameters of an EGM on its torque losses in a similar manner to the popular Stribeck curves is achieved. In order to develop a more robust formulation, future work could possibly include studying an extensive range of operating conditions, in addition to various working fluids.

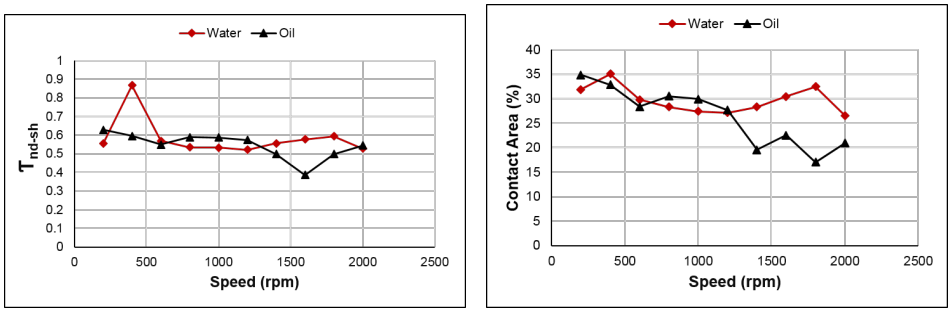

(a) (b)

Figure 9.4. Plots showing (a) The T_{nd-sh} against different operating speeds at 200 bar for water and oil and (b) The corresponding % of contact area (right) obtained from the mixed-TEHD model.

9.2 Comparison of Power Losses in the Lateral Gap between the Reference Working Fluids

Although the study in the previous section formulated a tool for identifying the lubrication regime in the lateral gap for the two reference fluids with varying viscosities, a comparison of their lubrication performance remains to be investigated. One of the most optimal indicators of the performance in the lubricating interface is the resulting power losses in the gap, which are especially significant in the case of a positive displacement machines. In this section, the power losses obtained with both oil and water are analyzed along with their respective contributions from the individual sources of the losses in the lateral gap, namely the viscous shear and the leakages. It must be noted here that the viscosity of the fluid is present in both the equations for viscous shear and leakages as shown in Equations (3.27), (3.28) and (3.33). It can be deduced from these equations that the shear losses decrease with increasing viscosity while the leakages display an opposing trend of increasing with increasing viscosity. The aim of this section is to highlight and investigate this behavior of the power losses in the gap with changing viscosity of the working fluids.

The reference EGM design (displacement 11.2 cc/rev) used in this analysis for both the fluids is identical to the one used in Chapter 8 for presenting the simulation results for water. The analysis considers the nominal reference design with oil since it is a working EGM design available currently in the market. For water, the cases presented in Chapter 8 for the nominal reference design, the design with 1 μm linear wedge and the design with 30% step followed by 1 μm wedge are considered. Thus, this analysis can also relate the improvements suggested for water-based EGMs (in Chapter 8) with a known oil-based EGM design. Two reference operating conditions of delivery pressure $p/p_{ref} = 0.32$, shaft speed of 1000 rpm and delivery pressure $p/p_{ref} = 0.8$, shaft speed of 2000 rpm are chosen for the analysis in this study. The mixed-TEHD model detailed in Chapter 3 is used for all the simulations presented in this section.

Figure 9.5 shows the total power losses evaluated in the lateral gap at the two reference operating conditions for the nominal reference EGM design with oil and all the selected designs with water. It can be seen that the total power losses from the nominal design with water has the highest value at the operating condition of $p/p_{ref} = 0.8$ and shaft speed of 2000 rpm. However, it can be seen that the total power losses (in units of Watts) evaluated with both the water-based EGM designs with linear wedge and the step wedge are lesser than that obtained with oil. This implies that a properly designed water hydraulic EGM will have a further improved performance over more common oil-based EGMs.

The contribution of leakages and viscous shear to the total power loss in the lateral gap from both the fluids is an important analysis in this study owing to the fact that the viscosity of fluid strongly influences both these sources of power losses. Figure 9.6 shows the percentage contribution from these individual sources of power losses to the total loss in the lateral gap at both the reference operating conditions (Figures 9.6(a) and 9.6(b) respectively) for the selected EGM cases with both oil and water.

While the dominant contribution for the oil based EGM is from the viscous shear (95 %) at both the reference operating conditions, such a dominating effect of the

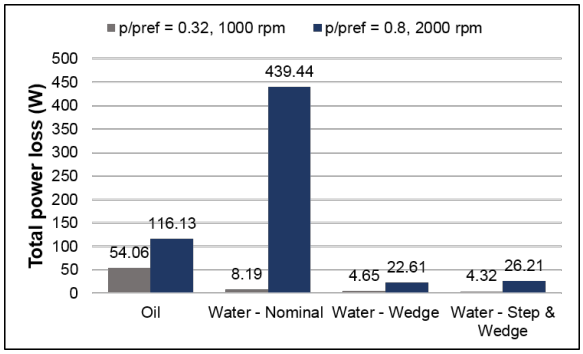

Figure 9.5. Comparison between the nominal design with oil and the elected designs with water for (a) Total power loss (b) % of the lateral leakages with respect to the total flow rate.

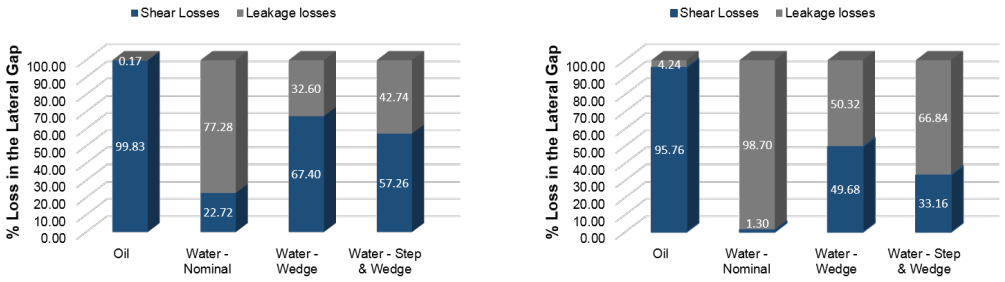

(a) (b)

Figure 9.6. % Contribution of the viscous shear and the leakages to the total power loss in the gap for the nominal design with oil and the selected designs with water at (a) $p/p_{ref} = 0.32$, 1000 rpm (b) $p/p_{ref} = 0.8$, 2000 rpm.

shear losses is not found for the case of water. This is primarily due to the fact that the low viscosity of water decreases the magnitude of the viscous shear losses and increases the magnitude of the leakages with respect to oil. This is largely observed in the nominal design for water where the leakages are the most dominating source of power losses. However, with the modified designs for water with the surface shaping, the percentage contribution from both the sources of power losses remains close to

each other. Although contribution due to the leakages is higher for water than oil, the magnitude of the total power losses in the lateral gap is lesser as seen in Figure 9.5.

Since contribution from the leakages is quite significant for the case of water, it is useful to compare the actual magnitude of these lateral leakages between the two fluids. In this analysis, the magnitude of the lateral leakages from each of the cases is divided by the expected theoretical flow rate at the operating condition which is given by the following equation, where V_i is the displacement and n is the operating speed,

$$\eta_{lat} = \frac{Q_{lat}}{V_i n} * 100 \tag{9.2}$$

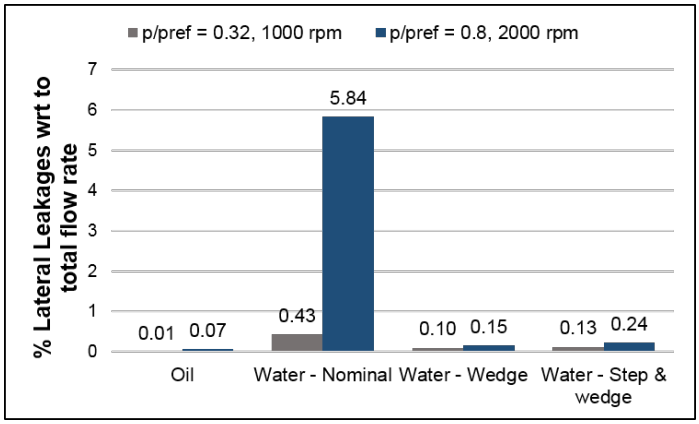

Figure 9.7. Plot of the percentage lateral leakages with respect to the total flow rate at the reference operating conditions for selected EGM designs with oil and water.

The resulting percentage of lateral leakages with respect to the total expected flow rate (η_{lat}) is plotted in Figure 9.7 for the two reference operating conditions and the EGM designs with oil and water. It can be observed from this plot that the leakages encountered in the nominal design for water are orders of magnitude higher than that for oil. Although there is an increase in the lateral leakages for the modified designs with water when compared to oil, the fraction of lateral leakages with respect to the total flow rate is still reasonable enough for a reliable operation of the proposed EGM

design with water, which is one of the most significant conclusions of the present study.

10. SUMMARY AND CONCLUSIONS

In the present research, advanced approaches for designing and analyzing lubricating interfaces in EGMs were presented. The developed methodologies in this work were also shown to be applicable for working fluids with an extended range of viscosities which included reference fluids with very different values of viscosities namely, mineral oil, kerosene jet fluid and water. Important contributions were made to develop novel modeling approached to understand the physical behavior of lateral lubricating interfaces in EGMs and in utilizing the developed model to propose design solutions for more energy efficient EGMs. This included the formulation and development of a comprehensive mixed-TEHD model, where the effects of surface topography on the lubricating interface were coupled with the fluid, structural and thermal phenomena in the lateral gap. The mixed lubrication model was based on a stochastic approach towards solving an average flow Reynolds equation for partial lubrication in the lateral gaps. The model also accounts for the influence of surface asperities in sharing the pressure loads in the interface by implementing an elastic plastic deformation model for the asperities. The resulting contribution of the surface features to the force equilibrium on the lateral bushing as well as the heat dissipation in the interface was also accounted in the mixed film model. The mixed film model in this study was formulated in a manner that it reduces to a full film lubrication model whenever the conditions for mixed lubrication are not present in the gap. Studies to verify the stochastic assumptions of the mixed film model with the help of a commercially available EGM were also completed in this research.

Owing to the fact that oil-based EGMs are relatively more common, the mixed-TEHD model was first used to study the performance of these units at severe operating conditions of pressure as well as speed. It was shown that the performance of the mixed film model was more stable and reliable than the full film model at dominant

mixed lubrication conditions. A study on the contribution of the surface asperities in sharing the lubrication load was also presented with the help of the mixed-TEHD model.

To test the modeling techniques proposed in this work, four different pump designs with varying working fluids were used as reference cases that are representative of the broad applications of EGMs. Case 1A and Case 1B were symmetrically balance EGMs commercially available in the market for conventional hydraulic applications, using oil as the main working fluid, while Case 2 was an asymmetrically balanced aerospace fuel injection pump with low viscous kerosene as the working fluid and Case 3 was the symmetrically balanced water-based EGM with novel design modifications proposed in this work. Case 1B EGM design was used to validate the mixed-TEHD model using experimentally measured torque losses. It was shown that at certain operating conditions which had dominant mixed film characteristics, the mixed film model predicted torque losses closer to the measured values than the full film model. A complementary contribution of this work includes developing a novel numerical approach to predicting the torque losses in an EGM that does not depend on experimental data. In order to further prove the fidelity of the mixed lubrication model, leakages predicted by the model were also validated using direct drain leakages measurements in a specially made prototype for this purpose. Since the sensitivity of the leakages with the film thickness predictions is quite high, the improved prediction by the mixed lubrication model over the full film model was demonstrated using the leakage measurements at higher pressures, where increased chances of mixed lubrication were found. A unique contribution to the current state of the art was achieved in experimentally investigating the influence of varying surface roughness of the lateral bushings on the performance of the unit using measured leakages and it was observed that higher surface roughness contributed to higher leakages from the lateral gap. The corresponding predictions from the mixed-TEHD model simulations also agreed well with the experimental findings for surface roughness effects.

Contributions to the modeling of lubricating gaps presented in this research also include the implementation of a mass conserving cavitation algorithm with coupled fluid and structural solvers of the lateral gap model. It was shown that with the improved cavitation model, the predictions of pressure distribution in the lubricating interface are numerically more stable without the presence of any unrealistic pressure peaks and valleys in the domain. It was also observed that when this cavitation model was integrated with the mixed film model, the resultant simulations offer higher fidelity in the predictions while carefully accounting for the physical effects of the surface features at low film thickness conditions.

In addition, efforts were made in this work to extend the capabilities of the current structural solver to accommodate lateral bushings and gears with more than a single material. This has been accomplished using an automated algorithm with the help of a FEM based commercial software and has been demonstrated by using the reference Case 2.

The current research also presents a novel approach to account for the influence of frictional forces between the lateral bushing and the casing on the lubrication performance of a EGM. This phenomenon typically become substantial with bearing block type of bushings where the bushing width has considerable contact with the housing of the EGM as opposed to plate type designs of lateral bushing. A translational frictional force model was incorporated with the force balance module of the lateral gap model to consider the effect of radial forces acting on the bushing on its axial micro-motion and consequently on the lubrication performance of the unit. Case 2 EGM design was used to demonstrate that the addition of the friction force model could capture the "hysteresis behavior of the lateral bushing movements observed in experimental measurements, thereby substantiating the importance of considering radial forces on the lateral bushing to predict such a phenomenon. Thus, the ability of this work to predict this unique behavior of lubricating interfaces was exhibited on a gear pump with low viscosity working fluid and high operating speeds and pressure, which was one of the chief research goals of this dissertation.

Experimental validation of adding a micro surface shaped wedge gears to reduce the torque losses in EGMs was presented in this work using Case 1B EGM with flat step and wedge profile on the gears. The EGM with the wedge gears prototype was experimentally proven to exhibit a higher hydro-mechanical efficiency over a nominal reference design.

With the help of an advanced numerical model for the lateral gaps and previously developed design techniques to improve the lubrication performance of EGMs, a more challenging Case 3 EGM with water as its working fluid was considered. It was shown in simulations that a properly designed micro surface wedge shape on the gears along with an optimal axial balance design solution for the lateral bushing can considerably improve the lubrication performance even for a low viscous fluid like water which causes challenges in the lubricating ability of the interface. To test the claims of the proposed design modifications for water as a working hydraulic fluid, a novel EGM prototype was conceived and proposed as Case 3 design. This prototype is representative of a first of its kind water-based EGM, which has the potential to operate at high pressures (up to 200 bar). Additionally, a novel radial compensation approach using external needle roller bearings was developed and integrated into the design of the water based prototype. Future research directions of this work will potentially include the experimental testing of this prototype to practically realize the feasibility of water in high pressure hydraulic applications.

A comparison of the lubrication performance between water and oil on the same EGM prototype was also presented in this work. It was shown through simulations, that the total power losses (due to both leakages and viscous shear) obtained by using water as the working fluid were lower than that of oil when the suggested design modifications for water-based EGMs were applied. Despite these modifications, the leakages obtained from water were higher than oil, the actual magnitudes of these leakages were still shown to be reasonably small enough for an efficient operation of the EGM. It was also shown in these studies that the viscous shear losses were the dominating part of the losses for oil-based EGMs and such a trend of losses was not

observed for the water units. Moreover, a new approach for estimating the effect of viscosity of the fluid on the lubrication regime was formulated and presented using the developed mixed-TEHD film model.

The formulated techniques and numerical tools in this research has an immense potential to drive the design of reliable EGMs which can consistently perform at a wide range of operating conditions as well as with different working fluids. However, a more complex approach of using actual surface measurements of gears and lateral bushings can be used for predicting the influence of surface features on the lubrication performance in EGMs. Future potential work in this domain could include developing an advanced model for the journal bearing interfaces incorporating the effects of its surfaces as well as including the deformation of the EGM casing in predicting the performance of the lubricating interfaces.

10.1 Publications

The following are the various publications that reflect different aspects of research which was achieved during the course of this PhD dissertation. This includes four journal publications, three conference publications and one of which included a best paper award, a patent application and three conference talks.

10.1.1 Journal Publications

- Thiagarajan, D., Dhar, S. and Vacca, A. (2015). A Novel Fluid Structure Interaction-EHD Model and Optimization Procedure for an Asymmetrical Axially Balanced External Gear Machine. *Tribology Transactions*,58(2), 274-287.

- Thiagarajan, D., Dhar, S., and Vacca, A. (2017). Improvement of Lubrication Performance in External Gear Machines through Micro-surface Wedged Gears. *Tribology Transactions*, 60(2), 337-348.

- Thiagarajan, D., Vacca, A., (2017). Mixed Lubrication Effects in the Lateral Lubricating Interfaces of External Gear Machines: Modelling and Experimental Validation. *Energies*, 10(1), 111.

- Thiagarajan, D., Vacca, A., and Watkins, S. (2018). On Predicting the Lubrication Performance of External Gear Pumps for Aerospace Fuel Injection Applications. *Mechanical Systems and Signal Processing* (submitted)

10.1.2 Conference Publications

- Thiagarajan, D. and Vacca, A. (2014). A Numerical Procedure to Design the Optimal Axial Balance of Pressure Compensated Gear Machines. *8th ASME/FPNI PhD Symposium on Fluid Power*, Lappeenranta, Finland.

- Thiagarajan, D. and Vacca, A. (2016). Investigation of Hydro-mechanical Losses in External Gear Machines: Simulation and Experimental Validation. *2016 Bath/ASME Symposium on Fluid Power and Motion Control*, Bath, UK.

- Thiagarajan, D., Bratto, A. and Vacca, A. (2017), Influence of Surface Roughness Effects in Lubricating Interfaces of External Gear Machines, *2017 Bath/ASME Symposium on Fluid Power and Motion Control*, Sarasota, USA. **Best paper award**.

- Thiagarajan, D. and Vacca, A. (2018). Modeling of the Lateral Lubricating Interfaces in External Gear Machines Considering the Effects of Cavitation. (under preparation) *2018 Bath/ASME Symposium on Fluid Power and Motion Control*, Bath, UK.

10.1.3 Patent

Vacca, A., Thiagarajan, D. and Dhar, S. (2016). Pressure Compensated External Gear Machines, *Provisional Patent Filed* (Application number: 62/296,670), *United States Patent and Trademark Office*.

10.1.4 Conference Talks

- Thiagarajan, D. and Vacca, A. (2014). A novel optimization procedure for designing the axial balance in EGMs using a FSI-EHD model for the internal lubricating gap flow, *2014 STLE Tribology Frontiers Conference*, Chicago, USA.
- Thiagarajan, D. and Vacca, A. (2015). Investigation of micro surface shaping effects for improving the lubrication performance of water based high pressure EGMs, *Fluid Power Innovation and Research Conference*, Chicago, USA.
- Thiagarajan, D. and Vacca, A. (2016). Formulation and Validation of a Mixed-TEHD model for the Lateral Lubricating Interfaces in External Gear Machines, *2016 STLE Tribology Frontiers Conference*, Chicago, USA.

REFERENCES

REFERENCES

[1] E. Koc. An investigation into the performance of hydrostatically loaded end-plates in high pressure pumps and motors: movable plate design. *Wear*, 141(2):249–265, 1 1991.

[2] E. Koç. Bearing misalignment effects on the hydrostatic and hydrodynamic behaviour of gears in fixed clearance end plates. *Wear*, 173(1-2):199–206, 4 1994.

[3] E. Koç, K. Ng, and C. Hooke. An analysis of the lubrication mechanisms of the bush-type bearings in high pressure pumps. *Tribology International*, 30(8):553–560, 7 1997.

[4] M. Borghi, M. Milani, F. Paltrinieri, and B. Zardin. Studying the Axial Balance of External Gear Pumps. 11 2005.

[5] M. Zecchi, A. Vacca, and P. Casoli. Numerical analysis of the lubricating gap between bushes and gears in external spur gear machines. In *Fluid Power and Motion Control 2010*, pages 397–416, 2010.

[6] D. Morgridge, H. P. Evans, R. W. Snidle, and M. K. Yates. A Study of Seal Lubrication in an Aerospace Fuel Gear Pump Including the Effects of Roughness and Mixed Lubrication. *Tribology Transactions*, 54(4):657–665, 7 2011.

[7] S. Dhar and A. Vacca. A fluid structure interactionEHD model of the lubricating gaps in external gear machines: Formulation and validation. *Tribology International*, 62:78–90, 6 2013.

[8] S. Dhar and A. Vacca. A novel FSI-thermal coupled TEHD model and experimental validation through indirect film thickness measurements for the lubricating interface in external gear machines. *Tribology International*, 82(PA):162–175, 2015.

[9] S. Dhar. *A Study of Fluid Structure and Thermal Interactions in the Lubricating Interface Between Gears and Lateral Bushes in External Gear Machines*. PhD thesis, Purdue University, West Lafayette, USA, 2014.

[10] D. Thiagarajan, S. Dhar, and A. Vacca. A Novel Fluid Structure Interaction-EHD Model and Optimization Procedure for an Asymmetrical Axially Balanced External Gear Machine. *Tribology Transactions*, 58(2):274–287, 3 2015.

[11] S. Dhar and A. Vacca. A novel CFD Axial motion coupled model for the axial balance of lateral bushings in external gear machines. *Simulation Modelling Practice and Theory*, 26:60–76, 8 2012.

[12] T. E. Beacham. High-Pressure Gear Pumps. *Proceedings of the Institution of Mechanical Engineers*, 155(1):417–452, 6 1946.

[13] C. Bonacini and R. Carra. A numerical method to evaluate axial force in pressure compensated gears pumps and motors. In *Proceedings of the 43rd Annual Meeting, National Conference on Fluid Power, NFPA, Chicago, Illinois*, pages 403–408, 1988.

[14] N. D. Manring and S. B. Kasaragadda. The Theoretical Flow Ripple of an External Gear Pump. *Journal of dynamic systems, measurement, and control*, 125(3):396–404, 2003.

[15] P. Casoli, A. Vacca, and G. L. Berta. Optimization of Relevant Design Parameters of External Gear Pumps. In *Proceedings of the JFPS International Symposium on Fluid Power*, pages 277–282. The Japan Fluid Power System Society, 2008.

[16] J. Ivantysyn and M. Ivantysynova. *Hydrostatic pumps and motors*. Academic Books International, New Delhi, 2001.

[17] S. Falfari and P. Pelloni. Setup of a 1D Model for Simulating Dynamic Behaviour of External Gear Pumps. In *SAE 2007 Commercial Vehicle Engineering Congress and Exhibition*, 10 2007.

[18] B. Zardin and M. Borghi. Modelling and simulation of external gear pumps and motors. In *5th FPNI PhD Symposium*, Cracow, Poland, 2008.

[19] W. Wustmann, S. Helduser, and W. Wimmer. CFD-simulation of the reversing process in external gear pumps. In *6th International Fluid Power Conference - IFK 2008*, pages 455–468, TU Dresden, Germany, 2008.

[20] Simerics Inc. Pumplinx: External Gear Pumps at https://www.simerics.com/.

[21] D. del Campo, R. Castilla, G. Raush, P. Gamez-Montero, and E. Codina. Pressure effects on the performance of external gear pumps under cavitation. *Proceedings of the Institution of Mechanical Engineers, Part C: Journal of Mechanical Engineering Science*, 228(16):2925–2937, 11 2014.

[22] A. Vacca and M. Guidetti. Modelling and experimental validation of external spur gear machines for fluid power applications. *Simulation Modelling Practice and Theory*, 19(9):2007–2031, 2011.

[23] B. J. Hamrock, S. R. Schmid, and B. O. Jacobson. *Fundamentals of fluid film lubrication*. CRC Press, 2004.

[24] H. A. Spikes and A. V. Olver. Basics of mixed lubrication. *Lubrication Science*, 16(1):1–28, 2003.

[25] D. Zhu and Y.-Z. Hu. A Computer Program Package for the Prediction of EHL and Mixed Lubrication Characteristics, Friction, Subsurface Stresses and Flash Temperatures Based on Measured 3-D Surface Roughness. *Tribology Transactions*, 44(3):383–390, 2001.

[26] Y.-Z. Hu and D. Zhu. A Full Numerical Solution to the Mixed Lubrication in Point Contacts. *Journal of Tribology*, 122(1):1, 2000.

[27] D. Dowson. A generalized Reynolds equation for fluid-film lubrication. *International Journal of Mechanical Sciences*, 4(2):159–170, 3 1962.

[28] F. Shi and Q. J. Wang. A Mixed-TEHD Model for Journal-Bearing Conformal ContactsPart I: Model Formulation and Approximation of Heat Transfer Considering Asperity Contact. *Journal of Tribology*, 120(2):198, 4 1998.

[29] Q. J. Wang, F. Shi, and S. C. Lee. A Mixed-TEHD Model for Journal-Bearing Conformal ContactPart II: Contact, Film Thickness, and Performance Analyses. *Journal of Tribology*, 120(2):206, 4 1998.

[30] Y. Wang, C. Zhang, Q. J. Wang, and C. Lin. A mixed-TEHD analysis and experiment of journal bearings under severe operating conditions. *Tribology International*, 35(6):395–407, 2002.

[31] M. B. Dobrica, M. Fillon, and P. Maspeyrot. Mixed Elastohydrodynamic Lubrication in a Partial Journal BearingComparison Between Deterministic and Stochastic Models. *Journal of Tribology*, 128(4):778, 2006.

[32] Q. J. Wang, D. Zhu, H. S. Cheng, T. Yu, X. Jiang, and S. Liu. Mixed Lubrication Analyses by a Macro-Micro Approach and a Full-Scale Mixed EHL Model. *Journal of Tribology*, 126(1):81, 2004.

[33] H. P. Evans and R. W. Snidle. The future of engineering tribology in concentrated contacts. *Proceedings of the Institution of Mechanical Engineers, Part C: Journal of Mechanical Engineering Science*, 223(12):2939–2948, 12 2009.

[34] A. de Kraker, R. A. van Ostayen, and D. J. Rixen. Calculation of Stribeck curves for (water) lubricated journal bearings. *Tribology International*, 40(3):459–469, 3 2007.

[35] N. Patir and H. S. Cheng. An Average Flow Model for Determining Effects of Three-Dimensional Roughness on Partial Hydrodynamic Lubrication. *Journal of Lubrication Technology*, 100(1):12, 1978.

[36] N. Patir and H. S. Cheng. Application of Average Flow Model to Lubrication Between Rough Sliding Surfaces.pdf. *Transactions of the ASME*, 101(April):220–230, 1979.

[37] C. Wu and L. Zheng. An Average Reynolds Equation for Partial Film Lubrication With a Contact Factor. *Journal of Tribology*, 111(1):188, 1 1989.

[38] F. Meng, Q. J. Wang, D. Hua, and S. Liu. A Simple Method to Calculate Contact Factor Used in Average Flow Model. *Journal of Tribology*, 132(2):24505, 2010.

[39] J. A. Greenwood and J. B. P. Williamson. Contact of Nominally Flat Surfaces. *Proceedings of the Royal Society A: Mathematical, Physical and Engineering Sciences*, 295(1442):300–319, 12 1966.

[40] F. P. Bowden and D. Tabor. *The friction and lubrication of solids*. Clarendon Press, 2001.

[41] K. L. Johnson. *Contact mechanics*. Cambridge University Press, 1987.

[42] S. R. Harp and R. F. Salant. An Average Flow Model of Rough Surface Lubrication With Inter-Asperity Cavitation. *Journal of Tribology*, 123(1):134, 2001.

[43] N. Ren and S. C. Lee. The effects of surface roughness and topography on the contact behavior of elastic bodies. *Journal of tribology*, 116(4):804–810, 1994.

[44] S. C. Lee and N. Ren. Behavior of Elastic-Plastic Rough Surface Contacts as Affected by Surface Topography, Load, and Material Hardness. *Tribology Transactions*, 39(1):67–74, 1996.

[45] A. Martini, D. Zhu, and Q. Wang. Friction Reduction in Mixed Lubrication. *Tribology Letters*, 28(2):139–147, 2007.

[46] A. Yamaguchi and H. Matsuoka. A Mixed Lubrication Model Applicable to Bearing/Seal Parts of Hydraulic Equipment. *Journal of Tribology*, 114(1):116, 1992.

[47] T. Kazama and A. Yamaguchi. Optimum design of bearing and seal parts for hydraulic equipment. *Wear*, 161:161–171, 1993.

[48] T. Kazama. Numerical Simulation of a Slipper Model for Water Hydraulic Pumps/Motors in Mixed Lubrication. *Proceedings of the JFPS International Symposium on Fluid Power*, 2005:509–514, 2005.

[49] S. Hashemi, A. Kroker, L. Bobach, and D. Bartel. Tribology International Multibody dynamics of pivot slipper pad thrust bearing in axial piston machines incorporating thermal elastohydrodynamics and mixed lubrication model. 96:57–76, 2016.

[50] Y. Fang and M. Shirakashi. Between the Piston and Cylinder in Hydraulic Piston Pump-Motor. (94):0–5, 1995.

[51] D. S. Wegner, F. Löschner, S. Gels, and H. Murrenhoff. Validation of the physical effect implementation in a simulation model for the cylinder block / valve plate contact supported by experimental investigations. In *Proceedings of the 10th International Fluid Power Conference*, pages 269–282, Dresden, Germany, 2016.

[52] T. Kazama and A. Yamaguchi. Experiment on Mixed Lubrication of Hydrostatic Thrust Bearings for Hydraulic Equipment. *Journal of Tribology*, 117(3):399, 7 1995.

[53] M. Pelosi and M. Ivantysynova. Heat Transfer and Thermal Elastic Deformation Analysis on the Piston/Cylinder Interface of Axial Piston Machines. *Journal of Tribology*, 134(4):041101, 10 2012.

[54] M. Zecchi. *A novel fluid structure interaction and thermal model to predict the cylinder block/valve plate interface performance in swash plate type axial piston machines*. PhD thesis, Purdue University, West Lafayette, USA, 2013.

[55] A. Schenk and M. Ivantysynova. A Transient Thermoelastohydrodynamic Lubrication Model for the Slipper/Swashplate in Axial Piston Machines. *Journal of Tribology*, 137(3):031701, 2015.

[56] T. Nanbu, N. Ren, Y. Yasuda, D. Zhu, and Q. J. Wang. Micro-Textures in Concentrated Conformal-Contact Lubrication: Effects of Texture Bottom Shape and Surface Relative Motion. *Tribology Letters*, 29(3):241–252, 2008.

[57] X. Wang, K. Kato, and K. Adachi. The Lubrication Effect of Micro-Pits on Parallel Sliding Faces of SiC in Water. *Tribology Transactions*, 45(3):294–301, 1 2002.

[58] I. Křupka and M. Hartl. The effect of surface texturing on thin EHD lubrication films. *Tribology International*, 40(7):1100–1110, 7 2007.

[59] Q. J. Wang and D. Zhu. Virtual Texturing: Modeling the Performance of Lubricated Contacts of Engineered Surfaces. *Journal of Tribology*, 127(4):722, 2005.

[60] M. Ivantysynova and J. Baker. Power Loss in the Lubricating Gap between Cylinder Block and Valve Plate of Swash Plate Type Axial Piston Machines. *International Journal of Fluid Power*, 10(2):29–43, 1 2009.

[61] A. M. Wondergem and M. Ivantysynova. The impact of the surface shape of the piston on power losses. In *Proc. 8th FPNI Ph. D Symposium on Fluid Power, American Society of Mechanical Engineers*, Lappeenranta, Finland, 2014.

[62] R. Chacon and M. Ivantysynova. An Investigation of the Impact of Micro Surface on the Cylinder Block/Valve Plate Interface Performance. In *8th FPNI Ph. D Symposium on Fluid Power*, Lappeenranta, Finland, 2014.

[63] W. Wilson. Rotary pump theory. *Transactions of ASME*, 68(371), 1946.

[64] W. Wilson. Performance criteria for positive displacement pumps and fluid motors. In *ASME semi-annual meeting*, pages paper No. 48–SA–14, 1948.

[65] W. Schlösser. Mathematical model for displacement pumps and motors. *Hydraulic power transmission*, pages 252–257, 1961.

[66] J. Thoma. Mathematical models and effective performance of hydrostatic machines and transmissions. *Hydraulic and Pneumatic Power*, pages 642–651, 1969.

[67] A. Hibi and T. Ichikawa. Torque performance of hydraulic motor in whole operating condition from start to maximum speed and its mathematical model. In *4th International Fluid Power Symposium*, United Kingdom, 1975.

[68] G. Zarotti and N. Nervegna. Pump efficiencies approximation and modelling. In *6th International Fluid Power Symposium*, pages 145–164, Cambridge, United Kingdom, 1981.

[69] D. McCandlish and R. E. Dorey. The Mathematical Modelling of Hydrostatic Pumps and Motors. *Proceedings of the Institution of Mechanical Engineers, Part B: Management and engineering manufacture*, 198(3):165–174, 8 1984.

[70] P. W. Michael, H. Khalid, and T. Wanke. An Investigation of External Gear Pump Efficiency and Stribeck Values. In *SAE Technical Paper*, 9 2012.

[71] N. D. Manring. Measuring Pump Efficiency: Uncertainty Considerations. *Journal of Energy Resources Technology*, 127(4):280, 12 2005.

[72] G. C. Knight. Water hydraulics Application of water-based fluids to hydraulic systems. *Tribology International*, 10(2):105–108, 1977.

[73] G. Krutz and P. Chua. Water hydraulicstheory and applications 2004. *Workshop on Water Hydraulics*, pages 1–33, 2004.

[74] H. A. Spikes. Wear and fatigue problems in connection with water-based hydraulic fluids. *Journal of Synthetic Lubrication*, 4(2):115–135, 22 1987.

[75] A. Ravikiran and B. Bai. Water-lubricated sliding of Al2O3 against steel. *Wear*, 171(1-2):33–39, 1994.

[76] B. C. Majumdar, R. Pai, and D. J. Hargreaves. Analysis of water-lubricated journal bearings with multiple axial grooves. *Proceedings of the Institution of Mechanical Engineers, Part J: Journal of Engineering Tribology*, 218(2):135–146, 2004.

[77] X. Wang and A. Yamaguchi. Characteristics of hydrostatic bearing/seal parts for water hydraulic pumps and motors. Part 1: Experiment and theory. *Tribology International*, 35(7):425–433, 7 2002.

[78] S. Nie, G. Huang, and Y. Li. Tribological study on hydrostatic slipper bearing with annular orifice damper for water hydraulic axial piston motor. *Tribology International*, 39(11):1342–1354, 2006.

[79] M. Rokala. *Analysis of Slipper Structures in Water Hydraulic Axial Piston Pumps*. PhD thesis, Tampere University of Technology, 2012.

[80] M. H. Ernst and M. Ivantysynova. Micro Surface Shaping for the High-Pressure Operation of Piston Machines With Water as a Working Fluid. In *2015 ASME/BATH Symposium on Fluid Power and Motion Control*, Chicago, IL, USA, 2015.

[81] *LMS Imagine SA (2015) Hydraulic library, User Manual, Rev 14*. 2015.

[82] OpenFOAM : https://www.openfoam.com/.

[83] Gsl. GNU Scientific Library. (March):1–501, 2007.

[84] Y. G. Shah, A. Vacca, S. Dabiri, and E. Frosina. A fast lumped parameter approach for the prediction of both aeration and cavitation in Gerotor pumps. *Meccanica*, pages 1–17, 7 2017.

[85] A. Vacca, S. Dhar, and T. Opperwall. A Coupled Lumped Parameter and CFD Approach for Modeling External Gear Machines. In *SICFP2011 The Twelfth Scandinavian International Conference on Fluid Power*, 2011.

[86] M. Pellegri and A. Vacca. A CFD-Radial Motion Coupled Model for the Evaluation of the Features of Journal Bearings in External Gear Machines. In *Proceedings of the ASME/BATH 2015 Symposium on Fluid Power and Motion Control*, pages 12–14, Chicago, IL, USA, 2015.

[87] X. Zhao and A. Vacca. Numerical analysis of theoretical flow in external gear machines. *Mechanism and Machine Theory*, 108:41–56, 2017.

[88] Ansys Academic Research Mechanical, Release 15.0.

[89] National Institute of Standards and Technology. Thermophysical Properties of Fluid Systems : http://webbook.nist.gov/chemistry/fluid/. Technical report.

[90] H. Jasak and H. G. Weller. Application of the finite volume method and unstructured meshes to linear elasticity. *International Journal for Numerical Methods in Engineering*, 48(2):267–287, 5 2000.

[91] D. Thiagarajan and A. Vacca. A Numerical Procedure to Design the Optimal Axial Balance of Pressure Compensated Gear Machines. In *8th ASME/FPNI Ph. D. Symposium on Fluid Power*, Lappeenranta, Finland, 2014.

[92] D. Thiagarajan. A numerical procedure to design the optimal axial balance in external gear machines and its potential in formulating novel efficient design solutions. *Masters thesis, Purdue University, USA*, 2014.

[93] R. Booser. *CRC handbook of lubrication: theory and practice of tribology*. CRC Press, 1984.

[94] Q. J. Wang and Y.-W. Chung, editors. *Encyclopedia of Tribology*. Springer US, Boston, MA, 2013.

[95] J. Magnusson. Numerical analysis of the lubricant gap in external gear pumps considering micro level surface features. *Masters thesis, Chalmers University, Sweden*, 2011.

[96] H. W. Swift. The Stability of Lubricating Films in Journal Bearings. *Minutes of the Proceedings of the Institution of Civil Engineers*, 233(1932):267–288, 1 1932.

[97] P. Payvar and R. F. Salant. A Computational Method for Cavitation in a Wavy Mechanical Seal. *Journal of Tribology*, 114(1):199–204, 1992.

[98] F. Shi and R. F. Salant. A Mixed Soft Elastohydrodynamic Lubrication Model With Interasperity Cavitation and Surface Shear Deformation. *Journal of Tribology*, 122(1):308, 2000.

[99] B. Armstrong and C. de Wit. *Friction Modeling and Compensation*. CRC Press, 1995 edition.

[100] ISO4391-1983. *Hydraulic fluid power pumps, motors and integral transmissions parameter definitions and letter symbols*. USA, 1983.

[101] E. Buckingham. *Analytical mechanics of gears*. Courier Corporation, 1988.

[102] G. Toet. The determination of the theoretical stroke volume of hydrostatic displacement pumps and motors from volumetric measurements. *Hydraulic Pneumatic Power*, (16):346–356, 1970.

[103] ISO8426. *International Standard : Hydraulic fluid power positive displacement pumps and motors determination of derived capacity*. 1988.

[104] M. M. Khonsari and R. E. Booser. An engineering guide for bearing selection. *Tribology & lubrication technology*, 60(2):26, 2004.

APPENDICES

A. DERIVATION OF FLUID PROPERTIES FOR LOW VISCOUS WORKING FLUID − WATER

In this section, the formulation of the fluid properties model used in the work for water is presented. Tap water properties at various temperatures and pressures can be obtained from the NIST database [89] and a polynomial regression model for water can be empirically developed with the help of these experimental measurements.

A.1 Density relationship with pressure and temperature

It has been assumed in the present derivation that the density has a quadratic relationship with pressure and temperature, which can be assumed in the form of the following equation,

$$\rho(p,T) = \rho_0[1 + c_T(T - T_0) + c_{TT}(T - T_0)^2 + c_p(p - p_0) + c_{pp}(p - p_0)^2] \quad \text{(A.1)}$$

The reference values for pressure and temperature in this derivation have been assumed at $p_0 = 1$ bar and $T_0 = 30°$C. The empirical coefficients in Equation (A.1) can be obtained from the experimental measurements for tap water provided in [89] which are also represented in the graphs in Figure A.1. It can be noted from the figure that the variation of density with pressure and temperature follows a second order relationship as previously assumed in the generalized equation Equation (A.1). The empirical coefficients c_T,c_{TT},c_p,c_{pp} can be determined with the help of least squares curve fitting and regression analysis from the experimental curves in Figure A.1 and substituting them in the generalized equation Equation (A.1). Setting a value of the reference pressure $\rho_0 = 997.19\ kg/m^3$, the following equation for the density variation with respect to pressure and temperature can be obtained,

$$\rho(p,T) = 997.19[1 - 0.0744(T - T_0) - 0.0047(T - T_0)^2 + 0.0404(p - p_0) - 2e^{-6}(p - p_0)^2] \quad \text{(A.2)}$$

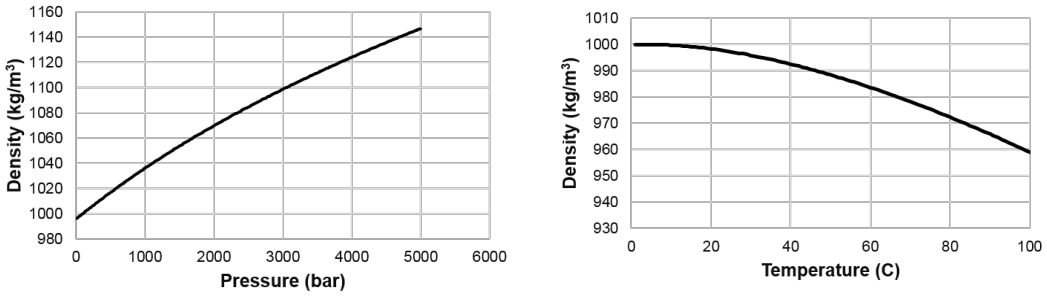

(a) (b)

Figure A.1. Variation of density of water with (a) Pressure and (b) Temperature.

The density obtained from Equation (A.2) will have the units of kg/m^3 while the input pressure is in *bar* and the input temperature will have units of °C.

A.2 Viscosity relationship with pressure and temperature

Similar to the derivation of the density relationship, the following quadratic relationship is assumed for the variation of viscosity with pressure and temperature where the reference temperature and pressure are at $p_0 = 1$ bar and $T_0 = 30°\text{C}$,

$$\mu(p,T) = \mu_0[1 + d_T(T - T_0) + d_{TT}(T - T_0)^2 + d_p(p - p_0) + d_{pp}(p - p_0)^2] \quad \text{(A.3)}$$

The empirical coefficients d_T,d_{TT},d_p,d_{pp} can be obtained by means of least square fitting of the experimental curves for variation of viscosity with pressure and temperature shown in Figure 91. It can be seen from the plots that the quadratic relationship between viscosity and pressure as well as temperature is a reasonable assumption.

After determining the empirical coefficients, with a reference viscosity of $\mu_0 = 0.0008Pa - s$, the following viscosity relationship for water is obtained as part of the development of the current fluid properties model,

$$\mu(p,T) = 0.0008[1 - 6e^{-5}(T - T_0) + 4e^{-7}(T - T_0)^2 + 1e^{-8}(p - p_0) + 7e^{-12}(p - p_0)^2] \quad \text{(A.4)}$$

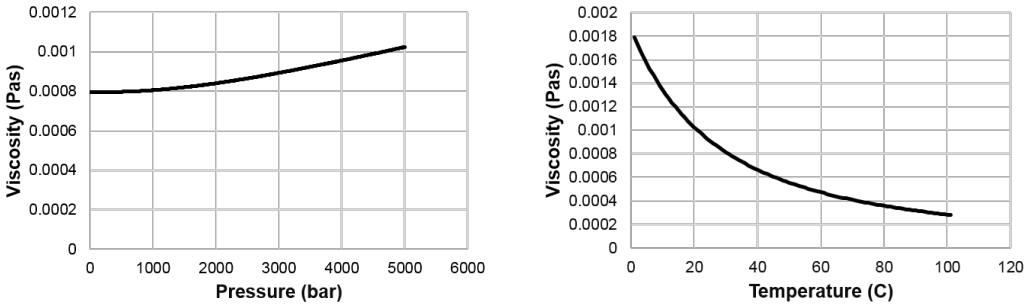

(a) (b)

Figure A.2. Variation of viscosity of water with (a) Pressure and (b) Temperature.

The resulting viscosity from the above equation has units of $Pa - s$ whereas the inputs for pressure has units of *bar* and temperature units are in °C.

B. FLOW FACTORS USED IN THE MIXED-TEHD LATERAL LUBRICATING GAP MODEL

This section presents the non-dimensional relationships for the flow factors used in modeling the average flow Reynolds equations in EGMs. These expressions are based on the assumption of a Gaussian asperity height distribution (as expressed in Equation (B.1)) where z is the asperity height and μ_h is the mean of the distribution) on both the interacting surfaces in the lubricating interfaces and are dependent only on the film thickness and the surface roughness parameter R_q. An isotropic surface was also assumed in the present case and thus the asperity aspect ratio reduces to $\gamma = 1$. The equations presented here are obtained from the works of [37, 94]. Further details regarding the derivation of these expressions can be found in these works.

$$\phi(z) = \frac{1}{R_q\sqrt{2\pi}} \exp \quad \frac{(z-\mu_h)^2}{2R_q^2} \Bigg) \Bigg(\tag{B.1}$$

The pressure flow factor ϕ_x can be expressed with the help of the following relationship where the value of $C = 0.9$ and $r = 0.56$,

$$\phi_x = 1 - C\exp(-r(h/R_q)) \tag{B.2}$$

The empirical relationship for the shear flow factor ϕ_s can be determined by the following equation where $A_1 = 1.899$, $\alpha_1 = 0.98$,$\alpha_2 = 0.92$, $\alpha_3 = 0.05$, $A_2 = 1.126$,

$$\phi_s = A_1\left(\frac{h}{R_q}\right)^{\alpha_1} \exp\left(-\alpha_2\frac{h}{R_q} + -\alpha_3\frac{h}{R_q}\right)\Bigg(: h/R_q \leq 5 \tag{B.3}$$

$$\phi_s = A_2 \exp\Bigg(\Bigg(-0.25\left(\frac{h}{R_q}\right)\Bigg)\Bigg(: h/R_q{>}5 \tag{B.4}$$

Contact flow factor ϕ_c for rough surfaces are presented in the following equation,

$$\phi_c = \exp \quad -0.6912 + 0.782\left(\frac{h}{R_q}\right)\Bigg(- 0.304\left(\frac{h}{R_q}\right)^2 + 0.0401\left(\frac{h}{R_q}\right)^3\Bigg) : h/R_q \leq 3 \tag{B.5}$$

$$\phi_c = 1 : h/R_q{>}3 \tag{B.6}$$

The different shear stress factors used for calculating the modified form of the shear stress equation can be expressed with the help of the following equations where $D = 1.40$, $s = 0.66$, $A_3 = 11.1$, $\alpha_4 = 2.31$, $\alpha_5 = 2.39$, $\alpha_6 = 0.11$,

$$\phi_{fp} = 1 - D\exp\left(-s\left(\frac{h}{R_q}\right)\right) \tag{B.7}$$

$$\phi_{fs} = A_3\left(\frac{h}{R_q}\right)^{\alpha_4} : h/R_q \leq 7 \tag{B.8}$$

$$\phi_{fs} = 0 : h/R_q{>}7 \tag{B.9}$$

A special relationship has been obtained in the work of [36] for the flow factor ψ_f as represented below where $z = h/3R_q$,$\epsilon^* = 0.0033$. Equation (B.10) is valid for $h/R_q \leq 3$ and Equation (B.11) holds for $h/R_q{>}3$.

$$\begin{aligned}\phi_f = \frac{35}{32}z\Bigg\{&(1-z)^2\ln\frac{z+1}{\epsilon^*} + \frac{1}{60}\Big[-55+\\ &z\Big(132 + z\big(345 + z(-160 + z(-405 + z(60 + 147z)))\big)\Big)\Big]\Bigg\}\end{aligned} \tag{B.10}$$

$$\phi_f = \frac{35}{32}z\Big\{(1-z)^3\ln\frac{z+1}{z-1} + \frac{z}{15}\Big[66 + z^2(30z^2 - 80)\Big]\Big\} \tag{B.11}$$

VITA

VITA

Divya Thiagarajan was born and raised in Chennai, India. After obtaining her bachelors in mechanical engineering from Anna University, India with honors distinction, she joined the Maha Fluid Power Research Center at Purdue University to pursue masters in mechanical engineering in 2012. Her masters thesis was supervised by Prof. Andrea Vacca and focused on designing optimal axial balance solutions for efficient external gear machines. She continued her doctoral work in mechanical engineering from 2014 under the supervision of Prof. Vacca and her dissertation research involved modeling lubricating flow in external gear machines. Her graduate school research resulted in a patent, several publications in international journals and conferences including a best paper award. Divya was also a recipient of Bilsland Dissertation Fellowship from the Purdue Graduate school, which is awarded to outstanding PhD students at Purdue in their final year of study.